

ELECTRONS, X-RAYS, AND SOIL AUGERS: PROBING SOIL ORGANO-
MINERAL INTERACTIONS WITH A CROSS-SCALE ANALYTICAL TOOLBOX

A Dissertation

Presented to the Faculty of the Graduate School

of Cornell University

In Partial Fulfillment of the Requirements for the Degree of

Doctor of Philosophy

by

Angela Ruth Possinger

August 2019

© 2019 Angela Ruth Possinger

ELECTRONS, X-RAYS, AND SOIL AUGERS: PROBING SOIL ORGANO-MINERAL INTERACTIONS WITH A CROSS-SCALE ANALYTICAL TOOLBOX

Angela Ruth Possinger

Cornell University 2019

Abstract

The ability of soils to serve as a carbon (C) reservoir depends on the processes that drive the accumulation and persistence of soil organic matter (SOM). The suite of stabilizing interactions between SOM and soil minerals includes surface adsorption, complexation, and co-precipitation with mineral phases. However, organo-mineral associations are not static or indefinitely persistent, and depend on mineralogy, SOM composition, and environmental variables. Here, the differences in both SOM and mineral structure and composition between surface adsorption and co-precipitation of SOM were investigated in a semi-crystalline iron (Fe) oxide–dissolved OM (DOM) synthesis experiment. The addition of DOM during mineral co-precipitation induced changes in both DOM and Fe composition, with a bi-directional set of reactions that ultimately resulted in reduced Fe aggregation, Fe(III) reduction to Fe(II), and spatial separation of aromatic- and non-aromatic C forms. The study of redox and associated processes on organo-mineral interactions was expanded to the landscape scale by testing the effect of legacy soil saturation frequency on composition and mineralizability of mineral-associated SOM. From low to high saturation frequency, a shift from Fe(III)-organic to Fe(II) and Al-dominated SOM interactions was detected

using bulk X-ray adsorption and nuclear magnetic resonance (NMR) spectroscopy. At high saturation frequency, an order of magnitude increase in mineralizability of dissolved organic carbon (DOC) mobilized during cyclic aerobic-anaerobic incubation was identified. In addition to field-scale studies and synthesis experiments, direct observation and characterization of both organo-mineral and organo-organic interfaces in natural soil samples was conducted at the <5 nm nanometer scale with cryogenic thin-sectioning and analytical electron microscopy. Enrichment of nitrogen (N) at both organo-organic and organo-mineral interfaces was detected. Alkyl C was enriched by 4.1% at an organo-organic interface, in contrast to enrichment of N-substituted carboxylic C (by 32%) at an organo-mineral interface. Identification of unique organo-organic in comparison to organo-mineral interfaces provides novel insights into previously unknown mechanisms of SOM stabilization, and challenges the assumption of OM accumulation in ordered gradients as a function of distance to mineral surfaces. Collectively, these observations provide motivation to shift the one-dimensional conceptual model of SOM organo-mineral association to account for organo-organic interactions and other spatially complex, multidimensional interaction processes.

BIOGRAPHICAL SKETCH

Angela grew up exploring the woods, river, and wetlands near her home in Southeastern Massachusetts. As part of her homeschool education, she developed lifelong interests in literature, music, art, travel, gardening, theater, and the natural sciences. She studied the topics of forestry, water, wildlife, and soils as part of a 4-H Envirothon team, and became a residential volunteer at an educational farm associated with Heifer International. These experiences led to an interest in sustainable agriculture, which she pursued through undergraduate studies in biology and chemistry with a focus on plant-soil interactions at Roger Williams University (Bristol, RI). She conducted undergraduate research on buckwheat (*Fagopyrum esculentum*) root exudation and phosphorus uptake with research advisors Loren Byrne and Nancy Breen. She continued research in soil health and agricultural amendment materials (such as seaweed) with a M.S. in Biological and Environmental Sciences with a focus on Sustainable Agriculture and Food Systems at the University of Rhode Island (advisor José Amador). At Cornell University, Angela's research focused on soil organic matter formation and persistence. As a trainee in the Cross-Scale Biogeochemistry and Climate NSF IGERT program, she conducted research on interactions between soil minerals and organic matter, from the nanometer to the landscape scale.

This dissertation is dedicated to the memory of Max and Olga Houtzager, lifelong stewards of the land who passed on their appreciation of soil to me as a young child.

ACKNOWLEDGMENTS

My advisor, Johannes Lehmann, has been a consistent, thoughtful, and creative guide through the development of the research process, from helping think through preliminary ideas to refining the final research product. Committee members Joseph Yavitt and Louis Derry have provided essential perspectives, ideas, and feedback. The Cross-Scale Biogeochemistry NSF IGERT program provided funding for a majority of my Ph.D. work and many opportunities for broader impacts. I am indebted to Akio Enders and Kelly Hanley of the Lehmann Lab. Akio's technical skills and creativity allow for research ideas that would otherwise be impossible, and Kelly's capability to balance lab technical work, administration, and the overall needs of the lab is critical to our lab's function. The many members and associates of the Lehmann Lab and associates through the years have offered feedback, ideas, and friendship: Leilah Krounbi, Rachel Hestrin, Dominic Woolf, Laurel Lynch, Tara Clancy, Tianran Sun, Katie Grant, and many others have been directly involved research problem solving.

Friends Collin Edwards and David "Dgs" Sinclair and the Cornell Statistical Consulting Unit have provided much help with statistics and data analysis. I am thankful to my parents, John and Nancy Possinger, my extended family, and lifelong friends for providing constant encouragement. Michael Schmidt has never tired of discussions about science, long walks exploring Ithaca and new places, trips to see the Auburn Doubledays, and being a faithful and patient supporter. I am truly grateful for lasting friendships from my time in Ithaca (First Presbyterian Church of Ithaca, BESS, The Barn, D&D, Sunday Disk Toss, brunch at Northstar, the Soil and Crop Sciences GSA, the GPSPB, Grassroots, and many more).

TABLE OF CONTENTS

	Page
Biographical Sketch.....	v
Dedication.....	vi
Acknowledgements.....	vii
Table of Contents.....	viii
List of Figures.....	xv
List of Tables.....	xviii
List of Abbreviations.....	xix
List of Symbols.....	xx
Preface.....	xxi
Chapter 1: NANOMETER-SCALE CHANGES TO IRON AND CARBON CHEMISTRY IN DISSOLVED ORGANIC MATTER- FERRIHYDRITE CO-PRECIPTATES.....	1
1. Introduction.....	1
2. Methods.....	5
2.1 Experiment Overview.....	5
2.2 Dissolved Organic Matter Preparation.....	5
2.3 Co-Precipitation and Adsorption Sample Preparation.....	6
2.4 Total Carbon.....	7
2.5 Carbon K-edge XANES.....	8
2.6 High Resolution Imaging and Spectroscopy (STEM-EELS).....	9

2.6.1 STEM-EELS Mapping.....	9
2.6.2 Elemental Spatial Distribution.....	10
2.6.3 Iron Distribution and Clustering.....	11
2.6.4 EELS Carbon and Iron Fine Structure.....	12
2.7 Iron K-edge X-ray Absorption Spectroscopy.....	13
3. Results.....	16
3.1 Total Carbon Analysis.....	16
3.2 Carbon K-edge X-ray Absorption Spectroscopy.....	16
3.3 High Resolution Imaging and Spectroscopy (STEM-EELS).....	18
3.3.1 STEM-EELS Imaging Overview.....	18
3.3.2 Elemental Spatial Distribution.....	19
3.3.3 Iron Distribution and Clustering.....	19
3.3.4 EELS Carbon and Iron Fine Structure.....	22
3.4 Iron K-edge X-ray Absorption Spectroscopy.....	28
4. Discussion.....	34
4.1 Co-precipitation vs. Adsorption: Changes to Fe Chemistry.....	34
4.1.1 Iron Spatial Association and Clustering.....	34
4.1.2 Iron Oxidation State.....	35
4.1.3 Iron-Organic Bonding.....	36
4.2 Co-precipitation vs. Adsorption: Changes in Carbon Chemistry and Spatial Distribution.....	36
5. Conclusions.....	40

6. Acknowledgements.....	41
Chapter 1 References.....	43
Chapter 2: ORGANO-MINERAL INTERACTIONS AND SOIL	
CARBON MINERALIZABILITY WITH VARIABLE SATURATION	
FREQUENCY.....	47
1. Introduction.....	47
2. Materials and Methods.....	50
2.1 Study Site Description.....	50
2.2 Mineral-Organic Interaction Dynamics.....	52
2.2.1 Basil Soil Characterization.....	52
2.2.2 Metal Selective Extraction.....	52
2.2.3 Elemental Spatial Relationships.....	54
2.2.4 Bulk Soil Statistical Analyses.....	55
2.3 Probing Iron-Carbon Interactions: X-ray Absorption and NMR	
Spectroscopy.....	55
2.3.1 Fe K-edge XAS.....	55
2.3.2 Carbon K-edge XAS.....	58
2.3.3 ¹³ C-NMR Variable Contact Time Experiments.....	59
2.3.4 Statistical Analyses of Spectroscopic Results.....	60
2.4 Anaerobic-Aerobic Cycle Incubation.....	60
3. Results.....	63
3.1 Mineral-Organic Interaction Dynamics.....	63

3.1.1 Basic Soil Characterization	63
3.1.2 Selective Extractions.....	64
3.1.3 Elemental Spatial Relationships.....	68
3.1.4 Mineral Soil Drivers of C Content.....	70
3.2 Probing Iron-Carbon Interactions: X-ray Absorption and NMR Spectroscopy.....	70
3.2.1 Fe K-edge XAS.....	70
3.2.2 Carbon K-edge XANES.....	75
3.2.3 ¹³ C-NMR Variable Contact Time Experiment.....	76
3.3 Anaerobic-Aerobic Cycle Incubation	76
4. Discussion.....	80
4.1 Contrasting Mineral-Organic Interactions Across Saturation Frequency.....	80
4.2 Mechanisms of Organo-Mineral Interaction.....	84
4.3 Implications for SOC Mineralizability.....	86
5. Conclusions.....	88
6. Acknowledgements.....	89
Chapter 2 References.....	90
 Chapter 3: ORGANO-ORGANIC AND ORGANO-MINERAL INTERFACES IN SOIL AT THE NANOMETER SCALE.....	 96
1. Introduction.....	96
2. Materials and Methods.....	98

2.1 Study Site and Sample Collection.....	98
2.2 Cryogenic Thin-Section Preparation.....	99
2.2.1 Background.....	99
2.2.2 Aggregate Cryo-Ultramicrotome Pre-Thinning.....	100
2.2.3 Cryo-FIB Transfer.....	101
2.2.4 Cryogenic FIB Milling.....	101
2.3 Cryogenic EDX Analysis.....	101
2.4 Cryogenic STEM-EELS.....	102
2.5 Image and Spectral Analysis.....	103
2.5.1 Electron Energy Loss Spectra.....	103
2.5.2 EELS Fine Structure Analysis.....	104
3. Results and Discussion.....	105
3.1 Organo-Mineral Interface: Enrichment of N and Oxidized C.....	105
3.2 Patchiness in OM Composition at the Micrometer Scale.....	108
3.3 Organo-Organic Interface: Enrichment of N and Alkyl C.....	112
3.4 Implications for Soil Carbon Modeling and Sequestration.....	116
4. Acknowledgements.....	117
Chapter 3 References.....	119
Appendix.....	124
A1. Supplementary Methods.....	124
A1.1 Chapter 1 Supplementary Methods.....	124
A1.1.1 EELS Image Selection for Spatial Analysis.....	124

A1.2 Chapter 2 Supplementary Methods.....	124
A1.2.1 Random Forest Modeling.....	124
A1.2.2 Fe K-edge XANES Estimation of Reduced Fe(II).....	125
A1.2.3 Carbon K-edge XANES Damage Test.....	125
A1.2.4 Nuclear Magnetic Resonance Variable Contact Time (NMR VCT) Calculation.....	126
A1.3 Chapter 3 Supplementary Methods.....	126
A1.3.1 Sample Damage Assessment of Cryo-FIB and Cryo- STEM-EELS Techniques.....	126
A1.3.2 Room Temperature FIB Sample Preparation.....	127
A1.3.3 Cryo-STEM-EELS Damage Assessment	128
A1.3.3.4 Organo-Organic Interface Sample (Titan Instrument).....	128
A1.3.3.5 Organo-Mineral Interface Sample (F20 Instrument).....	129
A2. Supplementary Results and Discussion.....	130
A2.1 Chapter 1 Supplementary Results and Discussion.....	130
A2.1.1 Chemical Composition of DOM: Rationale for Pooled Observations.....	130
A2.2 Chapter 2 Supplementary Results and Discussion.....	130
A2.2.1 Carbon K-edge XANES Damage Test.....	130
A2.3 Chapter 3 Supplementary Results and Discussion.....	131

A2.3.1 Room Temperature vs. Cryogenic Temperature FIB Damage.....	131
A2.3.2 Cryo-STEM-EELS Damage Assessment.....	131
A2.3.2.1 Organo-Organic Sample (Titan Instrument).....	131
A2.3.2.2 Organo-Mineral Sample (F20 Instrument).....	132
Appendix References.....	133
A3. Supplementary Figures.....	135
A4. Supplementary Tables.....	165

LIST OF FIGURES

Figure	Description	Page
1.1	Normalized carbon K-edge X-ray absorption near-edge structure for co-precipitated and adsorbed dissolved organic matter	17
1.2	Co-precipitated and adsorbed ferrihydrite-organic matter overview scanning transmission electron microscope image and electron energy loss spectroscopy map	18
1.3	Co-precipitation and adsorption pixel intensity and iron-carbon correlation relationship to iron clustering	20
1.4	Average carbon and iron electron energy loss spectra for co-precipitation and adsorption samples	23
1.5	Carbon and iron electron energy loss multivariate curve resolution results and component spatial correlation	24
1.6	Carbon and iron fine structure changes across a 26-nm transect in a co-precipitate electron energy loss map	29
1.7	Correlation of aromatic/non-aromatic C ratio to reduced Fe(II) across 26-nm transect in co-precipitate electron energy loss map	30
1.8	Visualization of changes in iron K-edge X-ray absorption near-edge structure	31
1.9	Simplified schematic of proposed spatial distribution of co-precipitate carbon and iron forms	38
2.1	Simplified schematic of variation in mineral soil profile horizons and transport associated with Spodosol hydrogeological units	51
2.2	Bulk and extractable soil iron and aluminum	65
2.3	Water and hydroxylamine-extractable carbon, iron, and aluminum	68
2.4	Nanoscale secondary ion mass spectrometry images and elemental spatial correlation	69
2.5	Soil iron oxidation state determined by iron K-edge X-ray absorption near edge structure	73
2.6	Iron extended X-ray absorption fine structure and X-ray absorption near edge structure linear combination fitting	75
2.7	Carbon K-edge X-ray absorption near edge structure spectra and functional group composition	77
2.8	Carbon (^{13}C) nuclear magnetic resonance variable contact time experiment effect magnitude and proton relaxation time	79
2.9	Carbon mineralizability, dissolved organic carbon, and reduced Fe(II) as affected by anaerobic-aerobic cycle incubation	81

3.1	High-resolution cryo-imaging and spectroscopy of organic matter-mineral interface in a volcanic soil sample	106
3.2	High resolution imaging and spectroscopy of organo-organic interface with cryo-electron microscopy and electron energy loss	109
3.3	Distinct combinations of elemental ratios across organo-organic interface	110
3.4	Shifting conceptual view of organo-mineral and organo-organic interfaces in soil	115
A3.1.1	Electron energy loss spectroscopy multivariate curve resolution output results for range of co-precipitate and adsorption samples	135
A3.1.2	Total carbon of co-precipitation and adsorption samples	136
A3.1.3	Gaussian and arctangent functions for carbon X-ray absorption near edge structure	137
A3.1.4	Spatial quantification of iron clustering with Ripley's K(t) function	138
A3.1.5	Average carbon and iron electron energy loss spectra for regions of co-precipitate image transect	139
A3.1.6	Iron X-ray absorption near edge structure Gaussian fit for reduced Fe(II)	140
A3.1.7	Iron extended X-ray absorption fine structure and X-ray absorption near edge structure K- and R-space	141
A3.1.8	Iron standard extended X-ray absorption fine structure K-space	142
A3.2.1	Sampling location map and predicted locations of hydrogeological units at Hubbard Brook Watershed 3	143
A3.2.2	Bulk soil and extractable manganese	144
A3.2.3	Random Forest predicted vs. observed soil carbon content	145
A3.2.4	Iron X-ray absorption near edge structure Gaussian fit for reduced Fe(II) in standard compounds and minerals	146
A3.2.5	Iron extended X-ray absorption fine structure and X-ray absorption near edge structure linear combination spectral fit results	147
A3.2.6	Carbon K-edge X-ray absorption near edge structure spectra and functional group composition	148
A3.2.7	Carbon nuclear magnetic resonance signal intensity as a function of contact time	149
A3.2.8	Damage test assessment for carbon K-edge X-ray absorption near-edge structure	150
A3.3.1	Electron dispersive X-ray spectrum for organo-mineral interface soil sample	151
A3.3.2	Overview electron microscopy images and electron dispersive X-ray map for organo-mineral interface soil sample	152

A3.3.3	Electron dispersive X-ray spectrum for organo-organic interface soil sample	153
A3.3.4	Cryogenic focused ion beam sample preparation for soil samples	154
A3.3.5	Simplified schematic of focused ion beam milling approaches	155
A3.3.6	Organo-mineral interface electron energy loss spectra	156
A3.3.7	Adjacent carbon to organo-mineral interface electron energy loss spectra	157
A3.3.8	Organo-organic interface overview image	158
A3.3.9	Organo-organic interface high-resolution image and electron energy loss spectra	159
A3.3.10	Three-component multivariate curve resolution	161
A3.3.11	Organo-organic interface (1x44 pixel resolution)	162
A3.3.12	Cryogenic vs. room temperature focused ion beam sample preparation	163
A3.3.13	Carbon K-edge electron energy loss spectroscopy damage assessment	164

LIST OF TABLES

Table	Description	Page
1.1	Iron K-edge X-ray absorption near-edge structure results for adsorption and co-precipitation samples	32
1.2	Iron K-edge X-ray absorption near-edge structure results for standard compounds and minerals	33
2.1	Variable importance ranking for Random Forest model	71
2.2	Anaerobic-aerobic incubation soluble element, mineralization, and dissolved organic carbon ANOVA table	82
A4.1.1	Carbon K-edge X-ray absorption near edge structure deconvolution model parameters	165
A4.1.2	Carbon K-edge X-ray absorption near edge structure results for dissolved organic matter and co-precipitate/adsorption samples	166
A4.1.3	Carbon K-edge X-ray absorption near edge structure deconvolution results for standard compounds	167
A4.2.1	Field descriptions of sampling locations for hydrogeological units with varying saturation frequency	168
A4.2.2	Field soil profile descriptions for hydrogeological units with varying saturation frequency	169
A4.2.3	Tree (>0.1 m diameter) species identification for sampling locations	171
A4.2.4	List of sample subsets used for incubation and spectroscopic characterization	172
A4.2.5	Average bulk characterization data for mineral soils	173
A4.2.6	Average selective metal extraction values for mineral soils	174
A4.2.7	Iron K-edge X-ray absorption near-edge structure results for soil samples	175
A4.2.8	Carbon K-edge X-ray absorption near-edge structure results for soil samples	176
A4.3.1	Soil properties of samples used for cryogenic electron microscopy	177
A4.3.2	Summary of data collection parameters for cryogenic electron microscopy	178
A4.3.3	Calculated ratios of elemental enrichment for organo-mineral interface	180
A4.3.4	Calculated ratios of elemental enrichment across organo-organic interface	181

LIST OF ABBREVIATIONS

SOM	Soil organic matter
SOC	Soil organic carbon
Cryo-STEM-EELS	Cryogenic scanning transmission electron microscopy- electron energy loss spectroscopy
FIB	Focused ion beam
XANES	X-ray absorption near edge structure
EXAFS	Extended X-ray absorption fine structure
NMR	Nuclear magnetic resonance
HPU	Hydropedological unit
DOM	Dissolved organic matter
VCT	Variable contact time
EDX	Electron dispersive X-ray spectroscopy
T _{1ρ} H	Proton relaxation time
CHESS	Cornell High Energy Synchrotron Source
CLS	Canadian Light Source

LIST OF SYMBOLS

r_s	Spearman Rank correlation coefficient
I_0	X-ray absorption spectroscopy incidence flux
$\mu(E)$	X-ray absorption fluorescence spectrum
$dx/d\mu(E)$	First derivative of X-ray absorption fluorescence spectrum
eV	Electron volts

PREFACE

“Life on earth depends on the non-equilibrium of systems we call plants, animals, and soils. Thermodynamics tells us that soils exist precariously -- like people. But experience tells us that both soils and people are wonderfully resistant to degradation in spite of unfavorable thermodynamic odds.”

-- Richmond J. Bartlett in Soil Physical Chemistry (Sparks, 1986)

Background and Justification

Global Implications of Soil Carbon (C) Storage

The accumulation and loss of carbon (C) from soils is a critical balance in the global C budget, with total soil C stocks (~1500-2400 Pg C) estimated to be greater than C in the atmosphere and terrestrial vegetation combined (Ciais et al., 2013). Increasing the amount of persistent SOC is consequently one pathway towards reduction of atmospheric greenhouse gases and mitigation of climate change (Lal, 2004; Minasny et al., 2017). Additionally, SOC content is a defining indicator of soil quality in agricultural systems, with increasing SOC correlated with availability of plant nutrients (e.g., nitrogen, N, and phosphorus, P), increased moisture retention, and improved structure (Karlen et al., 1997; Gugino et al., 2009). Despite the relevance of SOC cycling dynamics to both soil fertility and climate regulation, the fundamental processes regulating the stabilization and persistence of SOC are not completely understood (Lal, 2004; Jandl et al., 2013).

Historical and Emerging Views of SOC Persistence

Historically, “stable” SOC was considered to be composed of large, complex, chemically recalcitrant macromolecules resistant to decomposition, termed humic substances (Kleber and Johnson, 2010; Lehmann and Kleber, 2015). Humic substances are operationally defined based on extractability in acid or base solutions (Sparks, 2002). However, with microscopic and spectroscopic observation of natural soil samples, SOC has not been found to exist predominantly as complex humic substances but as smaller, identifiable biomolecules (Kelleher and Simpson, 2006; Lehmann et al., 2008). In contrast to chemical recalcitrance as the primary mechanism of SOC stabilization, biophysicochemical interactions among the biotic and abiotic components of soil, including associations between SOC and the mineral phase, are expected to drive the persistence of SOC (Schmidt et al., 2011).

In sediments, prevention of OC degradation via mineral associations has been widely recognized since the mid-20th century, with early studies linking organo-mineral association with reduced microbial accessibility (Oppenheimer, 1960), ultimately leading to OC burial and sequestration in large quantities on a geologic timescale (Weiler and Mills, 1965). The well-established role of mineral OC stabilization in sediments motivated a large body of research, and informed early understanding of soil organo-mineral interactions, including assumption of monolayer-equivalent surface coverage, surface area-dependent OC accumulation, and the existence of a largely inert mineral-stabilized pool (Mayer et al., 1994; Sanderman et al., 2016).

In soils, formation, transport, and fate of organo-mineral colloids and metal-organic complexes have been historically well-studied processes in soil pedogenesis and contaminant bioremediation (Allison et al., 1949; McKeague et al., 1983; Calvet, 1989), but widespread recognition of the importance of mineral protection specifically in SOC turnover and stabilization developed more recently (~1990s) (e.g., Torn et al., 1997). In particular, semi-crystalline minerals with short-range order (SRO) and high reactivity towards organic matter (e.g., the SRO iron (Fe) and aluminum (Al) oxides) are linked with SOC stabilizing interactions (Gu et al., 1994; Torn et al., 1997; Kramer et al., 2012). However, the emerging view of SOC persistence incorporates mineral protection as one of many interacting ecosystem properties (Schmidt et al., 2011), and extends beyond a focus on clay particle size/surface area (inferred in part from sediment studies) to account for mineral, SOC, and soil biotic community composition, variable organo-mineral interaction mechanisms, and fluctuating environmental conditions (Torn et al., 1997; Rasmussen et al., 2018; Woolf and Lehmann, 2019).

The view of mineral-associated SOC as largely static and inert has shifted towards recognition of organo-mineral associations as subject to dissolution and SOC mineralization, particularly with shifts in environmental variables (e.g., changing redox or soil solution conditions) (Buettner et al., 2014; Keiluweit et al., 2015). The recognized complexity of processes driving SOC persistence leaves much uncertainty in prediction of SOC accumulation. This dissertation contributes to the understanding of environmental controls on organo-mineral interactions through study of non-

equilibrium (e.g., co-precipitation) and environmentally dynamic (e.g., redox) processes influencing persistence of SOC.

Overview of Chapters

Chapter 1: Nanometer-Scale Changes to Iron and Carbon Chemistry in Dissolved

Organic Matter-Ferrihydrite Co-precipitates

Co-precipitation, or incorporation of SOC with mineral phases as they form (Kleber et al., 2015), occurs in environments with high SOC input and frequent fluctuations in mineral dissolution/precipitation. Co-precipitation is known to reduce mineral structure crystallinity and change mineral chemistry (Vilge-Ritter et al., 1999; Eusterhues et al., 2008; Mikutta et al., 2010; Mikutta, 2011; Mikutta et al., 2014), but differences in SOC composition between co-precipitation and surface adsorption are unresolved, and ultimately may affect SOC bioavailability and susceptibility to decomposition. Using laboratory synthesis experiments, hypothesized changes in spatial distribution of Fe and C in ferrihydrite ($\text{Fe}_2\text{O}_3 \cdot 0.5\text{H}_2\text{O}$)-dissolved organic matter (DOM) co-precipitates compared to adsorption were assessed using a combination of high-resolution imaging and spectroscopy and bulk spectroscopic characterization techniques.

Chapter 2: Organo-Mineral Interactions and Soil Carbon Mineralizability with

Variable Saturation Frequency

In contrast to the prevailing concept of increased moisture leading to accumulation of SOC due to decreased microbial metabolism, reducing conditions resulting from short-term saturation events in otherwise aerobic soils may drive mineral dissolution and thereby increase mobilization of mineral-associated SOC

(Buettner et al., 2014; Herndon et al., 2017; Coward et al., 2018). In this chapter, the study of redox and associated processes on organo-mineral interactions was expanded to the landscape scale by testing the effect of legacy soil saturation frequency on composition and mineralizability of mineral-associated SOM using a combination of selective extraction, bulk spectroscopy, and laboratory incubation approaches.

Chapter 3: Organo-Organic and Organo-Mineral Interfaces in Soil at the Nanometer Scale

Direct visualization and characterization of SOC and organo-mineral interactions with imaging and spectroscopy have enabled many insights informing the current view of SOC stabilization, by allowing for confirmation of proposed interaction mechanisms and discovery of new mechanisms (Lehmann et al., 2008; Chia et al., 2012; Solomon et al., 2012). Using a novel approach for cryogenic high-resolution electron microscopy and spectroscopy, imaging of organo-mineral and organo-organic interfaces in natural volcanic soil samples was conducted at the <5 nm nanometer scale, providing novel insights into previously unknown mechanisms of SOC stabilization and a shifting conceptual model of SOC spatial distribution.

REFERENCES

- Allison, F.E., Sherman, M.S., Pinck, L.A., 1949. Maintenance of soil organic matter: I. Inorganic soil colloid as a factor in retention of carbon during formation of humus. *Soil Sci.* 68, 463-478.
- Buettner, S.W., Kramer, M.G., Chadwick, O.A., Thompson, A., 2014. Mobilization of colloidal carbon during iron reduction in basaltic soils. *Geoderma* 221-222, 139-145.
- Calvet, R., 1989. Adsorption of organic chemicals in soils. *Environ. Health Perspec.* 83, 145-177.
- Chia, C.H., Munroe, P., Joseph, S.D., Lin, Y., Lehmann, J., Muller, D.A., Xin, H.L., Neves, E., 2012. Analytical electron microscopy of black carbon and microaggregated mineral matter in Amazonian Dark Earth. *J. Micros.* 245(2), 129-139.
- Ciais, P., Sabine, C., Bala, G., Bopp, L., Brovkin, V., Canadell, J., Chhabra, A., DeFries, R., Galloway, J., Heimann, M., Jones, C., Le Quéré, C., Myneni, R.B., Piao, S., Thornton, P., 2013. Carbon and other biogeochemical cycles, in: Stocker, T.F., Qin, D., G.-K. Plattner, G.-K., Tignor, M., Allen, S.K., Boschung, J., Nauels, A., Xia, Y., Bex, V., Midgley, P.M. (Eds.), *Climate Change 2013: The Physical Science Basis. Contribution of Working Group I to the Fifth Assessment Report of the Intergovernmental Panel on Climate Change.* Cambridge University Press, Cambridge, UK and New York, NY, pp. 465–570.
- Coward, E.K., Thompson, A., Plante, A.F., 2018. Contrasting Fe speciation in two humid forest soils: Insight into organomineral associates in redox-active environments. *Geochim. Cosmochim. Acta*, 238, 68-84.
- Eusterhues, K., Wagner, F.E., Häusler, W., Hanzlik, M., Knicker, H., Totsche, K.U., Kögel-Knabner, I., Schwertmann, U., 2008. Characterization of ferrihydrite-soil organic matter coprecipitates by X-ray diffraction and Mossbauer spectroscopy. *Environ. Sci. Technol.* 42, 7891-7897.
- Gu, B., Schmitt, J., Chen, Z., Liang, L., McCarthy, J.F., 1994. Adsorption and desorption of natural organic matter on iron oxide: mechanisms and models. *Environ. Sci. Technol.* 28, 38-46.
- Gugino, B.K., Idowu, O.J., Schindelbeck, R.R., van Es, H.M., Wolfe, D.W., Moebius-Clune, B.N., Thies, J.E., Abawi, G.S., 2009. *Cornell Soil Health Assessment Training Manual*, 2nd Ed. Cornell University, Ithaca, NY.

- Herndon, E., AlBashaireh, A., Singer, D., Chowdhury, T.R., Gu, B., Graham, D., 2017. Influence of iron redox cycling on organo-mineral associations in Arctic tundra soil. *Geochim. Cosmochim. Acta* 207, 210-231.
- Jandl, R., Rodeghiero, M., Martinez, C., Cotrufo, M.F., Bampa, F., van Wesemael, B., Harrison, R.B., Guerrini, I.A., Richter Jr., D. deB., Rustad, L., Lorenz, K., Chabbi, A., Miglietta, F., 2014. Current status, uncertainty, and future needs in soil organic carbon monitoring. *Sci. Tot. Env.* 468-469, 376-383.
- Karlen, D.L., Mausbach, M.J., Doran, J.W., Cline, R.G., Harris, R.F., Schuman, G.E., 1997. Soil quality: A concept, definition, and framework for evaluation. *Soil Sci. Soc. Am. J.* 61, 4-10.
- Kelleher, B.P., Simpson, A.J., 2006. Humic substances in soils: are they really chemically distinct? *Environ. Sci. Technol.* 40, 4605-4611.
- Keiluweit, M., Bougoure, J.J., Nico, P.S., Pett-Ridge, J., Weber, P.K., Kleber, M., 2015. Mineral protection of soil carbon counteracted by root exudates. *Nat. Clim. Chang.* 5, 588-295.
- Kleber, M., Johnson, M.G., 2010. Advances in understanding the molecular structure of soil organic matter: Implications for interactions in the environment. *Adv. Agron.* 106, 77-142.
- Kleber, M., Eusterhues, K., Keiluweit, M., Mikutta, C., Mikutta, R., Nico, P.S., 2015. Mineral-organic associations: formation, properties, and relevance in soil environments. *Adv. Agron.* 130, 1-140.
- Kleber, M., Sollins, P., Sutton, R., 2007. A conceptual model of organo-mineral interactions in soils: self-assembly of molecular fragments into zonal structural on mineral surfaces. *Biogeochem.* 85(1), 9-24.
- Kramer, M.G., Sanderman, J., Chadwick, O.A., Chorover, J., Vitousek, P.M., 2012. Long-term carbon storage through retention of dissolved aromatic acids by reactive particles in soil. *Global Change Biol.* 18(8), 2594-2605.
- Lal, R., 2004. Soil carbon sequestration impacts on global climate change and food security. *Science* 304, 1623-1627.
- Lehmann, J., Kleber, M., 2015. The contentious nature of soil organic matter. *Nature* 528, 60-68.
- Lehmann, J., Solomon, D., Kinyangi, J., Dathe, L., Wirrick, S., Jacobsen, C., 2008. Spatial complexity of soil organic matter forms at nanometre scales. *Nature Geosci.* 1, 238-242.

- Mayer, L.M., 1994. Relationships between mineral surfaces and organic carbon concentrations in soils and sediments. *Chem. Geol.* 114(3–4), 347-363.
- Mikutta, C., 2011. X-ray absorption spectroscopy study on the effect of hydroxybenzoic acids on the formation and structure of ferrihydrite. *Geochim. Cosmochim. Acta* 75, 5122-5139.
- Mikutta, C., Frommer, J., Voegelin, A., Kaegi, R., Kretzschmar, R., 2010. Effect of citrate on the local Fe coordination in ferrihydrite, arsenate binding, and ternary arsenate complex formation. *Geochim. Cosmochim. Acta* 74, 5574-5592.
- Mikutta, R., Lorenz, D., Guggenberger, G., Haumaier, L., Freund, A., 2014. Properties and reactivity of Fe-organic matter associations formed by coprecipitation versus adsorption: Clues from arsenate batch adsorption. *Geochim. Cosmochim. Acta* 144, 258-276.
- Minasny, B., Malone, B.P., McBratney, A.B., Angers, D.A., Arrouays, D., Chambers, A., Chaplot, V., Chen, Z-S., Cheng, K., Das, B.S., Field, D.J., Gimona, A., Hedley, C.B., Hong, S.Y., Mandal, B., Marchant, B.P., Martin, M., McConkey, B.G., Mulder, V.L., O'Rourke, S., Richer-de-Forges, A.C., Odeh, I., Padarian, J., Paustian, K., Pan, G., Poggio, L., Savin, I., Stolbovoy, V., Stockmann, U., Sulaeman, Y., Tsui, C-C., Vågen, T-G., Wasemael, B, Winowiecki, L., 2017. Soil carbon 4 per mille. *Geoderma* 292, 59-86.
- McKeague, J.A., DeConinck, F., Franzmeier, D.P., 1983. Spodosols, in: Wilding, L.P., Smeck, N.E., Hall, G.F. (Eds.), *Developments in Soil Science (Volume 11 Part B), Pedogenesis and Soil Taxonomy II. The Soil Orders*. Elsevier Science Publishing Company Inc., New York, NY, pp. 217-252.
- Oppenheimer, C.H., 1960. Bacterial activity in sediments of shallow marine bays. *Geochim. Cosmochim. Acta* 18, 244-260.
- Rasmussen, C., Heckman, K., Weider, W.R., Keiluweit, M., Lawrence, C.R., Berhe, A.A., Blankinship, J.C., Crow, S.E., Druhan, J.L., Hicks Pries, C.E., Marin-Spiotta, E., Plante, A.F., Schädel, C., Schimel, J.P., Sierra, C.A., Thompson, A., Wagai, R., 2018. Beyond clay: towards an improved set of variables for predicting soil organic matter content. *Biogeochem.* 137(3), 297-306.
- Sanderman, J., Baisden, W.T., Fallon, S., 2016. Redefining the inert organic carbon pool. *Soil Biol. Biochem.* 92, 149-152.
- Schmidt, M.W.I., Torn, M.S., Abiven, S., Dittmar, T., Guggenberger, G., Janssens, I.A., Kleber, M., Kögel-Knabner, I., Lehmann, J., Manning, D.A.C.,

- Nannipieri, P., Rasse, D.P., Weiner, S., Trumbore, S.E., 2011. Persistence of soil organic matter as an ecosystem property. *Nature* 478, 49-56
- Solomon, D., Lehmann, J., Harden, J., Wang, J., Kinyangi, J., Heymann, K., Karunakaran, C., Lu, Y., Wirick, S., Jacobsen, C., 2012. Micro- and nano-environments of carbon sequestration: Multi-element STXM-NEXAFS spectromicroscopy assessment of microbial carbon and mineral associations. *Chem. Geol.* 329(3), 53-73.
- Sparks, D.L., 2002. *Environmental Soil Chemistry*, 2nd Edition. Academic Press, San Francisco, CA.
- Sparks, D.L., 1986. *Soil Physical Chemistry*. CRC Press Inc., Boca Raton, FL.
- Torn, M.S., Trumbore, S.E., Chadwick, O.A., Vitousek, P.M., Hendricks, D.M., 1997. Mineral control of soil organic carbon storage and turnover. *Nature* 389, 170-173.
- Vilge-Ritter, A., Rose, J., Masion, A., Bottero, J.Y., Laine, J.M., 1999. Chemistry and structure of aggregates formed with Fe-salts and natural organic matter. *Colloids Surf. A* 147, 297-308.
- Weiler, R.R., Mills, A.A., 1965. Surface properties and pore structure of marine sediments. *Deep Sea Res.* 12, 511-529.
- Wolf, D., Lehmann, J., 2019. Microbial models with minimal mineral protection can explain long-term soil organic carbon persistence. *Sci. Rep.* 9, 6522.

CHAPTER 1

NANOMETER-SCALE CHANGES TO IRON AND CARBON CHEMISTRY IN DISSOLVED ORGANIC MATTER-FERRIHYDRITE CO-PRECIPTATES

1. Introduction

The potential for soil to act as a carbon (C) reservoir is limited by the environmental drivers of soil organic matter (SOM) accumulation, including interactions between SOM and soil minerals, which are expected to vary widely with geophysical variables (e.g., climate) (Deng and Dixon, 2002; Schmidt et al., 2011; Lehmann and Kleber, 2015). The spatial and chemical complexity of SOM motivates the need to account for non-equilibrium SOM stabilization processes, such as co-precipitation of dissolved organic matter (DOM) with newly-formed minerals in the soil solution (Kleber et al., 2015). Co-precipitation is a pathway of organo-mineral interaction that may allow for greater C accumulation than would be expected based on surface coverage alone. In the environment, DOM-mineral co-precipitation is an especially relevant process in natural wetlands, rice paddies, hydric soils, or other zones of fluctuating anaerobic and aerobic conditions with abundant DOM (Chen et al., 2014). Co-precipitates can also be found in well-drained soils with microsites of oxygen (O₂) depletion, such as the rhizosphere, suggesting that the process may be common across terrestrial and aquatic ecosystems (Kleber et al., 2015). As such, DOM-mineral co-precipitates could be an important contribution to overall soil C stocks, and their properties relevant for describing soil C persistence.

Surface adsorption of DOM to pre-existing minerals and co-precipitation processes are expected to differ in their spatial and chemical composition. Co-precipitation with organic compounds has been linked to disruption of mineral structure and slowed crystallization, largely shown through experiments using ferrihydrite (nominally $\text{Fe}_2\text{O}_3 \cdot 0.5\text{H}_2\text{O}$) both with model C compounds (Mikutta et al., 2010; Mikutta, 2011) and natural OM (Vilge-Ritter et al., 1999; Henneberry et al., 2012). Similarly, increased Fe-organic bond formation has been demonstrated for co-precipitation compared to adsorption (Chen et al., 2014; Chen et al., 2016). These structural changes in organo-mineral associations may have relevance for microbial degradation or abiotic reduction (Shimizu et al., 2013; Eusterhues et al., 2014; Mikutta et al., 2014).

Additionally, co-precipitation with mixed soluble Fe(II)/Fe(III) phases has shown to increase in the presence of insoluble Fe(II) (Henneberry et al., 2012; Fritzsche et al., 2015), and co-precipitation of initially only oxidized Fe(III) has also been shown to induce Fe reduction in model systems (Mikutta, 2011). However, the presence of a reduced Fe phase after co-precipitation of natural OM with Fe(III) has been rarely detected, even across a range of C:Fe ratios, with either no detection of Fe(II) or no attempt to distinguish Fe redox state (Vilge-Ritter et al., 1999; Chen et al., 2014; Chen et al., 2016). Consequently, though changes to mineral structure have become an accepted characteristic of DOM-Fe co-precipitates, uncertainty still exists in the degree and nature of changes to Fe speciation. Additionally, structural changes have been largely assessed through bulk characterization (e.g., X-ray diffraction), and

statistical spatial analysis of Fe spatial distribution as a result of co-precipitation vs. adsorption is lacking.

The potential for physical occlusion of DOM via co-precipitation with relatively little change compared to its original composition has led to expectation of less-selective retention compared to adsorption (Kleber et al., 2015). Yet, many combined potential interaction processes have been proposed, including complex formation and precipitation, occlusion, and surface adsorption (Kleber et al., 2015). Co-precipitation as a predominantly physical incorporation, lacking bonding interactions that otherwise limit microbial accessibility, has been linked to increased biotic and abiotic SOM reactivity (Kleber et al., 2015). In contrast, selective incorporation of C functional groups in co-precipitates compared to source DOM has also been detected, but the C form preferentially retained varies widely: experiments with bulk spectroscopic characterization of natural OM-ferrhydrite co-precipitates have shown both an increase (Chen et al., 2014) and decrease (Chen et al., 2016) in aromatic C, and an increase (Eusterhues et al., 2011; Henneberry et al., 2012) and decrease (Chen et al., 2014) in polysaccharide C. Additionally, microspectroscopic imaging (e.g., scanning transmission X-ray microscopy with X-ray absorption near edge structure, STXM-XANES) with ~40-50 nm spatial resolution has shown divergent spatial distribution of DOM, with some studies identifying complete intermixing of C and Fe phases and others patchy distribution of OM in co-precipitates (Henneberry et al., 2012; Chen et al., 2014).

Previous imaging and spectroscopy approaches may be limited by spatial and chemical resolution, particularly for minerals with single nanometer-scale structure

(e.g., ferrihydrite) (Schwertmann and Taylor, 1989). Due to these divergent views on alteration of DOM forms with co-precipitation, the presence and degree of differences between adsorbed and co-precipitated DOM remain unresolved. The question underpins the assumption of divergent bioavailability, ultimately driving the C accumulation potential of co-precipitation. To provide new understanding of the DOM-Fe interaction processes distinct to co-precipitation, high-resolution visualization of spatial and chemical co-precipitate properties is needed. Scanning transmission electron microscopy with electron energy loss spectroscopy (STEM-EELS) is one approach for high-resolution structural and chemical analysis, allowing for assessment of elemental spatial distribution and Fe and C speciation. Additionally, STEM-EELS under cryogenic conditions (cryo-STEM-EELS) allows for improved analysis of soft materials and low-molecular weight elements, such as C, with reduced sample damage, allowing for both higher spatial and spectral resolution (Kourkoutis et al., 2012; Miot et al., 2014).

Here, we applied STEM-EELS and cryo-STEM-EELS to describe the structural and chemical characteristics of DOM-ferrihydrite co-precipitates in comparison to adsorption complexes at the nanometer scale: specifically, (1) Fe spatial distribution and aggregation, (2) frequency of Fe(II), (3) changes to DOM composition and spatial distribution of DOM forms, and (4) spatial association of DOM forms with Fe. Additionally, we aimed to contextualize interpretation of high-resolution measurements using bulk X-ray absorption spectroscopy (XAS) approaches commonly used for OM and Fe minerals.

2. Methods

2.1 Experiment Overview

This study used DOM derived from organic horizons of forest soils as a source of OM for co-precipitation and adsorption experiments with ferrihydrite (nominally $\text{Fe}_2\text{O}_3 \cdot 0.5\text{H}_2\text{O}$). Co-precipitation treatments were prepared by addition of DOM to dissolved Fe(III) followed by increase in pH and precipitation of a DOM-ferrihydrite co-precipitated solid phase. In contrast, adsorption treatments were prepared by addition of DOM to previously precipitated, solid-phase ferrihydrite in suspension. To assess spatial elemental distribution, changes to Fe and C composition, and spatial association between Fe and C forms, high-resolution analytical STEM-EELS was paired with bulk characterization of total C (by combustion), bulk C and Fe K-edge X-ray absorption near-edge structure (XANES), and bulk Fe K-edge extended X-ray absorption fine structure (EXAFS).

2.2 Dissolved Organic Matter Preparation

Dissolved OM was prepared by water extraction of organic horizons collected from upland forested Spodosols (Tunbridge-Lyman-Becket Series) in Watershed 3 (hydrological reference watershed) of the Hubbard Brook Experimental Forest (North Woodstock, NH). Water extracts of organic horizons were prepared from two sites with hydropedological unit (HPU) classifications following Bailey et al. (2014): (1) “Typical” podzol (lat/long 43.955533, -71.718826), and (2) “E” podzol (shallow-to-bedrock, higher elevation) (lat/long 43.956998, -71.717241). Organic horizons were collected quantitatively from three replicate profiles within <20 m distance for each site. Dominant forest vegetation was characterized for the sites by inventory of basal

area and identification to species of trees >0.1 m DBH within a 314 m² area surrounding sampling locations. Assessments of the dominant vegetation at the “typical” podzol site showed a dominance of Northern hardwood species with no coniferous tree species identified in the 314 m² sampling area. At the higher-elevation “E” podzol site, coniferous basal area increased to 35% (Chapter 2, this dissertation). For both locations, yellow birch (*Betula alleghaniensis*) occupied the most basal area of any individual species, at 11% in the typical podzol size and 17% in the E podzol site (Chapter 2, this dissertation).

Water extractions were completed using a composite of Oa horizons from 3 replicate profiles for each site. Extractions were completed at a 1:1 w/v soil (wet weight) to water ratio with overnight shaking, following by 30 min centrifugation at 12,000 rpm. DOM extracts were filtered to 0.45 μm (Whatman GF/A glass fiber filters) and stored at <9°C until used for characterization analysis and co-precipitation/adsorption experiments. Total OC content was determined for the DOM extracts using a Shimadzu TOC-V_{CPH/CPN} instrument (Shimadzu Corporation, Kyoto, Japan) in a 1% hydrochloric acid (HCl) matrix. Total C of DOM extracts was determined to be 700 mg C L⁻¹ DOM for the typical site and 469 mg C L⁻¹ for the E podzol site.

2.3 Co-precipitation and Adsorption Sample Preparation

Ferrihydrite was prepared by titration of Fe (III) nitrate (0.005 M) by addition of base (0.05 M KOH) to pH 7 (low-concentration modification of Schwertmann and Cornell, 2000) followed by purification using dialysis (1000D MWCO) until reaching electrical conductivity <3 mS m⁻¹. For co-precipitates, DOM was added at a 10:1

molar C:Fe ratio (determined based on TOC measurements described above) for both DOM types prior to titration (n=4 for each synthesis). For Fe K-edge XAS of E podzol DOM, n=1 for each synthesis.

DOM-ferrihydrate adsorption complexes (n=4 for each synthesis) were prepared by addition of DOM after precipitation of ferrihydrate at a 10:1 molar C:Fe ratio. For Fe K-edge XAS of E podzol DOM, n=1 for each adsorption reaction. The DOM-ferrihydrate suspension was shaken overnight in Teflon® centrifuge tubes to prevent adsorption to the container surfaces, followed by dialysis as described above. The co-precipitate and adsorption synthesis process was repeated prior to bulk spectroscopic and imaging analyses (<2 weeks) to prevent crystallization. For imaging and spectroscopy, all synthesis replicates were equally pooled. Samples were stored in water suspension at <9°C to prevent artifacts resulting from freeze- or air-drying up to <1 day before thin layer deposition for imaging or spectroscopy. Prior to deposition of co-precipitate and adsorption suspensions for imaging and spectroscopy, ~2 mL of suspension was centrifuged at 13,000 rpm for 10 minutes, followed by immediate resuspension in 0.5 mL Nanopure™ water to increase sample concentration and C signal yield.

2.4 Total Carbon

Co-precipitate and adsorption complex solids were collected by filtration through 0.45 μm-pore GFF syringe filters, which were air-dried and analyzed for total C and N using a Carlo-Erba NC2500 elemental analyzer (CE Instruments Ltd, Wigan, UK), with adjustments for GFF filter weight and background (filter <0.07 %C). Total C values compared statistically using the two-sample Wilcoxon Mann-Whitney Test (a

non-parametric test robust to outlier data points) with base R (Version 3.4.1) (R Core Team, 2017) in RStudio (RStudio Team, 2015).

2.5 Carbon K-edge XANES

The C composition of initial DOM, co-precipitates, and adsorption solids was characterized by C K-edge XANES. Measurements were conducted at the high-resolution spherical grating monochromator (SGM) endstation of the Canadian Light Source (CLS) (Saskatoon, SK). Samples were prepared by thin-layer deposition of $\sim 60 \mu\text{L}$ DOM or suspension on gold (Au)-coated silicon wafers and air-drying. Partial fluorescence yield (PFY) scans (60s) were collected with an $\sim 50 \times 50 \mu\text{m}$ probe in slew mode. The PFY with maximum C signal (detector 90° to incident beam) was normalized to the PFY scattering signal from a clean Au-coated Si wafer to account for in-line C contamination. For samples and standards, 32 and 10 scans were collected from a new spot on the sample and averaged, respectively.

Spectrum normalization and flattening procedures were performed in Athena v. 0.9.26 (Ravel and Newville, 2005), with the edge step set to 1. A deconvolution modeling approach was used for C K-edge XANES that fits 8 Gaussian functions to energy positions defined by multiple previous standard organic compound XANES studies (Solomon et al., 2009; Heymann et al., 2011). Non-negative Gaussian functions (G1-G8) were defined with the parameters: (1) square root of peak height, (2) peak center, and (3) peak full-width half-maximum (FWHM) (Hestrin et al., 2019), with peak centers allowed to float within 0.2 eV energy for G1-G7 and 0.1 eV for G8 and peak FWHM allowed to float by 0.4 eV for all functions (Appendix Table A4.1.1). The model was fit for samples and verified with standard compounds

(Appendix Tables A4.1.2 and A4.1.3) in Fityk v. 0.9.8 (Wojdyr, 2010) using the Levenberg-Marquardt algorithm with 1000 maximum iterations to minimize the maximum sum of squared residuals (MSSR). Model R^2 was accepted if $R^2 > 0.98$.

2.6 High Resolution Imaging and Spectroscopy (STEM-EELS)

2.6.1 STEM-EELS Mapping

Element distribution and ferrihydrite spatial clustering were analyzed with STEM-EELS mapping for co-precipitated and adsorbed DOM-ferrihydrite using DOM from both E and typical podzol O horizons. Additionally, C and Fe speciation were determined with high spatial resolution (<5 nm) for co-precipitated and adsorbed E podzol DOM-ferrihydrite using cryogenic STEM-EELS. Samples were prepared by drop-casting $\sim 3 \mu\text{L}$ of each suspension on a Cu TEM grid (400-mesh) without a C film, with co-precipitate and adsorption sample droplets spatially separated, allowing for characterization of both treatments in the same timeframe. Experiments were conducted on an aberration-corrected FEI Titan Themis S/TEM instrument (FEI Company, Hillsboro, OR) equipped with a Gatan GIF Quantum 965 spectrometer (Gatan Inc., Pleasanton, CA) operated at 120 kV. For cryogenic STEM-EELS, used to determine Fe and C speciation, the samples were maintained at approximately -180°C with spectrometer aperture and monochromator settings adjusted to improve spectral resolution (~ 0.5 eV) while maintaining a moderate beam current (0.025-0.16 nA). To assess the structure and elemental distribution of the samples, 2D EELS maps were collected ranging in magnification from 225 kx to 2500 kx for the C K-edge (270-320 eV) and Fe $L_{2,3}$ edge (700-730 eV). Additionally, N K-edge (380-430 eV) and O K-edge (500-540 eV) spectra were collected for typical podzol DOM-ferrihydrite

samples at room temperature. For elemental distribution maps, simultaneous collection of low-loss (-20 – 200 eV) EELS maps containing the zero-loss peak (ZLP) accounted for spectrum shifts occurring during map acquisition. For C and Fe speciation, spectra were aligned to the ZLP of an EELS low-loss map collected in close proximity.

Damage tests (Appendix A1.3.3. and A2.3.1) for the co-precipitate sample were used to determine an electron dose of $\sim 15,000 \text{ e}^- \text{ \AA}^{-2}$ was required to induce changes in C fine structure under cryogenic imaging conditions, which is approximately twice the energy applied during acquisition of maps used for C fine structure analysis in this study ($\sim 7,700 \text{ e}^- \text{ \AA}^{-2}$) (Appendix Figure A3.1.1).

2.6.2 Elemental Spatial Distribution

Elemental EELS maps of Fe, C, N, and O in typical DOM-ferrihydrite samples and Fe and C in E DOM-ferrihydrite samples were obtained by background-subtracting spectra and integrating edges with the Cornell Spectrum Imager package (Cueva et al., 2012) in ImageJ v. 2.0.0 (Schneider et al., 2012). A standard linear combination of power laws (LCPL) approach was used to subtract the background signal with 3-pixel local background averaging. Spatial analyses of maps produced by this method were performed in RStudio (RStudio Team, 2015). Pixel intensity correlation between element pairs (Fe-C, Fe-N, and Fe-O) and C and Fe components was determined using Spearman Rank Correlation. Images were normalized (max pixel intensity = 1) and the lower 30% of pixels filtered to exclude non-sample area in the maps. For maps with $>\sim 20\%$ empty space (vacuum), reduced dimensions were selected for the analysis to avoid overestimation of correlation and for subsequent clustering analyses. The variation in elemental spatial correlation was assessed by two-way ANOVA of the

correlation coefficients in base R, comparing the values of elemental pair (Fe-C, Fe-N, and Fe-O) and co-precipitation vs. adsorption.

2.6.3 Iron Distribution and Clustering

To determine the effect of co-precipitation on the spatial clustering of Fe relative to surface adsorption, elemental Fe maps were analyzed using the Ripley's K(t) and Moran's I functions using the "spatstat" (Baddeley et al., 2015) and "ape" (Paradis et al., 2004) packages and base R (R Core Team, 2017). Ripley's K(t) gives a distribution as a function of distance from randomly sampled points in a spatial point pattern, providing information on the distribution of features within an image. Ripley's K(t) distributions are plotted in comparison to the Poisson distribution that is expected with a complete spatially random distribution; values above the Poisson distribution are considered clustered, while values below the Poisson distribution are considered evenly spaced (Baddeley et al., 2015). Moran's I tests autocorrelation of Fe-contained pixels in each image. For Fe clustering, background-subtracted elemental maps were normalized (max pixel intensity = 1) and converted to binary images, with pixel intensities >50% set to 1. Ripley's K(t) plots were generated using the border method for edge estimation and ~99% confidence envelopes.

To characterize variability in spatial tests across sample images, the values for Moran's I autocorrelation were grouped for co-precipitation and adsorption and compared with the Wilcoxon Rank Sum Test. The relationship between Fe clustering and Fe-C pixel intensity correlation was determined with multiple linear regression using Moran's I, Fe-C pixel intensity, and an interaction effect as fixed effects. Model

F-tests (ANOVA) were used to determine the significance of terms in the model ($\alpha = 0.05$).

2.6.4 EELS Carbon and Iron Fine Structure

Changes in C and Fe spectral features associated with chemical composition (i.e., fine structure) for high-magnification adsorption and co-precipitation samples were evaluated statistically using multivariate curve resolution (MCR) performed in Matlab v. R2017a. The number of putative components was set to 2 and initial regions for spectrum guesses were selected close to and more distant from high-Fe structures. Images >1.3 Mx magnification were selected for MCR analysis. MCR results used for subsequent spatial analyses and comparison of co-precipitation and adsorption were selected based on criteria (e.g., lack of edge artifact) discussed in Supplementary Methods (see Appendix A1.1.1 and Figure A3.1.1). Spatial pixel correlation was performed as above (Spearman Rank correlation) (Section 2.6.2), with modified pixel intensity cut-offs to reduce non-sample image area and correlation bias (20-35%).

The average C and Fe EELS spectrum for the images used in MCR analysis was acquired for the majority of the sample area as above for elemental maps (Section 2.6.2). For additional detailed analysis of a high-resolution co-precipitate image (1.8 Mx magnification), 4x8 pixel boxes in sequence across a ~25 nm region were used to generate average background-subtracted C and Fe spectra. Variation in total C intensity was estimated by integration of the background-subtracted spectrum (280.0-315.0 eV) using the area under the curve (AUC) function in the R “DescTools” package (Signorell et al., 2019). Changes in near-edge structure of C spectra for each 4x8 nm box were assessed by determination of peak heights within the regions 284.5-

286.0 eV (aromatic C), 286.0-287.0 eV (substituted aromatic C), 287.0-288.0 eV (aliphatic C), and 288.0-289.0 eV (carboxylic C). Peak heights were normalized to the total C integrated area and the aromatic/substituted aromatic and aliphatic/carboxylic peaks averaged to show the ratio of aromatic and non-aromatic C, respectively.

Changes in Fe L_{2,3}-edge associated with increasing Fe(II) contents were determined by calculation of the ratio of 710.5 eV to 709.0 eV peak height in the Fe L₃ white line (Garvie and Buseck, 1998). Correlation between C K-edge EELS aromatic/non-aromatic peak height ratios and the Fe L₃ 710.5/709.0 eV ratio was determined using Spearman's correlation (r_s) in base R (R Core Team, 2017).

2.7 Iron K-edge X-ray Absorption Spectroscopy (XAS)

Changes in Fe composition between ferrihydrite with adsorbed or co-precipitated DOM were assessed in bulk samples with Fe K-edge X-ray XANES and EXAFS. For the Fe K-edge, changes in energy position of the pre-edge centroid, white line, and edge inflection (E_0) (XANES) and changes to the Fe bonding environment (EXAFS) were determined at the Cornell High Energy Synchrotron Source (CHESS) F3 beamline (hard-bend magnet source with silicon (111) monochromator and silicon drift detector) (Ithaca, NY). Fluorescence yield was collected with in-line energy calibration (Fe foil) and normalized to incidence flux (I₀). The Fe K-edge was set to 7112 eV following Prietzel et al. (2007). Ferrihydrite, co-precipitated DOM-ferrihydrite, and adsorbed DOM-ferrihydrite were prepared for XAS measurements by thin-layer deposition of a 60- μ L suspension on 1-mil polyimide (Kapton®) tape. Solid standard minerals were ball-milled and suspended in DI water for thin-layer

deposition, while Fe-organic complex standards (dry) were deposited as a thin layer directly on Kapton® tape windows.

Spectra were normalized (3rd-order) and flattened in Athena v. 0.9.26 (Ravel and Newville, 2005) with a pre-edge range of -150 to -30 eV and post-edge range of 150 to ~ -600 eV relative to the edge position. Normalized fluorescence yield ($\mu(E)$) was used to determine white line and energy positions of the $\mu(E)$ pre-edge centroid. The first derivative of normalized fluorescence yield (hereafter referred to as $dx/d\mu(E)$) was computed and the E_0 (edge position inflection point) was calculated as the maximum of $dx/d\mu(E)$. With sensitivity of the Fe K-edge XANES region to changes in oxidation state (shift to lower energy of the edge onset and pre-edge feature) (Berry et al., 2003), a set of Gaussian functions was developed to determine relative changes in 7120 eV peak area in $dx/d\mu(E)$ (1s-4s transition) (Berry et al., 2003). In addition to changes in Fe oxidation state, shifts to lower energy in the pre-edge centroid could also be associated with increasing Fe-organic complex content, due to increasing Fe 1s \rightarrow 4p transition-like character as a result of 3d-4p mixing with ligands (Westre et al., 1997; Prietzel et al., 2007). Therefore, we determined the pre-edge centroid position of $dx/d\mu(E)$ and used the energy position in combination with spectral shifts associated with Fe(II) fitting to tease apart XANES spectral features in standard compounds with variable Fe(II) and/or Fe-organic complex content. An overview of standard compound synthesis methods is included in Inagaki et al. (in revision).

Briefly, changes in the ~7120 eV peak area of $dx/d\mu(E)$ with increasing Fe(II) content as well as the pre-edge centroid position were determined for samples and a

set of standard materials containing a range of Fe oxidation states, including both Fe(III) and Fe(II) organic complexes (Fe (III) citrate, Fe (II) citrate, and Fe (III) ethyldiamine tetra-acetic acid (EDTA)) and crystalline minerals (goethite, (FeO(OH)), fayalite (Fe₂SiO₄), and Fe(II)-substituted nontronite (Fe-rich smectite). Additionally, reference ferrihydrite subjected to identical synthesis conditions was prepared for each set of co-precipitated and adsorbed samples. To describe the shift in energy associated with Fe(II), the K-edge XANES model used four non-negative Gaussian functions with varying height, energy position, for Gaussian functions at ~7112 (pre-edge centroid), 7118-7120, 7124, and 7128 eV. The function at the ~7118-7120 eV energy position was constrained to $\sim 7118 \pm 3 \sin(\sim 0)$. The FWHM of all functions was constrained to $2\text{eV} \pm 2 \sin(\sim 0)$. The model was fit in Fityk v. 0.9.8 using the Levenberg-Marquardt algorithm as described above for C K-edge XANES. The relative change in spectral shape associated with increasing Fe(II) was estimated by the proportion of 7118-7120 eV area as a function of total Gaussian area.

The Fe K-edge EXAFS region was collected simultaneously with XANES measurements and used to qualitatively assess the presence of Fe-organic bonding in co-precipitated and adsorbed samples. The EXAFS forward Fourier transform (K-space) was computed for the 2-11 Å⁻¹ wavenumber range and plotted as k³-weighted spectra following Chen et al. (2014) in Athena (Ravel and Newville, 2005). The inverse Fourier transform (R-space) of k³-weighted K-space spectra was computed using the radial distance range of 1-3 Å.

3. Results

3.1 Total Carbon Analysis

No significant differences were found in the total C content of the co-precipitation or adsorption samples derived from the “typical” or “E” DOM (Wilcoxon Mann-Whitney test, all $p > 0.3$) (Appendix Figure A3.1.2). Due to the lack of significant differences in the total C content between DOM sources, the total C data for co-precipitation or adsorption were pooled across DOM types (Appendix Figure A3.1.2). The median total C followed an overall trend of lower C for adsorption in comparison to co-precipitation samples. However, the difference between co-precipitated and adsorbed total C was not statistically significant (Wilcoxon Mann-Whitney test, $p = 0.40$).

3.2 Carbon K-edge X-ray Absorption Spectroscopy

Carbon K-edge XANES spectra were similar between both DOM sources (Figure 1.1, Appendix Figure A3.1.3), in both overall shape and fine structure and deconvolution results (Figure 1.1, Appendix Figure A3.1.3, Appendix Table A4.1.2). Due to the lack of compositional differences between DOM sources and due to normalization of preparation based on DOM C concentration, results are hereafter pooled with respect to DOM source (see Supplementary Results and Discussion, Appendix A2.1.1). The largest contribution to the DOM C K-edge XANES signal was derived from the aromatic region, with the sum of functions (G1-G4) resulting in $45 \pm 3\%$ (average of DOM sources) of the total Gaussian function area of the XANES spectrum (Figure 1.1, Appendix Figure A3.1.3, Appendix Table A4.1.2).

Carbon K-edge XANES data for adsorbed vs. co-precipitated DOM were similar, with only subtle changes in spectral shape and fine structure (Figure 1.1,

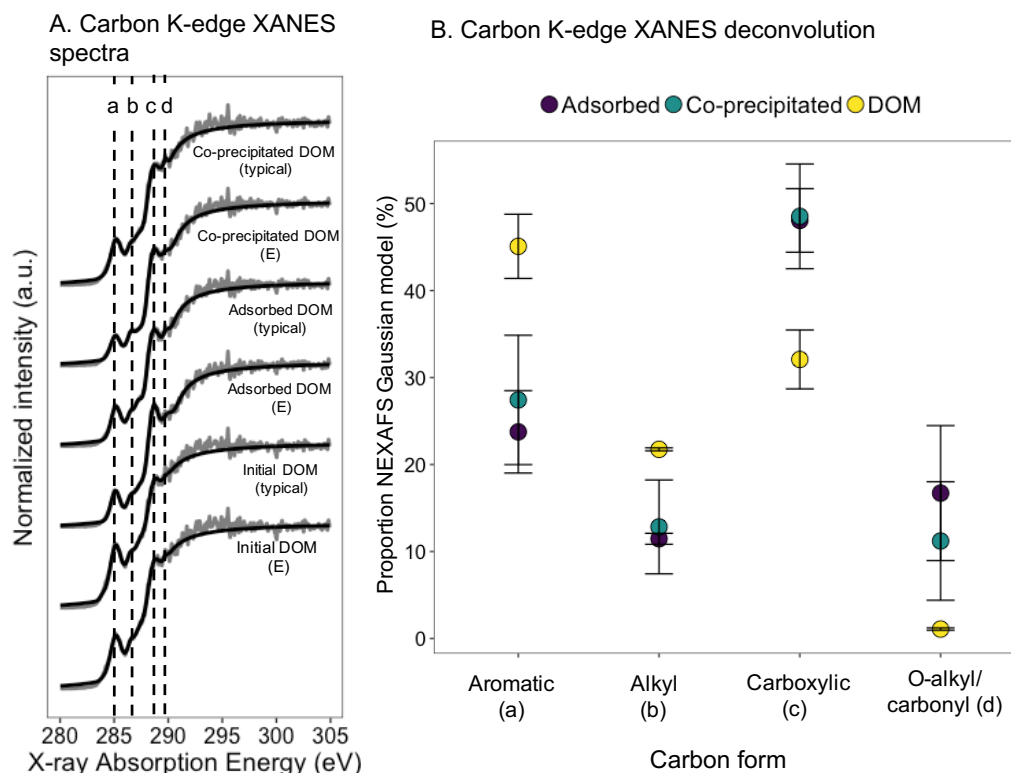


Figure 1.1. A. Normalized carbon (C) K-edge X-ray absorption near-edge structure (XANES) spectra for initial source dissolved organic matter (DOM) derived from typical podzol (0% conifer) and E podzol (35% conifer) sites. Lines a, b, c, and d indicate spectral features at ~285.0, 287.5, 288.7, and 289.0 eV, corresponding to aromatic, aliphatic, carboxylic, and O-alkyl/carbonyl C functional groups, respectively. B. Changes in the relative contribution of C functional groups to the C K-edge XANES Gaussian deconvolution model. Composition values for both sources of DOM (typical and E podzol) are averaged (\pm standard deviation). The primary shift in composition between source DOM and both co-precipitated and adsorbed DOM-ferrihydrite samples is a loss of aromatic groups, enrichment of carboxylic groups, and slight enrichment of O-alkyl/carboxyl groups.

Appendix Figure A3.1.3). This similarity is reflected in spectral deconvolution results, which do not show appreciable differences between adsorbed and co-precipitated samples (Figure 1.1, Appendix Table A4.1.2). However, the contribution of the aromatic signal was reduced by approximately two-fold for both adsorbed and co-precipitated samples compared to the initial DOM source (Figure 1.1, Appendix

Figure A3.1.3, Appendix Table A4.1.2). Additionally, alkyl C decreased with co-precipitated and adsorbed Fe-DOM compared to the original DOM, with an associated proportional increase in oxidized C (e.g., carboxylic and O-alkyl/carbonyl functional groups).

3.3 High Resolution Imaging and Spectroscopy (STEM-EELS)

3.3.1 STEM-EELS Imaging Overview

Lower-magnification (<910 kx-magnification) overview annular dark field (ADF) images and EELS Fe and C elemental maps showed a different spatial arrangement between the co-precipitation and adsorption Fe-DOM samples (Figure 1.2). In general, Fe with adsorbed DOM was more spatially clustered while co-precipitated Fe with DOM was more evenly mixed at this scale.

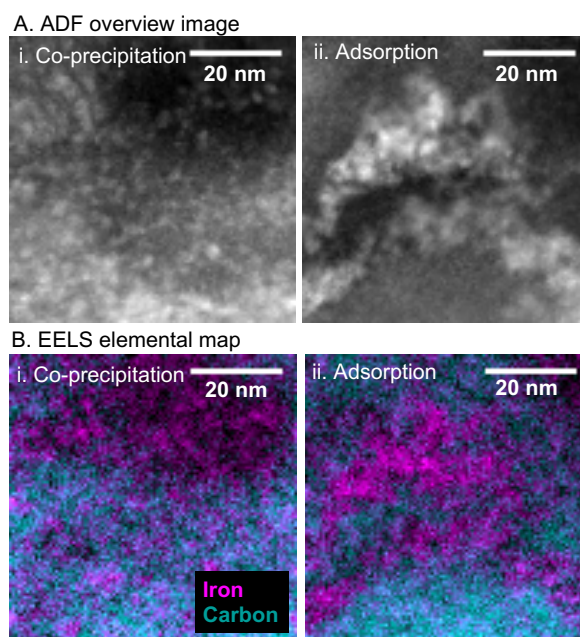


Figure 1.2. Overview scanning transmission electron microscopy (STEM) annular dark field (ADF) image (A) and electron energy loss spectroscopy (EELS) elemental map (B) of co-precipitated and adsorbed dissolved organic matter (DOM)-ferrihydrite, showing a pattern of aggregation for adsorption and a disaggregated, dispersed Fe distribution for co-precipitation.

3.3.2 Elemental Spatial Distribution

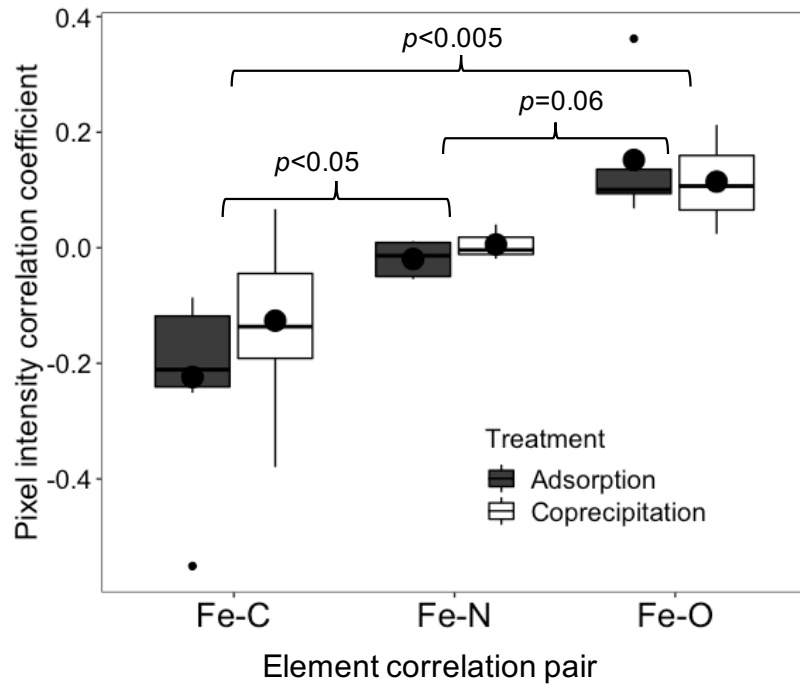
For high-resolution EELS maps (>1.3 Mx magnification), the correlation between Fe and C was generally negative for both co-precipitation and adsorption (average $r_s = -0.16$, $n=16$ images, treatments pooled), indicating significant (Spearman Rank $p < 0.005$) spatial separation of Fe and C. Relative to Fe-N and Fe-O, Fe-C correlation values were significantly more negative (ANOVA $p < 0.05$) (Figure 1.3). For Fe-N (typical DOM only), the correlation coefficient was close to zero (average $r_s = -0.01$, $n=8$ images), indicating significant (Spearman Rank $p < 0.005$) lack of either co-location or spatial separation (i.e., uniform N distribution). For Fe and O (typical DOM only), pixel intensity was co-located (average $r_s = 0.13$, $n=8$ images, Spearman Rank $p < 0.005$), indicative of overlapping Fe and O content in the Fe solid phase. However, no differences between adsorption and co-precipitation were observed for Fe-N or Fe-O (both $p = 0.998$) (Figure 1.3). The average and median Spearman Rank correlation (r_s) of Fe and C pixel intensity was about two times lower for adsorbed than co-precipitated DOM-Fe (Figure 1.3), though variability in the maps within the same sample result in a lack of significant difference in Fe-C spatial correlation between co-precipitation and adsorption (Two-way ANOVA $p = 0.62$).

3.3.3 Iron Distribution and Clustering

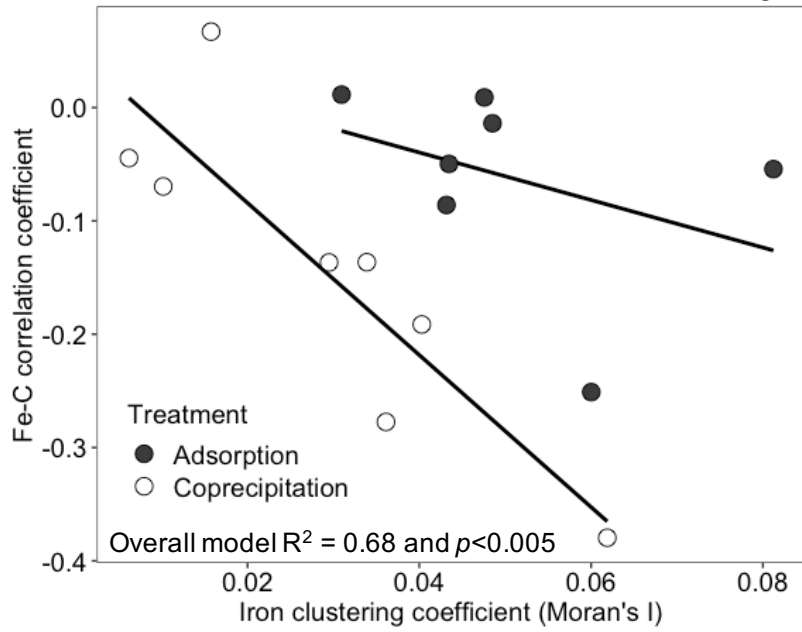
Ripley's $K(t)$ metric showed significant clustering (observations outside confidence envelope) for adsorption in the majority of maps used for Fe spatial statistics ($n=7$ maps) (Appendix Figure A4.1.4). Similarly to elemental spatial distribution, there was variability in the Fe clustering within co-precipitates ($n=9$ maps), but the maximum clustering was less than that observed for adsorption, and the average across the maps

Figure 1.3. A. Spearman Rank correlation coefficient (r_s) for pixel intensities of carbon (C), nitrogen (N), iron (Fe), and oxygen (O) elemental maps derived using electron energy loss spectroscopy (EELS). Correlation coefficient values >0 indicate co-location of elements (Fe-O, showing increased O content in the mineral phase), negative values indicate spatial separation of elements (Fe-C), and values close to 0 indicate random distribution (Fe-N). Lower and upper edges of boxes show first and third quartiles (25th and 75th percentiles) and lower and upper whiskers show the smallest and largest value no further than $1.5 \times$ interquartile range (IQR) of the box edges. Individual points beyond whiskers are considered outliers. Black circles represent the average r_s value. **B.** Multiple linear regressions comparing the spatial association of Fe and C as a function of Fe clustering (Moran's I coefficient) in high resolution EELS maps for co-precipitated and adsorbed dissolved organic matter (DOM)-ferrihydrite samples (pooled DOM source). While the overall effect of Fe clustering on Fe-C correlation is marginally significant ($p=0.06$), there is a significant difference between the slope of co-precipitated and adsorption ($p<0.005$) with no significant interaction, indicating that there is a stronger relationship between Fe clustering and Fe-C correlation for co-precipitation.

A. Pixel intensity correlation



B. Fe-C correlation as a function of Fe clustering



falls within the confidence envelope, indicating that there is no significant difference between observations and a random distribution. Further, Moran's I statistic (Fe spatial autocorrelation) was significantly higher (Wilcoxon Rank Sum $p < 0.05$) for adsorption vs. co-precipitation, confirming that within the samples analyzed, co-precipitation reduced Fe spatial distribution and clustering to a greater extent than adsorption.

The influence of variability in Fe clustering within the co-precipitate and adsorption samples on the observed spatial association between Fe and C was evaluated with multiple linear regression analysis (Figure 1.3). Overall, a significant effect (at $\alpha = 0.1$) of Moran's I coefficient (proxy for Fe clustering) on the correlation between Fe and C pixel intensity was detected, irrespective of sample type (co-precipitation or adsorption) (ANOVA F-test $p = 0.06$). However, the relationship between Fe clustering and Fe-C correlation was greater for co-precipitation than adsorption (ANOVA F-test $p < 0.005$).

3.3.4 EELS Carbon and Iron Fine Structure

At comparable magnification (1.8Mx), both Fe and C spectra (averaged across the majority of the sample image area) differed between co-precipitation and adsorption (Figure 1.4). For Fe, a more prominent shoulder at 709.0 eV was detected, indicating a shift towards increased Fe(II). Additionally, spatially-resolved separation of Fe components with MCR detected two components for co-precipitation: (1) oxidized Fe(III) with a prominent white line (L_3) at 710.5 eV, and (2) reduced Fe(II) with a L_3 peak at 709.0 eV (Figure 1.5).

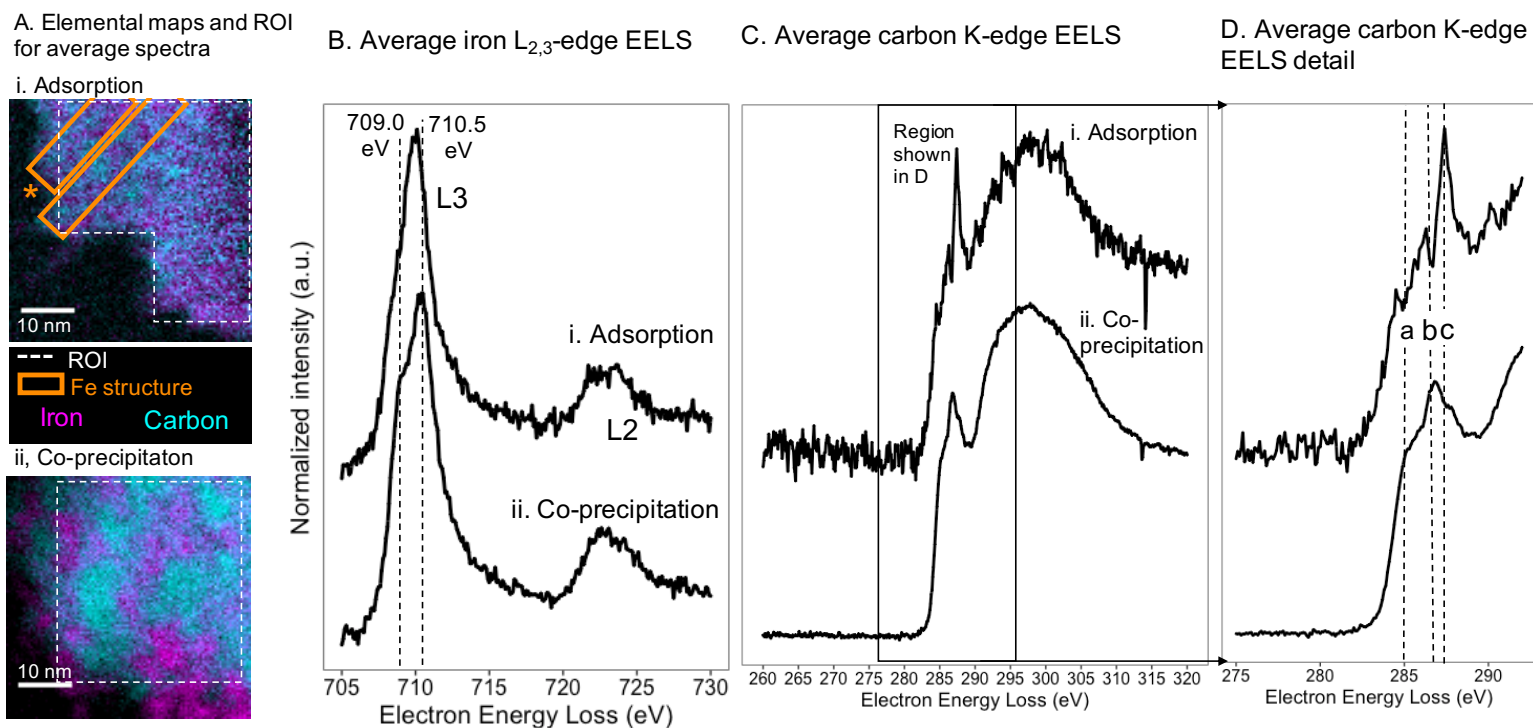
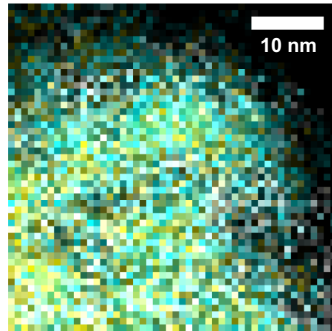


Figure 1.4. Average carbon (C) and iron (Fe) electron energy loss spectroscopy (EELS) spectra for regions of interest (ROI) encompassing the majority of sample area for 1.8 Mx magnification scanning electron microscopy (STEM)-EELS adsorption and co-precipitation images. **A.** EELS elemental maps for C (cyan) and Fe (magenta) showing regions (white dotted line) used to obtain average EELS spectra shown in B, C, and D. Ferrihydrite chain structure is visible for adsorption, noted by orange boxes, while co-precipitated Fe-DOM has a loosely aggregated structure. **B.** Average Fe $L_{2,3}$ -edge EELS with a white line (L_3) peak at 710.5 eV for both adsorption and co-precipitation but appearance of a shoulder at 709.0 eV associated with increased Fe(II) for co-precipitation. **C.** Average C K-edge EELS for adsorption and co-precipitation. Spectrum detail (**D**) shows shifts towards lower energy with co-precipitation, with horizontal lines a, b, and c associated with energy features at 285.0, 286.8, and 287.4 eV, putatively associated with aromatic, substituted aromatic, and aliphatic C, respectively.

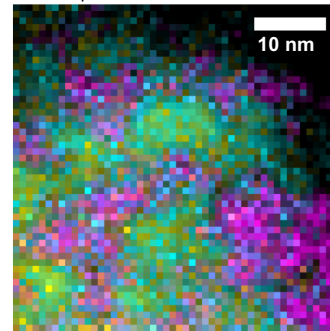
Figure 1.5. Carbon (C) and iron (Fe) electron energy loss spectroscopy (EELS) multivariate curve resolution (MCR) results for high-resolution Fe L-edge and C K-edge EELS maps collected for co-precipitated (**A**) and adsorbed (**B**) dissolved organic matter (DOM)-ferrihydrite solids. The EELS images used for MCR analysis were collected at 1.8 Mx magnification with ~0.8 nm pixel size and ~0.5 eV energy resolution. **A.i.** Composite image of MCR fit spatial distribution for the reduced Fe MCR spectrum (**A.iii.**) (grey), and lower- and higher- energy C component spectra (**A.v.**) (cyan and yellow, respectively). **A.ii.** Composite image of MCR fit spatial distribution for the oxidized Fe MCR spectrum (**A.iv.**) (magenta), and lower- and higher- energy C component spectra (**A.v.**) (cyan and yellow, respectively). **A.iii.** Co-precipitation Fe L_{2,3}-edge EELS MCR component with lower-energy shift (L₃ ~ 709.0 eV) and increased L₂/L₃ ratio associated with reduced Fe(II). **A.iv.** Co-precipitation Fe L_{2,3}-edge EELS MCR component with prominent L₃ peak at 710.5 eV associated with oxidized Fe(III). **A.v.** Co-precipitation MCR fit C component results, showing shifts towards lower-energy features (<287.0 eV) in “b”, including aromatic (~285.0 eV) and substituted aromatic (~286.5 eV) C, referred to as “aromatic C” (cyan). In “a”, features are higher-energy (>287.0 eV) including aliphatic (~287.5 eV) and carboxylic (~288.1-288.7 eV) C, referred to here as “non-aromatic C” (yellow). **A.vi.** List of Spearman Rank correlation coefficients for pixel intensities of Fe and C components for the co-precipitate image in descending order, with associated adsorption correlation coefficients when applicable (with detection of only one C and Fe component, only total C and Fe correlation is shown). In **A.i.**, pixel intensity between both aromatic and non-aromatic C and reduced Fe is positively correlated. In **A.ii.**, pixel intensity between both aromatic and non-aromatic and oxidized Fe is negatively correlated. **B.i.** Composite image of MCR fit spatial distribution for the oxidized Fe MCR spectrum (**B.ii.**) (magenta), and the primary C component spectrum detected for adsorbed DOM-ferrihydrite (**B.iii.**) (yellow). **B.ii.** MCR results for the Fe L_{2,3}-edge, showing the strong oxidized Fe component and a weak second component lacking a lower-energy shift associated with a true reduced Fe component, as detected in **A.iii.** **B.iii.** MCR results for C in adsorbed DOM-ferrihydrite, showing only one detectable C component with relatively strong signal in the higher-energy, non-aromatic region (287.0-289.0 eV).

A. Co-precipitate EELS MCR Components

i. C components with reduced Fe



ii. C components with oxidized Fe

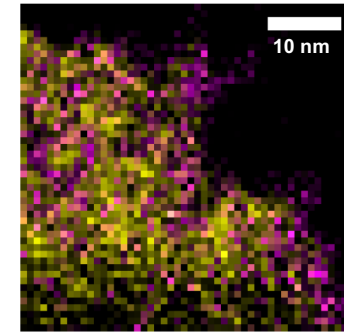


Color Legend

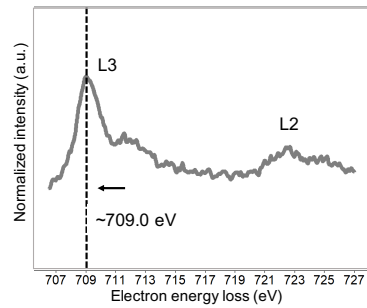
For all images and spectra:
 Grey :
 Reduced Fe
 Magenta =
 Oxidized Fe
 Cyan =
 Aromatic and substituted
 aromatic C
 Yellow = Non-
 aromatic C

B. Adsorption EELS MCR Components

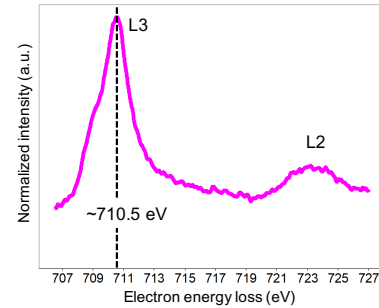
i. Non-aromatic C and oxidized Fe



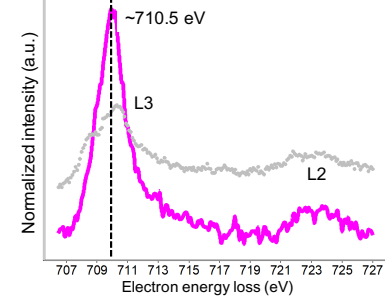
iii. Fe EELS MCR component 1 (reduced Fe)



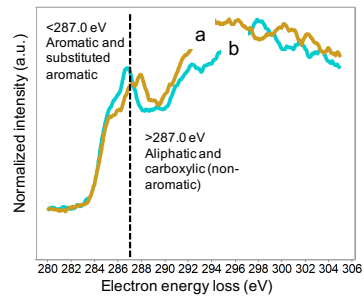
iv. Fe EELS MCR component 2 (oxidized Fe)



ii. Fe EELS MCR components



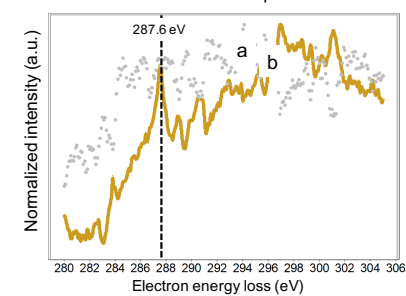
v. Carbon EELS MCR components



vi. Pixel intensity correlation

Correlation type	Correlation coefficient	
	Co-precip.	Adsorption
Fe(II) - Total C	0.15	NA
Fe(II) - Non-aromatic C ("a")	0.06	NA
Fe(II) - Aromatic C ("b")	0.06	NA
Fe(II) - Aromatic C	0.00	NA
Total Fe - Non-aromatic C	-0.03	NA
Total Fe - Total C	-0.06	0.18
Fe(III) - Aromatic C	-0.13	NA
Fe(III) - Non-aromatic C	-0.15	NA
Iron components	-0.17	0.08
Carbon components	-0.27	-0.05
Fe(III) - total C	-0.32	NA

iii. Carbon EELS MCR components



The oxidized Fe component was aggregated in loose clusters that were spatially separated from C, while the reduced Fe component was distributed more evenly distributed, particularly throughout the space between oxidized Fe clusters (Figure 1.5). In contrast, MCR did not clearly identify two Fe oxidation states for adsorption, with a predominant Fe(III) component only (Figure 1.5).

The average C K-edge EELS spectra (across the image) differed between the co-precipitation and adsorption samples, with a shift towards lower energy for co-precipitation, associated with increased aromatic and substituted aromatic C at ~ 285.0 and ~ 286.8 eV, respectively (Figure 1.4) (Solomon et al., 2009; Heymann et al., 2011). In contrast, the average C K-edge EELS spectrum of adsorbed DOC showed a primary feature occurred at 287.4 eV, associated with non-aromatic C (putatively C-H bonds in aliphatic C), with a reduced signal in the aromatic C region (Figure 1.4).

In addition to overall differences in average C fine structure, coprecipitated Fe-DOM showed both lower- and higher-energy components resolved with MCR, identified as aromatic (< 287.0 eV) and non-aromatic (> 287.0 eV) C, respectively (Figure 1.5). For adsorption, only a higher-energy component was detected, similar in structure to the average C spectrum (Figures 1.4 and 1.5). For both co-precipitation and adsorption, the energy regions are grouped here by: (1) lower-energy features (284.0-287.0 eV), generally associated with aromatic and substituted aromatic functional groups, and (2) higher-energy features (287.0-289.0 eV) associated with non-aromatic aliphatic and carboxyl/carbonyl functional groups (Solomon et al., 2009; Heymann et al., 2011).

In the higher-energy co-precipitate spectrum (spectrum “a” in Figure 1.5), the energy position of the primary peak was at 288.1 eV, likely associated with carboxylic or carbonyl groups with N-substitution (Solomon et al., 2009), indicative of microbial matter. In contrast, the higher-energy adsorption peak fell at 287.6 eV, putatively identified as aliphatic C-H bonds (Solomon et al., 2009). For adsorption, spectral properties in general shifted towards higher energy, and were consequently labeled “non-aromatic” C.

For co-precipitation, the Fe and C components (reduced vs. oxidized Fe and aromatic vs non-aromatic C) were negatively correlated with each other (Spearman Rank correlation (r_s) \approx -0.2), suggesting the phases were not randomly distributed (Figure 1.5). In contrast, with adsorption the components were either more weakly positively (Fe components r_s =0.08) or negatively correlated (C components r_s =-0.05), indicating a more overlapping and/or random distribution and supporting the interpretation above that MCR secondary components made minor contributions to total Fe and C. Overall, for adsorption, total Fe (i.e., oxidized Fe) and total C (i.e., oxidized C) were positively correlated (r_s =0.18) (Figure 1.5). For co-precipitation, the strongest positive spatial correlation was identified between reduced Fe and total C, with approximately equal correlation between the aromatic and non-aromatic C components and reduced Fe (Figure 1.5). Due to the loosely-aggregated clustering of Fe in this co-precipitate sample, both C components were more spatially separate from oxidized Fe at this scale (negative spatial correlation).

The series of average (4x8 nm box) C and Fe EELS spectra along a ~26 nm transect showed shifts in C and Fe composition that further refined spatial associations

between Fe(II) and C forms (Figure 1.6). Across the ~26 nm transect, aromatic/non-aromatic C ratio varied (Figure 1.6, Appendix Figure A3.1.5). Reduced Fe (i.e., decreasing Fe L₃ edge 710.5/709.0 eV peak height ratio) followed a similar pattern to aromatic/non-aromatic C across the transect (Figure 1.6), with an overall significant positive correlation ($r_s = 0.54$, $p < 0.05$) between aromatic/non-aromatic C and reduced Fe (Figure 1.7). Likewise, as a direct inverse of the aromatic and reduced Fe ratios, non-aromatic C and oxidized Fe were positively correlated with equivalent statistical significance (Figure 1.7). While the correlation between aromatic C and reduced Fe was positive overall, variability in the degree of separation between reduced Fe, aromatic C, and oxidized Fe varied across the transect (regions a-f in Figure 1.6), with segments of more homogenous distribution (e.g., region b) and segments with strong separation of reduced Fe and aromatic C from oxidized Fe (e.g., region e).

3.4 Iron K-edge X-ray Absorption Spectroscopy

For co-precipitation, there was no increase in the ~7120 eV Gaussian function peak area (indicative of Fe(II)) relative to the reference ferrihydrite detected using the Fe K-edge first-derivative XANES fitting procedure (Figure 1.8, Table 1.1, Appendix Figure A3.1.6). In comparison, adsorption caused a slight (2%) increase in peak area at ~7120 eV, which falls within the variation observed among pooled reference ferrihydrite Fe(II) estimates (average $5.8 \pm 2.7\%$). In contrast, Fe(II) standard compounds showed much greater peak area at 7120 eV (55% for fayalite) with an intermediate peak area (32%) for a Fe(II)/Fe(III) mineral (Fe(II)-substituted nontronite) (Figure 1.8, Table 1.2, Appendix Figure A3.1.6).

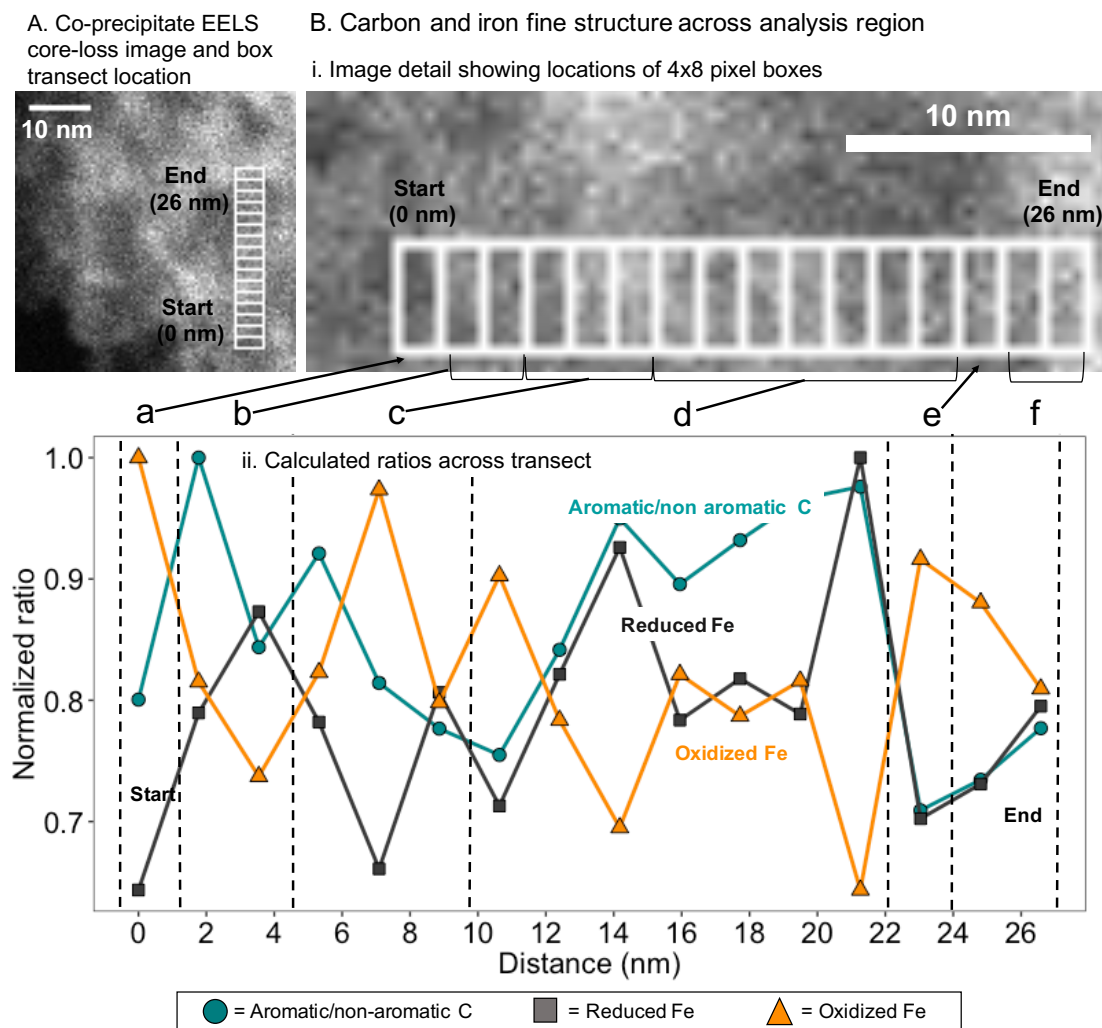


Figure 1.6. Carbon (C) K-edge and iron (Fe) L-edge electron energy loss spectroscopy (EELS) fine structure changes across a ~26-nm transect of a high-resolution co-precipitate EELS map. **A.** Overview image (EELS core-loss intensity) showing transect location with brighter areas linked to higher Fe content (Fe map shown in Figure 1.5). **B.i.** Detail of the transect with regions (a through f) of the linescan corresponding to shifts in fine structure ratio, with computed values shown in **B.ii.** **B.ii.** shows a plot profile of changes in C and Fe fine structure (aromatic/non-aromatic C ratio), reduced Fe (L_3 709.0/710.5 peak height ratio), and oxidized Fe (L_3 710.5/709.0 peak height ratio). Average spectra for regions a-f are shown in Appendix Figure A3.1.5.

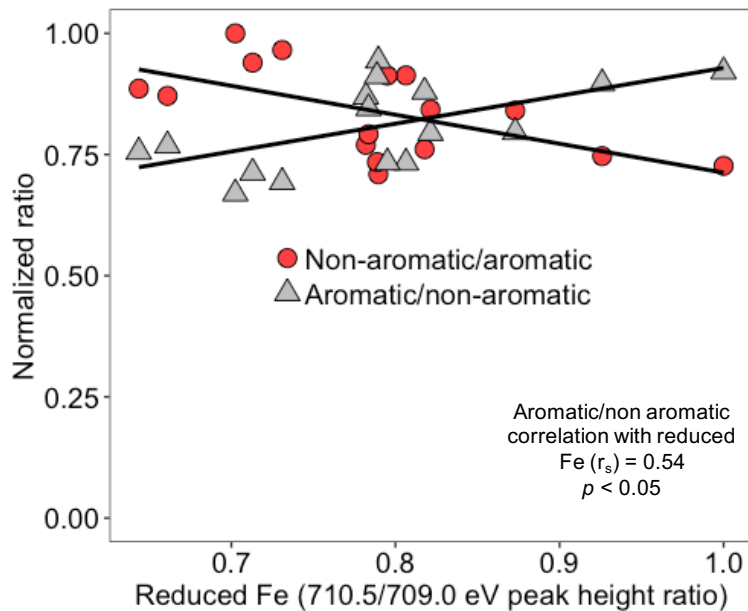


Figure 1.7. Spearman Rank correlation of aromatic/non-aromatic carbon ratio and the inverse with reduced Fe (Fe L₃ edge 710.5/709.0 eV peak height ratio) across the co-precipitate image transect in Figure 1.6. Black lines show a simple linear regression for C peak height ratio as a function of reduced Fe.

A lower-energy shift (~ -0.3 eV) in the first-derivative ($dx/d\mu E$) pre-edge centroid was detected for co-precipitated DOM-Fe only (Figure 1.8, Table 1.1), with $< \pm 0.06$ eV shift for adsorption (Table 1.1). The co-precipitate shift was not detected in the initial fluorescence yield spectrum (μE) pre-edge or E_0 , but a ~ -1 eV shift was detected for the white line energy position (Table 1.1). For Fe-organic complexes, a shift of ~ -0.6 eV was detected for the first-derivative pre-edge centroid (Figure 1.8, Table 1.2). With high Fe(II) complexes and mineral standards, a strong pre-edge shift was detected (Figure 1.8, Table 1.2).

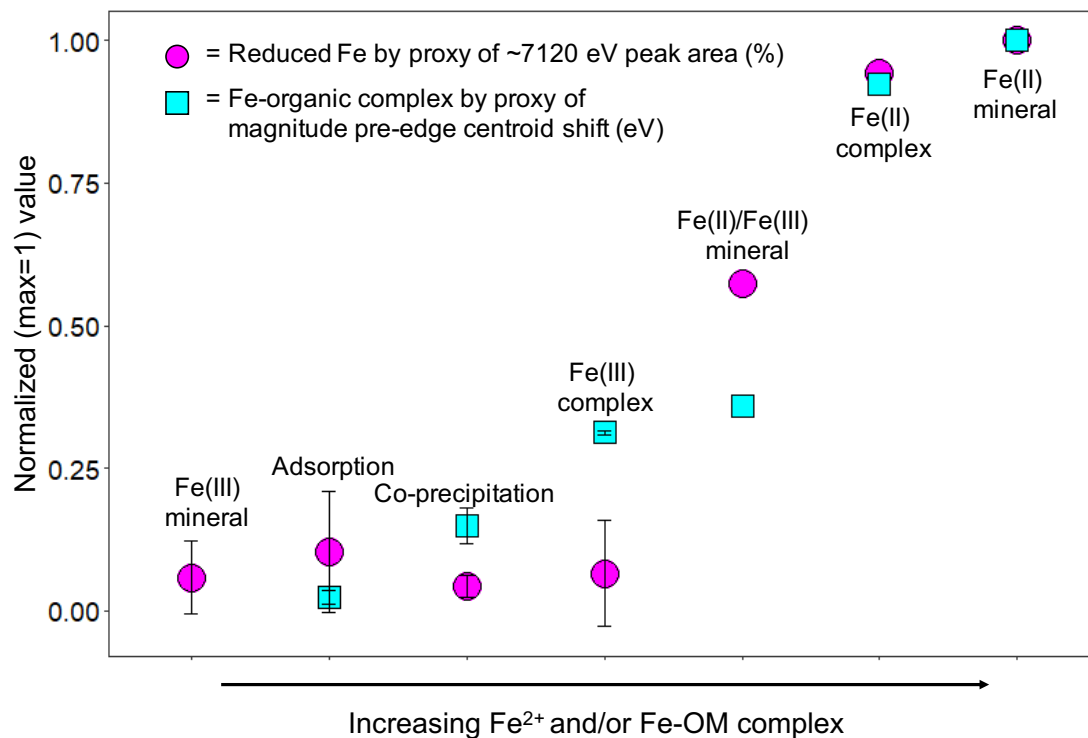


Figure 1.8. Visualization of combined changes in iron (Fe) K-edge X-ray absorption near edge structure (XANES), showing changes in ~ 7120 eV peak area (% of Gaussian model) and centroid position for standard compounds and adsorbed vs. co-precipitated Fe-OM materials normalized to 1. For Fe(II)/Fe(III) mineral, Fe(II) complex, and Fe(II) mineral points, values are for Fe(II)-substituted nontronite, iron (II) citrate, and fayalite, respectively. The average of two materials is shown for the Fe(III) mineral (goethite and ferrihydrite), adsorption (typical and E podzol DOM), co-precipitation (typical and E podzol DOM), and Fe(III) complex (iron (III) citrate and iron (III) EDTA) points (spectra in Appendix Figure A3.1.6). For the magnitude (absolute value) of the pre-edge centroid shift, the values for adsorption and co-precipitation were determined relative to the associated ferrihydrite reference, while the standard material shift was determined relative to the average of Fe(III) mineral positions (goethite and ferrihydrite).

Table 1.1. Iron (Fe) K-edge X-ray absorption near-edge structure (XANES) results for adsorption and co-precipitation samples prepared using dissolved organic matter (DOM) from higher-conifer (E podzol) and low-conifer (typical podzol) sites. μE = fluorescence spectrum, E_0 = edge inflection point, and $dx/d(\mu\text{E})$ = the first derivative of μE .

	DOM sourced from E podzol (35% conifer)				DOM sourced from typical podzol (0% conifer)			
	Adsorption		Co-precipitation		Adsorption		Co-precipitation	
	Ferrihydrite reference	10:1 C:Fe	Ferrihydrite reference	10:1 C:Fe	Ferrihydrite reference	10:1 C:Fe	Ferrihydrite reference	10:1 C:Fe
μE pre-edge centroid (eV)	7114.0	7114.0	7114.0	7114.0	7114.5	7114.8	7114.5	7114.5
μE white line (eV)	7132.0	7132.0	7133.0	7132.0	7132.8	7132.3	7133.0	7132.5
E_0 (eV)	7127.0	7127.0	7127.0	7127.0	7127.3	7127.0	7127.3	7127.3
$dx/d(\mu\text{E})$ 7120 eV area (%)	2.0	1.6	5.3	1.6	7.7	9.9	8.0	3.2
$dx/d(\mu\text{E})$ pre-edge centroid (eV)	7112.3	7112.4	7112.1	7111.8	7113.2	7113.2	7113.3	7113.0
$dx/d(\mu\text{E})$ pre-edge centroid shift (eV)	NA*	+0.06	NA	-0.31	NA	+0.03	NA	-0.23

*NA = not applicable. Pre-edge centroid shift is determined relative to oxidized Fe (ferrihydrite) reference position.

Table 1.2. Iron (Fe) K-edge X-ray absorption near-edge structure (XANES) results for standard mineral and Fe-organic complexes with a range of Fe oxidation state. μE = fluorescence spectrum, E_0 = edge inflection point, $dx/d(\mu\text{E})$ = the first derivative of μE .

	Standards						
	Fe(III) minerals		Fe(III)/Fe(II) mineral	Fe(II) mineral	Fe(III) organic complexes		Fe(II) organic complex
	Goethite	Ferrihydrite (average, n=4)	Fe(II)- substituted nontronite	Fayalite	Fe (III) citrate	Fe (III) EDTA	Fe (II) citrate
μE pre- edge centroid (eV)	7114.0	7114.3	7113.0	7112.0	7114.0	7113.0	7113.0
μE white line (eV)	7131.0	7132.7	7131.0	7127.0	7134.0	7134.0	7126.0
E_0 (eV)	7123.0	7127.1	7124.0	7123.0	7125.0	7126.0	7124.0
$dx/d(\mu\text{E})$ 7120 eV (%)	0.7	5.8	31.8	55.4	7.3	0.0	52.2
$dx/d(\mu\text{E})$ pre-edge centroid (eV)	7112.5	7112.7	7112.0	7110.8	7112.0	7112.0	7110.9
$dx/d(\mu\text{E})$ Pre-edge centroid shift (eV)	NA*	NA	-0.7	-1.8	-0.6	-0.6	-1.7

*NA = not applicable. Pre-edge centroid shift is determined relative to oxidized Fe (goethite or ferrihydrite) reference position.

The Fe-K edge EXAFS Fourier transform spectra (K-space) showed a slight increase in Fe-organic bonding, with a decreased amplitude of the oscillation at 7.5 \AA^{-1} compared to adsorption samples and reference ferrihydrite, corresponding to high-shell backscatter due to Fe-organic bonding (Chen et al., 2014) that was reflected in Fe-organic EXAFS standard spectra (Appendix Figures A3.1.7 and A3.1.8). However, these changes were not reflected in the inverse Fourier transform (R-space), which predominantly showed features associated with Fe-O and Fe-Fe bonds (Appendix Figure A3.1.7). Taken together, the similar magnitude of pre-edge centroid shifts to Fe-organic standards, and the slight changes in the EXAFS K-space amplitude, suggest that co-precipitated DOM showed greater Fe-organic bonding than adsorbed DOM.

4. Discussion

4.1 Co-precipitation vs. Adsorption: Changes to Fe Chemistry

4.1.1 Iron Spatial Association and Clustering

The demonstrated decrease in Fe clustering association with co-precipitation provided additional visual evidence for changes in bulk Fe crystallinity that was detected both in this study (Fe XAS) and by other researchers (Mikutta et al., 2010; Mikutta, 2011; Chen et al., 2014; Chen et al., 2016). While the overall Fe spatial clustering was higher with adsorption, there was a wide range of Fe clustering values with co-precipitation, and this variability was linked to the degree of Fe-C association (Figure 1.3). The assessment of within-sample variability is consequently meaningful for the interpretation of structural changes and indicated the broad range of Fe structural

changes induced by co-precipitation that may be a function of the wide range of C compounds expected in natural DOM.

4.1.2 Iron Oxidation State

In this study, identification of reduced Fe(II) with co-precipitation was enabled by the combination of high spatial and spectral resolution with STEM-EELS (Figure 1.5). While some studies have previously detected more reduced Fe(II) with co-precipitation in redox-active model systems (e.g., hydroquinone C) (Mikutta, 2011), this change has not been uniformly detected in co-precipitation studies, particularly in experiments using natural DOM sources with complex composition (Eusterhues et al., 2008; Chen et al., 2014; Chen et al., 2016). The detection of possible electron transfer reactions in this study implies that the redox-active functional groups in DOM were an important driver of Fe transformations. Despite the apparent variability in the degree and detection of Fe(II) via co-precipitation, processes of abiotic Fe reduction and formation of Fe(II)-organic complexes are ubiquitous, not only in soil environments but also in aquatic environments (Wan et al., 2018) and in organisms (Everett et al., 2014). In soils and wetlands, the formation of organic complexes with Fe(II) that increase the longevity of reduced Fe is a process of increasing recognition, particularly in peatland soils (Bhattacharyya et al., 2018; Wan et al., 2018). Consequently, the visual, spatially-resolved identification of Fe(II) with co-precipitation in our study provides an impetus to evaluate the Fe(II)-organic interactions occurring with co-precipitation in greater depth.

4.1.3 Iron-Organic Bonding

An increase in Fe-organic bonding with co-precipitation was observed in both the XANES (pre-edge centroid shift) (Figure 1.8) (Prietz et al., 2007) and EXAFS (reduced high-shell scattering) regions (Appendix Figure A3.1.7) (Chen et al., 2014). Similar increases in Fe-organic bonding have been identified with XAS for co-precipitation of DOM-ferrihydrite with increasing C:Fe ratios (Chen et al., 2014; Chen et al., 2016) and supported by Mössbauer spectroscopy (Eusterhues et al., 2008) and in-depth EXAFS shell-fitting procedures (Chen et al., 2016). Due to lower sensitivity of EXAFS to changes in oxidation state, Fe(II)-organic vs. Fe(III) organic standards were not quantitatively different in this study (Appendix Figure A3.1.8). However, taken together with high-resolution measurements, the observed Fe-organic effect combined with a prominent Fe(II) phase in EELS measurements suggests that the Fe-organic bonding detected may be a specific result of Fe(II)-organic bonding.

4.2 Co-precipitation vs Adsorption: Changes in Carbon Chemistry and Spatial Distribution

While alteration to Fe structure and chemistry is currently accepted as the expected outcome of co-precipitation compared to adsorption, the degree of alteration of C compared to the initial DOM as a result of co-precipitation remains a critical question for understanding potential changes in bioavailability of co-precipitated DOM. In this study, a two-fold decrease in aromatic C signal was observed for both co-precipitated and adsorbed samples compared to original DOM (Figure 1.1, Appendix Table A4.1.2), which contradicts the view of co-precipitation as a predominantly physical incorporation process that does not preferentially exclude specific C functional group

types (Kleber et al., 2015). With C K-edge XANES, only slight differences in bulk C chemistry between co-precipitation and adsorption were detected. However, the average (40x40 nm area) enrichment of aromatic and substituted aromatic C with co-precipitation compared to adsorption suggests that co-precipitated C may more closely reflect aromatic-rich source DOM (shown with XANES in Figure 1.1), indicating a less selective interaction compared to adsorption. Alternatively, co-precipitation and adsorption reactions may alter C composition directly via reactions with Fe, suggesting that a combination of less selective retention and transformation of C may result in differences of co-precipitated compared to adsorbed DOM.

The distribution of C and Fe forms across the 40x40 nm field of view (Figure 1.5) versus the 4x26 nm transect (Figure 1.6) points towards a distinct spatial arrangement of C within co-precipitates (Figure 1.9). Across a ~40x40 nm region (Figure 1.5), oxidized Fe was loosely clustered (lacking distinctive ferrihydrite chain-like structures) into C-free regions, resulting in a spatial separation of both C forms from oxidized Fe. In contrast, reduced Fe and C were spatially co-located and more homogeneously distributed, occurring in the spaces between oxidized Fe aggregations. When viewed as a high-resolution transect (Figure 1.6), the separation between aromatic and non-aromatic C in the space between oxidized Fe clusters becomes detectable, with variability in aromatic C association with reduced Fe and conversely, non-aromatic C association with oxidized Fe across the transect (Figure 1.6). Together, the spatial separation of C (both forms) with oxidized Fe on the larger scale and the spatial association of non-aromatic C with oxidized Fe at the finer scale points to a

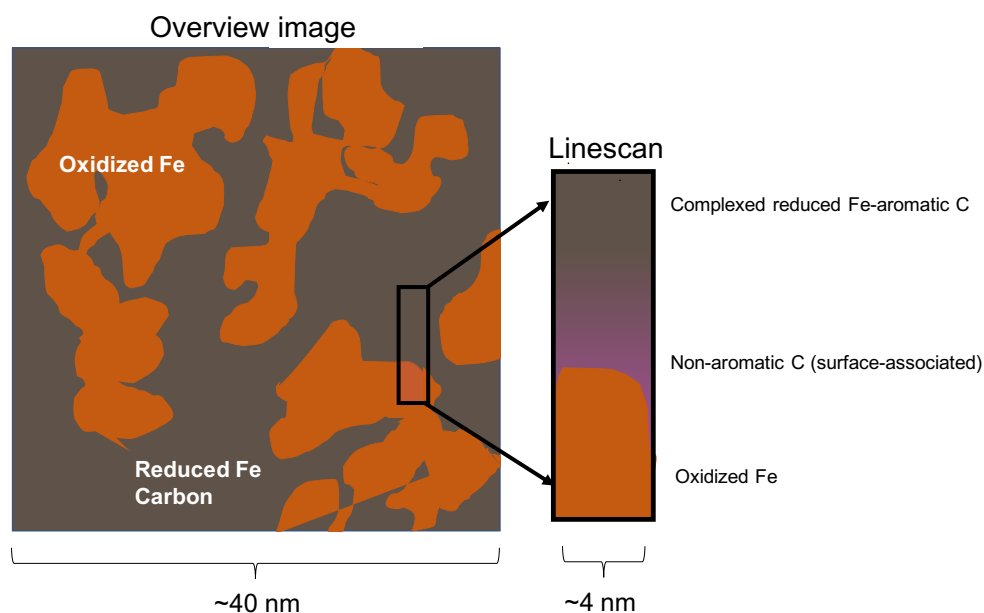


Figure 1.9. Simplified schematic of proposed spatial distribution of co-precipitate carbon (C) and iron (Fe) forms based on scanning transmission electron microscopy-electron energy loss spectroscopy (STEM-EELS) and bulk X-ray spectroscopy characterization. Oxidized Fe is loosely aggregated and largely separate from C on the 40x40 nm scale (taken from Figure 1.5), but spatial association between non-aromatic C and oxidized Fe at the 4x26 nm scale points to a separation of C forms (taken from Figure 1.6) undetectable within the full image pattern.

gradient of C composition as a function of distance from the center of oxidized Fe loose aggregates (Figure 1.9). With only one primary non-aromatic C form detected for adsorption that is spatially associated with oxidized Fe, our results show that co-precipitation caused a greater spatial separation of C forms than adsorption, indicating a greater heterogeneity of C functional groups and association diversity of potential Fe-OM interaction mechanisms (e.g., both Fe (II or III)-organic complex formation and surface adsorption). Additionally, the distinction between OM-Fe spatial distribution between reduced Fe (mixed with OM) and oxidized Fe (largely separate from OM at the 40x40 nm scale) may provide an explanation for previous

contradictory observations of both OM-Fe intermixing and patchy distribution with STXM-XANES (Henneberry et al., 2012; Chen et al., 2014).

Here, the detection of spatial associations between aromatic C (<287.0 eV) and reduced Fe with co-precipitates may indicate abiotic reduction of Fe, pointing towards the occurrence of not only selective retention and differences in spatial arrangement compared to adsorption, but also direct alteration of both OM and Fe composition via electron transfer reactions. Many groups with potential for abiotic Fe reduction are present in the ~284-286.5 eV region, including substituted aromatic compounds with C-O and C=O transitions associated with phenols (~286.0-286.5 eV) and quinones (~283.75 eV and 286.5 eV) (Solomon et al., 2009). In model-system co-precipitation experiments, hydroxybenzoic acids (containing phenol groups) were linked with abiotic Fe reduction (Mikutta, 2011). Phenol reduction of Fe(III) to Fe(II) and complexation of Fe(II) has also been linked with slowed oxidation and precipitation of Fe in high OM peatlands (Wan et al., 2018). Additionally, quinone functional groups in particular have been linked with a number of biogeochemically relevant electron-transfer reactions, in both highly aromatic materials such as pyrogenic organic matter (PyOM) (Sun et al., 2018) and more generally as a component of natural OM in soil and water (Uchimiya and Stone, 2009).

The potential for direct alteration of OM and Fe via direct electron transfer in co-precipitation may have important implications for the persistence of both organic and mineral compounds. For SOM, oxidation may result in direct abiotic DOM mineralization to carbon dioxide (CO₂), in addition to effects on C composition. In addition to observed increases in Fe reactivity due to disaggregated Fe distribution

(Eusterhues et al., 2014), the increased presence of Fe(II) may also influence Fe oxide transformation. While dissolution of Fe(II) on ferrihydrite surfaces is a known mechanism of increasing crystallization rate (Hansel et al., 2005; Yee et al., 2006), the detected Fe(II) was likely present in Fe(II)-organic complex form in this study, complicating the potential influence of increased Fe(II) on ferrihydrite transformation.

5. Conclusions

Using spatially-resolved, high-resolution STEM-EELS measurements in conjunction with bulk spectroscopic analyses, we demonstrate changes to both Fe and C composition with co-precipitation compared to adsorption, including: (1) reduced Fe spatial distribution and aggregation, (2) increased Fe(II) and Fe-organic bonding, (3) the presence of spatially-distinct aromatic/substituted aromatic vs. non-aromatic C forms, and (4) the spatial association of aromatic/substituted aromatic C with Fe(II). Therefore, co-precipitation constitutes not merely a physical encapsulation without interaction between C and Fe, but possibly causes bi-directional C-Fe reactions. These results also suggest that the primary distinction between co-precipitation and adsorption is not the degree of physical occlusion, but the extent of complex formation and abiotic reduction processes, where C forms play a major role. Consideration of co-precipitation processes and their environmental relevance should consequently focus on the parameters influencing abiotic reduction, such as the relative differences in redox-active substituted aromatic functional groups in source DOM (e.g., quinones and phenols). We would therefore expect co-precipitation reactions to differ between different ecosystems if DOM properties vary in their redox-active C forms. These

processes may be relevant not only for accumulation of DOM from a soil C sequestration perspective but also for contaminant transformation, water treatment, and broader geochemical cycling. Therefore, future studies should evaluate the effect of varying the composition of redox-active DOM compounds, as well as environmental redox drivers, on the characteristics of co-precipitates in different ecosystems and engineered systems, particularly at oxic-anoxic interfaces with high OM input.

6. Acknowledgements

Funding for this study was provided by the NSF IGERT in Cross-Scale Biogeochemistry and Climate at Cornell University (NSF Award #1069193) and the Technical University of Munich Institute for Advanced Studies. Additional research funds were provided by the Andrew W. Mellon Foundation and the Cornell College of Agriculture and Life Sciences Alumni Foundation. This work uses research conducted at the Cornell High Energy Synchrotron Source (CHESS) which is supported by the National Science Foundation under award DMR-1332208. Collaborators for this study for Cornell Applied and Engineering Physics (Lena F. Kourkoutis and Michael J. Zachman) acknowledge support by the NSF (DMR-1654596). This work made use of the Cornell Center for Materials Research Shared Facilities which are supported through the NSF MRSEC program (DMR-1719875). The FEI Titan Themis 300 was acquired through NSF-MRI-1429155, with additional support from Cornell University, the Weill Institute and the KIC. Research described in this paper was performed at the Canadian Light Source (CLS), which is supported by the Canada

Foundation for Innovation, Natural Sciences and Engineering Research Council of Canada, the University of Saskatchewan, the Government of Saskatchewan, Western Economic Diversification Canada, the National Research Council Canada, and the Canadian Institutes of Health Research. The authors also thank John Grazul and Malcolm Thomas of the CCMR facility, Rong Huang of CHESS, and Kelly Hanley and Akio Enders of Cornell University for technical assistance.

REFERENCES

- Baddeley, A., Rubak, E., Turner, R., 2015. Spatial Point Patterns: Methodology and Applications with R. Chapman and Hall/CRC Press, London.
- Bailey, S.W., Brousseau, P.A., McGuire, K.J., Ross, D.S., 2014. Influence of landscape position and transient water table on soil development and carbon distribution in a steep, headwater catchment. *Geoderma* 226-227, 279-289.
- Berry, A.J., O'Neill, H.St.C., Jayasuriya, K.D., Campbell, S.J., Foran, G.J., 2003. XANES calibrations for the oxidation state of iron in silicate glass. *Am. Mineral.* 88(7), 967-977.
- Bhattacharyya, A., Schmidt, M.P., Stavitski, E., Martínez, C.E., 2018. Iron speciation in peats: Chemical and spectroscopic evidence for the co-occurrence of ferric and ferrous iron in organic complexes and mineral precipitates. *Org. Geochem.* 115, 124-137.
- Chen, C., Dynes, J.J., Wang, J., Sparks, D.L., 2014. Properties of Fe-organic matter associations via coprecipitation versus adsorption. *Environ. Sci. Technol.* 48, 13751-13759.
- Chen, K., Chen, T., Chan, Y., Cheng, C., Tzou, Y., Liu, Y., Teah, H., 2016. Stabilization of natural organic matter by short-range-order iron hydroxides. *Environ. Sci. Technol.* 50, 12612-12620.
- Cueva, P., Hovden, R., Munday, J.A., Xin, H.L, Muller, D.A., 2012. Data processing for atomic resolution electron energy loss spectroscopy. *Micros. Microanal.* 18, 667-675.
- Deng, Y., Dixon, J.B., 2002. Soil organic matter and organic-mineral interactions, in: Dixon, J.B., Shulze, D.G. (Eds.), *Soil Mineralogy with Environmental Applications*, SSSA Book Series 7, Soil Science Society of America, Inc., Madison, WI. pp. 69-108.
- Eusterhues, K., Hadrich, A., Neidhardt, J., Kusel, K., Keller, T.F., Jandt, K.D., Totsche, K.U., 2014. Reduction of ferrihydrite with adsorbed and coprecipitated organic matter: microbial reduction by *Geobacter brementis* versus abiotic reduction by Na-dithionite. *Biogeosciences Discuss.* 11, 6039-6067.
- Eusterhues, K., Rennert, T., Knicker, H., Kögel-Knabner, I., Totsche, K.U., Schwertmann, U., 2011. Fractionation of organic matter due to reaction with ferrihydrite: coprecipitation versus adsorption. *Environ. Sci. Technol.* 45, 527-533.

- Eusterhues, K., Wagner, F.E., Häusler, W., Hanzik, M., Knicker, H., Totsche, K.U., Kögel-Knabner, I., Schwertmann, U., 2008. Characterization of ferrihydrite-soil organic matter co-precipitates by X-ray diffraction and Mössbauer spectroscopy. *Environ. Sci. Technol.* 42(21), 7891-7897.
- Everett, J., Céspedes, E., Shelford, L.R., Exley, C., Collingwood, J.F., Dobson, J., van der Laan, G., Jenkins, C.A., Arenholz, E., Telling, N.D., 2014. Ferrous iron formation following co-aggregation of ferric iron and the Alzheimer's disease peptide β -amyloid (1-42). *J. R. Soc. Interface* 11, 20140165.
- Fritzche, A., Schröder, C., Wieczorek, A.K., Händel, M., Ritschel, T., Totsche, K.U., 2015. Structure and composition of Fe-OM co-precipitates that form in soil-derived solutions. *Geochim. Cosmochim. Acta* 169, 167-183.
- Garvie, L.A.J., Buseck, P.R., 1998. Ratios of ferrous to ferric iron from nanometer-sized areas in minerals. *Nature* 396(6712), 667-670.
- Hansel, C.M., Benner, S.G., Fendorf, S., 2005. Competing Fe(II)-induced mineralization pathways of ferrihydrite. *Environ. Sci. Technol.* 39, 7147-7153.
- Henneberry, Y.K., Kraus, E.C., Nico, P.S., Horwath, W.R., 2012. Structural stability of coprecipitated natural organic matter and ferric iron under reducing conditions. *Org. Geochem.* 48, 81-89.
- Hestrin, R., Torres-Rojas, D., Dynes, J.J., Hook, J.M., Regier, T.Z., Gillespie, A.W., Smernik, R.J., Lehmann, J., 2019. Fire-derived organic matter retains ammonia through covalent bond formation. *Nat. Commun.* 10, 664.
- Heymann, K., Lehmann, J., Solomon, D., Schmidt, M.W.I., Regier, T., 2011. C 1s K-edge near edge X-ray absorption fine structure (NEXAFS) spectroscopy for characterizing functional group chemistry of black carbon. *Org. Geochem.* 42(9), 1055-1064.
- Inagaki, T.M., Possinger, A.R., Grant, K.E., Schweizer, S.A., Mueller, C.W., Derry, L.A., Lehmann, J., Kögel-Knabner, I. Subsoil organo-mineral associations under contrasting climate conditions. In revision, *Geochim. Cosmochim. Acta*.
- Lehmann, J., Kleber, M., 2015. The contentious nature of soil organic matter. *Nature* 528, 60-68.
- Kleber, M., Eusterhues, K., Keiluweit, M., Mikutta, C., Mikutta, R., Nico, P.S., 2015. Mineral-organic associations: formation, properties, and relevance in soil environments. *Adv. Agron.* 130, 1-140.

- Kourkoutis, L.F., Plitzko, J.M., Baumeister, W., 2012. Electron microscopy of biological materials at the nanometer scale. *Annu. Rev. Mater. Res.* 42, 33-58.
- Mikutta, C., 2011. X-ray absorption spectroscopy study on the effect of hydroxybenzoic acids on the formation and structure of ferrihydrite. *Geochim. Cosmochim. Acta* 75, 5122-5139.
- Mikutta, C., Frommer, J., Voegelin, A., Kaegi, R., Kretzschmar, R., 2010. Effect of citrate on the local Fe coordination in ferrihydrite, arsenate binding, and ternary arsenate complex formation. *Geochim. Cosmochim. Acta* 74, 5574–5592.
- Mikutta, R., Lorenz, D., Guggenberger, G., Haumaier, L., Freund, A., 2014. Properties and reactivity of Fe-organic matter associations formed by coprecipitation versus adsorption: Clues from arsenate batch adsorption. *Geochim. Cosmochim. Acta* 144, 258–276.
- Miot, J., Benzerara, K., Kappler, A., 2014. Investigating microbe-mineral interactions: recent advances in X-ray and electron microscopy and redox-sensitive methods. *Annu. Rev. Earth Planet. Sci.* 42, 271-289.
- Paradis, E., Claude, J., Strimmer, K., 2004. APE: analyses of phylogenetics and evolution in R language. *Bioinformatics* 20, 289-290.
- Prietzl, J., Thieme, J., Eusterhues, K., Eichert, D., 2007. Iron speciation in soils and soil aggregates by synchrotron-based X-ray microspectroscopy (XANES, μ -XANES). *Eur. J. Soil Sci.* 58, 1027-1041.
- Ravel, B., Newville, M., 2005. Athena, Artemis, Hephaestus: data analysis for X-ray absorption spectroscopy using IFEFFIT. *J. Synchrotron Rad.* 12, 537-541.
- RStudio Team, 2015. RStudio: Integrated Development for R. RStudio, Inc., Boston. URL <http://www.rstudio.com/>
- R Core Team, 2017. R: A language and environment for statistical computing. R Foundation for Statistical Computing, Vienna, Austria. URL <https://www.R-project.org/>.
- Schmidt, M.W., Torn, M.S., Abiven, S., Dittmar, T., Guggenberger, G., Janssens, I.A., Kleber, M., Kögel-Knabner, I., Lehmann, J., Manning, D.A.C., Nannipieri, P., Rasse, D.P., Weiner, S., Trumbore, S.E., 2011. Persistence of soil organic matter as an ecosystem property. *Nature* 478(7367), 49-56.
- Schneider, C.A., Rasband, W.S., Eliceiri, K.W., 2012. NIH Image to ImageJ: 25 years of image analysis. *Nature Methods* 9(7), 671-675.

- Schwertmann, U., Cornell, R.M., 2000. *Iron Oxides in the Laboratory: Preparation and Characterization*, 2nd Edition. Wiley-VCH Verlag GmbH, Weinheim, DE.
- Schwertmann, U., Taylor, R.M., 1989. Iron oxides, in: Dixon, J.B., Weed, S.B. (Eds.), *Minerals in Soil Environments*, 2nd Edition. Soil Science Society of America, Inc., Madison, WI. pp. 379-438.
- Shimizu, M., Zhou, J.H., Schroder, C., Obst, M., Kappler, A., Borch T., 2013. Dissimilatory reduction and transformation of ferrihydrite-humic acid coprecipitates. *Environ. Sci. Technol.* 47, 13375-13384.
- Signorell, A., et mult. al., 2019. DescTools: Tools for descriptive statistics. R package version 0.99.28.
- Solomon, D., Lehmann, J., Kinyangi, J., Liang, B., Heymann, K., Dathe, L., Hanley, K., Wirick, S., Jacobsen, C., 2009. Carbon (1s) NEXAFS spectroscopy of biogeochemically relevant reference organic compounds. *Soil Sci. Soc. Am. J.* 73, 1817-1830.
- Sun, T., Levin, B.D.A., Schmidt, M.P., Guzman, J.J.L., Enders, A., Martínez, C.E., Muller, D.A., Angenent, L.T., Lehmann, J., 2018. Simultaneous quantification of electron transfer by carbon matrices and functional groups in pyrogenic carbon. *Environ. Sci. Technol.* 52(15), 8538-8547.
- Uchimiya, M., Stone, A.T., 2009. Reversible redox chemistry of quinones: Impact on biogeochemical cycles. *Chemosphere* 77(4), 451-458.
- Vilge-Ritter, A., Rose, J., Masion, A., Bottero, J.Y., Laine, J.M., 1999. Chemistry and structure of aggregates formed with Fe-salts and natural organic matter. *Colloids Surf. A* 147, 297-308.
- Wan, X., Xiang, W., Wan, N., Yan, S., Bao, Z., Wang, Y., 2018. Complexation and reduction of iron by phenolic substances: Implications for transport of dissolved Fe from peatlands to aquatic ecosystems and global iron cycling. *Chem. Geol.* 298, 128-138.
- Westre, T.E., Kennepohl, P., DeWitt, J.G., Hedman, B., Hodgson, K.O., Solomon, E.I., 1997. A multiplet analysis of Fe K-edge 1s → 3d pre edge features of iron complexes. *J. Am. Chem. Soc.* 119, 6297-6314.
- Wojdyr, M., 2010. Fityk: a general-purpose peak fitting program. *J. Appl. Cryst.* 43(5-1), 1126-1128.
- Yee, N., Shaw, S., Benning, L.G., Nguyen, T.H., 2006. The rate of ferrihydrite transformation to goethite via the Fe(II) pathway. *Am. Mineral.* 91, 92-96.

CHAPTER 2
ORGANO-MINERAL INTERACTIONS AND SOIL CARBON
MINERALIZABILITY WITH VARIABLE SATURATION FREQUENCY

1. Introduction

The accumulation and persistence of soil organic carbon (SOC) is considered predominantly a function of environmental variables rather than inherent chemical composition (Schmidt et al., 2011; Lehmann and Kleber, 2015). Soil water content is a key variable influencing SOC mineralization, with a well-known relationship between soil moisture and microbial respiration, as well as well-defined links between pedogenic processes in anoxic environments and accumulation of soil C (e.g., wetlands, flood plains) (Kayranli et al., 2010; Sutfin et al., 2016; Mayer et al., 2018). However, redox conditions in otherwise aerobic, well-drained soils can vary widely due to both spatial heterogeneity (e.g., anaerobic microsites) and rapid saturation-drying cycles (Silver et al., 1999; Keiluweit et al., 2017; Coward et al., 2018). In contrast to the prevailing concept of increased moisture leading to accumulation of SOC due to decreased microbial metabolism, reducing conditions resulting from short-term saturation events in otherwise aerobic soils may drive mineral dissolution and thereby increase mobilization of mineral-associated SOC (Buettner et al., 2014; Herndon et al., 2017; Coward et al., 2018). This reversal of the relationship between water content and carbon accumulation is a point of uncertainty in SOC cycling, particularly in light of increased frequency and severity of weather events in many climates predicted with global climate change (Christensen et al., 2013).

The form of mineral-SOC interaction is expected to influence the degree of susceptibility to dissolution and subsequent transformations (Winkler et al., 2018). Overall, SOC association with redox-active elements, predominantly iron (Fe), may be more sensitive to fluctuating redox than other elements (e.g., aluminum, Al). For instance, semi-crystalline Fe oxides (e.g., ferrihydrite, nominally $\text{Fe}_2\text{O}_3 \cdot 0.5\text{H}_2\text{O}$) that rapidly dissolve and re-precipitate under fluctuating redox conditions may be one interaction with increased susceptibility to increased saturation frequency and associated mobilization of associated SOC (Buettner et al., 2014). However, reduced Fe(II) is also likely to form stable Fe(II)-organic complexes in the presence of high OM input (Bhattacharyya et al., 2018), and co-precipitation of SOC with reduced or re-oxidized Fe may provide surface-area independent stabilization reactions (Kleber et al., 2015). For semi-crystalline oxide minerals, Fe and Al solubilities are likely to covary, with Fe oxidation-reduction indirectly affecting the solubility of other colloidal materials via changes in soil solution chemistry (e.g., pH) (Thompson et al., 2006a). The potential for wide variation in Fe-Al-SOC dynamics with variable saturation frequency complicates prediction of the relative role of Fe vs. Al.

With increased saturation frequency, long-term shifts in soil mineralogy and elemental ratios are likely, resulting from leaching of mobile elements, changes to mineral weathering and/or crystallization, or indirect effects on soil solution chemistry (Thompson et al., 2006a, 2011; Das et al., 2019). In particular, lower-pH soils with high Fe and Al oxide contents may experience shifts in Fe crystallinity and elemental composition (e.g., increased Al/Fe ratio) in the long-term due to the mobilization of soluble Fe(II) with increased saturation frequency (Thompson et al., 2006b, 2011;

Bourgault et al., 2015; Inagaki et al., in revision). While Fe reduction is known to occur in generally aerobic soils (Yang and Liptzin, 2015; Hall et al., 2016), the effect of short-duration saturation and rapid draining events on soil mineralogy and organo-mineral interactions in upland, otherwise well-drained soils is not fully understood. Further, linking potential changes in organo-mineral association properties across saturation frequency with SOC mineralization potential is needed to understand the role of variable saturation in SOC stabilization.

To test the relationships among Fe oxidation state, mineral and metal chemistry, SOC composition, and SOC mineralization across variable saturation frequency categories, we used well-described variability in saturation frequency-driven soil formation of upland forest soils at Hubbard Brook Experimental Forest (Bailey et al., 2014; Bourgault et al., 2015, 2017; Gannon et al., 2017) representative of broadly observed hillslope transport and transient water table effects on Spodosol formation (Sommer et al., 2000; Jankowski, 2014). For spodic mineral horizons, we applied bulk characterization, selective extraction, bulk X-ray and nuclear magnetic resonance (NMR) spectroscopy, and incubation experiments to address the following objectives: (1) evaluate the organo-mineral association properties driving SOC contents relative to known variables affecting SOC, such as pH, depth, and water content; (2) identify changes in reactive metal and SOC properties and organo-mineral interactions as a function of saturation frequency; and (3) relate observations to SOC mineralization potential under fluctuating anaerobic-aerobic conditions.

2. Materials and Methods

2.1 Study Site Description

Soil sampling was conducted over a slope transect in Hubbard Brook Experimental Forest (North Woodstock/Lincoln, NH) Watershed 3 (W3), a hydrological reference watershed for which a hydropedological unit (HPU) classification system was initially developed and verified (Bailey et al., 2014) (Appendix Figure A3.2.1). Soils in W3 are Wisconsinan glacial deposits (basal and ablation till) over Silurian Rangeley Formation bedrock (sillimanite-grade pelitic schist and calc-silicate granulite) (Gannon et al., 2017). The effects of differing hydrological patterns on soil formation in Northeast forested Spodosols have been described in depth for W3 and used to predict soil profile characteristics and soil properties and develop Spodosol descriptive map units (i.e., HPUs) (Appendix Figure A3.2.1) (Bailey et al., 2014; Bourgault et al., 2015, 2017; Gannon et al., 2017). In particular, shallow-to-bedrock profiles (“E podzols”) experience lateral leaching of mobile elements, colloidal materials, and metal-organic complexes, with accumulation of transported materials in thick spodic (e.g., Bhs) horizons of adjacent “Bhs podzols” (Figure 2.1) (Bourgault et al., 2017). In contrast, the “typical” podzolization process is defined by vertical transport and accumulation of semi-crystalline metals and metal-organic complexes in the spodic horizon. Previous water table measurements show increasing frequency of water table presence in surface horizons for typical < Bhs < E podzols (Bailey et al., 2014; Figure 2.1). Based on these measurements, here we define saturation frequency categories as “low”, “medium”, and “high” for soils collected from typical, Bhs, and E podzol

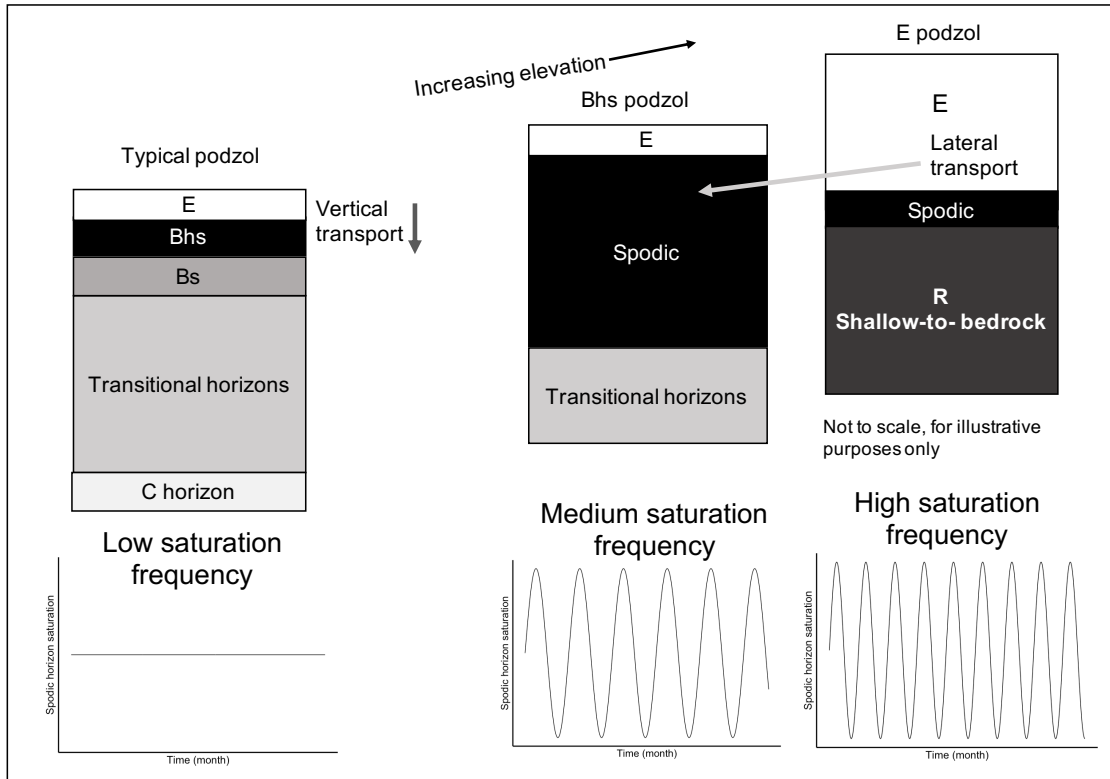


Figure 2.1. Simplified schematic of variation in mineral soil profile horization and transport associated with Spodosol variants, defined as typical, Bhs, and E podzol hydropedological units (HPUs) (Bailey et al., 2014). Lateral transport and transient water table influence on soil formation is representative of similar Spodosol observations globally (Sommer et al., 2000; Jankowski, 2014). Previous studies on hillslope transects at Hubbard Brook Experimental Forest (NH) found the number of instances of water reaching the spodic horizon over a period of 1-month to be 0, 6, and 9 times for typical, Bhs, and E podzols, respectively (Bailey et al., 2014). In this study, saturation frequency categories of low, medium, and high were consequently assigned to typical, Bhs, and E podzols, respectively.

locations, respectively (Figure 2.1). Typical, Bhs, and E podzol locations were determined by microtopography and HPU predictive models (Gannon et al., 2017) and confirmed based on in-field profile characteristics (Appendix Tables A4.2.1 and A4.2.2).

Tree species was determined for trees >0.1 m DBH in 0.0314 ha areas surrounding each HPU location. Across the transect, vegetation was generally mixed

hardwood forest with primary tree species American beech (*Fagus grandifolia*), striped maple (*Acer pensylvanicum*), sugar maple (*A. saccharum*), yellow birch (*Betula allghaniensis*), white birch (*B. papyrifera*), and coniferous species balsam fir (*Abies balsamea*) and red spruce (*Picea rubens*). Vegetation indices showed a minor (~35%) increase in coniferous tree species presence with increasing elevation, but similar tree species accounted for the majority of the site basal area (Appendix Table A4.2.3). In particular, white birch (*B. allegheniensis*) accounted for the largest proportion of basal area in all sites, with 11.7, 12.6, and 17.2% of basal area for low, medium, and high elevation sites, respectively (Appendix Table A4.2.3).

2.2 Mineral-Organic Interaction Dynamics

2.2.1 Basic Soil Characterization

Soil pH in 0.01 M calcium chloride (CaCl_2) was determined with air-dry soil at a 1:2 v/w soil ratio (Hendershot et al., 1993). Total SOC and total nitrogen (N) were determined by combustion with a Carlo-Erba NC2500 elemental analyzer (CE Instruments Ltd, Wigan, UK). Total metals were measured using the lithium (Li) meta/tetraborate flux method (Kurtz et al., 2000). Ball-milled, ashed (550°C) soils were reacted with a 1:1 mixture of Li-metaborate and Li-tetraborate added at a 4:1 flux reagent:soil ratio. The mixture was fused at 1050°C for 1 h, followed by dissolution of the fusion bead in 10% nitric acid (HNO_3). Extracted metals were analyzed in a 2% nitric acid matrix using a SpectroBlue inductively-coupled plasma optical emission spectrometry (ICP-OES) instrument (Ametek, Kleve, Germany).

2.2.2 Metal Selective Extractions

All selective extract metal contents were determined with ICP-atomic emission spectrometry (ICP-AES) (Thermo iCAP 6500 series, ThermoFisher Scientific, Bellafonte, PA) in a 2% nitric acid matrix. All soil samples were air-dried and ball-milled to a fine powder prior to extractions.

2.2.2.1. Acid Ammonium Oxalate. Non-crystalline and poorly crystalline Fe and Al (including magnetite) were measured by acid ammonium oxalate (0.2 M ammonium oxalate ((NH₄)₂C₂O₄) with 0.2 M oxalic acid (H₂C₂O₄) adjusted to pH 3) extraction at a 1:40-60 soil:extractant ratio (Ross and Wang, 1993). The extraction was completed in the dark with additional filtration (low-phosphate Whatman 512 1/2, Whatman Inc., North Bend, OH) prior to centrifugation (20 min at 1000 rpm). The optical density of the oxalate extract (ODOE) was determined by absorbance at 430 nm using a Shimadzu UV-Vis 2600 (Shimadzu Corp., Kyoto, Japan).

2.2.2.2 Hydroxylamine-HCl. Acid hydroxylamine-hydrochloric acid (HCl) extraction was used to determine non-crystalline (excluding magnetite) metal contents (Ross and Wang, 1993). For all mineral soil horizons, the extraction was completed at a 1:250 w/v soil:extract ratio using 0.25 M hydroxylamine-HCl in 0.25 M HCl (pH ~2). Supernatant aliquots were centrifuged at 11,500 rpm for 10 min prior to ICP analysis. For a subset of spodic horizons (n=3 for each saturation frequency), a separate hydroxylamine-HCl extraction was completed at a 1:60 w/v soil:extract ratio in order to determine changes in C content of the supernatant compared to a water-only extraction (1:60 w/v soil:water ratio). The supernatant C concentration was measured in solution using a Shimadzu TOC-V_{CPH/CPN} analyzer (combustion method) (Shimadzu Corp, Kyoto, JP).

2.2.2.3 Citrate-Dithionite. Non-silicate crystalline Fe was extracted using the citrate-dithionite method (Ross and Wang, 1993). Soils were extracted at a 1:25 to 1:50 w/v soil:extract ratio with 0.4 g solid sodium dithionite ($\text{Na}_2\text{S}_2\text{O}_4$) in 0.68 M sodium citrate ($\text{Na}_3\text{C}_6\text{H}_5\text{O}_7$). Filtration was completed prior to centrifugation (Whatman 595 1/2) at 2000 rpm for 30 min.

2.2.3 Elemental Spatial Relationships

Elemental maps (C, Fe, and Al) of fine-fraction particles for a low and high saturation frequency horizon were collected using nanoscale secondary ion mass spectrometry (NanoSIMS). Imaging was conducted using a Cameca NanoSIMS 50L instrument (Gannevilliers, FR) at the Chair of Soil Science, Technical University Munich (Freising, DE). Air-dry soil samples (<2 mm) were brought to field moist conditions for a 14-d incubation prior to air-drying for NanoSIMS analysis. Samples were prepared by brief (6-s) low-energy (water bath) sonication of 0.25 g air-dry soil suspended in 10 mL Nanopure® water. After allowing larger particles to settle, a ~100- μL suspension was drop-cast on Si wafers and air-dried. Prior to NanoSIMS imaging, the distribution of particles was characterized and regions of interest (ROI) selected by optical microscopy (Zeiss Axio Imager Z2, Oberkochen, DE) and scanning electron microscopy (JEOL JSM 5900LV, Tokyo, JP), with an ~5 nm-thick gold (Au) sputter coating. For NanoSIMS data collection, a high beam current was applied prior to image collected to remove sputter coating. NanoSIMS ion images (30x30 μm) were collected for $^{12}\text{C}^{14}\text{N}^-$, $^{27}\text{Al}^{16}\text{O}^-$ and $^{56}\text{Fe}^{16}\text{O}^-$ with 1 ms pixel⁻¹ dwell time. Images were aligned and summed in the OpenMIMS package (Gormanns et al., 2012) in ImageJ v 2.0.0 (Schneider et al., 2012). For low and high saturation frequency soils, images

from multiple regions were analyzed for pixel intensity correlation (n=5 for high and n=4 for low saturation frequency). Pixel intensity correlation between elements (C-Al, C-Fe, and Fe-Al) was determined using Spearman rank correlation (r_s) in base R (R Core Team, 2017).

2.2.4 Bulk Soil Statistical Analyses

Differences in spodic horizon total and extractable Fe, Al, and manganese (Mn), as well as the ratio of hydroxylamine-HCl to water-extractable C, Fe, and Al for each saturation frequency were determined using the non-parametric Kruskal-Wallis rank sum test with post-hoc comparisons with the Dunn test and the Bonferroni correction method in base R (R Core Team, 2017). Additionally, the bulk elemental and extraction data collected for all mineral soil horizons (eluvial, spodic, transitional, and substratum) were used to assess the strongest predictors of SOC content across all saturation frequencies. To account for covariation and potential non-linear relationships between SOC and variables, a Random Forest machine learning regression approach was used to compute variable importance rankings using the “caret” and “randomForest” packages in R v. 3.5.3 (Breiman, 2001; Kuhn, 2008; R Core Team, 2017). Further details describing the Random Forest approach are described in Supplementary Methods (Appendix A1.2.1).

2.3 Probing Iron-Carbon Interactions: X-ray Absorption and NMR Spectroscopy

2.3.1 Fe K-edge XAS

Changes in bulk Fe speciation across saturation frequency were determined for a set of nine spodic and/or transitional (E podzol only) horizons with Fe K-edge X-ray absorption near-edge structure (XANES) and extended X-ray absorption fine structure

(EXAFS) (Appendix Table A4.2.4). Fe XAS data were collected at the Cornell High Energy Synchrotron Source (CHESS) F3 hard X-ray beamline (Ithaca, NY), equipped with a hard-bend magnet source with a silicon (111) monochromator and silicon drift detector operated under room temperature and ambient pressure. Soil samples and standard minerals were ball-milled and suspended in DI water for thin-layer deposition on Kapton® tape (1-mil) windows, while Fe-organic complex standards (dry) were pressed as a thin layer directly onto windows. Standards were selected to represent a range of Fe redox state and Fe-organic bonding, with ferrihydrite (nominally $\text{Fe}_2\text{O}_3 \bullet 0.5\text{H}_2\text{O}$), goethite ($\alpha\text{-FeO(OH)}$), nontronite and Fe^{2+} -substituted nontronite (Fe-rich smectite), and fayalite (Fe_2SiO_4) as mineral standards and Fe (II) citrate ($\text{C}_6\text{H}_6\text{FeO}_7$), Fe (III) citrate ($\text{C}_6\text{H}_5\text{FeO}_7$), and Fe (III) ethyldiaminetetraacetic acid (EDTA) ($\text{C}_{10}\text{H}_{12}\text{N}_2\text{NaFeO}_8$) as Fe-organic complex standards. Reduced Fe standards were suspended, drop-cast, and air-dried in an anaerobic environment.

Total fluorescence yield was collected and normalized to incidence flux (I0) for the energy region of 6912 to 7537 eV to include pre-edge (-200 to -20 eV), near-edge (-20 to +12 eV), and post-edge (+12 to +425 eV) relative to the Fe K-edge (7112 eV). The step size was 5 eV for the pre-edge, 1 eV for the near-edge, and 0.05 wavenumber (\AA^{-1}) for the post-edge, with 1, 2, and 5 s dwell time, respectively. Multiple scans were collected for each sample (2-3 for standards and 5 for samples). Energy position was corrected with in-line calibration to a pure Fe (Fe^0) foil. Spectra were normalized (3rd-order) and flattened in Athena (Demeter 0.9.25) (Ravel and Newville, 2005) with a pre-edge range of -150 – -30 eV and post-edge 150 - ~400 eV relative to the edge position. The $\mu(\text{E})$ white line and pre-edge centroid energy

positions were determined by fitting a Gaussian function to restricted energy regions (7100-7118 eV and 7118-7160 eV) in Fityk v. 1.3.1 (Wojdyr, 2010). To assess changes in near-edge fine structure, the first derivative of normalized fluorescence yield ($dx/d\mu(E)$) and the maximum of $dx/d\mu(E)$ (E_0 , the edge position inflection point) were computed.

To determine fine structure changes in the Fe XANES region associated with Fe oxidation states, a model consisting of four Gaussian functions was applied to determine relative changes in the energy feature at 7120 eV associated with increasing Fe(II) (1s-4s transition) (Berry et al., 2003). Model parameters are described in Supplementary Methods (Appendix A1.2.2). Additionally, further analysis of the Fe XANES $dx/d\mu(E)$ spectra was conducted with linear combination fitting (LCF) in Athena (Demeter 0.9.25) (Ravel and Newville, 2005; Lengke et al., 2006). A reduced set of standard compounds was selected represent variation in both Fe(II) and Fe-organic bonding: Fe (II) citrate, Fe(III) citrate, ferrihydrite, Fe²⁺-substituted nontronite, and fayalite. The LCF was performed with component weights forced to 0-1 and to sum to 1. To further assess Fe-organic bonding, the EXAFS forward Fourier transform (K-space) was computed for the 3-10 Å⁻¹ wavenumber range and plotted as k²-weighted spectra in Athena (Demeter 0.9.25) (Ravel and Newville, 2005). Spectra were qualitatively assessed with emphasis on reduced amplitude at 7.5 Å⁻¹ associated with increased Fe-organic bonding in non-crystalline Fe (Chen et al., 2014). Additionally, LCF was applied in Athena as described above for the EXAFS K²-weighted spectra, using goethite, ferrihydrite, and Fe (III) EDTA as crystalline, semi-crystalline, and Fe-organic complex standards, respectively.

2.3.2 Carbon K-edge XAS

The C composition of a subset of the investigated spodic horizons was determined with C K-edge XANES (Appendix Table A4.2.4). Composition of C in water-extractable DOM (Section 2.2.2.2) and bulk soil with light POM removed was also determined with C K-edge XANES spectroscopy for horizons used for incubation experiments (Section 2.4) (Appendix Table A4.2.4). All C K-edge XANES measurements were conducted at the spherical grating monochromator (SGM) beamline of the Canadian Light Source (Saskatoon, SK), equipped with silicon drift detectors (SDD) for partial fluorescence yield (PFY). The SGM endstation was operated under 10^{-6} Torr.

Soil samples were air-dried, sieved to 2 mm, and ball-milled to a fine powder. Approximately 10 mg of soil was suspended in 500 μ L DI water and vortexed briefly (10 s). Water-extracted DOM was freeze-dried and finely pulverized. Due to the low volume of solid phase material in water-extractable DOM, all freeze-dried residue was resuspended in 50 μ L DI water and vortexed for ~60 s to ensure suspension homogeneity. For all suspensions, ~60 μ L suspension was deposited as a thin layer on Au-coated silicon wafers and air-dried. Carbon K-edge PFY spectra were collected for 40-60 point scans (probe size 50x50 μ m) in slew mode (>100 μ m spacing), interpolated and averaged using SGM Laboratory Analysis and Acquisition System GUI. A fluorescent line peak of 290.0 eV (width 100.0 eV) ROI was used. Energy position was calibrated by alignment of the carboxylic acid peak of a citric acid standard (288.70 eV). The maximum scattering signal of a plasma-cleaned Au-coated silicon wafer was used as for incidence flux normalization. Damage tests were

collected to assess development of spectral artifacts resulting from sample radiation damage (Appendix A1.2.3, Appendix A2.2.1).

Spectra were initially processed (edge-step normalization and flattening) in Athena (Demeter 0.9.25) (Ravel and Newville, 2005). For all spectra, the C K-edge XANES fine structural changes were compared by peak height ratios of the 3 primary spectral features: aromatic (C=C) at ~285.0 eV, substituted aromatic (e.g., C=C-OH) at ~286.5 eV, and carboxylic (C=O-OH) at ~288.7 eV (Solomon et al., 2009; Heymann et al., 2011). Peak heights were determined by the Gaussian function fitting algorithm in Fityk v. 1.3.1 (Wojdyr, 2010), identifying the maximum of a Gaussian function of FWHM = 0.6 eV within the defined ranges of 285.0-286.2 eV for aromatic C, 286.0-287.0 eV for substituted aromatic C, and 288.0-289.5 eV for carboxylic C (Solomon et al., 2009, Heymann et al., 2011).

2.3.3 ¹³C-NMR Variable Contact Time Experiments

The association between paramagnetic Fe and C forms was probed directly in a subset of bulk soils (Appendix Table A4.2.4) using ¹³C cross-polarization magic angle spinning (CPMAS) nuclear magnetic resonance (NMR) spectroscopy by determining the effect of variable contact time (VCT) on signal intensity for carboxylic, aromatic, O/N-alkyl, and alkyl C components of the NMR spectrum. The effect of paramagnetic Fe³⁺ on the transfer of polarization from the proton (¹H) to ¹³C spin systems was determined by varying the cross-polarization contact time, which gives an estimate of the ¹H spin-lattice relaxation time in the rotating frame (T_{1ρ}H), or the amount of time required for a complete loss of ¹H magnetization (Schöning et al., 2005). The value of T_{1ρ}H and the change in NMR signal intensity with increasing contact time (i.e., the

magnitude of VCT effect) were calculated separately for integrated regions of the NMR spectrum corresponding to carboxylic, aromatic, O/N-alkyl, and alkyl C (Knicker and Lüdemann, 1995) for spodic horizon soil samples (n=6) with a range of C/Fe ratios. The strength of the relationship between C/Fe and $T_{1\rho}H$ was taken to indicate the degree of Fe(III) interference and associated medium-range Fe-C interaction for each C functional group (Schöning et al., 2005).

Solid-state CPMAS- ^{13}C NMR spectra were collected using a Biospin DSX 200 NMR spectrometer (Bruker, Rheinstetten, Germany) on ball-milled soil samples using a pulse delay of 0.4 sec, frequency of 6800 Hz, and accumulation of 100,000 scans. Further description of the VCT calculations are included in Supplementary Methods (Appendix A1.2.4).

2.3.4 Statistical Analyses of Spectroscopic Results

Differences in Fe K-edge LCF proportions and C K-edge peak height ratios were determined using the non-parametric Kruskal-Wallis rank sum test with post-hoc comparisons with the Dunn test and the Bonferroni correction method in base R (R Core Team, 2017). The effect of C/Fe ratio on NMR VCT parameters was determined using multiple linear regression, with C/Fe ratio and carbon type (alkyl, carboxylic, aromatic, or O/N alkyl) as fixed effects and model F-tests (ANOVA) to determine the significance of model parameters.

2.4 Anaerobic-Aerobic Cycle Incubation

For representative soils of high, medium, and low saturation frequency (Appendix Table A4.2.4), macro-POM (defined here as POM >125 μm able to float in water) was removed prior to incubation by aspiration. Soils suspended in Nanopure water at a 2:1

water:soil ratio were shaken by hand for 2 min, allowed to settle for <30 s, and floating material water aspirated. Aspirated solution was returned after sieving to 125 μm and the remaining POM-removed soil was dried at 60°C.

With low soil weights (<5 g) for incubation, water content was determined using a modification of the method described in DeCiucies (2018) modified from Black (1965). Briefly, water content at saturation was determined by saturation of 3-5 g soil overnight in a mesh-lined PVC tube, matching the diameter of the incubation container. After saturation, soil with the PVC tube was allowed to drain freely; after draining of “free” water (1 h), the soil was determined to be at “field capacity”.

To drive Fe(III) reduction and determine associated C mobilization and mineralization, a spodic horizon soil from each saturation frequency was incubated for a series of three cycles: (1) aerobic only, (2) anaerobic or aerobic, and (3) aerobic only (from here on called “first cycle”, “second cycle”, “third cycle”, respectively), with measurement of cumulative carbon dioxide (CO_2) for each cycle using the potassium hydroxide (KOH) trap method (Whitman et al., 2014). Prior to the first incubation cycle, soils were brought to 50% field capacity and pre-incubated at 30°C for 2 d in 0.06-L glass vials within 0.4-L glass Mason jars modified with air-tight septa (n=4 jars for each soil). At the initiation of each incubation cycle, 2 mL CO_2 -free water was added to the jars to maintain a moist environment. For the first cycle (only aerobic), a KOH trap was added to each jar and the jar was purged for 5 min with CO_2 -free air (Zero Air Airgas, Inc, Elmira, NY). After this first 5-d cycle, dissolved CO_2 was measured in the KOH trap via changes in electrical conductivity and converted to CO_2 absorbed using a standard curve of known volumes of 99.99% CO_2 (Airgas, Inc,

Elmira, NY) injected via air-tight septa (Whitman et al., 2014; Krounbi et al., 2018). For the second cycle, anaerobic jars were purged with 99.99% N₂ (Airgas, Inc, Elmira, NY) and aerobic jars purged with 100% CO₂-free air. After a 7-d anaerobic incubation, cumulative CO₂ was determined as above.

After the second cycle, moist soils were sub-sampled in an anaerobic environment (N₂ and H₂ glove box with <1 ppm O₂), and an extraction with deoxygenated Nanopure™ water was performed at a 1:8 w/v soil:water ratio. Extracts were shaken 2.5 h at medium speed, followed by centrifugation for 30 min at 3000 rpm. The supernatant was decanted and filtered to 0.45 μm (nylon syringe filters, Restek Corporation, Bellafonte, PA) in an anaerobic environment as above. After sub-sampling, jars were capped tightly and stored overnight at 7°C. After subsampling, all treatments were purged for 10 min with 100% CO₂-free air and cumulative CO₂ measured after a third cycle lasting 5 d under only aerobic conditions.

Water-extractable Fe²⁺, DOC, total Fe, and total Al were quantified in the extracts after the second cycle as follows. In de-oxygenated water extracts, dissolved Fe²⁺ was determined immediately under anaerobic conditions using the ferrozine colorimetric method (Viollier et al., 2000; Huang and Hall, 2017). Ferrozine reagent (3-(2-pyridyl)-5,6-diphenyl-1,2,4-triazine-*p,p'*-disulfonic acid monosodium salt hydrate) (1 g L⁻¹ in 50 mM 2-[4-(2-hydroxyethyl)piperazin-1-yl]ethanesulfonic acid (HEPES) buffer at pH 8) was mixed with supernatant at a 1:10 v/v ratio and absorbance at 562 nm measured after 60 min incubation. Iron (III) chloride was used as an analytical standard following hydroxylamine-HCl reduction to Fe²⁺. Total dissolved Fe and Al were determined by ICP-AES (Thermo iCAP 6500 series,

ThermoFisher Scientific, Bellafonte, PA) in a 2% nitric acid matrix. Dissolved OC was determined using a Shimadzu Shimadzu TOC-V_{CPH/CPN} analyzer (combustion method) (Shimadzu Corp, Kyoto, JP). All extract measurement values were corrected for soil dry weight and water content after drying the extraction residue (70°C). For all incubation experiment results, data were tested for normality and log₁₀-transformed to achieve a Shapiro-Wilks test p -value >0.05 . Differences in initial aerobic CO₂ mineralization (cycle 1) across saturation frequency were compared by one-way ANOVA. Change in CO₂ mineralization rate, DOC mineralization and concentration, soluble total Al and Fe, and soluble Fe²⁺ after the second cycle (anaerobic or aerobic) were analyzed statistically using two-way ANOVA, testing the effects of saturation frequency, treatment (anaerobic or aerobic), and their interaction. When significant ($p < 0.1$) main effects were detected, post-hoc analysis was conducted with Tukey's HSD multiple comparisons test.

3. Results

3.1 Mineral-Organic Interaction Dynamics

3.1.1 Basic Soil Characterization

Overall, soil pH increased in deeper horizons for low and high saturation frequency categories, but did not change appreciably with depth for medium saturation frequency (Appendix Table A4.2.5). For transitional horizons and C horizons, the lack of observations at medium and high saturation frequency precluded comparisons across saturation frequency. However, an increase in pH was detected for eluvial and spodic horizons with changing saturation frequency (Appendix Table A4.2.5). Total C and N

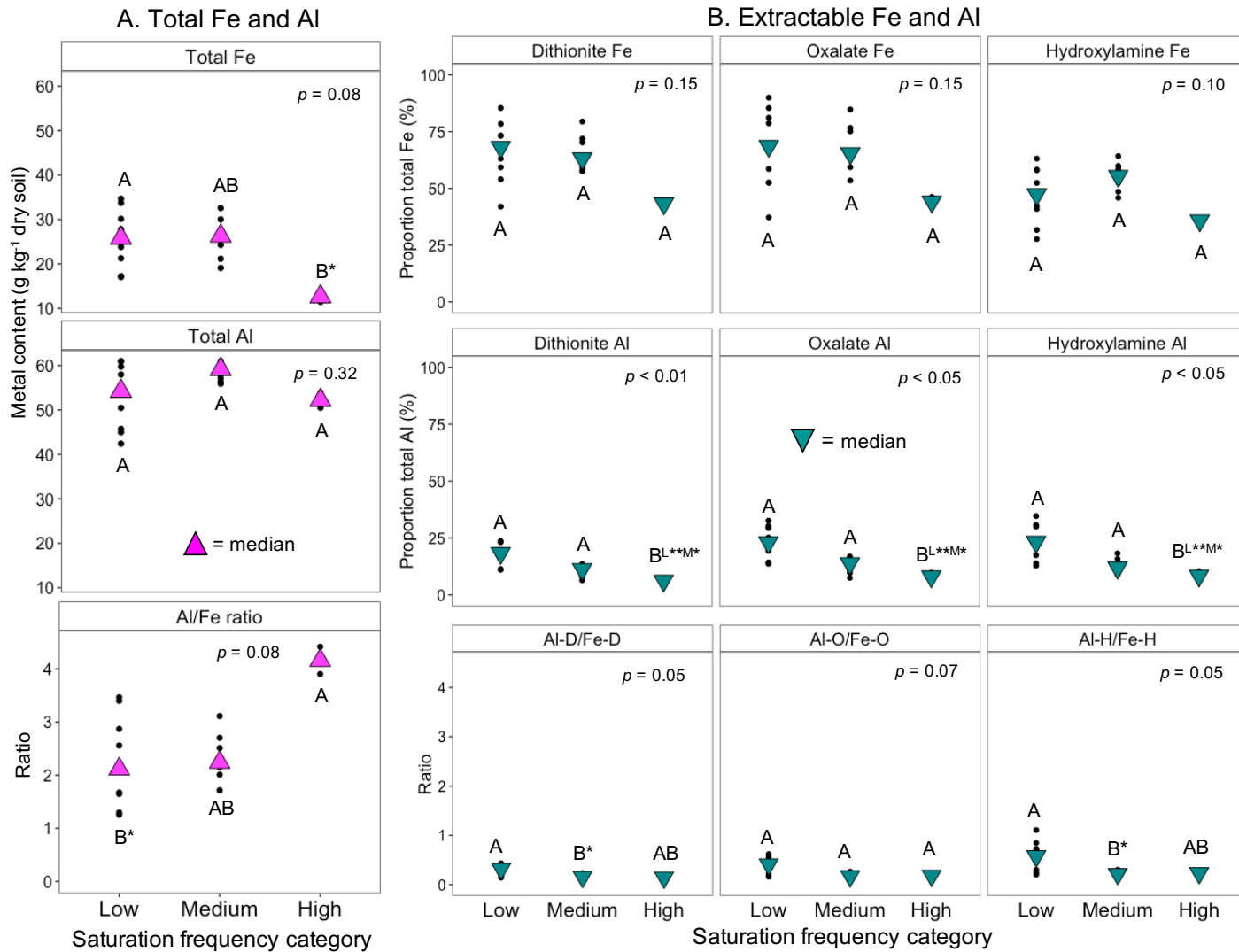
contents increased in spodic horizons compared to eluvial and transitional/C horizons for low and medium saturation frequency categories, but did not change with depth at high saturation frequency (Appendix Table A4.2.5). For eluvial and spodic horizons, C and N content decreased with increasing saturation frequency (Appendix Table A4.2.5). For spodic horizons, the distribution of total soil organic matter (determined by LOI), Fe, and Al also differed across saturation frequency, with LOI and Fe content generally comprising a larger fraction of soil mass in low saturation frequency, and Al as a larger fraction at high saturation frequency (Appendix Table A4.2.5). For spodic horizons, total Fe decreased significantly (at $\alpha=0.1$) (Kruskal-Wallis $p=0.08$) with increased saturation frequency (Figure 2.2). Total Al did not change across saturation frequency, resulting in a higher (Kruskal-Wallis $p=0.08$) ratio of total Al to total Fe at high saturation frequency (Figure 2.2). For spodic horizons, total Mn did not change across saturation frequency (Kruskal-Wallis $p=0.15$, Appendix Figure A3.2.2, Appendix Table A4.2.5).

3.1.2 Selective Extractions

The proportion of total metals extractable by citrate-dithionite (crystalline/non-silicate), acid ammonium oxalate (non-crystalline + magnetite), and hydroxylamine-HCl (non-crystalline excluding magnetite) varied across genetic horizons, with increased semi-crystalline mineral content in spodic and transitional horizons and decreases in eluvial horizons and substratum (Appendix Table A4.2.6). While the proportion of dithionite, oxalate, and hydroxylamine-extractable Fe was high (up to

Figure 2.2 A. Bulk soil total iron (Fe), total aluminum (Al), and Al/Fe ratio for spodic horizons of low (n=8), medium (n=7), and high (n=2) saturation frequency categories.

B. Bulk soil citrate-dithionite, acid ammonium oxalate, and hydroxylamine-HCl, extractable Fe and Al and the ratio of extractable Al/extractable Fe for spodic horizons. For both A and B, points are individual measurements and triangles show the arithmetic median. Within each element and extractant, *p*-values are shown for overall Kruskal-Wallis ANOVA on Ranks. Letters show post-hoc multiple comparisons (Dunn Test with Bonferroni correction), with different letters showing significant differences at $\alpha=0.1$ (*) and $\alpha=0.05$ (**).



60% of total Fe), the proportion of dithionite, oxalate and hydroxylamine-extractable Fe relative to total Fe did not differ significantly across saturation frequency (Figure 2.2). Further, a directional trend was not observed, with a slight increase in extractable Fe with medium saturation frequency for all extractions.

Extractable Mn (oxalate and hydroxylamine only) was generally low (<10% of total Mn), but a significant decrease in both oxalate and hydroxylamine-extractable Mn was detected between high and low saturation (Appendix Figure A3.2.2). Similarly, all selective extraction approaches showed significant differences in dithionite, oxalate, and hydroxylamine-extractable Al across saturation frequency, with the extractable proportion of total Al decreasing with increasing saturation frequency (Figure 2.2). For all Fe and Al extracts, the ratio of Al to Fe was lower (approximately 1:1 Al/Fe) than for total Al and total Fe (approximately 5:1 Al/Fe). In contrast to total Al/total Fe, the ratio of extractable Al to extractable Fe did not differ between low and high saturation frequency for dithionite, oxalate, or hydroxylamine extractions (Figure 2.2). However, a decrease in dithionite- and hydroxylamine-extractable Al/Fe ratio was detected for medium saturation frequency only (Figure 2.2).

For hydroxylamine extractions of spodic horizons, the ratio of hydroxylamine-extractable C to water-extractable C generally increased with increasing saturation frequency, but these differences were not statistically significant (overall Kruskal-Wallis $p=0.14$) (Figure 2.3). Similarly, an increase in hydroxylamine Al/water-extractable Al was detected (overall Kruskal-Wallis $p<0.1$). As with hydroxylamine-extractable Fe for all spodic and transitional mineral soils, a slight increase in

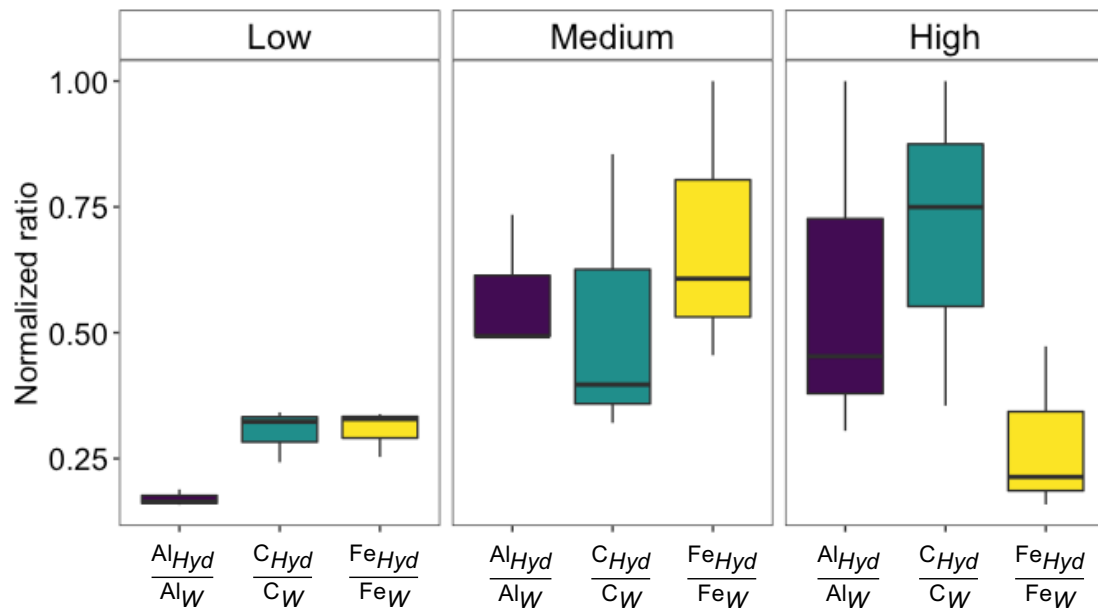


Figure 2.3. Aluminum (Al), carbon (C), and iron (Fe) released by hydroxylamine extraction (“Hyd”) relative to water extraction (“W”) for spodic horizons (n=3) from low, medium, and high saturation frequency categories. Ratios are normalized (max=1) within elements. Lower and upper edges of boxes show first and third quartiles (25th and 75th percentiles) and lower and upper whiskers show the smallest and largest value no further than 1.5*interquartile range (IQR) of the box edges.

hydroxylamine Fe/water Fe was increased relative to low and high saturation frequency, but the difference was marginally non-significant (Kruskall-Wallis $p=0.11$). Within each saturation frequency, the magnitude of DOC, Fe, and Al released with hydroxylamine extraction followed opposing trends for low and high saturation frequency, with DOC released more closely mirroring Fe for low and Al for high saturation frequency (Figure 2.3). For medium saturation frequency, the magnitude of DOC released was similar to both Fe and Al.

3.1.3 Elemental Spatial Relationships

Elemental maps derived from NanoSIMS images (Figure 2.4) generally show a high

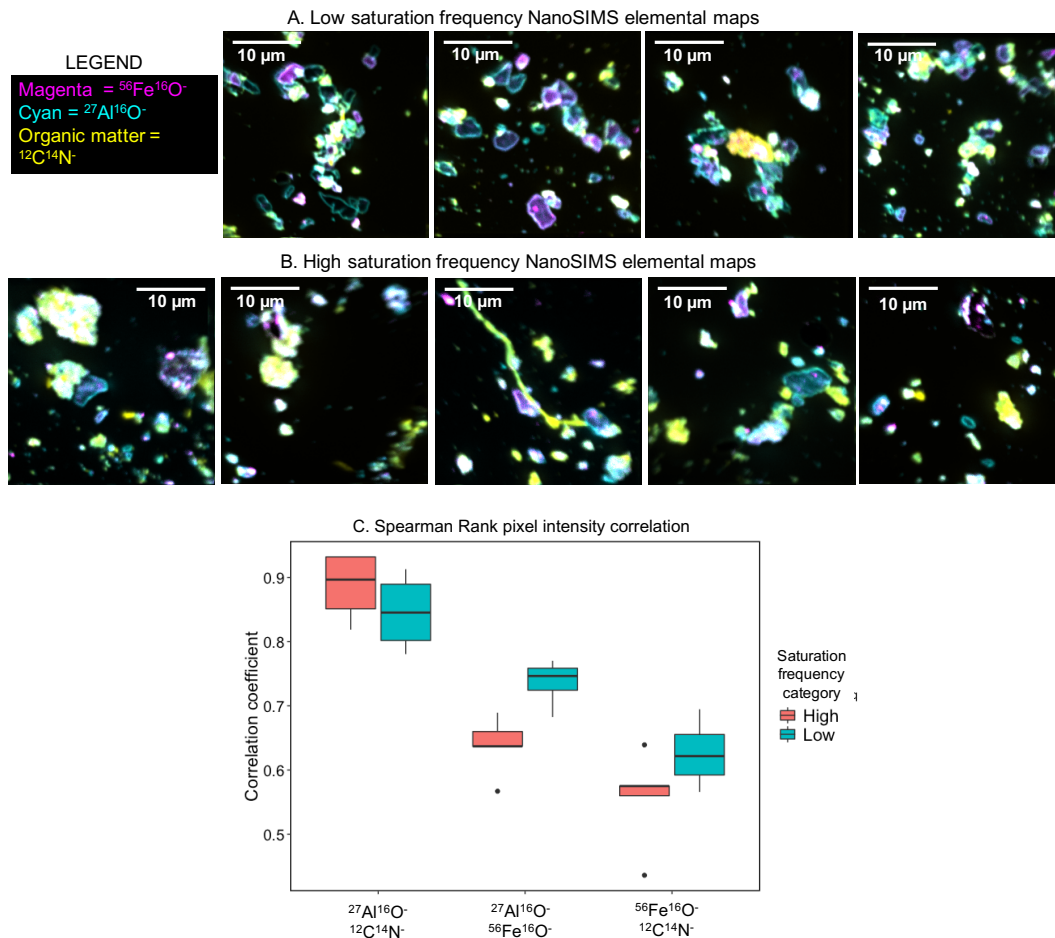


Figure 2.4. Elemental maps derived from nanoscale secondary ion mass spectrometry (NanoSIMS) imaging showing distribution of iron (as $^{56}\text{Fe}^{16}\text{O}^-$), aluminum ($^{27}\text{Al}^{16}\text{O}^-$) and organic matter ($^{12}\text{C}^{14}\text{N}^-$) for low (A) and high (B) saturation frequency categories. C. Element spatial correlations (Spearman Rank Correlation) derived from nanoscale secondary ion mass spectrometry (NanoSIMS) elemental maps. Lower and upper edges of boxes show first and third quartiles (25th and 75th percentiles) and lower and upper whiskers show the smallest and largest value no further than 1.5*interquartile range (IQR) of the box edges. Individual points beyond whiskers are considered outliers.

correlation (Spearman Rank correlation coefficient, r_s , >0.5) between Fe-Al, Fe-C and Al-C. A tendency towards weaker spatial correlation for Fe-C and Fe-Al was detected at higher saturation frequency, indicating more dispersed elemental distribution (Figure 2.4). In contrast, a stronger correlation for Al-C was detected at higher saturation frequency.

3.1.4 Mineral Soil Drivers of C Content

Over 5 independent iterations, the Random Forest regression model predicted values were strongly correlated with observed C content (linear regression $R^2=0.829$) (Appendix Figure A3.2.3). The variable importance rankings consistently ranked dithionite/oxalate/hydroxylamine Fe and dithionite/oxalate-extractable Al in the top 5 positions (Table 2.1). Spodic horizon identity (spodic/non-spodic) was also highly ranked. In contrast, pH, depth, volumetric water content, and saturation frequency were ranked in the mid-lower quartile.

3.2 Probing Iron-Carbon Interactions: X-ray Absorption and NMR Spectroscopy

3.2.1 Fe K-edge XAS

The normalized fluorescence intensity (μE) for Fe standards shifted towards lower energy for the pre-edge centroid, white line, and edge inflection (E_0) with increasing reduced Fe and for Fe-organic complexes (Appendix Table A4.2.7). Spodic horizon Fe K-edge spectra did not vary with respect to pre-edge centroid position, but a trend towards lower energy position was detected for the white line position and edge inflection with increasing saturation frequency (~ 1 eV shift between low and high saturation frequency) (Appendix Table A4.2.7). For the first derivative of normalized μE ($dx/d\mu E$), peak area at 7120.0 eV associated with reduced Fe (1s-4s transition) was

Table 2.1. Variable importance rankings for 5 independent Random Forest regression models testing predictor variables of soil organic carbon (SOC) content. Abbreviations: H = hydroxylamine-hydrochloric acid (HCl)-extractable Fe and Al (% total), O = acid ammonium oxalate-extractable metal (Fe and Al) total, content), D = citrate-dithionite extractable metal (Fe and Al), VolWater = volumetric water content (m³ water m⁻³ soil) at time of sampling, Depth = center of sampled horizon (m), Spodic/Transitional/Substratum = horizon identity, and SatFreqLow/Medium = saturation frequency identity. E horizon and High saturation frequency rankings fall <0 and are excluded.

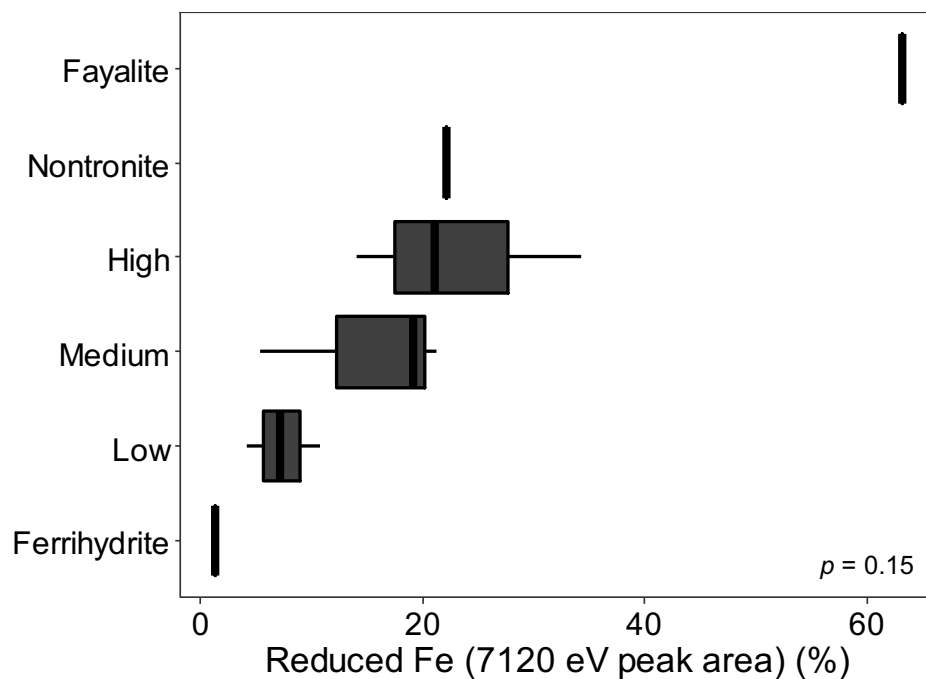
Iteration 1	Rank	Iteration 2	Rank	Iteration 3	Rank	Iteration 4	Rank	Iteration 5	Rank
Al-D	100.0	Fe-D	100.0	Al-D	100.0	Fe-D	100.0	Al-D	100.0
Fe-D	86.4	Fe-O	69.2	Fe-D	96.3	Al-D	87.6	Fe-O	92.4
Al-O	78.3	Fe-H	54.5	Spodic	93.4	Fe-H	83.8	Fe-D	85.5
Fe-H	77.1	Al-D	54.5	Al-O	88.7	Fe-O	77.0	Fe-H	85.0
Al-H	72.9	TotalFe	37.3	Fe-H	82.2	Spodic	76.8	Al-O	82.2
Fe-O	64.6	Al-O	29.3	TotalFe	80.1	Al-O	66.7	Spodic	79.9
pH	55.1	Substratum	27.2	Fe-O	79.5	VolWater	58.4	VolWater	76.0
Spodic	54.0	Al-H	25.9	pH	75.8	Al-H	52.6	pH	74.9
VolWater	52.1	pH	25.8	Al-H	72.5	pH	48.7	TotalFe	73.9
TotalFe	43.7	Spodic	25.1	VolWater	57.8	Transitional	42.6	Al-H	69.8
SatFreqLow	24.2	Transitional	23.9	Transitional	52.1	TotalFe	30.1	Transitional	57.8
Transitional	21.5	SatFreqLow	12.5	Substratum	48.0	Substratum	26.6	Substratum	49.6
Depth	12.9	Depth	10.1	Depth	33.1	Depth	16.0	Depth	39.4
Substratum	0.2	VolWater	9.9	SatFreqLow	31.6	SatFreqMed	3.5	SatFreqLow	21.5
SatFreqMed	0.0	SatFreqMed	0.0	SatFreqMed	0.0	SatFreqLow	0.0	SatFreqMed	0.0

detected for reduced Fe(II) standards and with increasing saturation frequency (Appendix Figure A3.2.4, Figure 2.5). High saturation frequency soils approached the 7120.0 eV peak area of Fe(II)-substituted nontronite (~30% 7120.0 eV area), which contains a mixture of Fe(II)/Fe(III) (Figure 2.5).

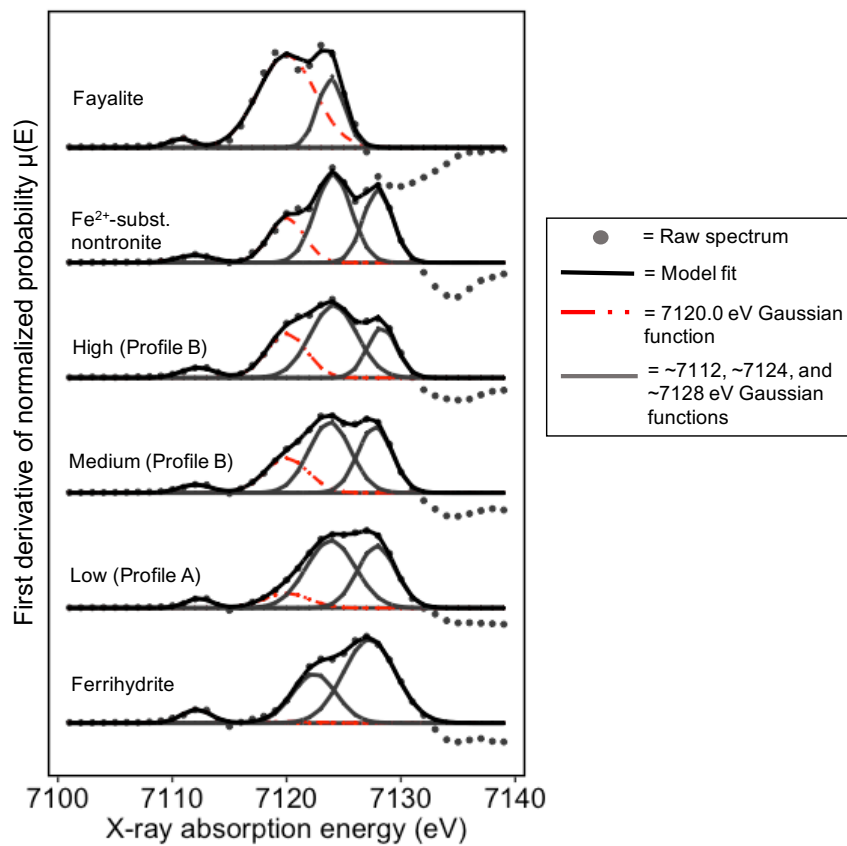
LCF models for both XANES and EXAFS spectral regions of spodic horizon soils confirmed the increase in reduced Fe components with increasing saturation frequency, and further refine information about Fe composition (Figure 2.6). For all saturation frequencies, the largest fraction of both XANES and EXAFS LCF models was associated with ferrihydrite, a short-range ordered (semi-crystalline) Fe(III) mineral. For the XANES LCF model, both Fe(II)-organic complex (Fe(II) citrate) and Fe(II)/Fe(III) mineral (Fe(II)-nontronite) phases increased with increasing saturation frequency (Figure 2.6, Appendix Figure A3.2.5). Additionally, Fe(III)-organic complexes decreased in both Fe XANES (Fe(III) citrate standard) and EXAFS (Fe(III) EDTA standard) LCF models with increasing saturation frequency (Figure 2.6, Appendix Figure A3.2.5). The feature associated with outer-shell Fe bond formation at 7.5 \AA^{-1} forward Fourier transform (K^2) EXAFS spectra also increased in magnitude at high saturation frequency, a direct indication of reduced Fe-organic bonding (Chen et al., 2014) (Appendix Figure A3.2.5). Together, the Fe XANES fine-structure analysis (7120.0 eV peak area) and LCF models indicated a shift in Fe composition from predominantly Fe(III)-organic complexes at low saturation (typical podzols) frequency towards mixed Fe(II)/Fe(III) mineral phases at higher saturation frequency (E podzols).

Figure 2.5. Iron K-edge X-ray absorption near-edge structure (XANES) oxidation state determination for standard compounds and soils across saturation frequency categories (low, medium, and high). Reduced Fe is shown by proxy as the area of the 7120.0 eV Gaussian function in the XANES first derivative spectrum associated with the 1s-4s transition (Berry et al., 2003). Boxplots show the distribution of the peak area at 7120.0 eV for spodic horizons (n=3), with differences among saturation frequencies marginally non-significant (Kruskal-Wallis $p=0.15$). Standard compounds represent a range of Fe oxidation states, from mostly Fe(III) in ferrihydrite to mostly Fe(II) in fayalite, with Fe(II)-substituted nontronite a mixture of Fe(III) and Fe(II). Lower and upper edges of boxes show first and third quartiles (25th and 75th percentiles) and lower and upper whiskers show the smallest and largest value no further than 1.5*interquartile range (IQR) of the box edges.

A. Reduced Fe for saturation frequency categories



B. Example Fe K-edge XANES spectra



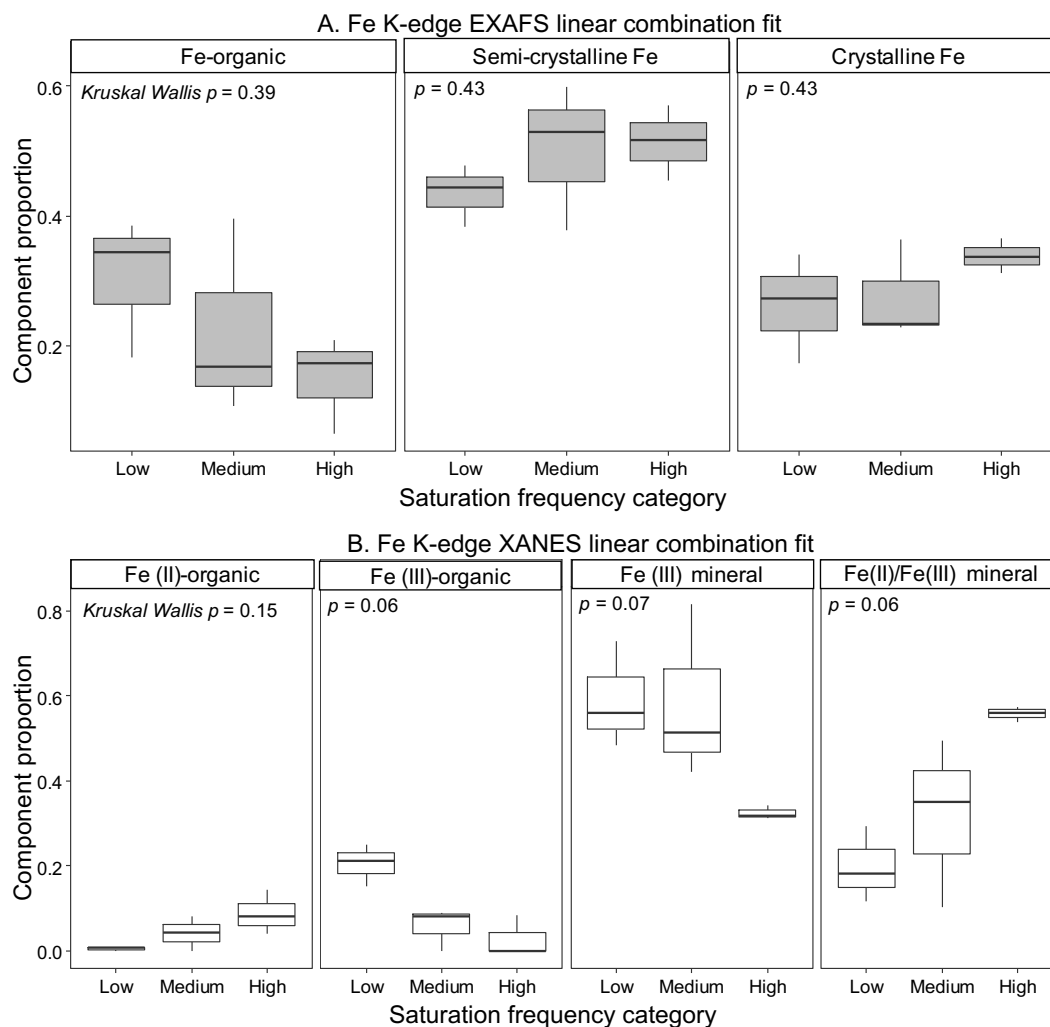


Figure 2.6. Iron (Fe) K-edge extended X-ray absorption fine structure (EXAFS) (A) and X-ray absorption near-edge structure (XANES) linear combination fit (LCF) results for soils of varying saturation frequency (B). Boxplots show the distribution of fit results for spodic horizons ($n=3$ for each saturation frequency). Lower and upper edges of boxes show first and third quartiles (25th and 75th percentiles) and lower and upper whiskers show the smallest and largest value no further than $1.5 \times$ interquartile range (IQR) of the box edges. Within each component, p-values are for Kruskal-Wallis ANOVA on Ranks.

3.2.2 Carbon K-edge XANES

A trend of increasing carboxylic/aromatic C ratio was detected with increasing saturation frequency, with a significantly higher ratio at high vs. low saturation

frequency (Kruskal-Wallis $p < 0.05$) (Figure 2.7, Appendix Table A4.2.8). The substituted-aromatic/aromatic ratio also increased with saturation frequency. Water-extractable DOC showed a higher carboxylic/aromatic C ratio for low and medium saturation frequency, but no change for high saturation frequency (Figure 2.7, Appendix Figure A3.2.6, Appendix Table A4.2.8). Soils with POM removed were also similar in composition to bulk soils, with a slight increase in carboxylic/aromatic C ratio at medium saturation frequency only. Ratios of substituted-aromatic/aromatic C were also greater at low and medium than high saturation frequency for both DOC and soils with POM removed, but for high saturation frequency the ratio was lower than in the bulk soil (Figure 2.7).

3.2.3 ^{13}C -NMR Variable Contact Time Experiment

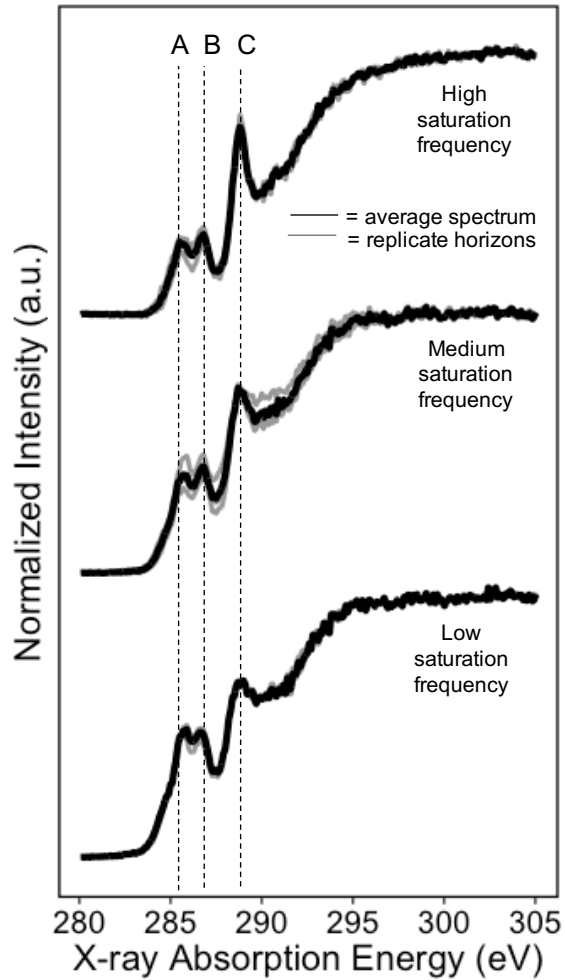
The signal intensity for all regions of the ^{13}C NMR spectrum (alkyl, O/N-alkyl, carboxylic, and aromatic C) decreased with increasing contact time (>1 s) (Appendix Figure A3.2.7). The magnitude of the contact time effect (|slope|) was similar across Fe contents normalized to C (C/Fe ratio) for alkyl and O/N-alkyl C, but varied for aromatic and carboxylic C (Figure 2.8, Appendix Figure A3.2.7). When converted to values of relaxation time ($T_{1\rho\text{H}}$), the effect of C/Fe ratios was significantly greater for aromatic and carboxylic C compared to alkyl and O/N-alkyl C (MLR $p < 0.005$) (Figure 2.8). With the contact time effect varying as a function of C/Fe ratio, aromatic and carboxylic C were inferred to be more strongly affected by Fe interference.

3.3 Anaerobic-Aerobic Cycle Incubation

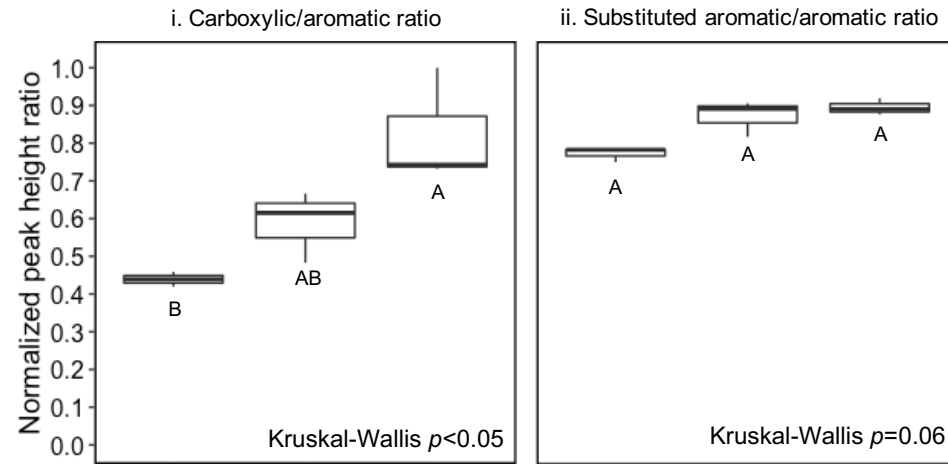
During the first cycle of a 5-d aerobic incubation, CO_2 mineralization normalized to SOC contents (from here on called “mineralizability”) increased in the order

Figure 2.7. A. Carbon (C) K-edge X-ray absorption near-edge structure (XANES) spectra for bulk soils with varying saturation frequency categories, normalized to edge step = 1 and unsmoothed. Vertical lines A, B, and C indicate aromatic (~285.0 eV), substituted aromatic (~286.5 eV), and carboxylic (~288.7 eV) C features, respectively. **B.** Normalized (max = 1) peak height ratios of carbon (C) K-edge XANES spectra. Aromatic, substituted-aromatic, and carboxylic C peak energy positions were set to 285.0, 286.5, and ~288.7 eV, respectively. For **B**, boxplots represent the distribution of measurements from spodic horizons (n=3 for each saturation frequency). Lower and upper edges of boxes show first and third quartiles (25th and 75th percentiles) and lower and upper whiskers show the smallest and largest value no further than 1.5*interquartile range (IQR) of the box edges. For **C**, points show individual measurements comparing bulk soils with dissolved organic matter (DOM) extracted from the same soil, and the soil with macro-particulate organic matter (POM) removed by water flotation. Spectra for DOM and POM-removed soil shown in Appendix Figure A3.2.6.

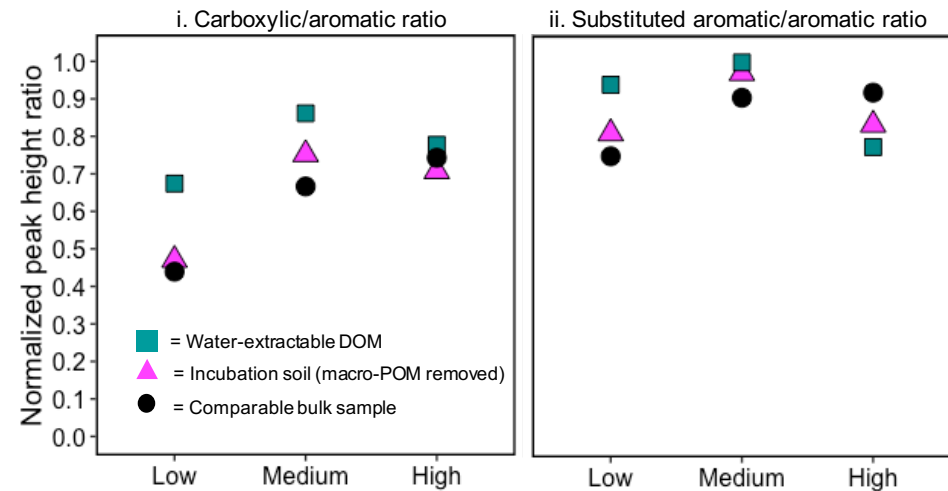
A. Bulk soil carbon K-edge XANES spectra



B. Spodic horizon bulk soils



C. DOM and incubation soils (after macro-POM removal)



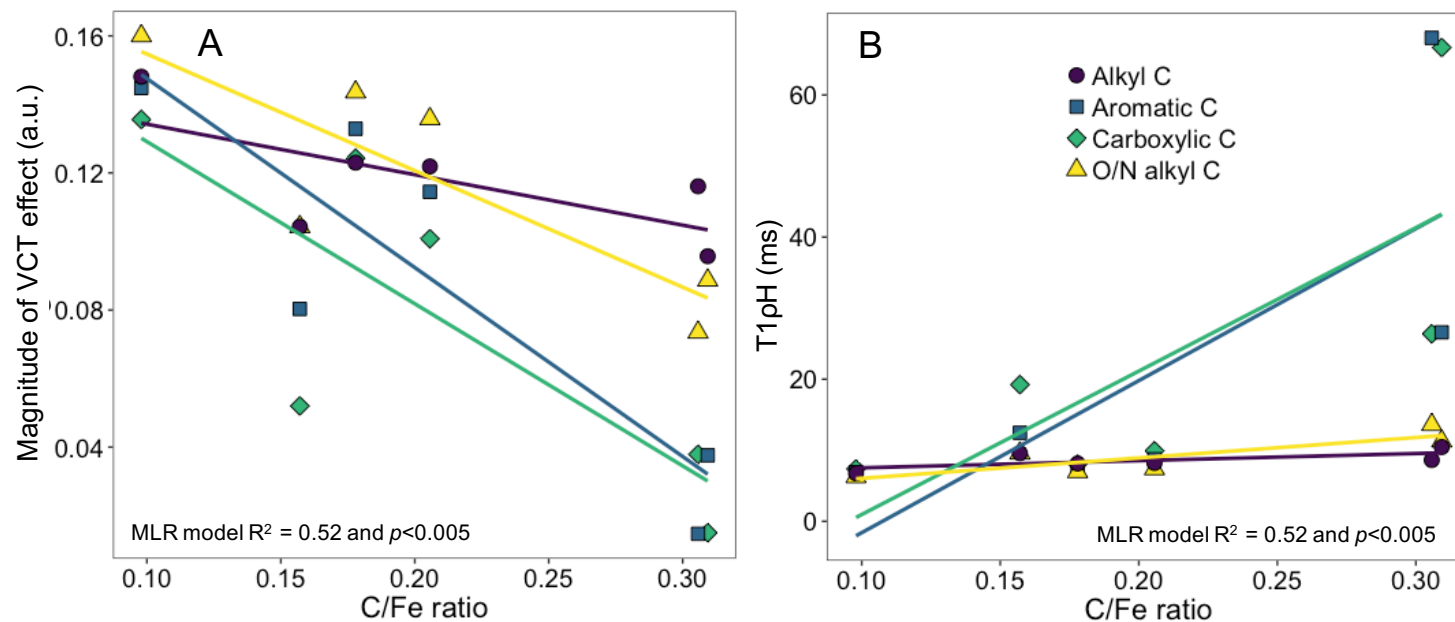


Figure 2.8. Carbon (^{13}C) nuclear magnetic resonance (NMR) variable contact time experiments showing (A) the total effect magnitude and (B) proton relaxation time ($T_{1\rho\text{H}}$) as a function of increasing iron (Fe) content (decreasing C/Fe ratio). A significant difference in the effect of C/Fe on VCT effect and relaxation time was detected for carbon forms (multiple linear regression F-test $p < 0.005$), with a stronger Fe interference for carboxylic and aromatic C compared to alkyl and O/N alkyl C.

low < medium < high saturation frequency (One-way ANOVA $p=0.09$) (Figure 2.9 A). During the following second cycle of a 7-d anaerobic incubation CO_2 mineralization rate only decreased for the low saturation frequency soil, with an approximately 10-fold difference compared to the aerobic treatment; however, two-way ANOVA main effects were not significant (Table 2.2). After the second cycle, extractable DOC (as a proportion of SOC) and soluble Al did not change under anaerobic incubation compared to the aerobic incubation across all saturation frequencies (Table 2.2). In contrast, both soluble total Fe and Fe^{2+} as a proportion of total soluble Fe increased with an anaerobic second cycle (ANOVA main effect $p=0.08$ and $p=0.07$) (Table 2.2). While the DOC amount did not change, the mineralizability of DOC increased significantly after an anaerobic cycle for high saturation frequency soil only (Tukey HSD $p<0.005$ for comparison to anaerobic treatment) (Figure 2.9 B). The mineralizability of DOC after an anaerobic vs. aerobic second cycle could be grouped by soluble Fe^{2+} for high saturation frequency soil only (Figure 2.9 C).

4. Discussion

4.1 Contrasting Mineral-Organic Interactions Across Saturation Frequency

The proportional DOC release to Fe at low saturation frequency and to Al at high saturation frequency (medium saturation frequency being intermediate) points to a divergence in organo-metal interaction mechanism, also supported by the shift in total elemental ratios and changes in extractable Al across saturation frequency, as shown in this study and by other researchers (Bourgault et al., 2015, 2017). Further,

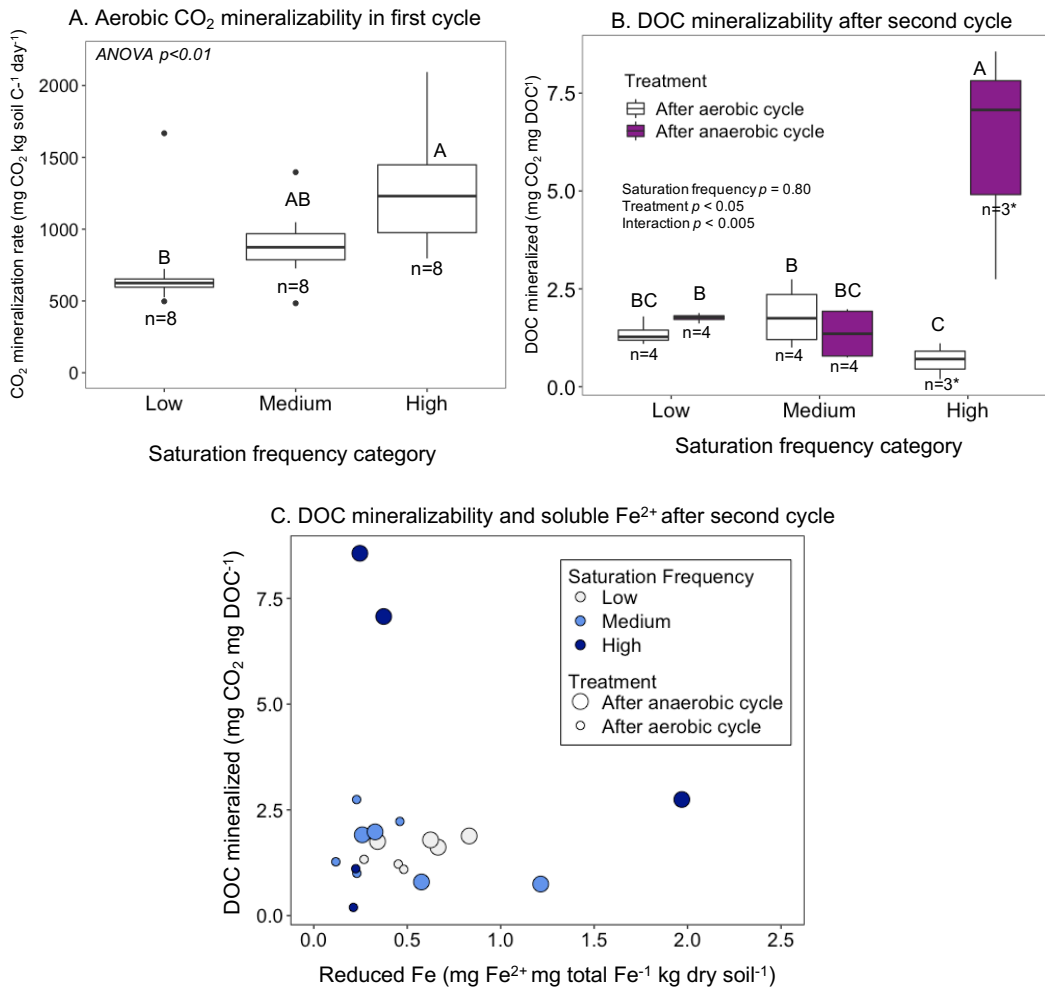


Figure 2.9. Carbon mineralizability, extractable dissolved organic carbon (DOC) and reduced iron as affected by anaerobic incubation for representative soils from high, medium, and low saturation frequency categories. **A.** Initial carbon dioxide (CO₂) mineralizability during the first cycle of a 5-d aerobic incubation (normalized to soil organic carbon content). **B.** CO₂ mineralization normalized to DOC extracted after the second cycle of a 7-d incubation under either aerobic or anaerobic conditions. For both A and B, boxplots show the distribution of replicate experimental units. Lower and upper edges of boxes show first and third quartiles (25th and 75th percentiles) and lower and upper whiskers show the smallest and largest value no further than 1.5*interquartile range (IQR) of the box edges. Significant differences (two-way ANOVA) from the highest value at $\alpha=0.10$ are indicated by different letters. * = one replicate excluded due to DOC below detection. **C.** Clustering of C mineralizability per unit extractable DOC during the third cycle of aerobic incubation after the second cycle of either anaerobic or aerobic incubation against extractable reduced iron (Fe) after anaerobic incubation.

Table 2.2. Average carbon dioxide (CO₂) mineralization rate change, soluble iron (Fe), soluble aluminum (Al), soluble Fe²⁺, and water-extracted dissolved organic carbon (DOC) following incubation with either anaerobic (anaer.) or aerobic (aer.) conditions. Mineralization rate change was calculated relative to initial respiration rates (Figure 2.9). Tukey HSD multiple comparisons are shown when ANOVA main effects have $p < 0.05$. Different letters indicate significant differences at $p < 0.1$ unless otherwise noted.

		CO ₂ mineralization rate change (%)		Soluble Fe (% total Fe)		Soluble Al (% total Al)*		Reduced Fe (% soluble Fe)*		DOC (g DOC kg SOC ⁻¹)*	
Saturation Freq.		Anaer.	Aer.	Anaer.	Aer.	Anaer.	Aer.	Anaer.	Aer.	Anaer.	Aer.
Low	Avg	5.9	98.3	0.11 ^A	0.06 ^{A**}	0.09 ^A	0.10 ^A	0.6	0.4	5.96	7.07
	SD	24.1	43.8	0.06	0.02	0.03	0.03	0.2	0.1	1.22	1.42
	n	4	4	4	4	4	4	4	4	4	4
Medium	Avg	49.0	89.7	0.02 ^B	0.01 ^B	0.02 ^B	0.02 ^B	0.6	0.3	6.30	6.89
	SD	49.8	99.8	0.002	0.005	0.001	0.003	0.4	0.1	1.05	2.29
	n	4	4	4	4	4	4	4	4	4	4
High	Avg	77.5	45.1	0.01 ^B	0.008 ^B	0.002 ^B	0.002 ^B	1.7	0.3	1.75	14.42
	SD	128.9	111.7	0.003	0.003	0.001	0.001	1.8	0.05	0.95	18.02
	n	4	4	4	4	4	4	4	3	3	3
Main effects	DF	F stat	<i>p</i> -value	F stat	<i>p</i> -value	F stat	<i>p</i> -value	F stat	<i>p</i> -value	F stat	<i>p</i> -value
Treatment	1	0.92	0.35	3.48	0.08	4.8E-05	0.15	3.69	0.07	2.14	0.16
Saturation frequency	2	0.08	0.92	25.33	5.9E-06	67.2	4.49E-09	1.43	0.27	0.12	0.89
Interaction effect	2	1.07	0.36	2.15	0.15	0.09	0.92	1.28	0.30	1.80	0.20

*When log transformation resulted in Shapiro-Wilks $p < 0.05$, the *p*-value was used as the conservative level of significance. Soluble Al $\alpha = 0.03$, reduced Fe $\alpha = 0.03$, DOC $\alpha = 0.006$. ** $p = 0.1$.

the stronger microscale spatial association of Al with C at high saturation frequency and of Fe with C at low saturation frequency underscores the relationships observed with bulk measurements.

The variability of Al and Al-associated organic matter observed in this study are likely not only driven by a shift in Fe/Al ratio due to Fe loss, but also by indirect effects of Fe reduction on soil solution chemistry. For instance, higher pH (~0.5 pH units) at high saturation frequency may be a result of long-term H⁺ consumption by Fe reduction reactions (Thompson et al., 2006a). Additionally, reduction of Fe(III)-organic complexes may result in increased solubility of organic complexing compounds that are available for reaction with Al and subsequent precipitation. In addition to surface adsorption and complex formation, the co-precipitation of Al with OM is also a likely pathway of organo-mineral stabilization (Scheel et al., 2007). With the majority of organo-mineral co-precipitation studies focused on Fe (e.g., Chen et al. 2014, Chen et al. 2016), the critical role of Al observed here at high saturation frequency points to the need for further focus on Al-OM interaction dynamics, particularly the drivers of Al solubility.

In addition to Fe and Al, redox transformations of Mn may influence SOC mobilization (Jones et al., 2018). While reactive Mn decreased with increasing saturation frequency, the explanatory power of all Mn variables (total and extractable) for prediction of SOC was very low (Table 2.1), suggesting that Mn did not influence SOC accumulation to the extent of Fe and Al. While Bourgault et al. (2015) identified differences in Mn composition for similar podzol HPUs of varying saturation frequency, high spatial variation in Mn content was also identified on the watershed

scale, suggesting the importance of Mn-mediated SOC stabilization may be localized to areas with Mn enrichment. Additionally, the close to order of magnitude difference in Mn content compared to Fe and Al may preclude identification of Mn-SOC interactions occurring on the micron-resolution scale (Jones et al., 2018).

4.2 Mechanisms of Organo-Mineral Interactions

By pairing imaging and bulk extraction approaches with analysis of organo-mineral bonding (e.g., Fe K-edge XAS and ^{13}C -NMR VCT), the synthesized dataset can be used to infer mechanisms of interaction, in addition to observation of changes in organo-mineral spatial association (i.e., co-location) and elemental correlation. At higher saturation frequency, both higher total Al/Fe and notable shifts in the composition and mineralogy of Fe were detected. Overall, the shift towards more reduced Fe at higher saturation frequency suggests that the duration of saturation in this system is sufficient to induce reducing conditions which result in not only mobilization and Fe loss, but also shifts to the remaining Fe mineral redox state. These shifts are reflected in increasing Fe(II)-organic complex, decreasing Fe(III)-organic complex, and increasing Fe(II)/Fe(III) mineral content with higher saturation frequency. Increasing Fe crystallinity with redox fluctuations was also identified by Thompson et al. (2006b, 2011) with laboratory wet-dry cycles and across a saturation gradient in basaltic soils. Here, the link between detectable changes in reduced Fe content and higher saturation frequency provides support for redox-driven changes to organo-mineral associations, including the potential for C mobilization under even short-term and fluctuating reducing conditions, observed in soil types with similarly high abundance of semi-crystalline Fe phases (e.g., Andisols) (Buettner et al., 2014).

Preferential interaction of carboxylic and/or aromatic acid functional groups with reactive Fe and Al phases has been demonstrated across a wide range of soil types, including semi-crystalline mineral-dominated soils (e.g., Andisols) (Kramer et al., 2012), forest soils of varied soil orders (Zhao et al., 2016), and specifically for Northeast spodic horizons (Ussiri and Johnson, 2004). The generally high carboxylic C content and shift in bulk C composition towards higher carboxylic/aromatic ratio with higher saturation frequency shown with C K-edge XANES points towards the ubiquitous role of carboxylic C and aromatic acids in Fe interactions irrespective of saturation frequency.

While the NMR study did not probe Al interactions with SOC directly, similar complexation and surface adsorption reactions with carboxylic and aromatic acids are expected for Fe and Al oxides (e.g., inner-sphere substitution reactions) (Kramer et al., 2012). With higher Al-dominated organo-mineral interactions at higher saturation frequency shown in this study, the high carboxylic C content observed at high saturation frequency suggests Al-carboxylic acid interactions drive overall Al-C interactions. The composition of DOM derived from Oa horizons at the site was shown to be similar (Chapter 1, this dissertation), and the difference in carboxylic/aromatic C ratio between soils with or without removal of POM was small irrespective of saturation frequency. Therefore, the enrichment of oxidized C at high saturation frequency is likely associated with overall carboxylic C accumulation due to Al-facilitated stabilizing interactions. Due to the potential role of heavier, smaller POM (i.e., POM not removed in this study), further isolation of the Al-associated C

phases and bulk soil analysis analogous to NMR VCT experiments is needed to directly probe changes in Al-C interactions as a function of saturation frequency.

4.3 Implications for SOC Mineralizability

The detected shifts in Fe, Al, and C composition suggest that C stabilization is occurring via different mechanisms that may respond differently to fluctuating saturation and resulting redox status. In contrast to previous studies that found no increased CO₂ mineralization after repeated wet-dry cycling (Degans and Sparling, 1995), we identified an increase of total SOC mineralizability (ANOVA $p=0.09$) in soils with a legacy of high saturation frequency. With Fe and Al shown to be important drivers of SOC accumulation via mechanisms described above, the detected increase in SOC mineralizability may be associated with the shift from Fe(III)-complexes to Al-dominated organo-mineral interactions. The nature and stability of SOC-metal interactions are not expected to be categorically different between Al and Fe, as such, due to the potential for stabilizing interactions with both elements via complex formation and co-precipitation (Basile-Doelsch et al., 2007; Kalbitz and Kaiser, 2008). However, potential for SOC-Al interactions resulting in decreased SOC mineralizability may be higher with soluble Al phases compared to crystalline Al (Kalbitz and Kaiser, 2008). Here, the proportion of soluble, non-crystalline Al of total Al is much less than that for Fe at all sites, and especially at high saturation frequency, which may impose a greater limitation on SOC stabilization potential due to the generally lower reactive surface area of primary and non-SRO aluminosilicate Al. Therefore, while the reactive Al present may account for a large proportion of organo-

mineral associations and confer SOC stabilization, SOC may be in excess of stabilization potential at high saturation frequency.

In addition to initial differences in SOC mineralizability, the significant increase in DOC mineralizability (ANOVA $p < 0.05$) observed for higher compared to lower saturation frequency indicated that reduced O_2 concentration remains an influence on SOC cycling under high saturation frequency despite the observed shift towards Al-dominated interactions. With anaerobic incubation, the overall increase in both soluble total Fe and Fe^{2+} demonstrated the induction of reducing conditions. At high saturation frequency, the increase in Fe^{2+} with anaerobic conditions was higher (5-fold) than that at low saturation frequency (1-fold), suggesting that despite an overall shift towards Al-dominated organo-mineral interactions and already increased Fe(II) as a proportion of total Fe, Fe redox dynamics remain relevant and a potential influence on DOC availability. However, we did not detect an increase in DOC at any saturation frequency associated with increased Fe solubility, possibly due to rapid DOC assimilation by anaerobic microorganisms, precipitation with soluble Fe^{2+} , or rapid adsorption to remaining solid Fe and Al phases.

While increased DOC under wet-dry cycling or flooding has been identified in both organic and mineral soils (Lundquist et al., 1999; Chow et al., 2006), the increase in DOC was not necessarily linked with increased microbial respiration and microbial biomass (Lundquist et al., 1999), highlighting the distinction between increased DOC amount and DOC mineralizability. DOC mineralizability may be influenced by the factors such as composition of original SOC and availability of other limiting nutrients (Kalbitz et al., 2003; Wieder et al., 2008; Petrone et al., 2009). In this study, the

observation of lower DOC with higher mineralizability provides an incentive for further studies focused on composition and fate of DOC released from mineral associations, particularly with respect to stabilizing element (Fe vs. Al) and interaction mechanism.

5. Conclusions

The extent of saturation frequency and hydrology-driven pedogenic processes in this system resulted in notable shifts in Fe redox state and in the composition of Fe phases, underscoring the influence of redox fluctuations even in short-duration, flashy saturation events. The observed transition from Fe(III)-organic complex-dominated organo-mineral interactions at lower saturation frequency towards Al-dominated interactions at higher saturation frequency as a result of saturation frequency legacy indicates relevant changes in SOC stabilization mechanisms between nearby locations. This will likely also apply to different locations within the same soil profile, such as between depths or between pores and interiors of aggregates. The higher DOC mineralizability in response to short-term changes in saturation over several days suggests that this shift is relevant for C accumulation and stabilization processes. This should be accounted for in modeling SOC stabilization potential in systems with frequent redox fluctuations. Future research should extend investigations to fine-scale spatial analyses that may capture elemental associations that vary on the fine scale (e.g., Mn-organic associations) and to in-field observations of real-time fluctuations of DOC mobilization, composition, and metal solubility at high temporal resolution.

6. Acknowledgements

Funding for this study was provided by the NSF IGERT in Cross-Scale Biogeochemistry and Climate at Cornell University (NSF Award #1069193) and the Institute for Advanced Study (IAS) from the Technical University of Munich (TUM) through the Hans-Fisher Senior Fellowship. Additional research funds were provided by the Andrew W. Mellon Foundation and the Cornell College of Agriculture and Life Sciences Alumni Foundation. Hubbard Brook Experimental Forest is operated and maintained by the US Forest Service, Northern Research Station, Newtown Square, PA. This work uses research conducted at the Cornell High Energy Synchrotron Source (CHESS) which is supported by the National Science Foundation under award DMR-1332208. Research was performed at the Canadian Light Source (CLS), which is supported by the Canada Foundation for Innovation, Natural Sciences and Engineering Research Council of Canada, the University of Saskatchewan, the Government of Saskatchewan, Western Economic Diversification Canada, the National Research Council Canada, and the Canadian Institutes of Health Research. The authors thank Rong Huang of CHESS; Kelly Hanley and Akio Enders of Cornell University for technical assistance; Dr. Carmen Höschen, Johann Lugmeier and Dr. Carsten Mueller of the Technical University of Munich for their support with the NanoSIMS measurements; and Dr. Linda Pardo, Stephanie Duston, Brittany LeBeau, and Johali Sotelo for soil sample collection and field characterization.

REFERENCES

- Bailey, S.W., Brousseau, P.A., McGuire, K.J., Ross, D.S., 2014. Influence of landscape position and transient water table on soil development and carbon distribution in a steep, headwater catchment. *Geoderma* 226-227, 279-289.
- Basile-Doelsch, I., Amundson, R., Stone, W.E.E., Borschneck, D., Bottero, J.Y., Moustier, S., Masin, F., Colin, F., 2007. Mineral control of carbon pools in a volcanic soil horizon. *Geoderma* 137(3-4), 477-489.
- Berry, A.J., O'Neill, H.St.C., Jayasuriya, K.D., Campbell, S.J., Foran, G.J., 2003. XANES calibrations for the oxidation state of iron in silicate glass. *Am. Mineral.* 88(7), 967-977.
- Bhattacharyya, A., Schmidt, M.P., Stavitski, E. Martínez, C.E., 2018. Iron speciation in peats: Chemical and spectroscopic evidence for the co-occurrence of ferric and ferrous iron in organic complexes and mineral precipitates. *Org. Geochem.* 115, 124-137.
- Black, C, Evals, D, White, J, Ensminger, L, Clark, F., 1965. *Methods of Soil Analysis Part 1: Physical and Mineralogical Properties, Including Statistics of Measurement and Sampling.* American Society of Agronomy, Madison, WI.
- Bourgault, R.R., Ross, D.S., Bailey, S.W., 2015. Chemical and morphological distinctions between vertical and lateral podzolization at Hubbard Brook. *Soil Sci. Soc. Am. J.* 79(2), 428-439.
- Bourgault, R.R., Ross, D.S., Bailey, S.W., Bullen, T.D., McGuire, K.J., Gannon, J.P., 2017. Redistribution of soil metals and organic carbon via lateral flowpaths at the catchment scale in a glaciated upland setting. *Geoderma* 307, 238-252.
- Breiman, L., 2001. Random forests. *Mach. Learn.* 45(1), 5-32.
- Buettner, S.W., Kramer, M.G., Chadwick, O.A., Thompson, A., 2014. Mobilization of colloidal carbon during iron reduction in basaltic soils. *Geoderma* 221-222, 139-145.
- Chen, C., Dynes, J.J., Wang, J., Sparks, D.L., 2014. Properties of Fe-organic matter associations via coprecipitation versus adsorption. *Environ. Sci. Technol.* 48, 13751-13759.
- Chen, K., Chen, T., Chan, Y., Cheng, C., Tzou, Y., Liu, Y., Teah, H., 2016. Stabilization of natural organic matter by short-range-order iron hydroxides. *Environ. Sci. Technol.* 50, 12612-12620.

- Chow, A.T., Tanji, K.K., Gao, S., Dahlgren, R.A., 2006. Temperature, water content, and wet-dry cycle effects on DOC production and carbon mineralization in agricultural peat soils. *Soil Biol. Biochem.* 38, 477-488.
- Christensen, J.H., Krishna Kumar, K., Aldrian, E., An, S.-I., Cavalcanti, I.F.A., de Castro, M., Dong, W., Goswami, P., Hall, A., Kanyanga, J.K., Kitoh, A., Kossin, J., Lau, N.-C., Renwick, J., Stephenson, D.B., Xie, S.-P., Zhou, T., 2013. Climate phenomena and their relevance for future regional climate change, in: Stocker, T.F., Qin, D., Plattner, G.-K., Tignor, M., Allen, S.K., Boschung, J., Nauels, A., Xia, Y., Bex, V., Midgley, P.M. (Eds.), *Climate Change 2013: The Physical Science Basis. Contribution of Working Group I to the Fifth Assessment Report of the Intergovernmental Panel on Climate Change*, Cambridge University Press, Cambridge, United Kingdom and New York, NY, pp. 1217-1308.
- Coward, E.K., Thompson, A., Plante, A.F., 2018. Contrasting Fe speciation in two humid forest soils: Insight into organomineral associates in redox-active environments. *Geochim. Cosmochim. Acta* 238, 68-84.
- Das, S., Richards, B.K., Hanley, K.L., Krounbi, L., Walter, M.F., Walter, M.T., Steenhuis, T.S., Lehmann, J., 2019. Lower mineralizability of soil carbon with higher legacy soil moisture. *Soil Biol. Biochem.* 130, 94-104.
- DeCiucies, S., 2018. When less is more: priming of soil organic matter by pyrogenic carbon (M.S. thesis). Cornell University, Ithaca, NY.
- Gannon, J., McGuire, K., Bailey, S., 2017. Lateral water flux in the unsaturated zone: A mechanism for the formation of spatial soil heterogeneity in a headwater catchment. *Hydrol. Process.* 31(20), 3568-3579.
- Gormanns, P., Reckow, S., Poczatek, C.J., Turck, C.W., Lechene, C., 2012. Segmentation of multi-isotope mass spectrometry data for semi-automatic detection of regions of interest. *PLoS One* 7(2), e30576.
- Degens, B.P., Sparling, G.P., 1995. Repeated wet-dry cycles do not accelerate the mineralization of organic C involved in the macro-aggregation of a sandy loam soil. *Plant Soil* 175(2), 197-203.
- Hall, S.J., Liptzin, D., Buss, H.L., DeAngelis, K., Silver, W.L., 2016. Drivers and patterns of iron redox cycling from surface to bedrock in a deep tropical forest soil: a new conceptual model. *Biogeochem.* 130(1-2), 177-190.
- Hendershot, W.H., Lalonde, H., Duquette, M., 1993. Soil reaction and exchangeable acidity, in: Carter, M.R. (Ed.), *Soil Sampling and Methods of Analysis*. Canadian Society of Soil Science, Lewis Publishers, Boca Raton, pp. 141-145.

- Herndon, E., AlBashaireh, A., Singer, D., Chowdhury, T.R., Gu, B., Graham, D., 2017. Influence of iron redox cycling on organo-mineral associations in Arctic tundra soil. *Geochim. Cosmochim. Acta* 207, 210-231.
- Heymann, K., Lehmann, J., Solomon, D., Schmidt, M.W.I., Regier, T., 2011. C 1s K-edge near edge X-ray absorption fine structure (NEXAFS) spectroscopy for characterizing functional group chemistry of black carbon. *Org. Geochem.* 42(9), 1055-1064.
- Huang, W., Hall, S.J., 2017. Optimized high-throughput methods for quantifying iron biogeochemical dynamics in soil. *Geoderma* 306, 67-72.
- Inagaki, T.M, Possinger, A.R., Grant, K.E., Schweizer, S.A., Mueller, C.W., Derry, L.A., Lehmann, J., Kögel-Knabner, I. Subsoil organo-mineral associations under contrasting climate conditions. In revision, *Geochim. Cosmochim. Acta*.
- Jankowski, M., 2014. The evidence of lateral podzolization in sandy soils of Northern Poland. *Catena* 112, 139-147.
- Jones, M.E., Nico, P.S., Ying, S., Regier, T., Thieme, J., Keiluweit, M., 2018. Manganese-driven carbon oxidation at oxic-anoxic interfaces. *Environ. Sci. Technol.* 52, 12349-12367.
- Kalbitz, K., Kaiser, K., 2008. Contribution of dissolved organic matter to carbon storage in forest mineral soils. *J. Plant. Nutr. Soil Sci.* 171, 52-60.
- Kalbitz, K., Schmerwitz, J., Schwesig, D., Matzner, E., 2003. Biodegradation of soil-derived dissolved organic matter as related to its properties. *Geoderma* 133, 273-292.
- Kayranli, B., Scholz, M., Mustafa, A., Hedmark, A., 2010. Carbon storage and fluxes within freshwater wetlands: a critical review. *Wetlands* 30(1), 111-124.
- Keiluweit, M., Wanzek, T., Kleber, M., Nico, P., Fendorf, S., 2017. Anaerobic microsites have an unaccounted role in soil carbon stabilization. *Nature Commun.* 8(1771).
- Knicker, H., Lüdemann H.D., 1995. N-15 and C-13 CPMAS and solution NMR studies of N-15 enriched plant material during 600 days of microbial degradation. *Org. Geochem.* 23, 329-341.
- Kleber, M., Eusterhues, K., Keiluweit, M., Mikutta, C., Mikutta, R., Nico, P.S., 2015. Mineral-organic associations: formation, properties, and relevance in soil environments. *Adv. Agron.* 130, 1-140.

- Kramer, M.G., Sanderman, J., Chadwick, O.A., Chorover, J., Vitousek, P.M., 2012. Long-term carbon storage through retention of dissolved aromatic acids by reactive particles in soil. *Global Change Biol.* 18(8), 2594-2605.
- Krounbi, L., van Es, H., Karanja, N., Lehmann, J., 2018. Nitrogen and phosphorus availability of biologically and thermochemically decomposed human wastes and urine in soils with different texture and pH. *Soil Sci.* 183(2), 51-65.
- Kuhn, M., 2008. Building predictive models in R using the “caret” package. *J. Stat. Soft.* 28(5), 1-26.
- Kurtz, A.C., Derry, L.A., Chadwick, O.A., Alfano, M.J., 2000. Refractory element mobility in volcanic soils. *Geology* 28(8), 683-686.
- Lehmann, J., Kleber, M., 2015. The contentious nature of soil organic matter. *Nature* 528, 60-68.
- Lundquist, E.J., Jackson, L.E., Scow, K.M., 1999. Wet-dry cycles affect dissolved organic carbon in two California agricultural soils. *Soil Biol. Biochem.* 31, 1031-1038.
- Lengke, M.F., Ravel, B., Fleet, M.E., Wanger, G., Gordon, R.A., Southam, G., 2006. Mechanisms of gold bioaccumulation by filamentous cyanobacteria from gold(III)-chloride complex. *Environ. Sci. Technol.* 40(20), 6304-6309.
- Mayer, S., Schwindt, D., Steffens, M., Völkel, J., Kögel-Knabner, I., 2018. Drivers of organic carbon allocation in a temperate slope-floodplain catena under agricultural use. *Geoderma* 327, 63-72.
- Petrone, K.C., Richards, J.S, Grierson, P.R., 2009. Bioavailability and composition of dissolved organic carbon and nitrogen in a near coastal catchment of south-western Australia. *Biogeochem.* 92(1-2), 27-40.
- Ravel, B, Newville, M., 2005. Athena, Artemis, Hephaestus: data analysis for X-ray absorption spectroscopy using IFEFFIT. *J. Synchrotron Rad.* 12, 537-541.
- R Core Team, 2017. R: A language and environment for statistical computing. R Foundation for Statistical Computing, Vienna, Austria. URL <https://www.R-project.org/>.
- Ross, G.J., Wang, C., 1993. Extractable Al, Fe, Mn, and Si, in: Carter, M.R (Ed.), *Soil Sampling and Methods of Analysis*. Canadian Society of Soil Science, Lewis Publishers, Boca Raton, pp. 239-246.
- Scheel, T., Dörfler, C., Kalbitz, K., 2007. Precipitation of dissolved organic matter

- stabilizes carbon in acidic forest soils. *Soil Sci. Soc. Am. J.*, 71, 64-74.
- Schneider, C.A., Rasband, W.S., Eliceiri, K.W., 2012. NIH Image to ImageJ: 25 years of image analysis. *Nature Methods* 9(7), 671-675.
- Schmidt, M.W., Torn, M.S., Abiven, S., Dittmar, T., Guggenberger, G., Janssens, I.A., Kleber, M., Kögel-Knabner, I., Lehmann, J., Manning, D.A.C., Nannipieri, P., Rasse, D.P., Weiner, S., Trumbore, S.E., 2011. Persistence of soil organic matter as an ecosystem property. *Nature* 478(7367), 49-56.
- Shöning, I., Knicker, H., Kögel-Knabner, I., 2005. Intimate association between O/N-alkyl carbon and iron oxides in clay fractions of forest soils. *Org. Geochem.* 36, 1378-1390.
- Silver, W.L., Lugo, A.E., Keller, M., 1999. Soil oxygen availability and biogeochemistry along rainfall and topographic gradients in upland wet tropical forest soils. *Biogeochem.* 44(3), 301-328.
- Solomon, D., Lehmann, J., Kinyangi, J., Liang, B., Heymann, K., Dathe, L., Hanley, K., Wirick, S., Jacobsen, C., 2009. Carbon (1s) NEXAFS spectroscopy of biogeochemically relevant reference organic compounds. *Soil Sci. Soc. Am. J.* 73, 1817-1830.
- Sommer, M., Halm, D., Weller, U., Zarei, M., Stahr, K., 2000. Lateral podzolization in a granite landscape. *Soil Sci. Soc. Am. J.* 64(4), 1434-1442.
- Sutfin, N.A., Wohl, E.E., Dwire, K.A., 2016. Banking carbon: a review of organic carbon storage and physical factors influencing retention in floodplains and riparian ecosystems. *Earth Surf. Process. Landf.* 41(1), 38-60.
- Thompson, A., Chadwick, O.A., Boman, S., Chorovor, J., 2006a. Colloid mobilization during soil iron redox oscillations. *Environ. Sci. Technol.* 40(18), 5743-5749.
- Thompson, A., Chadwick, O.A., Rancourt, D.G., Chorovor, J., 2006b. Iron-oxide crystallinity increases during soil redox oscillations. *Geochim. Cosmochim. Acta* 70(7), 1710-1727.
- Thompson, A., Rancourt, D.G., Chadwick, O.A., Chorovor, J., 2011. Iron solid-phase differentiation along a redox gradient in basaltic soils. *Geochim. Cosmochim. Acta* 75(1), 119-133.
- Ussiri, D.A.N., Johnson, C.E., 2004. Sorption of organic carbon fractions by Spodosol mineral horizons. *Soil Sci. Soc. Am. J.* 68, 253-262.

- Viollier, E., Inglett, P.W., Hunter, K., Roychoudhury, A.N., Van Cappellen, P., 2000. The ferrozine method revisited: Fe(II)/Fe(III) determination in natural waters. *Appl. Geochem.* 15, 785-790.
- Wieder, W.R., Cleveland, C.C., Townsend, A.R., 2008. Tropical tree species composition affects the oxidation of dissolved organic matter from litter. *Biogeochem.* 88(2), 127-138.
- Whitman, T., Zhu, Z., Lehmann, J., 2014. Carbon mineralizability determines interactive effects on mineralization of pyrogenic organic matter and soil organic carbon. *Environ. Sci. Technol.* 48 (23), 13727-13734.
- Winkler, P., Kaiser, K., Thompson, A., Kalbitz, K., Fiedler, S., Jahn, R., 2018. Contrasting evolution of iron phase composition in soils exposed to redox fluctuations. *Geochim. Cosmochim. Acta* 235, 89-102.
- Wojdyr, M., 2010. Fityk: a general-purpose peak fitting program. *J. Appl. Cryst.* 43(5-1), 1126-1128.
- Yang, W.H., Liptzin, D., 2015. High potential for iron reduction in upland soils. *Ecology* 96(7), 2015-2020.
- Zhao, Q., Poulson, S.R., Obrist, D., Sumaila, S., Dynes, J.J., McBeth, J.M., Yang, Y., 2016. Iron-bound organic carbon in forest soils: quantification and characterization. *Biogeosciences* 13, 4777.

CHAPTER 3

ORGANO-ORGANIC AND ORGANO-MINERAL INTERFACES IN SOIL AT THE NANOMETER SCALE

1. Introduction

Soil organic carbon (SOC) constitutes a critical reservoir in the global C cycle, which highlights the importance of understanding the processes that drive soil organic matter (SOM) persistence, ranging from global (e.g., climate) to very fine scales (e.g., organo-mineral surface interactions) (Lal, 2004; Schmidt et al., 2011; Ciais et al., 2013; Lehmann and Kleber, 2014). Improving the ability to describe drivers of SOM persistence, including mechanisms of biophysicochemical SOM protection, enables better prediction of changes in the soil C reservoir in light of global environmental change (Weider et al., 2014).

Soil OM is a mixture of organic compounds subject to organo-mineral interactions (Solomon et al., 2005; Kelleher and Simpson, 2006; Lehmann et al., 2008; Vogel et al., 2014). Such interactions between SOM and mineral phases result in lower microbial accessibility and availability for decomposition, which is seen as a dominant process for SOM stabilization (Torn et al., 1997; Deng and Dixon, 2002; Kleber et al., 2015; Lehmann and Kleber, 2015). Organo-mineral interactions are thought to lead to ordered gradients of organic substances as a function of distance to mineral surfaces (Kleber et al., 2007; Lehmann et al., 2007). However, with the emerging view that microbially-derived residues are the primary contributors to

mineral-stabilized OM (Cotrufo et al. 2013, Kallenbach et al., 2016), the suite of potential supramolecular interactions among individual biomolecules, microbial cell membranes, and extracellular products challenges previous understanding of single-molecule adsorption mechanisms and processes. While mono-layer SOM mineral surface adsorption and maximum OM accumulation potential (i.e., saturation) could be limited by mineral surface area and chemistry, adsorption of OM supramolecular associations and additive accumulation of OM may circumvent these limitations and is therefore critical for maximizing soil organic C sequestration (Mayer and Xing, 2001; Vogel et al. 2014; Schmidt and Martinez, 2018). Despite this critical role of organo-organic interactions in shifting the current view of SOM accumulation potential, these interactions have not been directly identified or described in natural soil samples. Further, the spatial arrangement of SOM at mineral surfaces – hypothesized to occur in ordered gradients at the micrometer scale (Kleber et al., 2007; Lehmann et al., 2007) – lacks direct visual evidence at the necessary scale to account for the potential confounding influence of organo-organic interactions.

The reason for this lack of recognition is that direct visualization and characterization of interfaces between different organic phases in soil is limited by the nanometer scale on which they occur. To ascertain the presence of organo-organic interactions and gain further insight into the properties of organo-organic and organo-mineral interactions in natural soil samples, we developed a novel approach for cryogenic sample preparation in conjunction with analytical cryogenic scanning transmission electron microscopy and electron energy loss spectroscopy (cryo-STEM-EELS), achieving single-digit nanometer spatial resolution paired with the ability to

resolve C fine structure across organo-mineral and organo-organic interfaces. This approach avoids the use of C-based stabilizing resins that typically make interpretation of C spectroscopy difficult and maintains soil spatial characteristics, which enables direct visualization and analysis of the interfaces between organic and mineral phases in soil. We applied cryo-STEM-EELS to identify and probe the nature of organo-organic and organo-mineral interactions in volcanic soils with high capacity for C accumulation.

2. Materials and Methods

2.1 Study Site and Sample Collection

Cryo-STEM procedures to reveal hypothesized organo-organic and organo-mineral interactions were applied to sub-soils with high C and high Fe content derived from volcanic parent materials (Andisols) with well-established relationships between mineralogy and OM stabilization as a model system (Torn et al., 1997). The soil samples were collected by horizon quantitatively from sub-soils from the Pololu Flow on Kohala, HI with approximately 350,000 years of soil development from tholeiitic lavas and contain high C, Fe, and Al (Appendix Table A4.3.1, Appendix Figures A3.3.1-A3.3.3) (Chadwick et al., 2003; Grant, 2019). Bulk ^{14}C measurements indicate an average of $\sim 10,000$ radiocarbon years with a dominant mineralogy of semi-crystalline Fe and Al oxides, including allophane, imogolite, and ferrihydrite (Grant, 2019). Soils were stored at field moisture conditions at 9°C prior to cryo-STEM sample preparation and imaging.

2.2 Cryogenic Thin-Section Preparation

2.2.1 Background

The heterogeneity of soil provides a methodological challenge for preparing soil samples for high-resolution transmission microscopy, particularly for C, N, and other light elements easily damaged by high-energy analysis techniques. Specifically, sample preparation approaches are needed that: (1) maintain mineral-organic, organic-organic, and pore space spatial distribution, (2) eliminate the use of C-based resins that preclude interpretation of C spectroscopic data, (3) reduce the risk of beam damage, (4) result in appropriate sample thicknesses (<100-200 nm) for electron transparency, and (5) avoid freeze-thaw and wet-dry fluctuations that alter mineral-OM interactions (Kaiser et al., 2015; Kim and Choi, 2018).

Embedding soil thin-sections while still allowing for discernment of soil OM forms provides a technical challenge. For nanoscale secondary ion mass spectrometry (NanoSIMS), this has been addressed by using C-based resins with distinctive isotope signatures or chemical markers (Höschen et al., 2015). However, EELS is not generally sensitive to isotope signatures. Elemental sulfur (S) has also been employed as a stabilizing material (Lehmann et al., 2005) but is sensitive to changes in temperature, and often does not fully permeate the aggregate microstructure (Höschen et al., 2015).

Performing sample thin-sectioning under cryogenic conditions – a common way to reduce sample damage in microscopy and spectroscopy of biological materials (van Heel et al., 2000) – is one approach that allows samples to stay hydrated by rapid freezing, which stabilizes the heterogeneous soil samples and precludes the need for

either C-based resins or elemental S (Kinyangi et al., 2006). Cryo-thin sectioning followed by room-temperature imaging and spectroscopy is a common approach, though sample thawing and drying is often required (Kinyangi et al., 2006).

Additionally, imaging and spectroscopy with cryo-thin sectioning and cryo-TEM imaging techniques has been applied for imaging of mineral-microbe associations in geobiological samples (Miot et al., 2014). To address the method challenges described above, we developed an integrated sample preparation procedure that maintained the soil aggregate in cryogenic conditions for initial sectioning, thinning to electron transparency, and STEM-EELS mapping (Appendix Figures A3.3.4-A3.3.5).

2.2.2 Aggregate Cryo-Ultramicrotome Pre-Thinning

Intact soil aggregates were stabilized with rapidly-frozen water and maintained under cryogenic conditions throughout the sectioning, focused ion beam (FIB) milling, and imaging processes. Aggregates in the 53-150 μm -diameter fraction were gradually saturated with deionized (DI) water using an ultrasonic humidifier at the lowest setting (SPT Ultrasonic Humidifier, Sunpentown, Inc., City of Industry, CA) (Kinyangi et al., 2006). After humidification, individual intact aggregates were selected under a dissecting microscope, and transferred to a deionized (DI) water droplet on an aluminum cryo-ultramicrotome pedestal. The droplet was then rapidly frozen by immersion in slush nitrogen (N_2) with average temperature of -207°C (Sansinena et al., 2012). To improve effectiveness and time efficiency of FIB milling, aggregates were pre-sectioned into 1-5 μm -thick cross-sections using a cryo-ultramicrotome equipped with a diamond blade (Leica EM UC7/FC7, Leica Microsystems, Inc., Buffalo Grove, IL). Cryo-ultramicrotome thinning was performed at -60°C using a

step size of 1000 nm, and thin sections were transferred to an adhesive-coated copper (Cu) TEM grid (300 or 400-mesh) and stored in cryo-TEM grid boxes under liquid N₂.

2.2.3 Cryo-FIB Transfer

Preparation of thin sections for STEM-EELS with a thickness <100-200 nm was completed using an FEI Strata 400 STEM DualBeam FIB (FEI Company, Hillsboro, OR) equipped with a Quorum PP3010T Cryo-FIB/SEM Preparation System (Laughton, East Sussex, UK). Samples prepared by cryogenic ultramicrotome pre-thinning were transferred from liquid N₂ storage to the cryo-FIB stage at temperatures near that of liquid N₂ and maintained in the cryo-FIB at -165°C. Further details describing the cryo-transfer system are published in Zachman et al. (2016).

2.2.4 Cryogenic FIB Milling

To maintain spatial characteristics and prevent sample loss or damage for relatively brittle and heterogeneous soil thin sections, two thinning approaches were adopted: (1) thinning with the Ga⁺ ion beam at a shallow angle to the surface of the soil section, creating a “wedge” with a tapered thickness and an edge approaching zero thickness; and (2) milling both above and below the region of interest in the soil section at a shallow angle to generate a “lamella” of nearly uniform thickness (<200 nm) in the material (Appendix Figures A3.3.4-A3.3.5). Scanning EM images to monitor the milling process were collected at 5 kV. Milling was completed at an ion beam voltage of 30 kV with varying current (between approximately 5 pA and 500 pA).

2.3 Cryogenic EDX Elemental Analysis

The elemental composition of the soil thin sections was assessed using electron dispersive X-ray (EDX) spectroscopy. For the organo-mineral interface soil sample

(“wedge” thin section), elemental maps were collected for regions located near the primary EELS analysis region during cryo-STEM-EELS analysis with an FEI F20 TEM-STEM instrument (FEI Company, Hillsboro, OR) equipped with an Oxford Instruments X-Max 80mm² EDX detector (Oxford Instruments, Abingdon, Oxfordshire, UK) (Appendix Figure A3.3.1). For the organo-organic interface soil sample (“lamella” thin section), an EDX point scan was collected (5 kV voltage) during cryo-FIB preparation with an Oxford Instruments X-Max 80mm² EDX detector installed on the FEI Strata FIB/SEM instrument described above (Appendix Figure A3.3.3).

2.4 Cryogenic STEM-EELS

Wedge thin-sections were transferred under liquid N₂ into a standard Gatan cryo-transfer TEM holder, and subsequently into a FEI F20 TEM STEM instrument (FEI Company, Hillsboro, OR) equipped with a Gatan Tridium spectrometer (Gatan Inc., Pleasanton, CA) which was operated at 200 kV for the EELS experiments. Lamella thin-sections were similarly transferred into an aberration-corrected FEI Titan Themis S/TEM instrument (FEI Company, Hillsboro, OR) with a Gatan GIF Quantum 965 spectrometer (Gatan Inc., Pleasanton, CA) operated at 120 kV. During experiments on both instruments, the samples were maintained at approximately -180°C.

Overview high-angle annular dark-field (HAADF) STEM images were obtained prior to collection of EELS point and line spectra (wedge) and 2D maps (lamella). EELS data were collected with parameters to optimize EELS counts with minimal sample damage. Methods and results for assessment of cryo-FIB sample preparation and cryo-STEM-EELS characterization damage are discussed in Appendix

sections A1.3 and A2.3, and image collection parameters are summarized in Appendix Table A4.3.2. For EELS maps collected on the Titan Themis instrument, DualEELS was used to simultaneously collect the low-loss and high-loss regions, and the zero-loss peak position was used to correct for energy shifts in the data due to large fields of view.

2.5 Image and Spectral Analysis

2.5.1 Electron Energy Loss Spectra

EELS data (spectrum images, line scans and point data) were initially processed using the Cornell Spectrum Imager package (Cueva et al., 2012) in ImageJ v. 2.0.0 (Schneider et al., 2012). Background subtraction was performed using a standard linear combination of power laws (LCPL) with the following background subtraction regions: C K-edge (210.0-259.5 eV), N K-edge (369.8-388.8 eV), and O K-edge (488.0-510.0 eV) for organo-organic interface and organo-mineral linescan spectra. For the adjacent OM region to the organo-mineral interface, the energy range of 369.7-380.7 eV was used for N. For the EELS spectrum images and linescans, energy alignment was completed using the peak position of the zero-loss peak in low-loss EELS datasets paired to each measurement by nearby location or simultaneous measurement. For the adjacent OM to the organo-mineral interface, the high magnification precluded use of zero-loss measurements and no energy shift was applied.

To estimate intensity of non-normalized spectra for elemental and fine structural ratios, integrated area was approximated by applying the area under the curve (AUC) function (trapezoidal method) in the “DescTools” package for R

(Signorell et al., 2019). For all spectra, total C and N integration regions were set 280.0-315.0 eV and 395.0-430.0 eV, respectively. For the organo-mineral interface, the higher- and lower-energy regions (regions “b” and “a”) were set to 286.0-289.0 eV and 284.0-286.5 eV, respectively. For the organo-organic interface, O integrated area was determined for 530.0-565.0 eV, and higher-energy (putatively alkyl C) and lower-energy (aromatic C) integrated areas were determined at 286.0-287.5 eV and 284.25-285.75 eV, respectively. The transition in energy intensity was also visualized using arctangent functions with a fixed position (290 eV) and inflection angle but variable height, manually fit to the raw data in Fityk v 1.3.1 (Wojder, 2010). The EELS spectra were not flattened or otherwise adjusted. For calculations of aromatic/alkyl ratios and other fine structure analyses of C, the integrated area was normalized to total C integrated area.

2.5.2 EELS Fine Structure Analysis

Statistical analysis of the EELS fine structure for the organo-organic interface was conducted by multivariate curve resolution (MCR) performed in Matlab v. R2017a. Briefly, MCR is an approach to decompose a spectrum image matrix into substituent components without *a priori* knowledge of chemical composition or use of analytical standards, given a set number of components and an initial selection of putative components. The resulting spectral components are then fit to the original data to produce maps showing component spatial distribution.

3. Results and Discussion

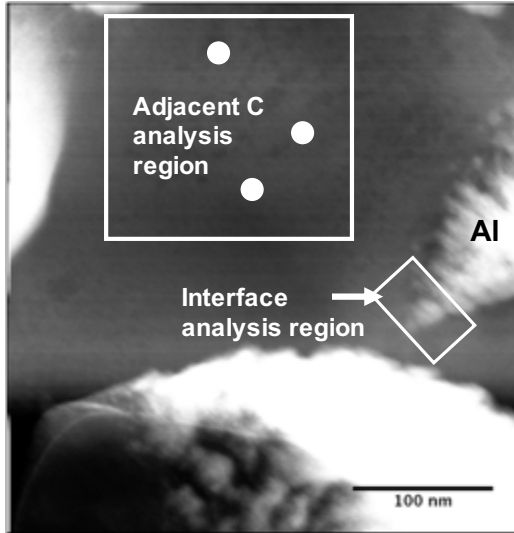
3.1 Organo-Mineral Interface: Enrichment of N and Oxidized C

Our observations of an organo-mineral interface at the nanometer scale point to the role of nitrogen (N)-containing functional groups of polar C compounds in interactions at Al oxide surfaces. Using cryo-STEM-EELS, we show enrichment of higher-energy (~288.1 eV) C K-edge EELS features (31.6%, range 18.2-40.0%) and of total N (91.8%, range 92.0-94.5%) closer to an Al mineral surface compared to an adjacent OM region in a volcanic soil sample (Figure 3.1, Appendix Figures A3.3.1, 2, 6 and 7, Appendix Table A4.3.3). Average intensity of the 286.6-289.0 eV signal relative to the 284.0-286.5 eV signal increased at the organo-mineral interface compared to the adjacent OM, indicating increased proportion of oxidized C (Figure 3.1). The C 1s- $\pi^*_{C=O}$ transition of carboxyl/carbonyl groups is typically assigned the energy of 288.7 eV, but substitution of -OH function groups with -NH₂ can result in a lower-energy shift (Kaznatcheyev et al., 2002; Solomon et al., 2009). The observed enrichment of N-substituted carboxyl/carbonyl C at ~288.1 eV and total N at the mineral interface in contrast to the adjacent C region provides visual and spectroscopic evidence of a mixture of polar functional groups and high-N material involvement in interactions at mineral surfaces (Kleber et al., 2007).

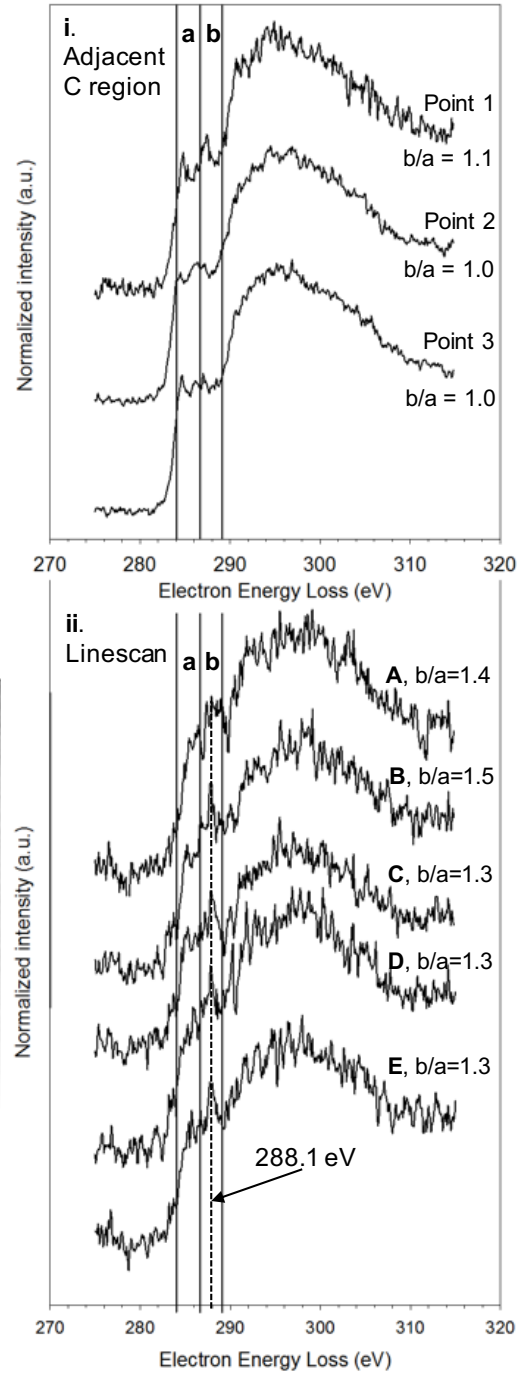
Specific to short-range ordered (SRO) iron (Fe) and Al oxides in volcanic soils such as the studied Andisols, aromatic carboxylic acids have been identified as the key C form in stabilizing interactions (Kramer et al., 2012). The spatially-resolved EELS data shown here point to the additional inclusion of N-substituted aromatic acids and other carboxyl/carbonyl groups to the OM-SRO interaction framework. In subsoils

Figure 3.1. High-resolution cryo-imaging and spectroscopy of organic matter (OM)–mineral interface in a volcanic soil sample. **A.** Overview annular dark field (ADF) image of analysis area, showing layered structure of aluminum (Al) mineral and adjacent OM region. **B.** Electron energy loss (EEL) spectra of organo-mineral interface and adjacent C region. **i.** Point EELS of three replicate points (estimated location shown with white dots) within the adjacent OM region. **ii.** Linescan EELS across organo-mineral interface with spectra A-E the average of two adjacent points on the linescan. Dotted vertical line indicates peak ~ 288.1 eV, putatively identified as N-substituted carboxylic/carbonyl groups (Solomon et al., 2009). For both **i.** and **ii.**, lower (284.0–286.5 eV) and higher (286.6–289.0 eV) energy regions are indicated with boxes a and b. Ratio b/a indicates the ratio of integrated EELS intensity within each region, normalized to total C integration area (280.0–315.0 eV). Additionally, increase in ratio b/a (average 32%) is shown, indicating increase in oxidized C at the organo-mineral interface compared to the adjacent C region. Spectra are shown unsmoothed and normalized to the edge step (edge = 1 a.u). **C.** Detailed ADF image of the organo-mineral interface, showing locations of linescan EELS data collection. Points A-E represent the average of two adjacent points on the linescan.

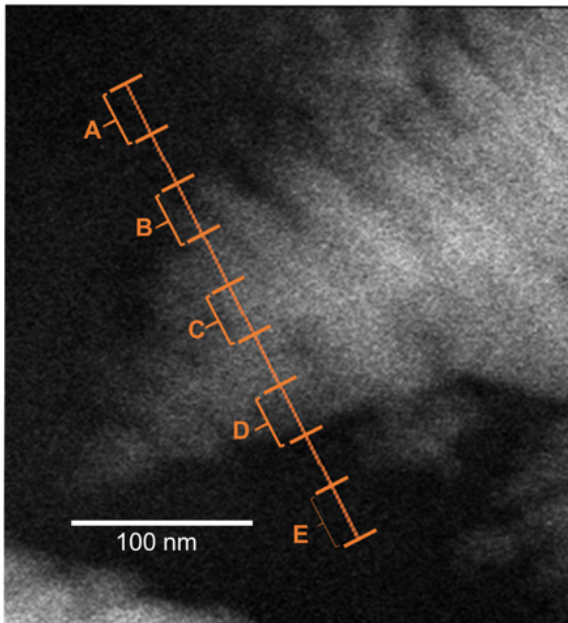
A. Organo-mineral region ADF image



B. Carbon K-edge EELS



C. OM-mineral interface ADF image



collected at the same location, N enrichment in proximity to mineral surfaces has been detected at the micrometer scale using secondary ion imaging (Inagaki et al., in revision). Additionally, the order of magnitude difference in C/N ratio between regions adjacent to and more distant from the mineral surfaces may offer an explanation for increased C/N values with depth at the study site (Grant, 2019). More broadly, decreased C/N is generally observed for the $<2 \mu\text{m}$ clay fraction across soil types relative to un-associated SOM (Parfitt et al., 1997), underscoring the likely role of N-bearing compounds in organo-mineral interactions. With increasing capabilities for dissolved OM and bulk SOM characterization with high-chemical resolution mass spectrometry techniques, the insight described here suggests a continued research focus on the links between N-compound composition and SOM persistence, particularly in SRO-rich soil types.

3.2 Patchiness in OM Composition at the Micrometer Scale

Cryo-STEM-EELS analysis of an OM-rich region in a soil aggregate with high OM content revealed micrometer-scale patchiness of separate OM phases, rather than the expected ordered, micrometer-scale gradients (Figure 3.2, Appendix Figures A3.3.2 and A3.3.8). The presence of aromatic-rich C, lower N, and higher O organic features of distinct C composition embedded in a more alkyl-rich C with higher N and lower O organic matrix (Figures 3.2-3.3, Appendix Figures A3.3.8-A3.3.9) contradicts the understanding that describes gradients of OM composition at the micrometer scale as a function of distance to mineral surfaces, typically supporting multi-layer models of organo-mineral interactions (Lehmann et al., 2007; Kleber et al., 2007, Milne et al., 2011). By observing C/N, C/O, and aromatic/alkyl C ratios across the boundaries of

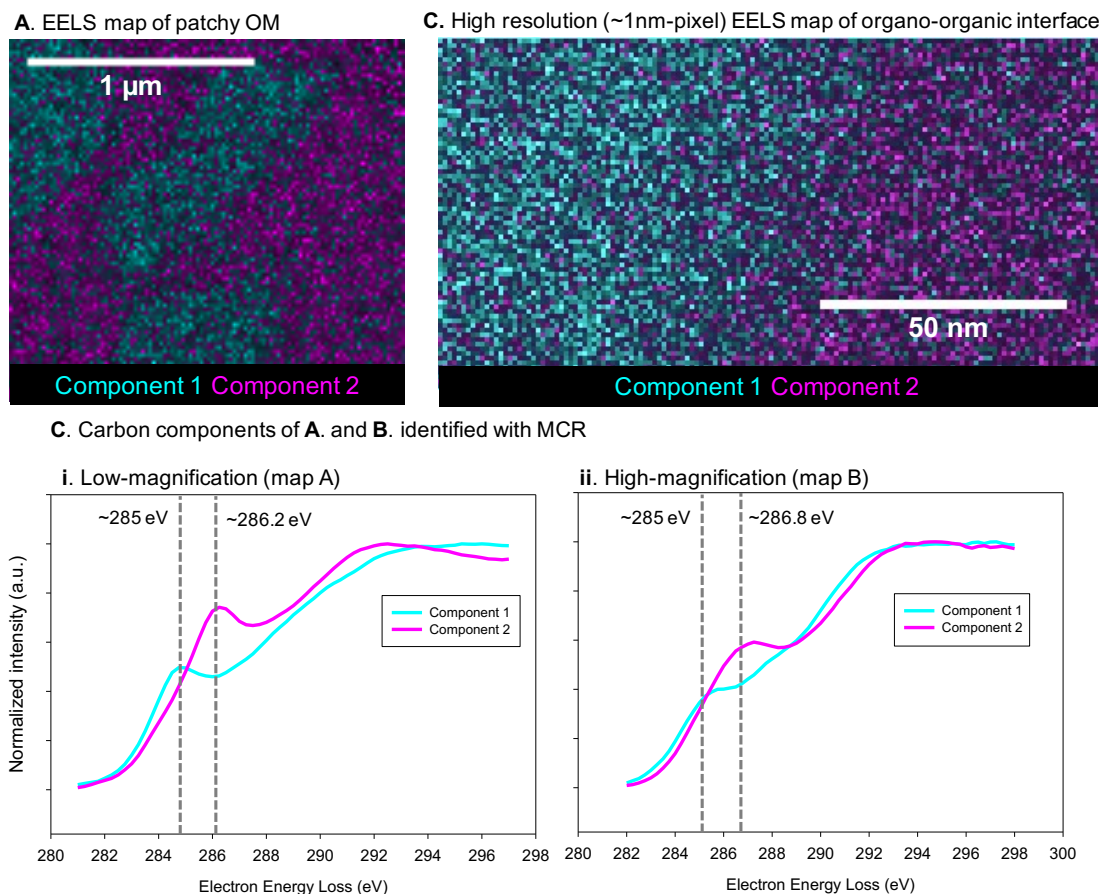
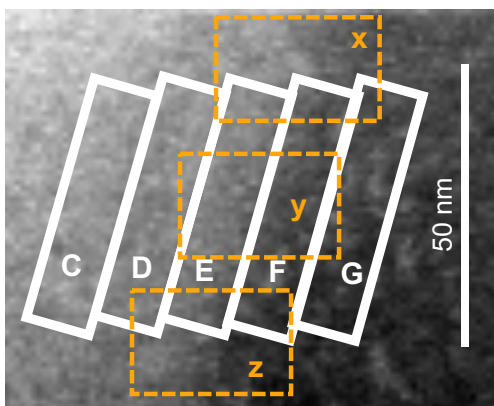


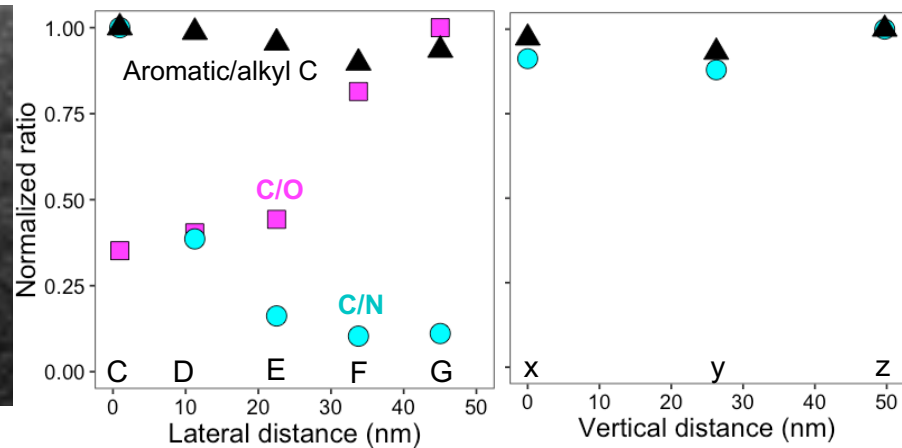
Figure 3.2. High-resolution imaging and spectroscopy of organo-organic interface with cryo-scanning transmission electron microscopy and electron energy loss spectroscopy (cryo-STEM-EELS). **A.** Patchy distribution of organic matter (OM) forms shown with EELS maps of the two distinct carbon (C) K-edge multivariate curve resolution (MCR) component fits (shown in C.i.). **B.** Nanometer scale EELS C K-edge MCR component maps of the interface between two OM patches (shown in C.ii.). **C.** The normalized C K-edge MCR component spectra corresponding to **A** and **B**, with distinctive transition from ~ 285.0 eV in component 1 (assigned to aromatic C=C bonds) to ~ 286.2 - 286.8 eV (assigned to alkyl C-H bonds) in component 2. Features in spectra are shown by dotted vertical lines. Spectra are shown as raw (unsmoothed) MCR fit outputs normalized to maximum output value.

Figure 3.3. Distinct combinations of C/N, C/O, and aromatic/alkyl C ratio across the organo-organic interface shows gradient of organic matter (OM) composition at the ~50 nm scale. **A.** Annular dark field (ADF) detail of the interface between organic phases in a soil thin section (full ADF image shown in Appendix Figure A3.3.9). Boxes C through G indicate regions used to compute average electron energy loss (EEL) spectra across the interface (lateral distance), and boxes x through z indicate regions to assess variability along the interface (vertical distance). **B.** Ratios of normalized (maximum=1) elemental integrated area for C/N, C/O and aromatic/alkyl C across the interface (lateral distance), and C/N and aromatic/alkyl C along the interface (vertical distance). The aromatic/alkyl C ratio is the ratio of integrated intensity in EELS spectral regions (“aromatic” from 284.25-285.75 eV and “alkyl” from 286.0-287.5 eV) normalized to total C integrated area (280.0-315.0 eV). Each location C-E across the interface shows a different combination of C/N, C/O and aromatic/alkyl C. At point F, the enrichment in alkyl C at the interface is apparent, with the trend decoupled from the change in C/N across the interface. **C.** Example average EEL signal intensities from boxes C and F. All spectra are shown in Appendix Figure A3.3.9. **C.i.** Carbon K-edge EELS, with similar intensity but change in fine structure. Vertical lines indicate features at ~285.0 and ~287.0 eV, associated with aromatic and alkyl C, respectively. **C.ii.** Nitrogen K-edge EELS, showing increased signal intensity in box F compared to box C. **C.iii.** Oxygen K-edge EELS, with decreased intensity across the interface.

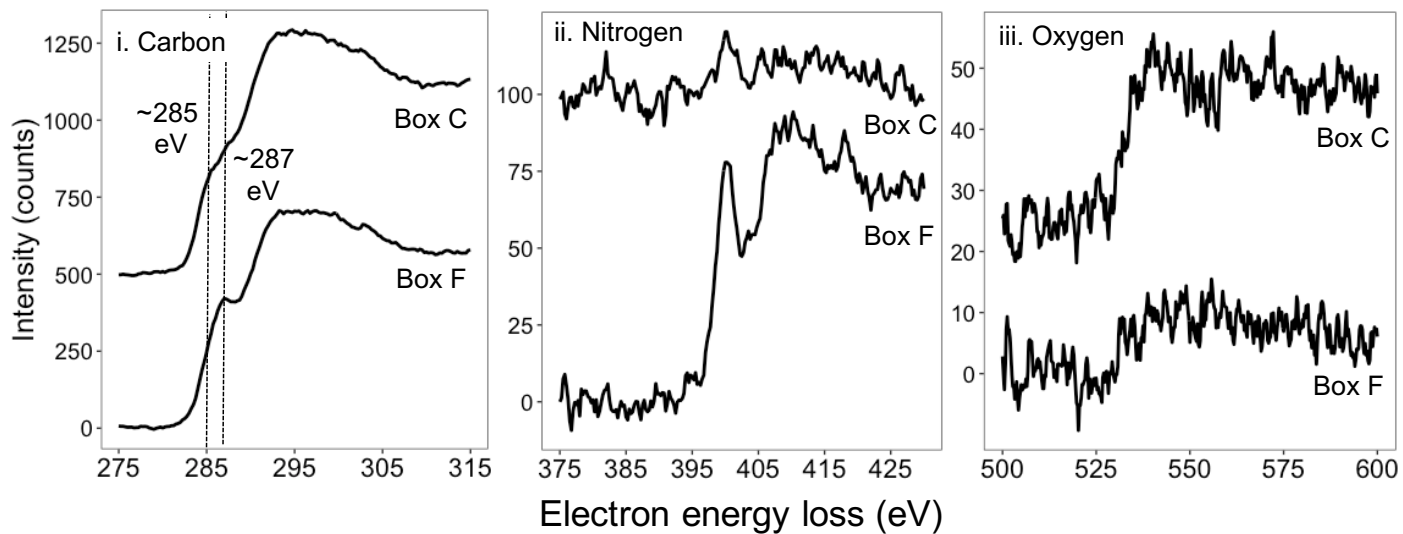
A. Organo-organic interface ADF image



B. EELS elemental and aromatic/alkyl ratios across interface



C. Average EELS spectra for boxes C and F



the OM patches, the improved spatial resolution of cryo-STEM-EELS over previously utilized techniques such as STXM-NEXAFS (Lehmann et al., 2007) enabled discovery of an ordered gradient of OM composition at the <50 nm scale in the present study (Figure 3.3). Gradients of OM composition only at the <50 nm scale highlights the need to consider multidimensionality of organo-mineral interaction models due to patchy, disordered OM accumulation. Along the interface, the change in aromatic/alkyl C ratio between boxes y and z constrains the homogeneity of the interface to ~25 nm in the vertical direction (Figure 3.3).

3.3 Organo-Organic Interface: Enrichment of N and Alkyl C

We identified hitherto undescribed yet abundant organo-organic interfaces as part of OM composition. EELS fine structure varied greatly between the features and the surrounding matrix which were identified as discrete C species using multivariate curve resolution (MCR) (Figure 3.2). Within the observed patchy features, the EELS fine structure is dominated by a low-energy feature at ~285.0 eV, which is assigned to the C 1s- π^* transition of C=C bonds associated with aromatic structures (Solomon et al., 2009). In contrast, the EELS fine structure of the surrounding matrix distinctly shifts from ~285.0 eV to higher energy, ~286.5-287.0 eV. While many overlapping transitions occur in this region, features can be broadly linked to alkyl C-H bonds with a variety of transitions (e.g., C 1s- π^*) (Solomon et al., 2009). The gradual change in N and O signal across the interface shows mixing between OM forms across a ~50-nm boundary (Figure 3.3, Appendix Figure A3.3.9). The change in C EELS fine structure (ROI C to F in Figure 3.3) from more aromatic (~285.0 eV) to alkyl C (~287.0 eV) shows a sharper transition than the gradual change in N and O composition.

Within aromatic-rich patches, the N signal increased approaching the interface with the alkyl phase (Figure 3.3). The shift from low to high N content was spatially separate from the shift from aromatic to alkyl C, with N content beginning to increase further from the interface. Additionally, the C/N ratio was 6.1% lower directly at the interface (box F) compared to the adjacent high-N phase (box G) (Appendix Table A4.3.4). This suggests N-containing components of the aromatic C phase may be preferentially involved in an interaction. Aromatic C=C groups are only thought to be responsible for interactions between organic and mineral phases in specific situations (Kleber et al., 2007). In contrast, N groups are expected to associate readily with other organic constituents via electrostatic interactions or covalent bonds, due to the potential for positive charge and electron-withdrawing character, respectively. In particular, N functional groups in N-rich biomolecules in soil (e.g., N-containing amino acids) are likely to drive interactions between biomolecules in solution and affect surface adsorption to mineral phases (Schmidt and Martinez, 2018). Consequently, an accrual of N-functional groups at the interface is consistent with their importance in driving organo-organic interactions.

The ratio of aromatic C (integrated 284.25-285.75 eV signal) and alkyl C (integrated 286.0-287.5 eV signal) to the total C edge showed an enrichment in alkyl C (by 4.2%) occurring directly at the interface of the organo-organic interface (box F vs. box G in Figure 3.3, Appendix Figure A3.3.9, Appendix Table A4.3.4). No unique third C component at the interface was identified by MCR, indicating a shifting aromatic/alkyl C ratio rather than appearance of a new C feature (Appendix Figure A3.3.10). To further refine the location of the alkyl C enrichment, we examined fine

structure changes with finer resolution (~1 x 44 nm regions) (Appendix Figure A3.3.11). While the transition between aromatic and alkyl C was gradual and overall tracked 11x44 nm resolution EELS data, individual spectra with strong alkyl signal (e.g., spectrum “e” in Appendix Figure A3.3.11) may be indicative of a more specific location for alkyl C enrichment. The presence of fluctuating alkyl signal intensity between adjacent 1x44 nm regions also suggests that ordered gradients of C composition may be occurring even at the <2 nm scale, but increased spectral resolution is needed to definitively identify the points of separation between layers.

The enrichment of N at the mineral interface as well as the organo-organic interface points at the likelihood of some overlapping mechanisms of interaction between phases in soil. However, no enrichment of carboxyl/carbonyl C was detected at the organo-organic boundary. In contrast, alkyl C is enriched, which suggests the need to consider a combination of convergent and unique interaction pathways of organo-organic interactions in addition to the current focus only on the variations among organo-mineral interaction mechanisms.

Taken together, these observations provide evidence for a shifting view (Figure 3.4) of the spatial distribution of OM phases in soil and thereby the mechanism of OM accumulation facilitated by organo-organic interaction. We observe that instead of ordered gradients at the micrometer scale (Lehmann et al., 2007), gradients between OM phases as well as at mineral surfaces occur at a scale of less than 50 nm and possibly less than 2 nm, with irregular patches of distinct OM forms at the single

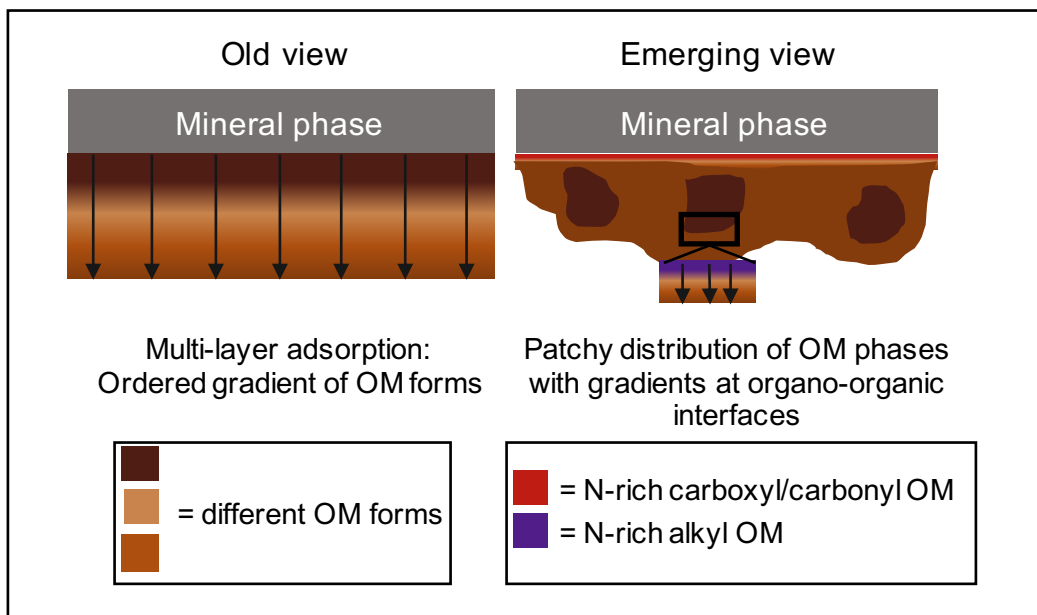


Figure 3.4. Shifting conceptual view from organo-mineral interactions in soil which occur on an ordered gradient to both organo-mineral and organo-organic interfaces occurring on a gradient at the smaller interface (<50 nm) scale but patchy in distribution at the larger (1000 nm) scale. Additionally, we propose different organic compounds may be enriched at the mineral vs. the organo-organic interface, but with similar enrichment of N.

micrometer scale. These observations stand in contrast to previous observations of patchiness at the 100s of micrometers scale and ordering at the single micrometer scale, as determined by NEXAFS and other spectromicroscopic techniques (Lehmann et al., 2007, 2009). The limited spatial resolution of NEXAFS may have precluded detection of patchiness within observed ordered gradients, which are now accessible by cryo-STEM-EELS.

3.4 Implications for Soil Carbon Modeling and Sequestration

The existence of organic patches and organo-organic interfaces with different C composition than those at organo-mineral interfaces generates important information for sequestering soil carbon and predicting its changes. The described organo-organic interfaces point towards the need to consider soil C stabilization mechanisms that are independent of mineralogy and involve N-rich surfaces. In litter decomposition, the role of polyphenol complexation of N-rich compounds has been linked to slower litter turnover (Verkaik et al., 2006). The aromatic, high C, low N features in a high N, alkyl C matrix described here suggest these interactions may also be relevant for soil OM.

The demonstrated existence of disordered and patchy organo-organic interactions may also help explain that saturation of soil C is often not clearly predictable in the field and may relate to the N content of litter input (Castellano et al., 2015), even though SOM saturation is a theoretically reasonable and experimentally sound expectation (Six et al., 2002; Stewart et al., 2008). Predicting SOC stabilization with next-generation models should connect with litter input quality as it relates to N contents (Cotrufo et al., 2013) where N-rich organo-organic interfaces may play a role in affecting litter decomposition.

The presented data on their own are not sufficient to quantify the persistence that organo-organic interactions may confer to SOC. But their existence provides incentive to perform targeted experiments testing the biogeochemical importance of organo-organic interactions in soils, including comparisons of plant and animal manures varying in N functional group composition (Maillard and Angers, 2014). It

also provides motivation to expand the one-dimensional model of SOC stabilization (Kleber et al., 2007) of changing OM composition with distance to mineral surfaces, to a multi-dimensional model (Stockmann et al., 2013; Totsche et al., 2018) to recognize multi-phase organic matter that does not align at a predictable gradient with respect to the soil mineral matrix. Future research should also include cryo-electron tomography and other approaches that reveal the full three-dimensional structure of organo-organic and organo-mineral interfaces, ultimately informing a multi-dimensional spatial model of SOM accumulation.

4. Acknowledgements

Funding for this study was provided by the NSF IGERT in Cross-Scale Biogeochemistry and Climate at Cornell University (NSF Award #1069193) and the Technical University of Munich Institute for Advanced Studies. Additional research funds were provided by the Andrew W. Mellon Foundation and the Cornell College of Agriculture and Life Sciences Alumni Foundation. Collaborators in Applied and Engineering Physics (Lena F. Kourkoutis and Michael J. Zachman) acknowledge support by the NSF (DMR-1654596). This work made use of the Cornell Center for Materials Research Shared Facilities which are supported through the NSF MRSEC program (DMR-1719875). Additional support for the FIB/SEM cryo-stage and transfer system was provided by the Kavli Institute at Cornell (KIC) and the Energy Materials Center at Cornell, DOE EFRC BES (DE-SC0001086). The FEI Titan Themis 300 was acquired through NSF-MRI-1429155, with additional support from Cornell University, the Weill Institute and the KIC. The authors thank Katherine E.

Grant and Louis A. Derry (Cornell University Earth and Atmospheric Sciences) for providing soil samples from the Polulu Flow, HI. The authors also thank John Grazul and Malcolm Thomas of the CCMR facility for technical assistance.

REFERENCES

- Castellano, M.J., Mueller, K.E., Olk, D.C., Sawyer, J.E., Six, J., 2015. Integrating plant litter quality, soil organic matter stabilization, and the carbon saturation concept. *Global Change Biol.* 21(9), 3200-3209.
- Ciais, P., Sabine, C., Bala, G., Bopp, L., Brovkin, V., Canadell, J., Chhabra, A., DeFries, R., Galloway, J., Heimann, M., Jones, C., Le Quéré, C., Myneni, R.B., Piao, S., Thornton, P., 2013. Carbon and other biogeochemical cycles, in: Stocker, T.F., Qin, D., G.-K. Plattner, G.-K., Tignor, M., Allen, S.K., Boschung, J., Nauels, A., Xia, Y, Bex, V., Midgley, P.M. (Eds.), *Climate Change 2013: The Physical Science Basis. Contribution of Working Group I to the Fifth Assessment Report of the Intergovernmental Panel on Climate Change.* Cambridge University Press, Cambridge, UK and New York, NY, pp. 465-570.
- Chadwick, O.A., Gavenda, R.T., Kelly, E.F., Ziegler, K., Olson, C.G., Elliot, W.C., Hendricks, D.M., 2003. The impact of climate on the biogeochemical functioning of volcanic soils. *Chem. Geol.* 202, 195-223.
- Cueva, P., Hovden, R., Mundy, J.A., Xin, H.L., Muller, D.A., 2012. Data processing for atomic resolution electron energy loss spectroscopy. *Micros. Microanal.* 18, 667-675.
- Cotrufo, M.F., Wallenstein, M.D., Boot, C.M., Denef, K., Paul, E., 2013. The Microbial Efficiency-Matrix Stabilization (MEMS) framework integrates plant litter decomposition with soil organic matter stabilization: do labile plant inputs form stable soil organic matter? *Global Change Biol.* 19, 988-995.
- Deng, Y., Dixon, J.B., 2002. Soil organic matter and organic-mineral interactions, in: Dixon, J.B., Shulze, D.G. (Eds.), *Soil Mineralogy with Environmental Applications*, SSSA Book Series 7, Soil Science Society of America, Inc., Madison, WI. pp. 69-108.
- Grant, K.E., 2019. Carbon cycling in Hawaiian soils: the role of soil mineral weathering on the age, energetics, and stability of soil organic carbon (Doctoral dissertation). Cornell University, Ithaca, NY.
- Höschel, C., Höschel, T., Mueller, C.W., Lugmeier, J., Elgeti, S., Rennert, T., Kögel-Knabner, I., 2015. Novel sample preparation technique to improve spectromicroscopic analyses of micrometer-sized particles. *Environ. Sci. Technol.* 49, 9874-9880.

- Inagaki, T.M., Possinger, A.R., Grant, K.E., Schweizer, S.A., Mueller, C.W., Derry, L.A., Lehmann, J., Kögel-Knabner, I. Subsoil organo-mineral associations under contrasting climate conditions. In revision, *Geochim. Cosmochim. Acta*.
- Kallenbach, C.M., Frey, S.D., Grandy, A.S., 2016. Direct evidence for microbial-derived soil organic matter formation and its ecophysiological controls. *Nature Commun.* 7(13630), DOI: 10.1038/ncomms13630.
- Kaiser, M., Kleber, M., Berhe, A.A., 2015. How air-drying and rewetting modify soil organic matter characteristics: An assessment to improve data interpretation and inference. *Soil Biol. Biochem.* 80, 324-340.
- Kaznatcheyev, K.A., Osanna, A., Jacobsen, C., Vahtras, O., Ågren, P., Carravetta, V., Hitchcock A.P., 2002. Inner-shell absorption spectroscopy of amino acids. *J. Phys. Chem. A* 106, 3153-3168.
- Kelleher, B.P., Simpson, A.J., 2006. Humic substances in soils: Are they really chemically distinct? *Env. Sci. Technol.* 40(15), 4605-4611.
- Kim, E-A., Choi, J.H., 2018. Changes in the mineral element compositions of soil colloidal matter caused by a controlled freeze-thaw event. *Geoderma* 318, 160-166.
- Kinyangi, J., Solomon, D., Liang, B., Lerotic, M., Wirick, S., Lehmann, J., 2006. Nanoscale biogeochemical complexity of the organomineral assemblage in soil: Application of STXM microscopy and C 1s-NEXAFS spectroscopy. *Soil Sci. Soc. Am. J.* 70, 1708-1718.
- Kleber, M., Sollins, P., Sutton, R., 2007. A conceptual model of organo-mineral interactions in soils: self-assembly of organic molecular fragments into zonal structures on mineral surfaces. *Biogeochem.* 85, 9-24.
- Kleber, M., Eusterhues, K., Keiluweit, M., Mikutta, C., Mikutta, R., Nico, P.S., 2015. Mineral-organic associations: formation, properties, and relevance in soil environments. *Adv. Agron.* 130, 1-140.
- Kramer, M.G., Sanderman, J., Chadwick, O.A., Chorover, J., Vitousek, P.M., 2012. Long-term carbon storage through retention of dissolved aromatic acids by reactive particles in soil. *Glob. Chang. Biol.* 18, 2594-2605.
- Lal, R., 2004. Soil carbon sequestration impacts on global climate change and food security. *Science* 304, 623-627.
- Lehmann, J., Kleber, M. 2015. The contentious nature of soil organic matter. *Nature* 528, 60-68.

- Lehmann, J., Liang, B., Solomon, D., Lerotic, M., Luizão, F., Kinyangi, J., Schäfer, T., Wirick, S., Jacobsen, C., 2005. Near-edge X-ray absorption fine structure (NEXAFS) spectroscopy for mapping nano-scale distribution of organic carbon forms in soil: Application to black carbon particles. *Global Biogeochem. Cy.* 19, GB1013, DOI: 10.1029/2004GB002435.
- Lehmann, J., Kinyangi, J., Solomon, D., 2007. Organic matter stabilization in soil microaggregates: implications from spatial heterogeneity of organic carbon contents and carbon forms. *Biogeochem.* 85, 45-57.
- Lehmann, J., Solomon, D., Kinyangi, J., Dathe, L., Wirick, S., Jacobsen, C., 2008. Spatial complexity of soil organic matter forms at nanometre scales. *Nature Geosci.* 1, 238-242
- Lehmann, J., Solomon, D., Brandes, J., Fleckensten, H., Jacobsen, C., Thieme, J., 2009. Synchrotron-based near-edge X-ray spectroscopy of natural organic matter in soils and sediments, in: Senesi, N., Xing, B., Huang, P.M. (Eds.) *Biophysico-Chemical Processes Involving Natural Nonliving Organic Matter in Environmental Systems*, John Wiley and Sons, Hoboken, NJ, pp. 723-775.
- Mayer, L.M., Xing, B., 2001. Organic matter-surface area relationships in acid soils. *Soil Sci. Soc. Am. J.* 65, 250-258.
- Maillard, É., Angers, D.A., 2014. Animal manure application and soil organic carbon stocks: A meta-analysis. *Global Change Biol.* 20(2), 666-679.
- Milne, A.E., Lehmann, J., Solomon, D., Lark, R.M., 2011. Wavelet analysis of soil variation at nanometre to micrometer-scales: an example of organic carbon content in a micro-aggregate. *Eur. J. Soil Sci.* 62, 617-628.
- Miot, J., Benzerara, K., Kappler, A., 2014. Investigating microbe-mineral interactions: recent advances in X-ray and electron microscopy and redox-sensitive methods. *Annu. Rev. Earth Planet. Sci.* 42, 271-289.
- Parfitt, R.L., Theng, B.K.G., Whitton, J.S., Shepherd, T.G., 1997. Effects of clay minerals and land use on organic matter pools. *Geoderma* 75(1-2), 1-12.
- Sansinena, M., Santon, M.V., Zaritzky, N., Chirife, J., 2012. Comparison of heat transfer in liquid and slush nitrogen by numerical simulation of cooling rates for French straws used for sperm cryopreservation. *Theriogenology* 77(8), 1717-1721.
- Schmidt, M.P., Martinez, C.E., 2018. Supramolecular association impacts biomolecule adsorption onto goethite. *Env. Sci. Technol.* 52, 4079-4089.

- Schmidt, M.W., Torn, M.S., Abiven, S., Dittmar, T., Guggenberger, G., Janssens, I.A., Kleber, M., Kögel-Knabner, I., Lehmann, J., Manning D.A.C., Nannipieri, P., Rasse, D.P., Weiner, S., Trumbore, S.E., 2011. Persistence of soil organic matter as an ecosystem property. *Nature* 478(7367), 49-56.
- Schneider, C.A., Rasband, W.S., Eliceiri, K.W., 2012. NIH Image to ImageJ: 25 years of image analysis. *Nature Methods* 9(7), 671-675.
- Signorell, A., et mult. al., 2019. DescTools: Tools for descriptive statistics. R package version 0.99.28.
- Six, J., Conant, R.T., Paul, E.A., Paustian, K., 2002. Stabilization mechanisms of soil organic matter: implications for C-saturation of soils. *Plant Soil*, 241(2), 155-176.
- Solomon, D., Lehmann, J., Kinyangi, J., Liang, B., Heymann, K., Dathe, L., Hanley, K., Wirick, S., Jacobsen, C., 2009. Carbon (1s) NEXAFS spectroscopy of biogeochemically relevant reference organic compounds. *Soil Sci. Soc. Am. J.* 73, 1817-1830.
- Solomon, D., Lehmann, J., Kinyangi, J., Liang, B., Schäfer, T., 2005. Carbon K-edge NEXAFS and FTIR-ATR spectroscopic investigation of organic carbon speciation in soils. *Soil Sci. Soc. Am. J.* 69, 107-119.
- Stewart, C.E., Paustian, K., Conant, R.T., Plante, A.F., Six, J., 2008. Soil carbon saturation: evaluation and corroboration by long-term incubations. *Soil Biol. Biochem.* 40(7), 1741-1750.
- Stockmann, U., Adams, M.A., Crawford, J.W., Field, D.J., Henakaarchchi, N., Jenkins, M., Minasny, B., McBratney, A.B., de Remy de Courcelles, V., Singh, K., Wheeler, I., Abbott, L., Angers, D.A., Baldock, J., Bird, M., Brookes, P.C., Chenu, C., Jastrow, J.D., Lal, R., Lehmann, J., O'Donnell, A., Parton, W.J., Whitehead, D., Zimmerman, M., 2013. The knowns, known unknowns and unknowns of sequestration of soil organic carbon. *Agric. Ecosyst. Environ.* 164, 80-99.
- Totsche, K.U., Amelung, W., Gerzabek, M.H., Guggenberger, G., Klumpp, E., Knief, C., Lehndorff, E., Mikutta, R., Peth, S., Pechtel, A., Ray, N., Kögel-Knabner, I., 2018. Microaggregates in soils. *J. Plant Nutr. Soil Sci.* 181(1), 104-136.
- Torn, M.S., Trumbore, S.E., Chadwick, O.A., Vitousek, P.M., Hendricks, D.M., 1997. Mineral control of soil organic carbon storage and turnover. *Nature* 389, 170-173.

- van Heel, M., Gowen, B., Matadeen, R., Orlova, E.V., Finn, R., Pape, T., Cohen, D., Stark, H., Schmidt, R., Schatz, M., Patwardhan, A., 2000. Single-particle electron cryo-microscopy: Towards atomic resolution. *Q. Rev. Biophys.* 33(4), 307-369.
- Verkaik, E., Jongkind, A.G., Berendse, F., 2006. Short-term and long-term effects of tannins on nitrogen mineralisation and litter decomposition in kauri (*Agathis australis* (D. Don) Lindl.) forests. *Plant Soil* 287, 337-345.
- Vogel, C., Mueller, C.W., Höschen, C., Buegger, F., Heister, K., Schulz, S., Schloter, M., Kögel-Knabner, I., 2014. Submicron structures provide preferential spots for carbon and nitrogen sequestration in soils. *Nat. Commun.* 5(2947), DOI: 10.1038/ncomms3947.
- Weider, W.R, Grandy, A.S., Kallenbach, C.M., Bonan, G.B., 2014. Integrating microbial physiology and physio-chemical principles in soils with the MIMICS model. *Biogeosci.* 11, 3899-3917.
- Wojdyr, M., 2010. Fityk: a general-purpose peak fitting program. *J. Appl. Cryst.* 43, 1126-1128.
- Zachman, M.J., Asenath-Smith, E., Estroff, L.A., Kourkoutis, L.F., 2016. Site-specific preparation of intact solid-liquid interfaces by label-free *in situ* localization and cryo-focused ion beam lift-out. *Microsc. Microanal.* 22, 1338-1349.

APPENDIX

A1. Supplementary Methods

A1.1 Chapter 1 Supplementary Methods

A1.1.1 EELS Image Selection for Spatial Analysis

In order to perform detailed spatial analysis of carbon (C) components derived from electron energy loss spectroscopy (EELS) maps using multivariate curve resolution (MCR), comparable images for co-precipitation and adsorption were selected. Criteria for selection were: (1) identical magnification (i.e., spatial resolution), (2) homogeneous spatial distribution of components (i.e., lack of a possible edge artifact), and (3) high spectral quality (co-precipitation sample taking priority). To illustrate the sample selection process, MCR outputs and associated component maps are shown in Appendix Figure A3.1.1. Two images at 1.8Mx magnification were selected for subsequent spatial analysis and spectral interpretations.

A1.2 Chapter 2 Supplementary Methods

A1.2.1 Random Forest Modeling

Mineral soil characterization data were randomly split into training and testing sets (75 and 25%, respectively) and a training data model constructed with the Random Forest algorithm using an out-of-bag bootstrapping approach (100X resampling), and the following parameters: (1) node size = 5, (2) maximum number of trees (ntree) = 500, and number of variables per level (mtry) = 2. A preliminary model including 16 parameters (pH, horizon type, horizon depth, saturation frequency, dithionite-

extractable Fe and Al, oxalate- and hydroxylamine-extractable Fe, Al, and Mn, and total Fe, Al, and Mn) was computed, and the variables with all levels ranked less than 10% in model importance were excluded. A reduced model (excluding total Al and all Mn parameters) was independently computed 5 times with unique training and testing sets to assess model stability in variable importance rankings. A linear model of predicted and observed C contents was used to assess model predictive ability.

A1.2.2 Fe K-edge XANES Estimation of Reduced Fe(II)

Positive (height fixed > 0) Gaussian functions at ~ 7112 (pre-edge centroid), 7124, and 7128 eV were allowed to float by $3 \cdot \sin(\sim 0)$. The 7120.0 eV function was fixed. The full-width half-maximum (FWHM) of all functions was allowed to vary by $2 \text{ eV} + 1 \cdot \sin(\sim 0)$. The model was fit using the Levenberg-Marquardt algorithm in Fityk v. 0.9.8 (Wojdyr, 2010) 1000 maximum iterations to minimize the maximum sum of squared residuals (MSSR). The relative increase in the 7120.0 eV peak area was determined as the proportion of the total peak area.

A1.2.3 Carbon K-edge XANES Damage Test

Potential spectral artifacts arising from beam damage were assessed by collecting 20 sequential spectra at a fixed point for a high-C (low saturation frequency) and low-C (high saturation frequency) bulk soil sample. Directional change in fine structure ratios over time was considered evidence of beam damage, as well as appearance of new features over time. Due to spectral noise of individual scans, 5 scans were interpolated and averaged to generate 4 time points (5, 10, 15, and 20 s). For the damage test, fine structural changes were compared as in Chapter 2 Section 2.3.2. Briefly, peak height ratios of the 3 primary spectral features (aromatic, substituted

aromatic, and carboxylic C) were determined by finding the maximum of a Gaussian function (FWHM = 0.6 eV) within the defined ranges of 285.0-286.2 eV for aromatic C, 286.0-287.0 for substituted aromatic C, and 288.0-289.5 eV for carboxylic C (Solomon et al., 2009; Heymann et al., 2011).

A1.2.4 Nuclear Magnetic Resonance Variable Contact Time (NMR VCT)

Calculations

A line broadening (smoothing) value of 75 was used for all samples and spectra. For each soil sample, 6 spectra were collected with contact times of 0.03, 0.25, 0.5, 1, 2, 3, and 4 ms, respectively. Spectra were integrated with the following C functional group regions: alkyl C (0 to 45 ppm), O/N alkyl C (45 to 110 ppm), aromatic C (110 to 160 ppm), and carboxylic C (160 to 220 ppm) (Knicker and Lüdemann, 1995). The log₁₀-transformed signal intensity of each region was plotted as a function of contact time (Preston et al., 1984). The absolute value of the slope was taken to determine the magnitude of the contact time effect. The slope of the line from 0.5-4 ms was converted to T_{1ρ}H by the formula:

$$\text{Eq. 1: Slope} = -1/T_{1\rho}H \quad (\text{Preston et al., 1984})$$

A1.3 Chapter 3 Supplementary Methods

A1.3.1 Sample Damage Assessment of Cryo-FIB and Cryo-STEM-EELS

Techniques

Cryogenic techniques for sample preparation and electron microscopy of damage-sensitive biological materials, including geobiological materials, are well-established and often employed as a means to reduce sample damage (Kourkoutis et al., 2012;

Miot et al., 2014). However, sample damage remains a consideration for both cryogenic focused ion beam (FIB) sample preparation and subsequent cryogenic analytical electron microscopy. In order to assess improvement in sample integrity with cryogenic focused ion beam (FIB) sample preparation versus room temperature FIB, we completed preparation and imaging of a volcanic soil sample thin-section via lift-out FIB techniques. Additionally, we assessed evidence of artifacts in the carbon (C) K-edge resulting from cryogenic scanning transmission electron microscopy-electron energy loss spectroscopy (cryo-STEM-EELS) analysis.

41.3.2 Room Temperature FIB Sample Preparation

Initial pre-thinning to approximately 1 μm -thickness was completed using cryogenic ultramicrotome thinning. Intact soil aggregates were stabilized with vitreous ice and maintained under cryogenic conditions throughout the sectioning, focused ion beam (FIB) milling, and imaging processes. Aggregates in a 53-150 μm -diameter class were gradually saturated with deionized (DI) water using an ultrasonic humidifier at the lowest setting (SPT Ultrasonic Humidifier, Sunpentown, Inc., City of Industry, CA) (Kinyangi et al., 2006). After humidification, individual intact aggregates were selected under a dissecting microscope, and transferred to a DI water droplet on an aluminum cryo-ultramicrotome pedestal. The droplet was then rapidly frozen by immersion in slush nitrogen (N_2) (average temperature -207°C , Sansinena et al. 2012). Aggregates were pre-sectioned into 1-5 μm -thick cross-sections using a cryo-ultramicrotome equipped with a diamond blade (Leica EM UC7/FC7, Leica Microsystems, Inc., Buffalo Grove, IL). Cryo-ultramicrotome thinning was performed at -60°C using a step size of 1000 nm, and thin sections were transferred to 400-mesh

copper TEM grids with self-prepared thin C coating, brought to room temperature, and air-dried. Samples were transferred to an FEI Strata 400 STEM FIB instrument (FEI Company, Hillsboro, OR) at room temperature. After air-drying, the aggregate cross-section broke apart along natural pore space borders, allowed for FIB lift-out of aggregate regions (20 x 15 x 1 μm) without on-grid cross section (e.g., trench) milling. The aggregate region of interest was fastened to a tungsten (W) FIB lift-out needle using deposited platinum (Pt) organo-metallic alloy and transferred to a Cu TEM lift-out grid (Electron Microscopy Sciences, Hatfield, PA). After transfer, the sample was coated with Pt for further thinning. The sample was stored dry at room temperature prior to STEM imaging in an FEI F20 TEM STEM instrument (FEI Company, Hillsboro, OR) at 200 kV.

A1.3.3 Cryo-STEM-EELS Damage Assessment

A1.3.3.4 Organo-Organic Interface Sample (Titan Instrument)

Potential sample damage from cryo-STEM-EELS analysis was assessed by repeated measurements of a semi-crystalline iron oxide-organic material serving as a reference material for the volcanic semi-crystalline soils analyzed. The reference material was prepared by precipitation of ferrihydrite (nominally $\text{Fe}_2\text{O}_3 \bullet 0.5\text{H}_2\text{O}$) in the presence of dissolved organic matter (DOM) derived from a soil organic horizon at a 10:1 C:Fe ratio. Precipitation of ferrihydrite was completed using a low-concentration modification of standard laboratory ferrihydrite synthesis (Schwertmann and Cornell, 2000) and purified by dialysis (1000 D MWCO). Ferrihydrite-DOM suspensions were applied to Cu grids and air-dried. Samples were transferred at room temperature to an aberration corrected FEI Titan Themis S/TEM instrument (FEI Company, Hillsboro,

OR) with a Gatan GIF Quantum 965 spectrometer (Gatan Inc., Pleasanton, CA) operated at 120 kV. The samples were cooled within the instrument for cryo-STEM-EELS at approximately -180°C.

Sample damage was assessed by 6 repeated EELS measurements (640 kx magnification) of the C K-edge over the same field of view (1247 Å²) with dwell time of 10s per measurement and 0.16 nA beam current, resulting in a total dose of ~54,000 electrons Å⁻². Spectra were processed using the Cornell Spectrum Imager package (Cueva et al., 2012) in ImageJ v. 2.0.0 (Schneider et al., 2012). Background subtraction was performed using a standard linear combination of power laws (LCPL) with the background subtraction region of 210.0-259.5 eV. The C K-edge intensity was estimated by calculation of area under the curve (AUC) from 280.0-315.0 eV in the R “DescTools” package (Signorell et al., 2019). The ratio of integrated area in higher (286.5-289.0 eV) and lower-energy (284.5-286.5 eV) spectral regions (normalized to the total C area) was used to assess change in fine structure as a function of electron dose.

A1.3.3.5 Organo-Mineral Interface Sample (F20 Instrument)

Due to limitations in probe size determination for point and linescan measurements, damage assessment for EELS analysis of the organic-mineral interface soil sample was completed by comparing potential fine-structural changes in EELS point spectra collected with increasing monochromator intensity and increased acquisition time. In particular, points scans 1-3 of the adjacent C region (Figure 3.1) were collected with monochromator settings of 60, 40, and 40 and acquisition time of 5, 8, and 10 s, respectively.

A2. Supplementary Results and Discussion

A2.1 Chapter 1 Supplementary Results and Discussion

A2.1.1 Chemical Composition of DOM: Rationale for Pooled Observations

DOM was collected for the co-precipitation and adsorption experiments from two sites on a hillslope transect. The upslope, “E” podzol site had slightly higher coniferous basal area (35% vs 0% for the sampling area) than the “typical” site; however, basal area was dominated by the same deciduous species (*Betula alleghaniensis*), and throughout the course of the experiment, no appreciable differences in DOM composition (via C K-edge XANES), C content, or bulk XAS associated with DOM sources were detected. The C:Fe molar ratio was adjusted to 10:1 for both DOM sources, accounting for differences in the initial C content. Since the interpretations focused on the spatial and compositional changes between co-precipitation and adsorption, DOM data were pooled across typical and E podzol sites.

A2.2 Chapter 2 Supplementary Results and Discussion

A2.2.1 Carbon K-edge XANES Damage Test

Though peak height ratios were variable across the 20 min measurement period, no directional or systematic changes were detected, suggesting variability may be due to low signal/noise of averaged scans rather than beam damage (Appendix Figure A3.2.8). Additionally, no systematic increase of a new spectral feature was identified over time (Appendix Figure A3.2.8).

A2.3 Chapter 3 Supplementary Results and Discussion

A2.3.1 Room Temperature vs. Cryogenic Temperature FIB Damage

With room temperature FIB, sample redeposition and distortion of sample structure was observed at both the millimeter and nanometer scale (Appendix Figure A3.3.12). Higher-contrast spots are likely a result of redeposition of sample material, or possibly implantation of gallium ions (Ga^+) directly from the ion beam milling. While some Ga^+ was detected in cryo-FIB samples (Appendix Figure A3.3.1), the sample distortion and higher-contrast spots observed with room-temperature FIB were not observed with cryo-FIB sample preparation (Figure 3.1).

A2.3.2 Cryo-STEM-EELS Damage Assessment

A2.3.2.1 Organo-Organic Sample (Titan Instrument)

Repeated scans at the same point in a ferrihydrite-DOM composite sample with analogous properties (semi-crystalline mineralogy, high organic C content) to the volcanic soils used in this study showed a slight increase in total C and in fine structure (high/low energy ratio) with $\sim 15,400 \text{ e}^- \text{ \AA}^{-2}$ dose (Appendix Figure A3.3.13). For both total C and high/low energy ratio, the increase at $\sim 15,400 \text{ e}^- \text{ \AA}^{-2}$ indicates that for the highest magnification EELS maps, the absolute value of higher-energy features may be overestimated relative to lower-magnification EELS maps. However, no appearance of features in the spectrum linked to beam damage artifacts were observed (i.e., new features that appear over time) (Appendix Figure A3.3.13). The lack of artifact development attests to EELS data quality, especially relative to other spectroscopic techniques (e.g., x-ray absorption spectroscopy) with common

appearance of beam damage artifacts in the low-energy (<285.0 eV) region of the spectrum.

A2.3.2.2 Organo-Mineral Sample (F20 Instrument)

With increasing monochromator intensity and exposure time, a slight decrease in ratio of high/low energy regions was observed (Figure 3.1). For point 1, ratio $b/a = 1.1$ and for points 2 and 3, $b/a = 1.0$. However, the lack of change between points 2 and 3 despite a 2 s increase in exposure time (8s vs 10s) suggests that these differences may be due to fine-scale sample heterogeneity rather than beam damage. Further, the same monochromator setting and exposure time (mono 60 and 5s) was used for the organo-mineral interface linescan as for point 1, supporting the validity of comparing high/low energy ratios. Accounting for ranges in b/a given potential sample damage, the enrichment of higher-energy C features at the organo-mineral interface could range from 18-40% (minimum $b/a = 1.1$ vs. 1.3 and maximum $b/a = 1.0$ vs. 1.5).

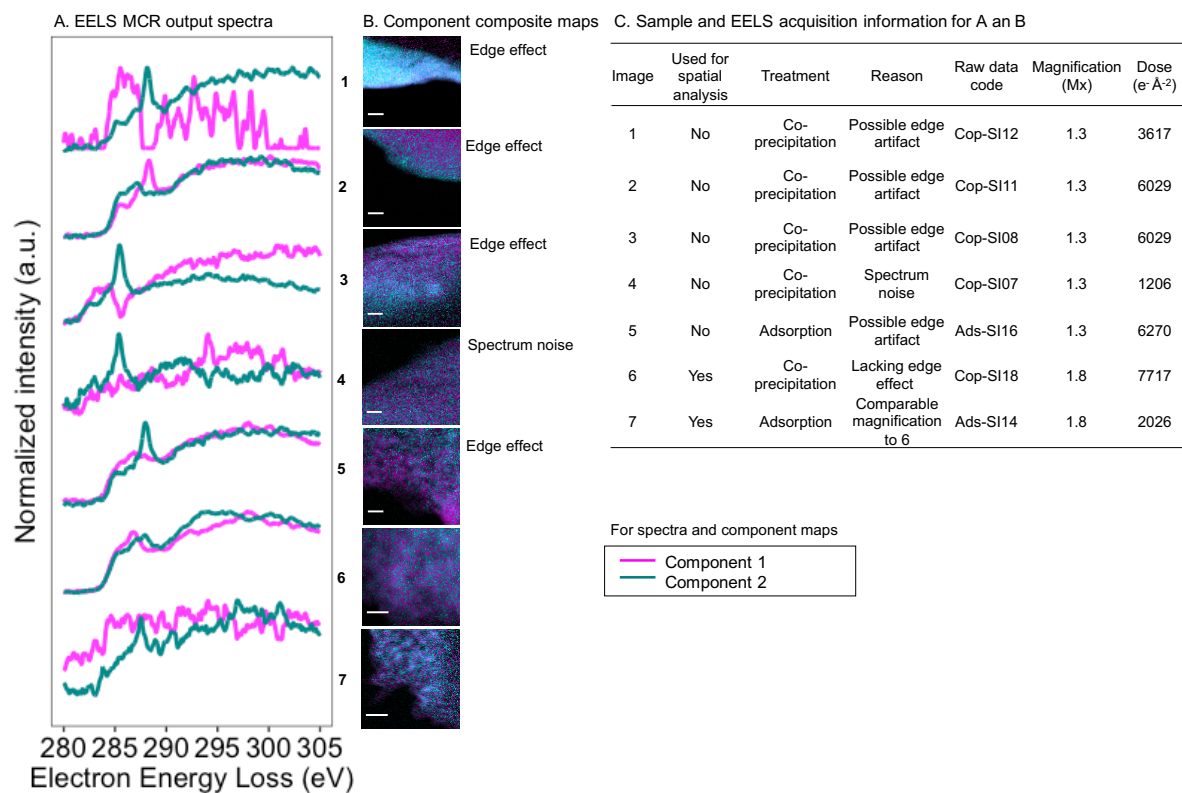
APPENDIX REFERENCES

- Berry, A.J., O'Neill, H.St.C., Jayasuriya, K.D., Campbell, S.J., Foran, G.J., 2003. XANES calibrations for the oxidation state of iron in silicate glass. *Am. Mineral.* 88(7), 967-977.
- Chen, C., Dynes, J.J., Wang, J., Sparks, D.L., 2014. Properties of Fe-organic matter associations via coprecipitation versus adsorption. *Environ. Sci. Technol.* 48, 13751-13759.
- Cueva, P., Hovden, R., Mundy, J.A., Xin, H.L., Muller, D.A., 2012. Data processing for atomic resolution electron energy loss spectroscopy. *Micros. Microanal.* 18, 667-675.
- Grant, K.E., 2019. Carbon cycling in Hawaiian soils: the role of soil mineral weathering on the age, energetics, and stability of soil organic carbon (Doctoral dissertation). Cornell University, Ithaca, NY.
- Heymann, K., Lehmann, J., Solomon, D., Schmidt, M.W.I., Regier, T., 2011. C 1s K-edge near edge X-ray absorption fine structure (NEXAFS) spectroscopy for characterizing functional group chemistry of black carbon. *Org. Geochem.* 42(9), 1055-1064.
- Hitchcock, A.P., Mancini, D.C., 1994. Bibliography and database of inner-shell excitation spectra of gas phase atoms and molecules. *J. Electron. Spectrosc. Relat. Phenom.* 67, 1-123
- Inagaki, T.M., Possinger, A.R., Grant, K.E., Schweizer, S.A., Mueller, C.W., Derry, L.A., Lehmann, J., Kögel-Knabner, I. Subsoil organo-mineral associations under contrasting climate conditions. In revision, *Geochim. Cosmochim. Acta.*
- Kinyangi, J., Solomon, D., Liang, B., Lerotic, M., Wirick, S., Lehmann, J., 2006. Nanoscale biogeocomplexity of the organomineral assemblage in soil: Application of STXM microscopy and C 1s-NEXAFS spectroscopy. *Soil Sci. Soc. Am. J.* 70, 1708-1718.
- Knicker, H., Lüdemann H.D., 1995. N-15 and C-13 CPMAS and solution NMR studies of N-15 enriched plant material during 600 days of microbial degradation. *Org. Geochem.* 23, 329-341.
- Kourkoutis, L. F., Plitzko, J.M., Baumeister, W., 2012. Electron microscopy of biological materials at the nanometer scale. *Annu. Rev. Mater. Res.* 42, 33-58.
- Miot, J., Benzerara, K., Kappler, A., 2014. Investigating microbe-mineral interactions: recent advances in X-ray and electron microscopy and redox-sensitive

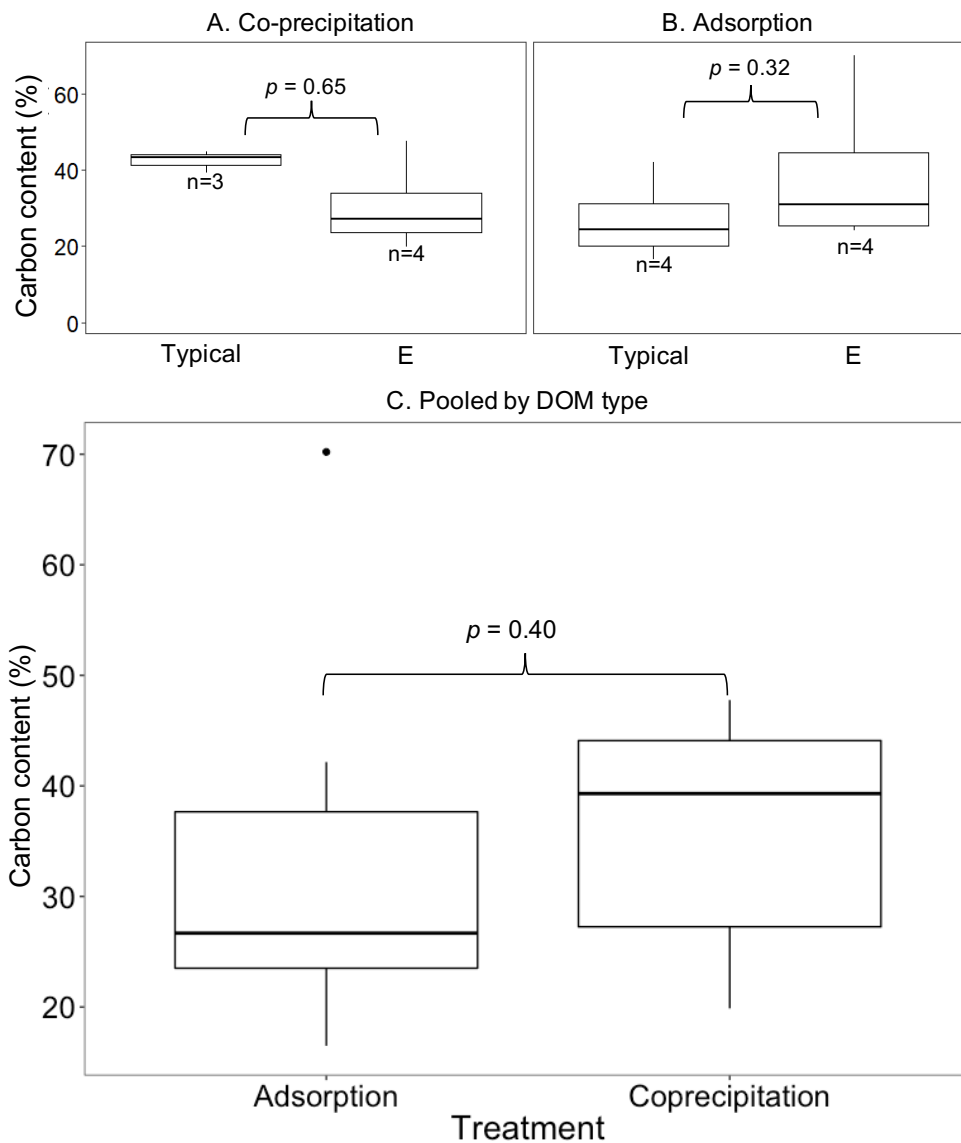
- methods. *Annu. Rev. Earth Planet. Sci.* 42, 271-289.
- Preston, C.M., Dudley, R.L., Fyfe, C.A., Mathur, S.P., 1984. Effects of variations in contact times and copper contents in a ^{13}C CPMAS NMR study of samples of four organic soils. *Geoderma* 33, 245-253.
- Sansinena, M., Santon, M.V., Zaritzky, N., Chirife, J., 2012. Comparison of heat transfer in liquid and slush nitrogen by numerical simulation of cooling rates for French straws used for sperm cryopreservation. *Theriogenology* 77(8), 1717-1721.
- Schneider, C.A., Rasband, W.S., Eliceiri, K.W., 2012. NIH Image to ImageJ: 25 years of image analysis. *Nature Methods* 9(7), 671-675.
- Schwertmann, U., Cornell R.M., 2000. *Iron Oxides in the Laboratory: Preparation and Characterization*, 2nd Edition. Wiley-VCH Verlag GmbH, Weinheim, DE.
- Signorell, A., et mult. al., 2019. DescTools: Tools for descriptive statistics. R package version 0.99.28.
- Solomon, D., Lehmann, J., Kinyangi, J., Liang, B., Heymann, K., Dathe, L., Hanley, K., Wirick, S., Jacobsen, C., 2009. Carbon (1s) NEXAFS spectroscopy of biogeochemically relevant reference organic compounds. *Soil Sci. Soc. Am. J.* 73, 1817-1830.
- Wojdyr, M., 2010. Fityk: a general-purpose peak fitting program. *J. Appl. Cryst.* 43, 1126-1128.

A3. Supplementary Figures

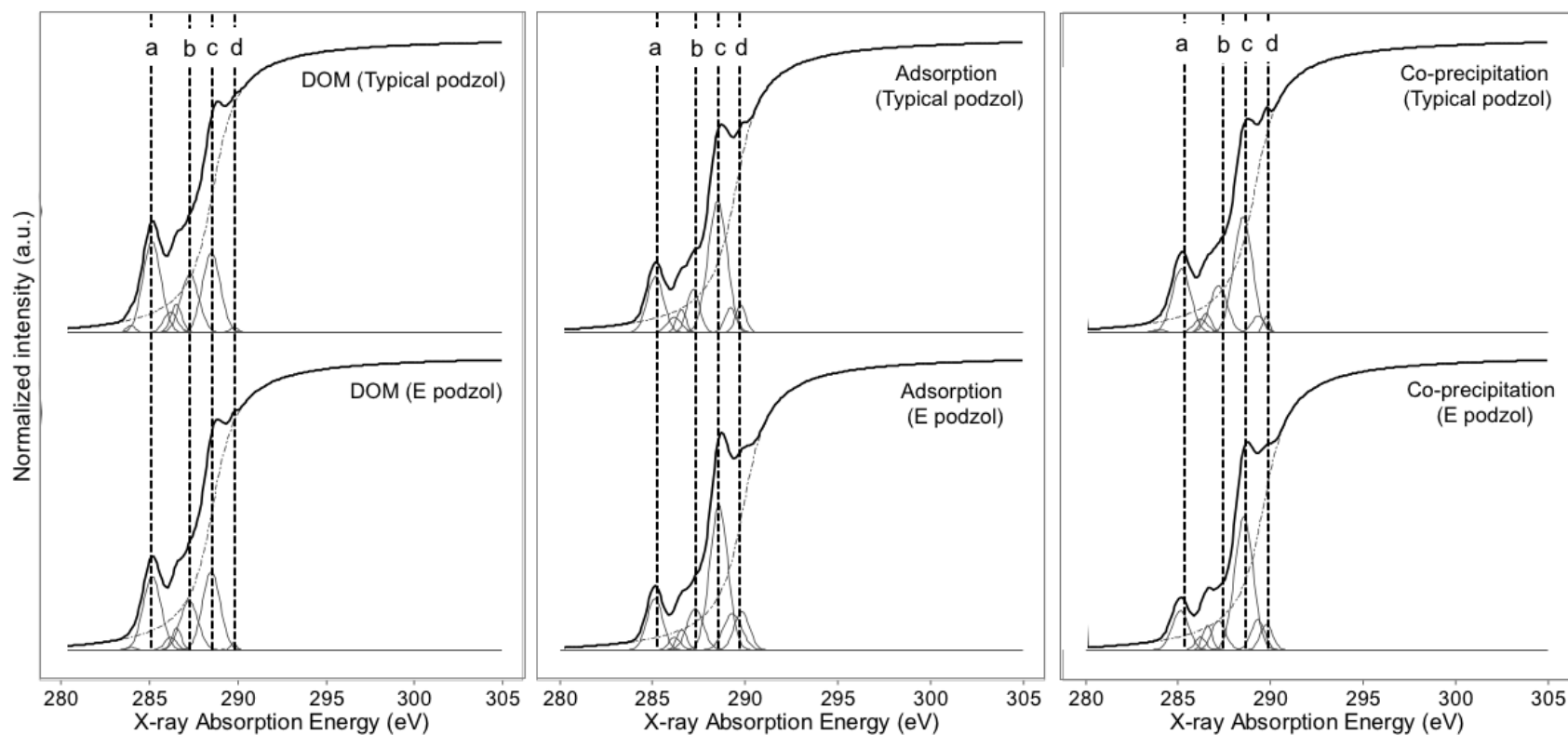
A3.1 Chapter 1 Supplementary Figures



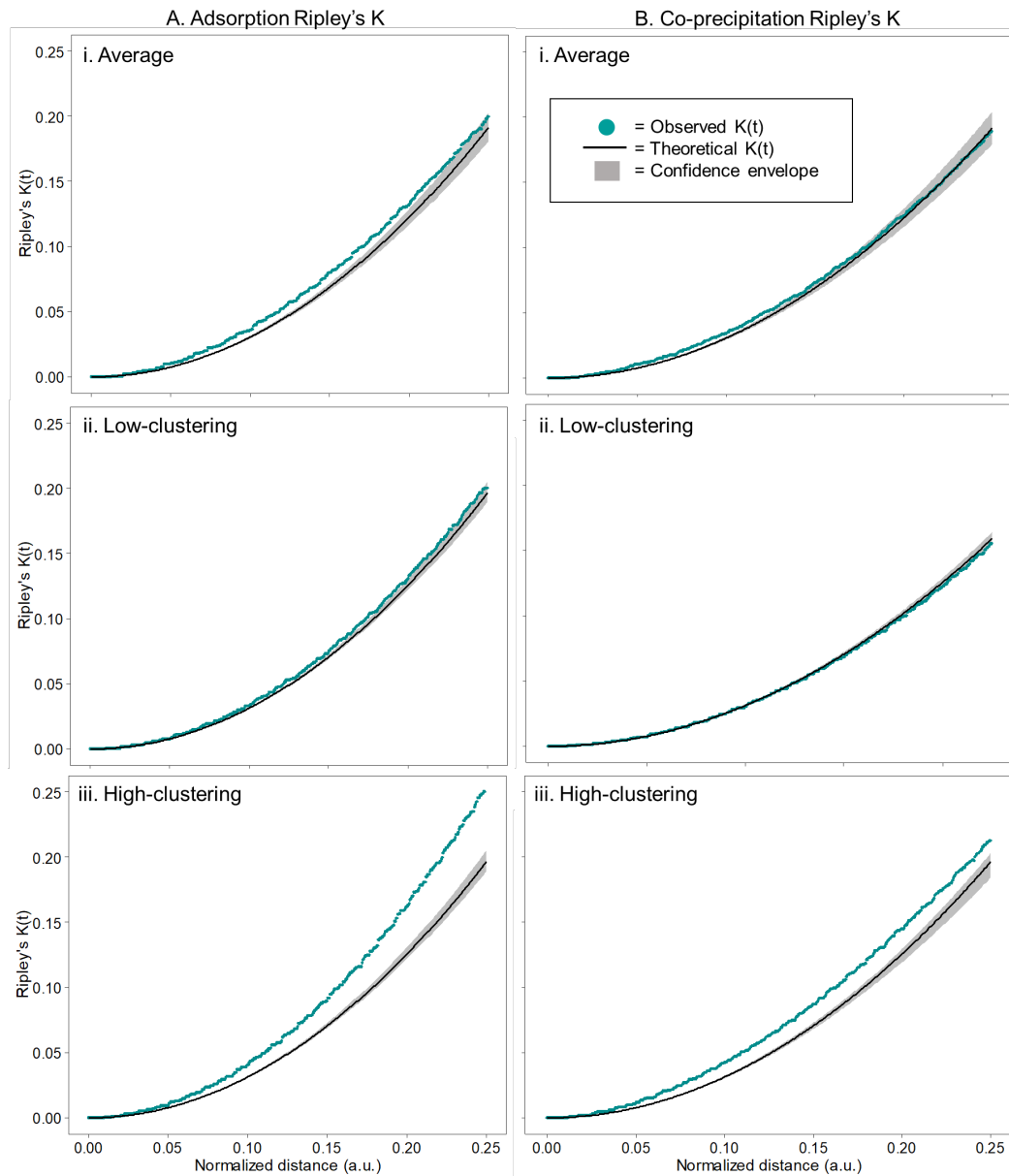
Appendix Figure A3.1.1. Electron energy loss spectroscopy (EELS) multivariate curve resolution (MCR) output results for a range of co-precipitate and adsorption dissolved organic matter (DOM)-ferrihydrite samples. **A.** MCR output spectra. **B.** Composite maps of MCR components. **C.** Spectrum/map identification, EELS acquisition parameters, and rationale for image selection.



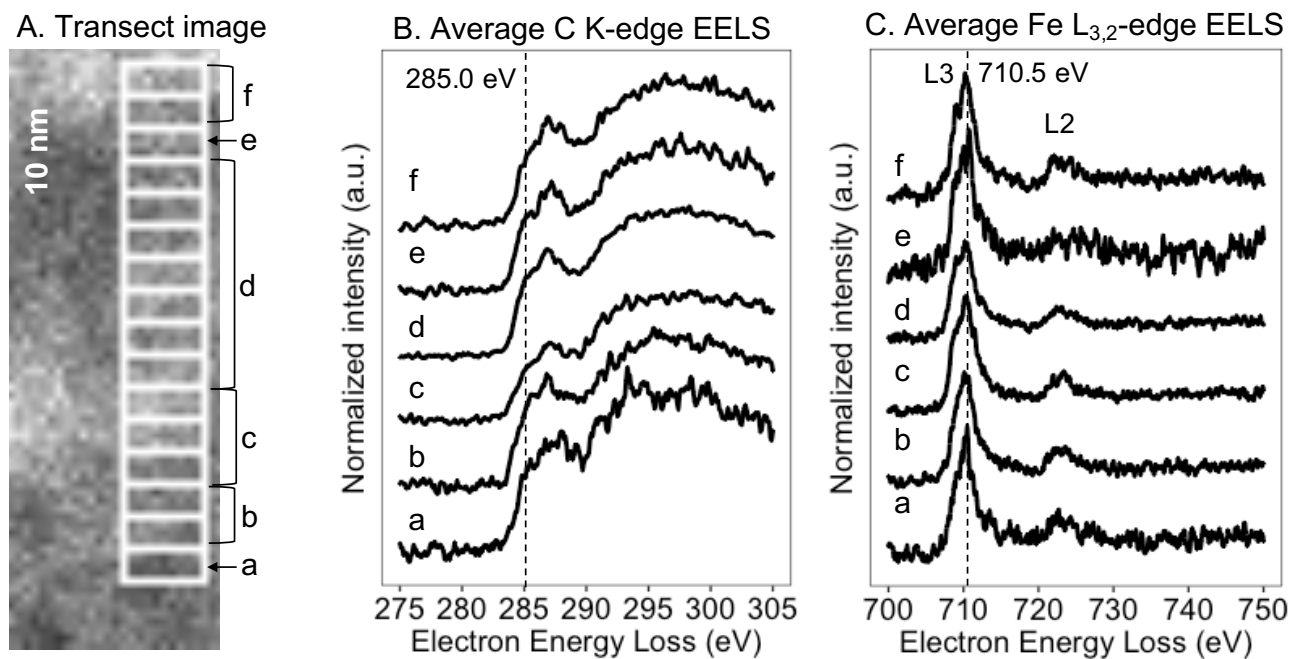
Appendix Figure A3.1.2. Total carbon (C) (%) for co-precipitate (A) and adsorption (B) samples at 10:1 C:Fe ratio prepared with DOM derived from sites classified as “typical” and “E” podzols. Typical and E-derived DOM are compared at $\alpha=0.05$ using the Wilcoxon Rank Sum Test, showing no significant differences between DOM source. Pooled by DOM time (C), the median carbon content was higher for co-precipitation but the difference was not significant (Rank-Sum $p=0.40$) due to variation in adsorption C content. Lower and upper edges of boxes show first and third quartiles (25th and 75th percentiles) and lower and upper whiskers show the smallest and largest value no further than $1.5 \times$ interquartile range (IQR) of the box edges. Individual points beyond whiskers are considered outliers.



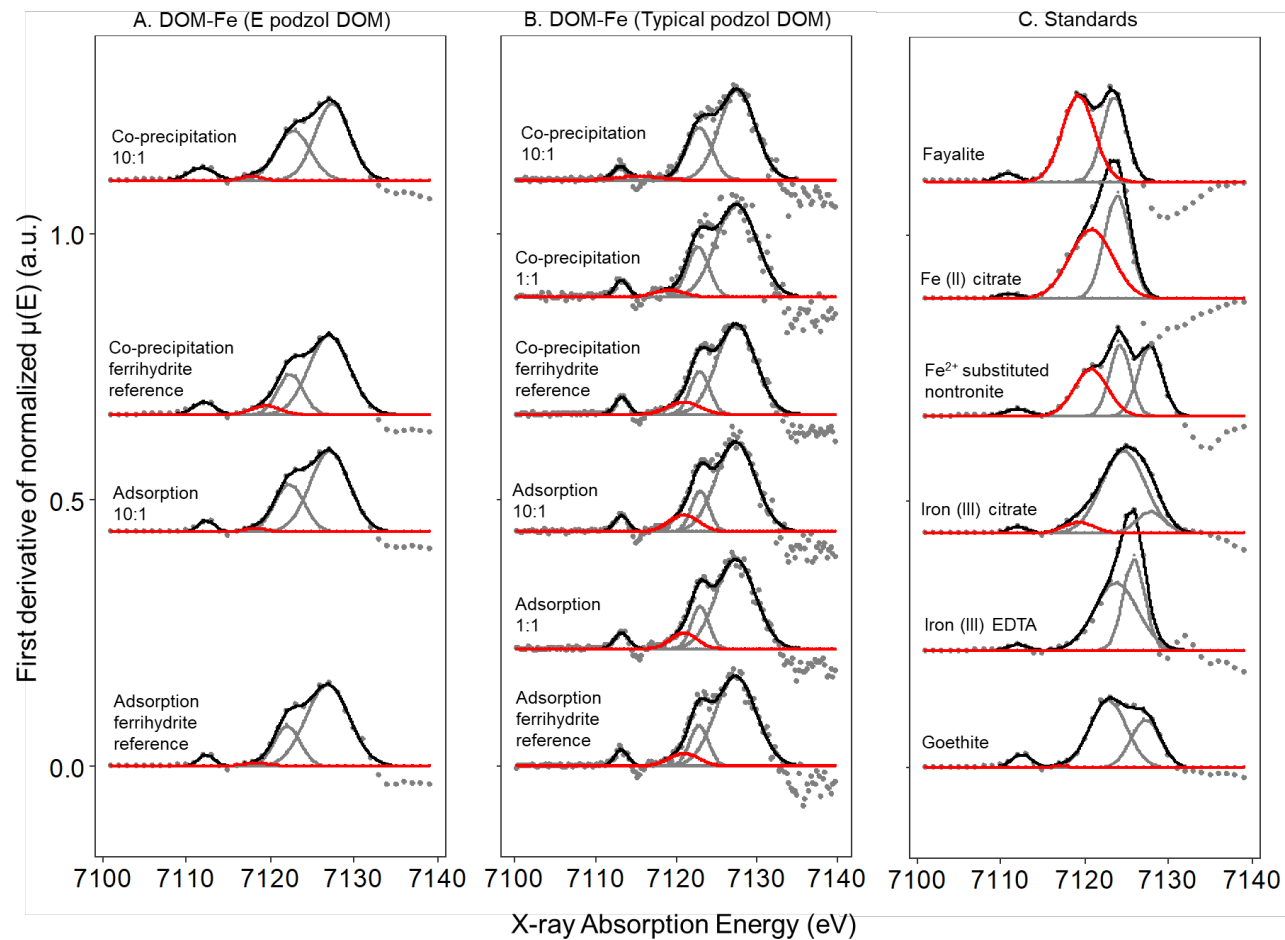
Appendix Figure A3.1.3. Gaussian and arctangent functions for deconvolution model of carbon (C) K-edge X-ray absorption near edge structure (XANES) for source dissolved organic matter (DOM) and adsorbed and co-precipitated DOM-ferrihydrite complexes. Lines a, b, c, and d indicate spectral features at ~ 285.0 , 287.5 , 288.7 , and 289.0 eV, corresponding to aromatic, aliphatic, carboxylic, and O-alkyl/carbonyl C functional groups, respectively.



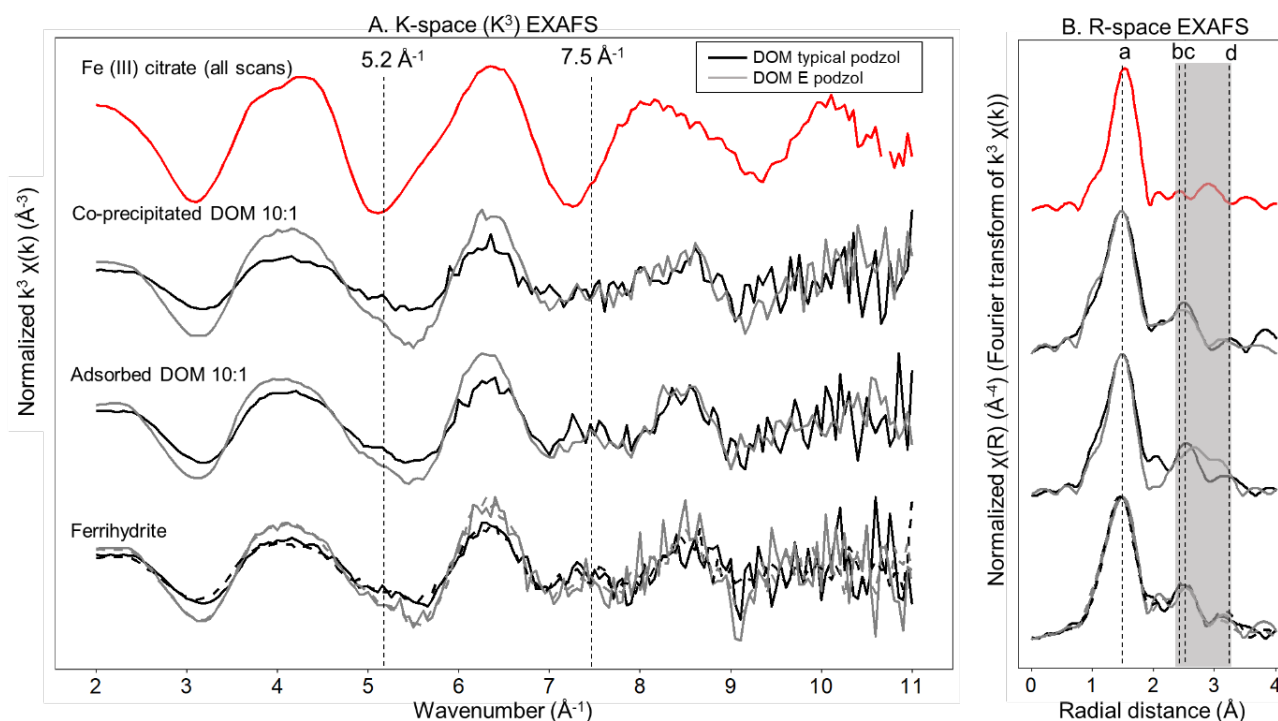
Appendix Figure A3.1.4. Spatial quantification of iron (Fe) clustering in co-precipitate and adsorption samples using Ripley's $K(t)$ as a function of normalized distance from each randomly sampled Fe point in a spatial point pattern for adsorbed (**A**) and co-precipitated (**B**) dissolved organic matter (DOM)-ferrihydrite sampled (DOM source pooled). Observations (dark cyan line) above the theoretical (Poisson) distribution (black line) and outside the confidence envelope are considered significantly spatially clustered. Plots i-iii show the Ripley's $K(t)$ distributions for the average, minimum, and maximum images (all >1.3 Mx magnification) within co-precipitate ($n=8$ images) and adsorption ($n=7$ images) samples.



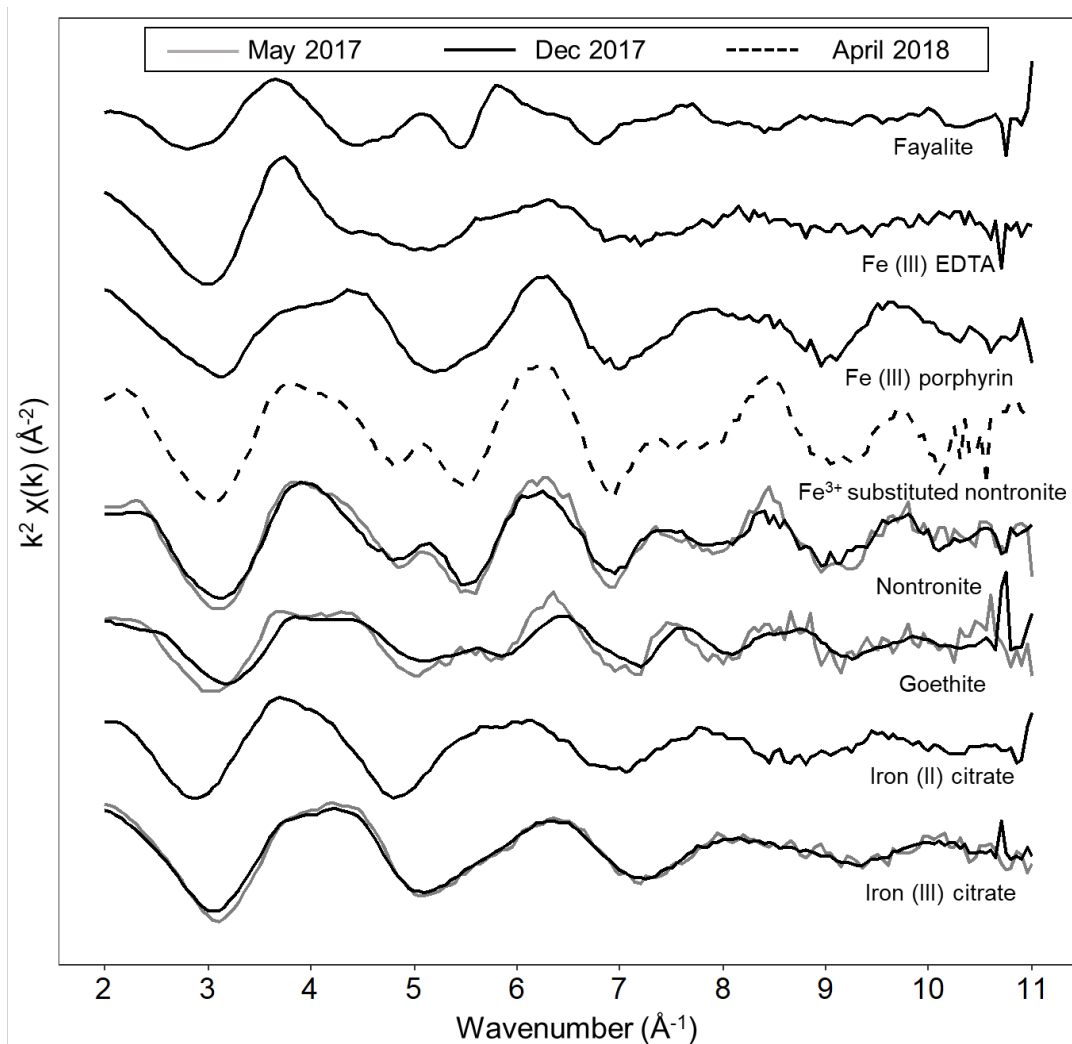
Appendix Figure A3.1.5. Average carbon (C) K-edge and iron (Fe) L-edge electron energy loss (EEL spectra) for regions a-f along transect in Figure 1.6. **A.** Detail of EELS core-loss map showing transect locations. **B.** Average C K-edge spectra. Vertical lines indicate features at 285.0 eV for C (aromatic C). **C.** Average Fe L_{2,3} edge spectra, showing increased peak at 710.5 eV for Fe for oxidized Fe(III).



Appendix Figure A3.1.6. Iron (Fe) K-edge X-ray absorption near-edge structure (XANES) Gaussian fit results to determine relative contribution of the peak/shoulder $\sim 7118\text{--}7120$ eV associated with increasing Fe(II) content. The Gaussian function associated with this feature is shown in red. Raw data are shown as points, other Gaussian functions in grey, and the combined model fit in black.



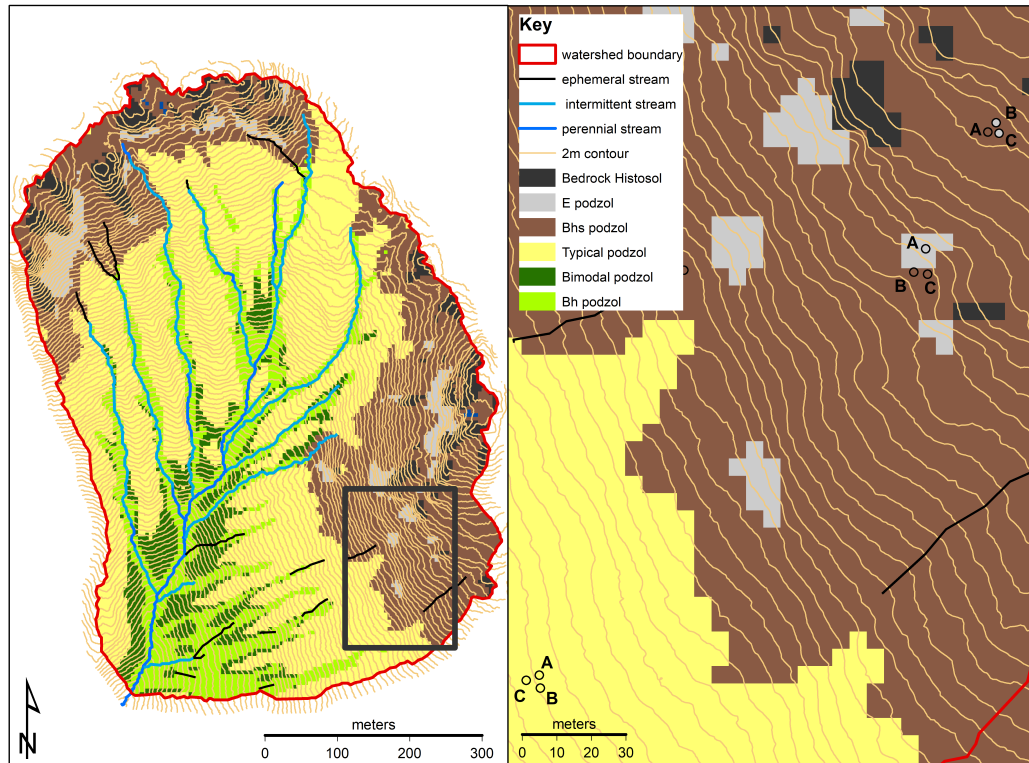
Appendix Figure A3.1.7. Iron (Fe) K-edge extended X-ray absorption fine structure (EXAFS) for co-precipitated and adsorbed DOM-Fe. Reference ferrihydrate for adsorbed and co-precipitated samples is shown with solid and dotted lines, respectively. Adsorbed and co-precipitated samples generally follow the oscillation pattern of associated ferrihydrate reference materials. **A.** Normalized (max=1) K-space (k^3 -weighted) EXAFS oscillations shows features at wavenumber ~ 5.2 and 7.5 \AA^{-1} that are lost with increased C bonding in Fe (III) citrate (red line), corresponding to decreased high-shell backscatter signal (Chen et al., 2014). **B.** Inverse Fourier-transform (R-space) of k^3 -weighted oscillations. Letters a-d correspond to Fe bonding environments assigned as follows: a = Fe-O, b = Fe-organic, and c and d = Fe-Fe (Chen et al., 2014). The shaded region (2.3-3.4 \AA) represents general high-shell backscatter (features at wavenumber 5.2 and 7.5 \AA^{-1} in **A**), lacking appreciable differences between co-precipitated and adsorbed DOM-Fe and associated ferrihydrate standards. Additional standards are shown in Appendix Figure A3.1.7.



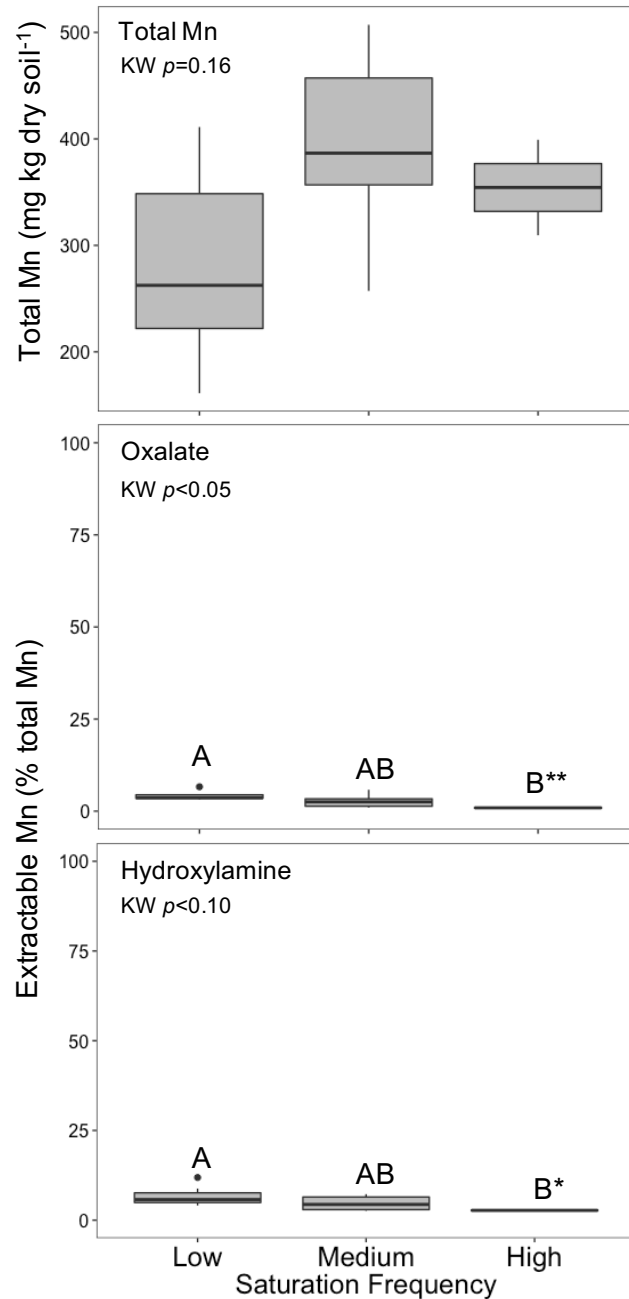
Appendix Figure A3.1.8. K-space (forward Fourier transform) of iron K-edge extended X-ray absorption fine structure (EXAFS) of standard reference materials for collection dates in May 2017, December 2017, and April 2018 with k^2 weighting.

A3.2 Chapter 2 Supplementary Figures

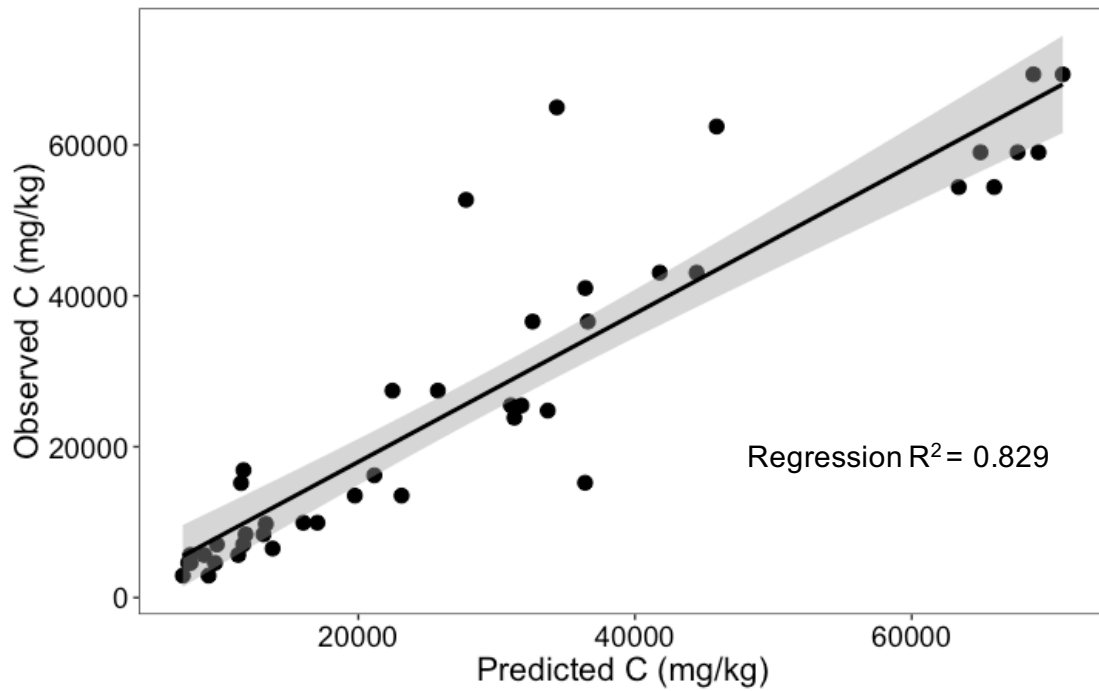
Hubbard Brook, Watershed 3, Predictive Soil Map and Sampling Sites



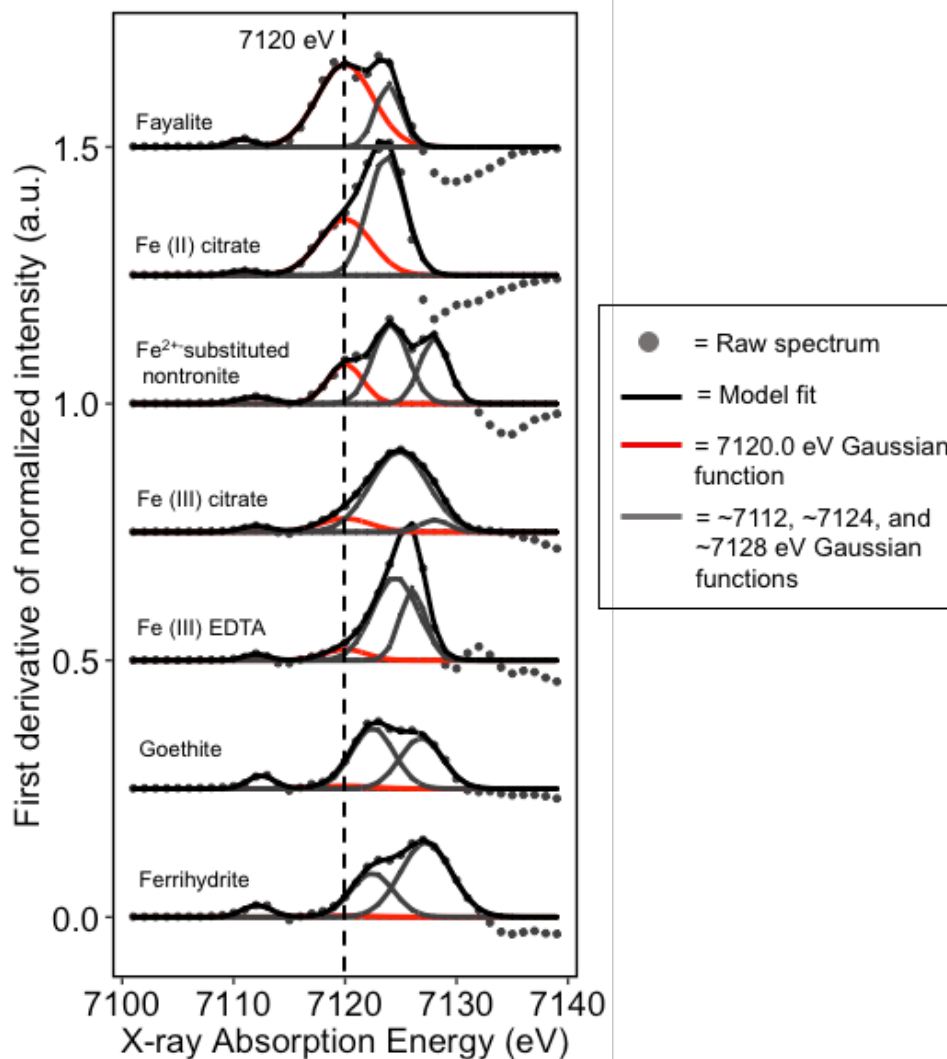
Appendix Figure A3.2.1. Map of Watershed 3, Hubbard Brook Experimental Forest, North Woodstock/Lincoln, NH. Predicted locations of hydrogeological units (HPUs) used to determine saturation frequency categories (Typical, E, and Bhs podzols) are shown in the left panel, as well as HPUs located at lower elevations in the watershed (Bimodal, Bh, Bedrock Histosol, not sampled in this study) and additional landscape features (e.g., perennial and intermittent streams). The right panel shows a detail of the area sampled in the study, with individual soil pits (A, B, and C for each soil type) colored by actual HPU designation based on field assessment.



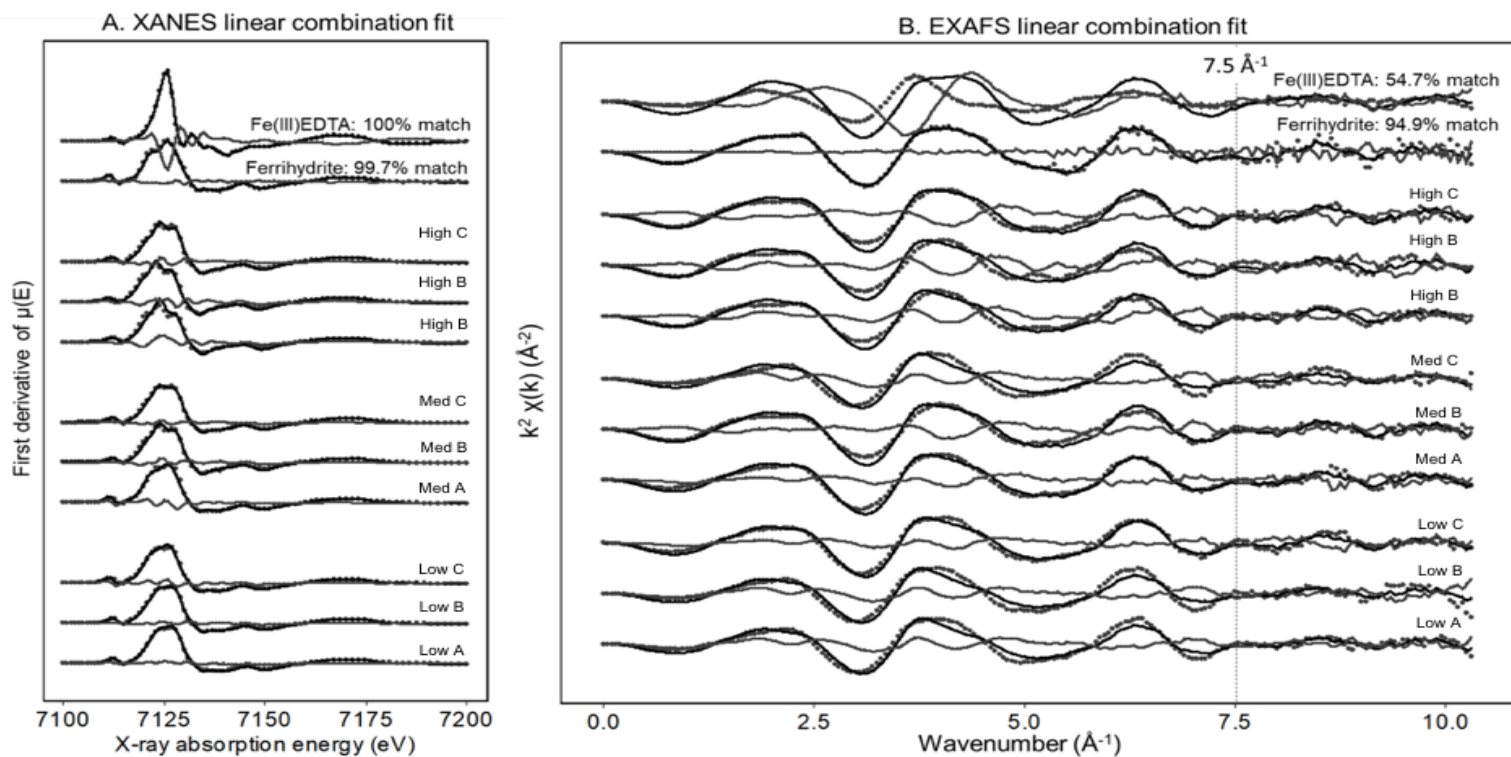
Appendix Figure A3.2.2. Bulk soil total and extractable manganese (Mn) for spodic horizons of low (n=8), medium (n=7), and high (n=2) saturation frequency soils. Within each extractant, p -values are shown for overall Kruskal-Wallis ANOVA on Ranks. Letters show post-hoc multiple comparisons (Dunn Test with Bonferroni correction), with different letters showing significant differences at $\alpha = 0.1$ (*) and $\alpha = 0.05$ (**). Lower and upper edges of boxes show first and third quartiles (25th and 75th percentiles) and lower and upper whiskers show the smallest and largest value no further than $1.5 \times$ interquartile range (IQR) of the box edges. Individual points beyond whiskers are considered outliers.



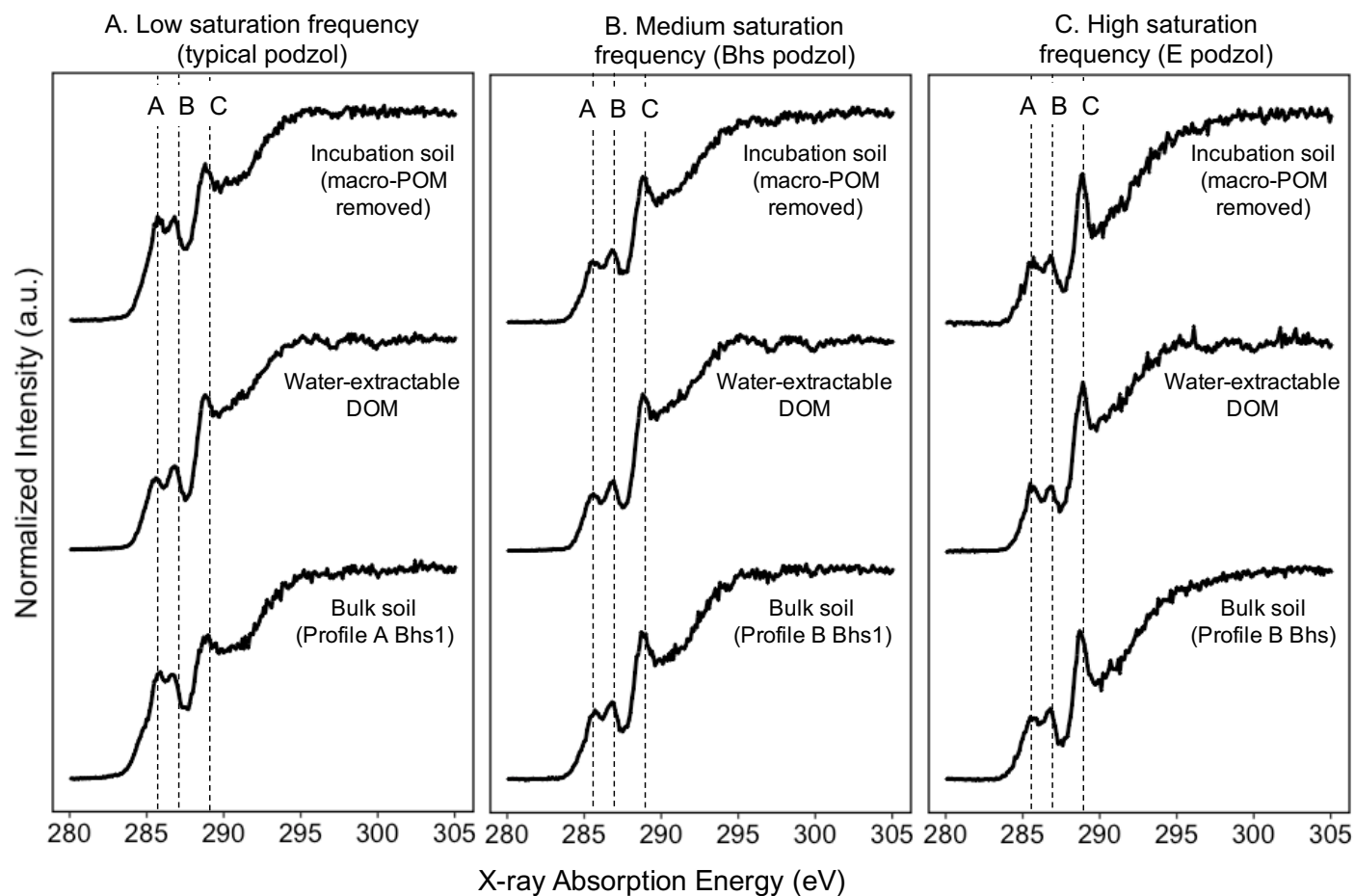
Appendix Figure A3.2.3. Random Forest regression predicted (model-derived) and observed (testing set) values of soil organic carbon (SOC). Point data show repeated (n=5) independent iterations of the regression model, fit by linear regression with the shaded region showing standard error.



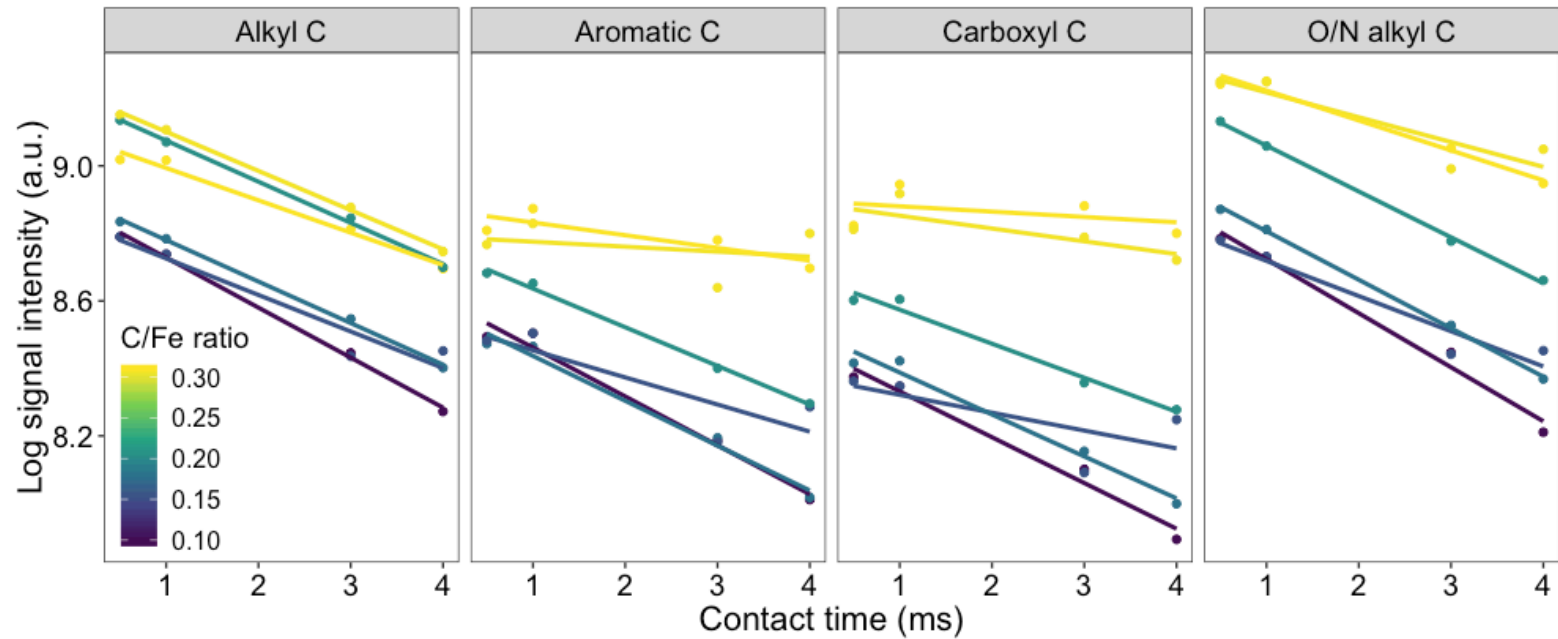
Appendix Figure A3.2.4. Iron K-edge X-ray absorption near-edge structure (XANES) first derivative of normalized fluorescent intensity ($dx/d\mu(E)$). The feature at 7120.0 eV (fixed position) is associated with the 1s-4s Fe K-edge transition (Berry et al., 2003) and is used as a proxy for increasing contribution of reduced Fe. Standard spectra show an increasing contribution of 7120 eV area from oxidized Fe mineral standards (ferrihydrite, goethite) to reduced Fe mineral standards (Fe (II) citrate, fayalite).



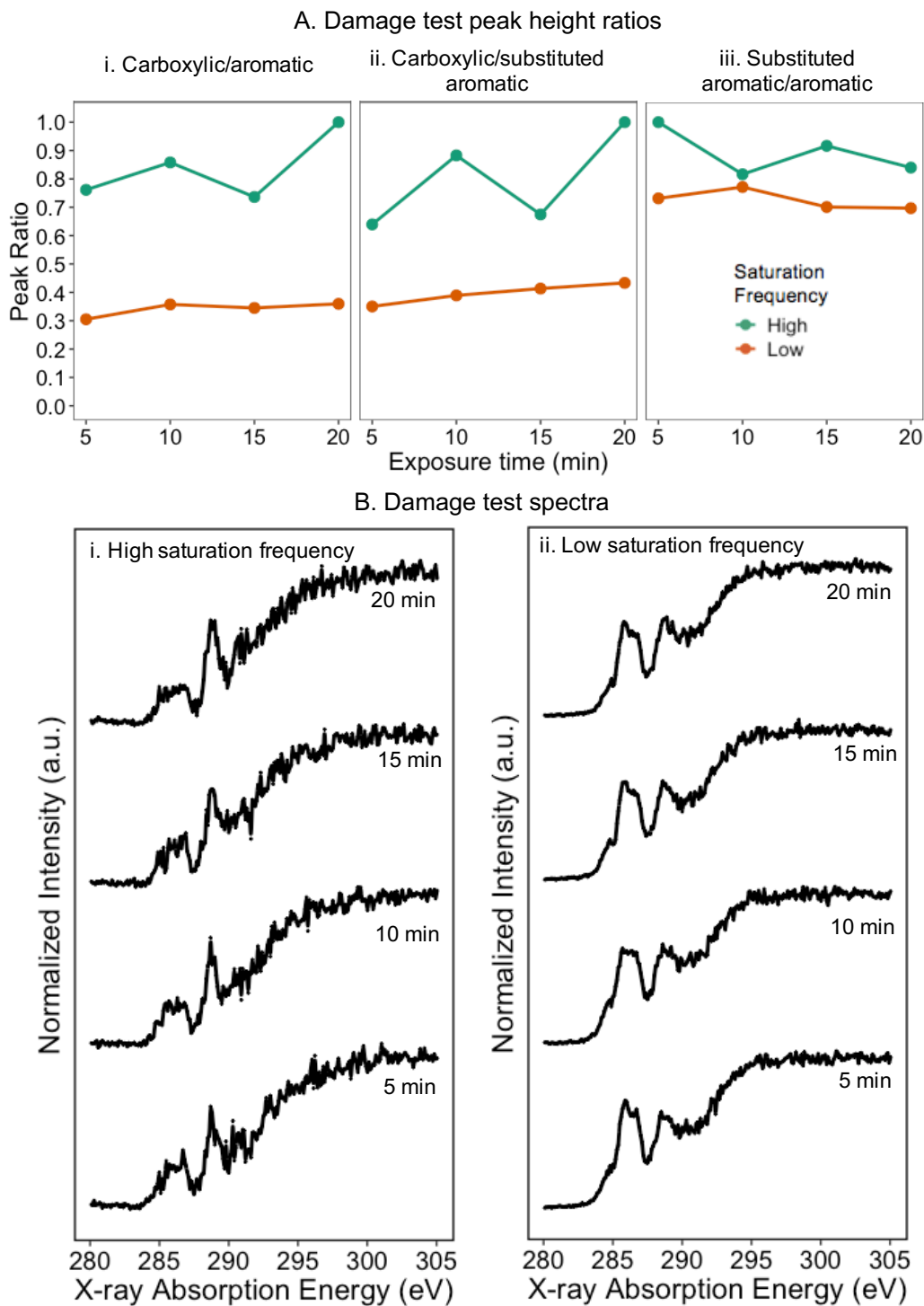
Appendix Figure A3.2.5. Linear combination fits for iron (Fe) K-edge X-ray absorption near-edge structure (XANES) (**A**) and extended X-ray absorption fine structure (EXAFS) (**B**) for replicate spodic/transitional horizons from low, medium, and high saturation frequency. Points show raw data, with the black curve showing the LCF best fit and grey line LCF residuals. For EXAFS (**B**), the feature at 7.5 \AA^{-1} is associated with outer-shell Fe bonding and is increased with decreasing Fe-organic bonding, most prominently in high saturation frequency sample B. For standards, LCF fitting procedures were applied to determine the accuracy of matching similar compounds; for XANES, Fe(III) EDTA matched 100% to Fe(III) citrate, and ferrihydrite matched 97.5% to ferrihydrite synthesized separately. For EXAFS, Fe(III) EDTA matches poorly to Fe(III) citrate (54.7%), mainly due to mismatch in the lower wavenumber region, but best represents the feature at 7.5 \AA^{-1} highlighted and was consequently used for LCF. Ferrihydrite was similarly accurate to XANES LCF at 94.9% match



Appendix Figure A3.2.6. Carbon (C) K-edge X-ray absorption fine structure (XANES) spectra for bulk soils with varying saturation frequency categories compared to water-extractable DOM and macro-particulate organic matter (POM) removed. Spectra are shown normalized to edge step = 1 and unsmoothed. Vertical lines A, B, and C indicate aromatic (~ 285.0 eV), substituted aromatic (~ 286.5 eV), and carboxylic (~ 288.7 eV) features, respectively.

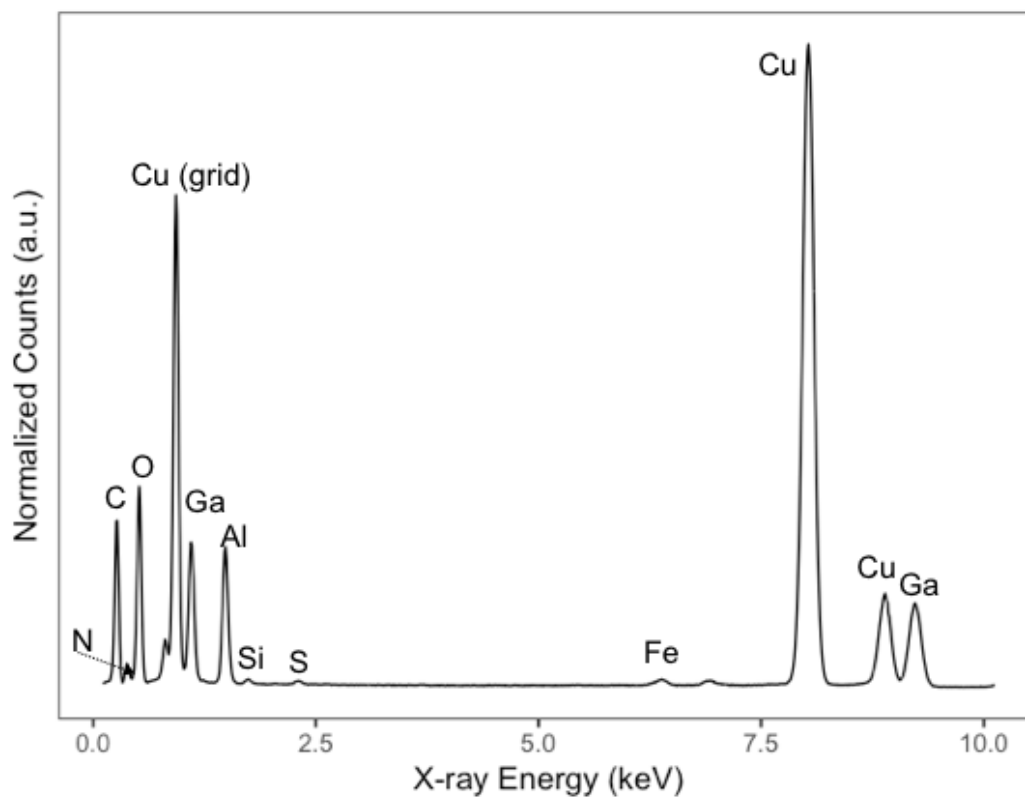


Appendix Figure A3.2.7. Signal intensity (log) decrease as a function of contact time for soil samples from shifting carbon (C) to total iron (Fe) ratios. The slope of the decrease in signal intensity is the parameter used to determine the variable contact time effect, with similar slope for alkyl and O/N alkyl C but differences in slope for aromatic and carboxylic C.

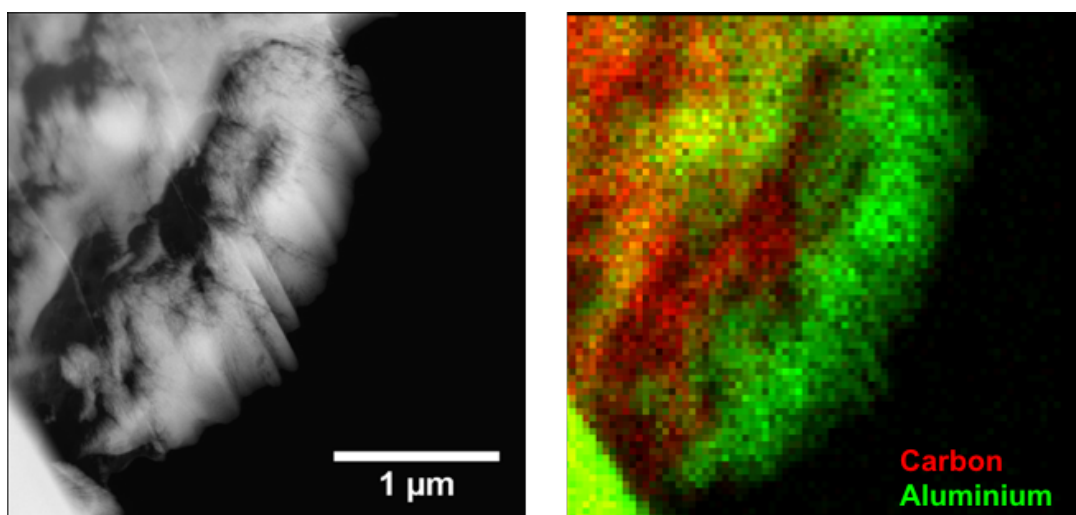


Appendix Figure A3.2.8. Damage test assessment for carbon (C) K-edge near-edge X-ray absorption fine structure. The change in carboxylic/aromatic (A.i), carboxylic/substituted aromatic (A.ii), and substituted aromatic/aromatic (A.iii.) C shows variation over time but lacks a strong direction trend associated with the large increase in dwell time. The spectra used to derive ratios are shown for high (B.i) and low (B.ii) saturation frequency, normalized to edge step=1 and unsmoothed.

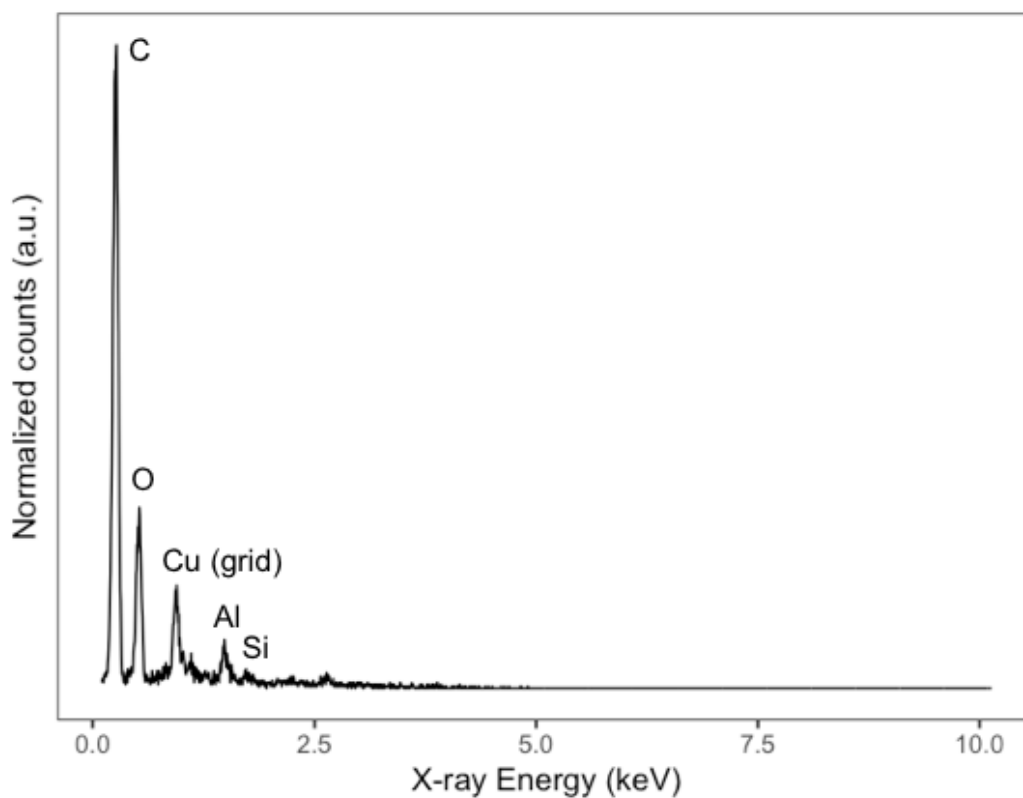
A3.3 Chapter 3 Supplementary Figures



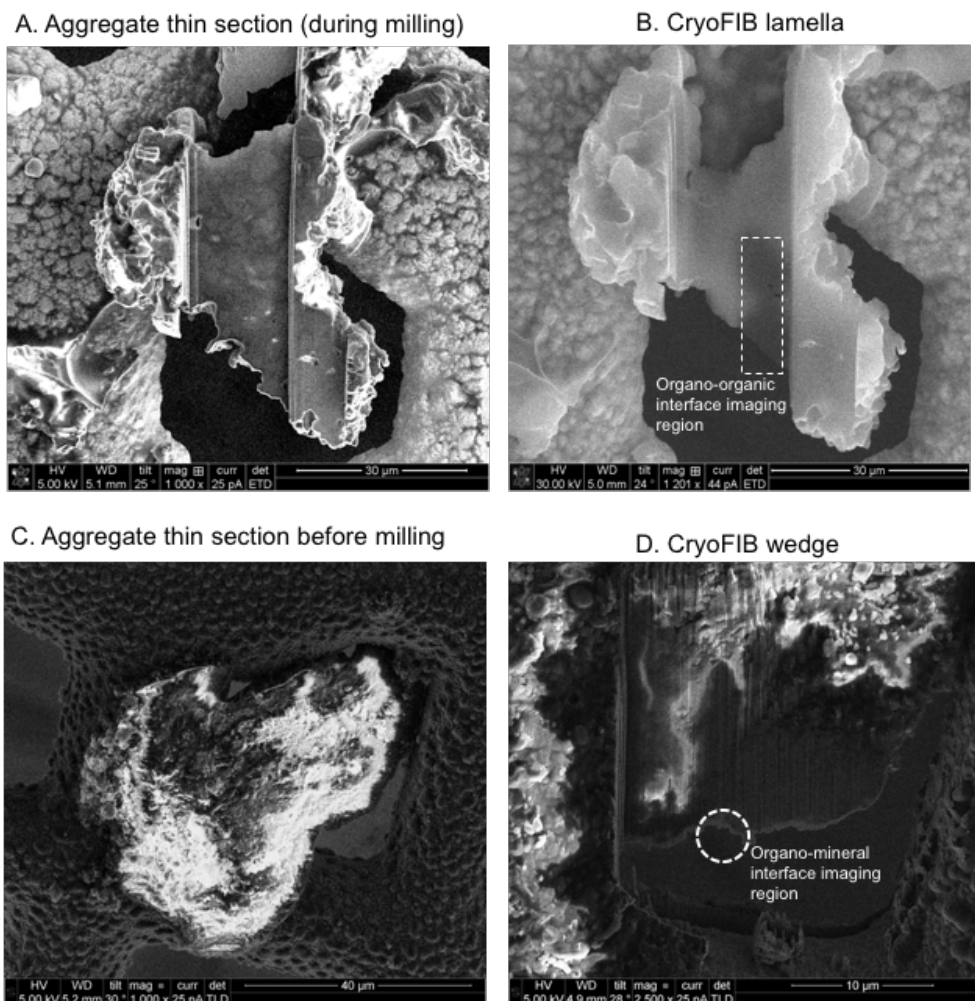
Appendix Figure A3.3.1 Scanning transmission electron microscopy-electron dispersive X-ray (STEM-EDX) sum spectrum (0.1-10 keV) for mineral region in proximity to mineral-organic interface in a volcanic soil sample analyzed with STEM-EELS (“wedge” sample). Elements were assigned to peaks using K- α edge energy positions.



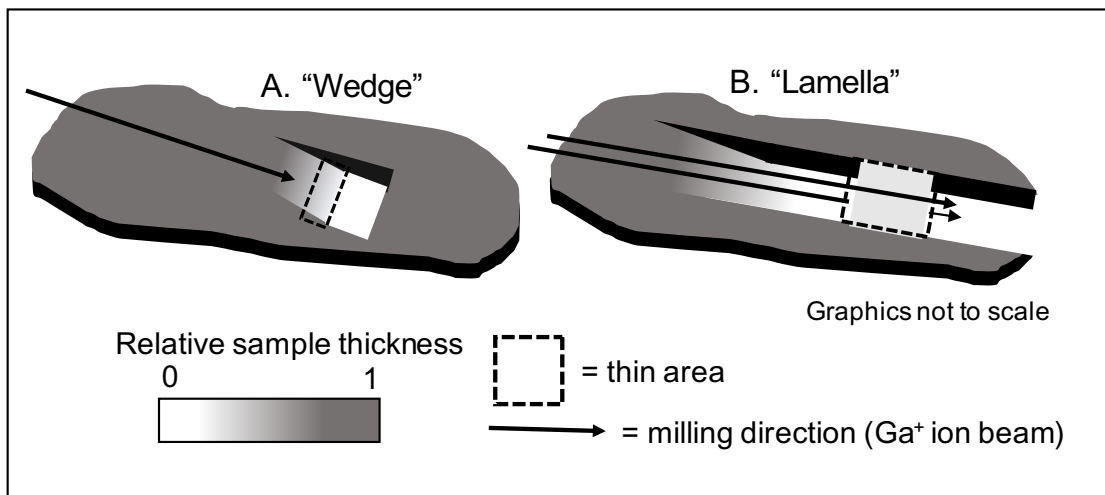
Appendix Figure A3.3.2. **A.** High angle annular dark field (HAADF) overview image of volcanic soil sample thin section with organo-mineral interface analyzed by point and linescan EELS. **B.** Elemental electron dispersive X-ray (EDX) spectroscopy map showing layered structures visible with the HAADF image identified as aluminum, with adjacent regions high in carbon.



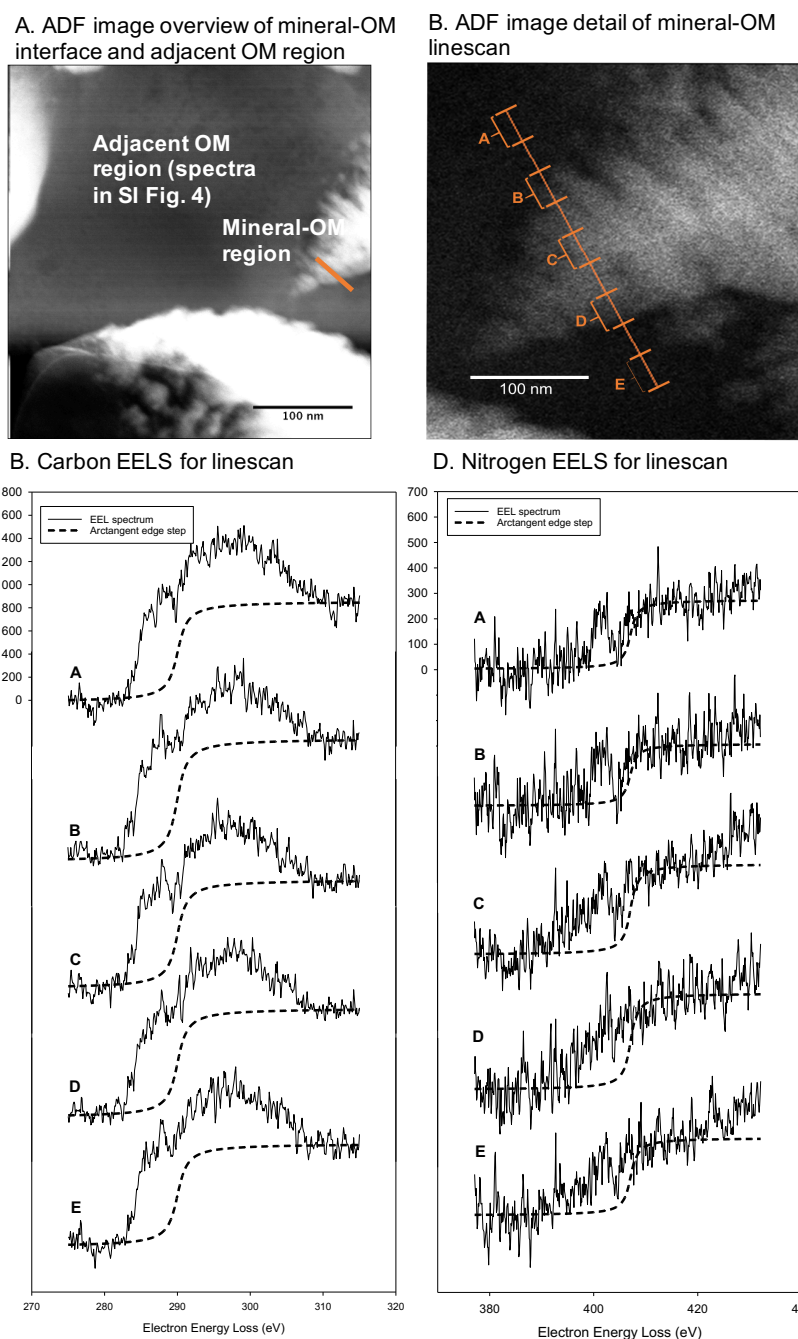
Appendix Figure A3.3.3. Scanning electron microscopy electron dispersive X-ray (SEM-EDX) spectrum (collected at 5kV) from point scan of volcanic soil sample for subsequent organo-organic interface EELS analysis prior to focused ion beam (FIB) milling and sample prep. EDX spectrum shows low Al and high C content. No features >4 keV were identified in this analysis due to 5 kV collection voltage. Elements were assigned to peaks using K- α edge energy positions.



Appendix Figure A3.3.4. Cryogenic FIB sample preparation for STEM-EELS line scan across interfaces of organo-organic and organo-mineral phases in a volcanic soil sample. **A.** Cryo-ultramicrotomed thin section of sample used for organo-organic interface analysis on grid, with initial additional thinning by cryo-FIB. Image contrast is increased to show differences associated with mineral components across the sample. **B.** Cryo-FIB thinned lamella, with electron-transparent area for STEM-EELS imaging. The white rectangle indicates the approximate area of high-spatial resolution imaging. **C.** Initial cryo-ultramicrotomed thin section for organo-mineral interface analysis on grid. **D.** Cryo-FIB thinned wedge, with electron-transparent edge for STEM-EELS imaging. The white circle indicates the approximate area of high-spatial resolution imaging.

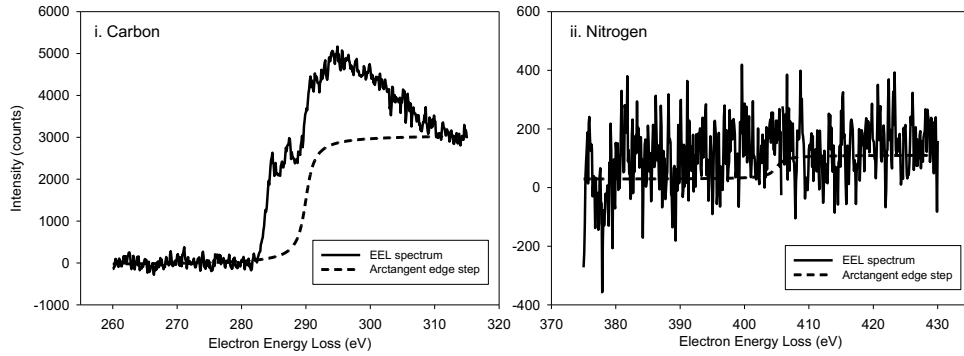


Appendix Figure A3.3.5. Simplified schematic of milling approaches. **A.** Milling to create a wedge with a gradient of thickness results generated in a thin edge for imaging (Appendix Figure A3.3.4 D). A remaining challenge is relatively small area of electron-transparent sample, and the lack of smoothing from below, which can create uneven sample topography. **B.** Milling from above and below to create a lamella of thin material (Appendix Figure A3.3.4 B) results in more electron-transparent sample of even thickness available for imaging, but the thin lamella may be less sturdy.

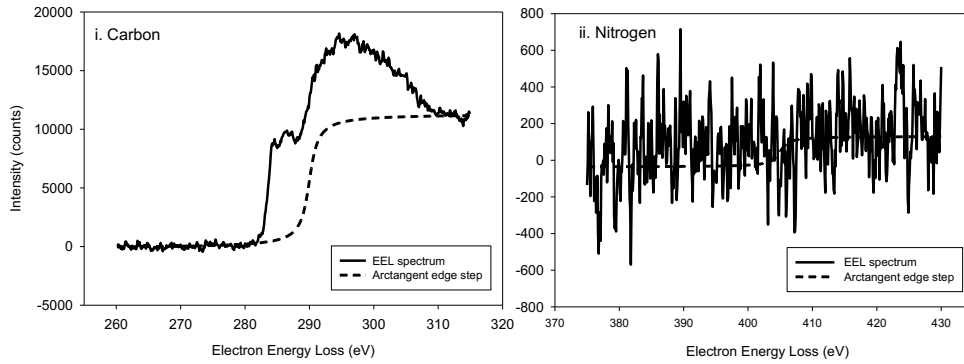


Appendix Figure A3.3.6. **A.** Annular dark field (ADF) image overview of organic matter (OM)-mineral interface and adjacent OM region. **B.** ADF image detail of linescan point locations. **C.** Carbon K-edge EELS for points A-D (average of two points on linescan) with arctangent edge step used to illustrate change in signal intensity. **D.** Nitrogen K-edge EELS for corresponding linescan points with arctangent edge step. C/N ratios determined by spectrum integration across linescan show an enrichment of N in the region closer to the mineral particle compared to adjacent OM region (spectra shown in Appendix Figure A3.3.7).

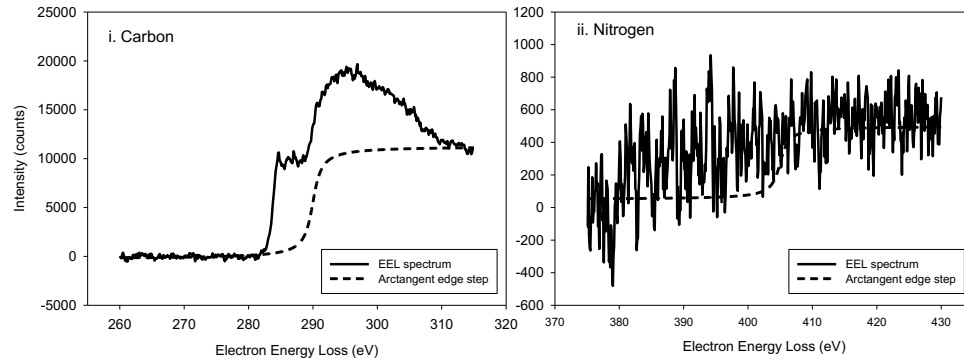
A. Point scan (lower-dose) of carbon region adjacent to organo-mineral interface



B. EELS point scan (higher-dose) of carbon region adjacent to organo-mineral interface



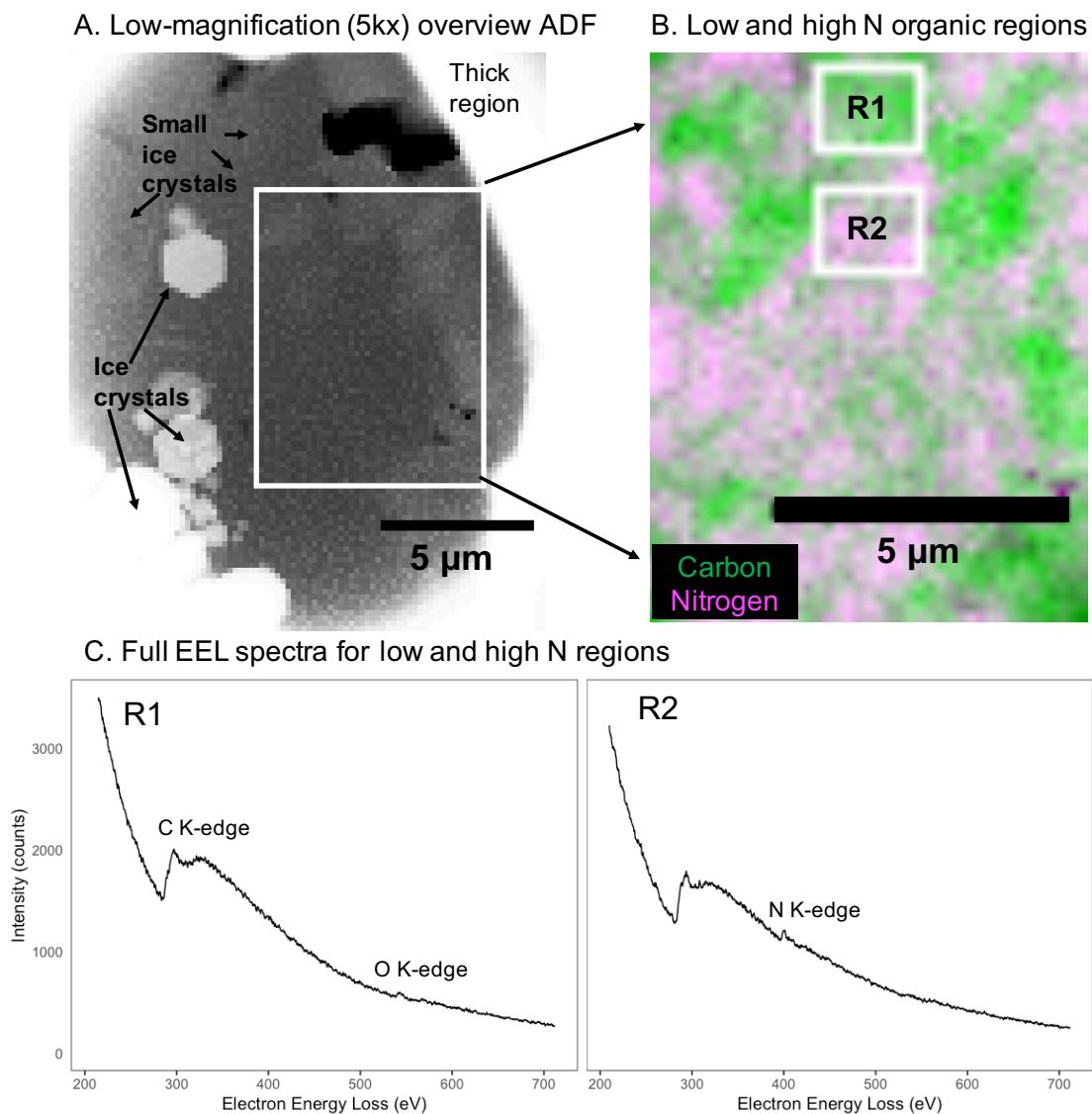
C. EELS point scan (higher-dose) of carbon region adjacent to organo-mineral interface



Appendix Figure A3.3.7. Point EELS data collected in thin carbon-rich organic region adjacent to OM-mineral interface (location shown in Appendix Figure A3.3.6).

While point scans are collected with different parameters and total counts cannot be compared between points, relative differences in C and N integrated areas show a higher (by 92%) C/N ratio compared to scans closer to the mineral interface. **A.** Point scan collected with settings of monochromator 60 with 5 s x 1 frame scan time and **B.** Point scan collected with settings of monochromator 40 with 8 s x 1 frame scan time.

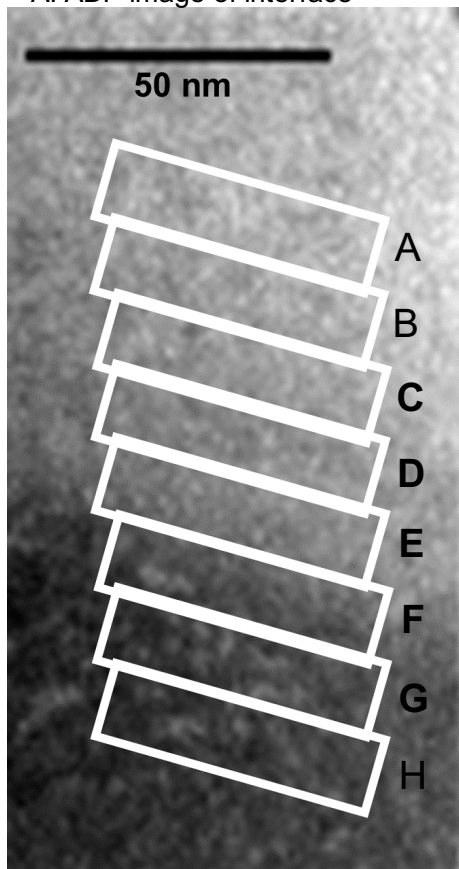
C. Point scan collected with settings of monochromator 40 with 8 s x 1 frame scan time.



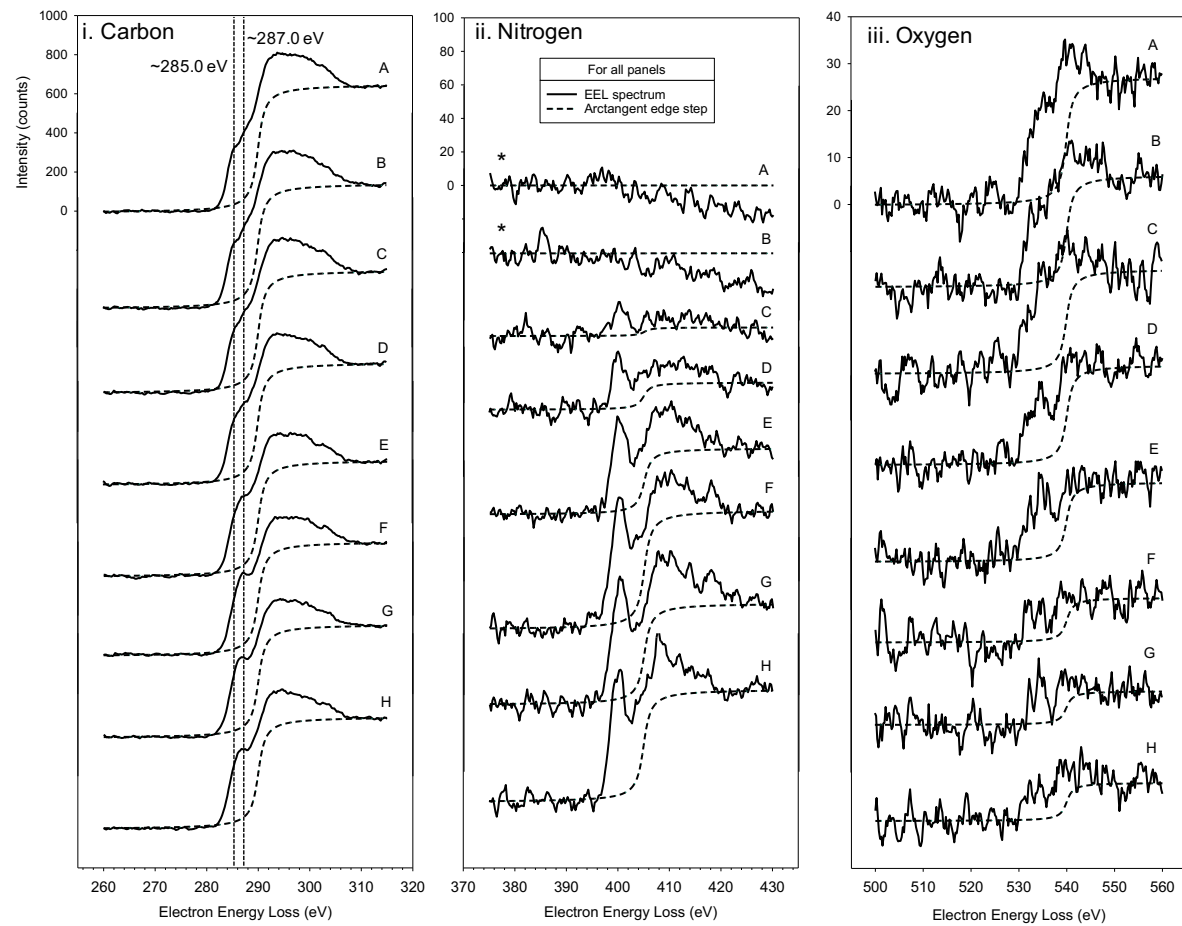
Appendix Figure A3.3.8. A. Overview low-magnification (5kx) annular dark field (ADF) image on cryo-focused ion beam (cryo-FIB) thin section of organic-rich volcanic soil. Region in white box used for subsequent electron energy loss spectroscopy (EELS) mapping of carbon (C) and nitrogen (N). **B.** EELS map of patchy distribution of low-N features in high-N matrix. **C.** Raw EELS data for representative low N (R1) and high N (R2) regions indicated by boxes in B. Spectra show the high C K-edge (~280.0 eV) intensity relative to N (~400.0 eV) and O (~530.0 eV) intensities

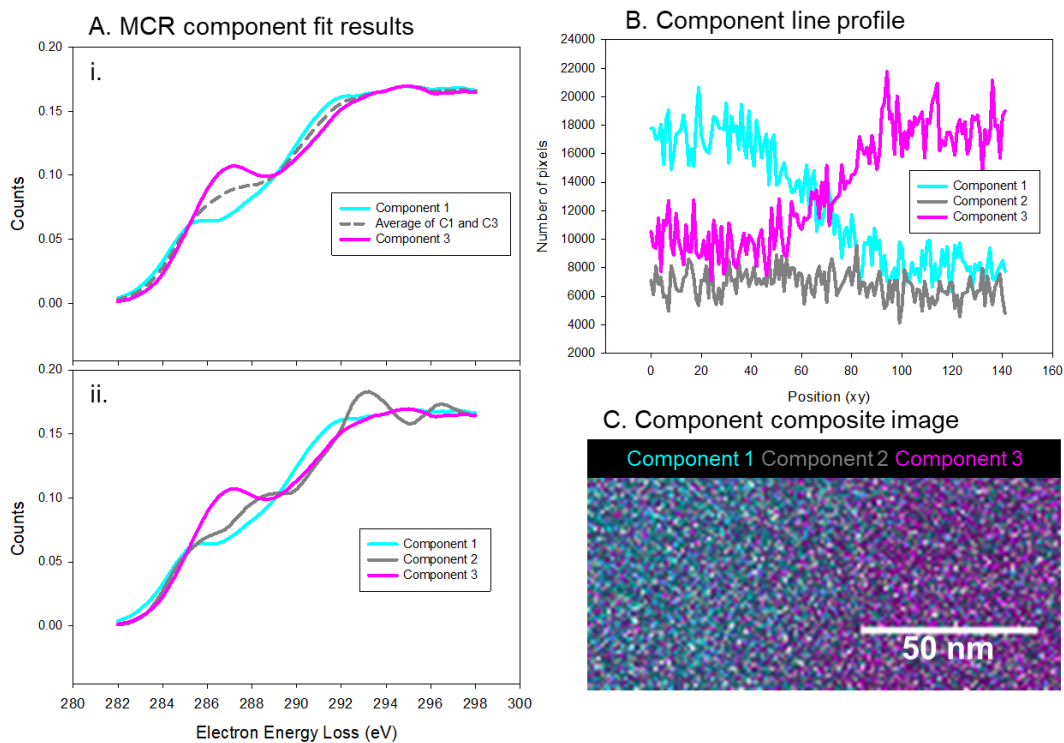
Appendix Figure A3.3.9. A. Annular dark field (ADF) image of the interface between two organic phases in a soil sample thin section. **B.** Electron energy loss spectroscopy (EELS) intensity (not normalized) for carbon (C), nitrogen (N), and oxygen (O) across the interface between two organic phases. Solid lines show EELS spectra and dashed lines show arctangent edge step fit to illustrate signal intensity changes across the interface. **B.i.** Average (11x44 nm box) electron energy loss spectroscopy (EELS) intensity for the C K-edge. Spectra show a similar intensity for C across the organic phases. Vertical dotted lines indicate features at ~285.0 and ~287.0 eV, associated with aromatic and alkyl C, respectively. **B.ii.** Average (11x44 nm box) EELS intensity for the nitrogen (N) K-edge, showing a gradual increase in N signal in the aromatic C phase approaching the interface with the N-rich, alkyl N phase. In boxes A and B (indicated by *), low N counts and proximity to the C K-edge resulted in failed background subtraction and no appreciable edge step, with N at these points considered below detection. **B.iii.** Average (11x44 nm box) EELS intensity for the oxygen (O) K-edge, showing a gradual decrease in O signal in the aromatic C phase approaching the interface with the N-rich, alkyl C phase.

A. ADF image of interface



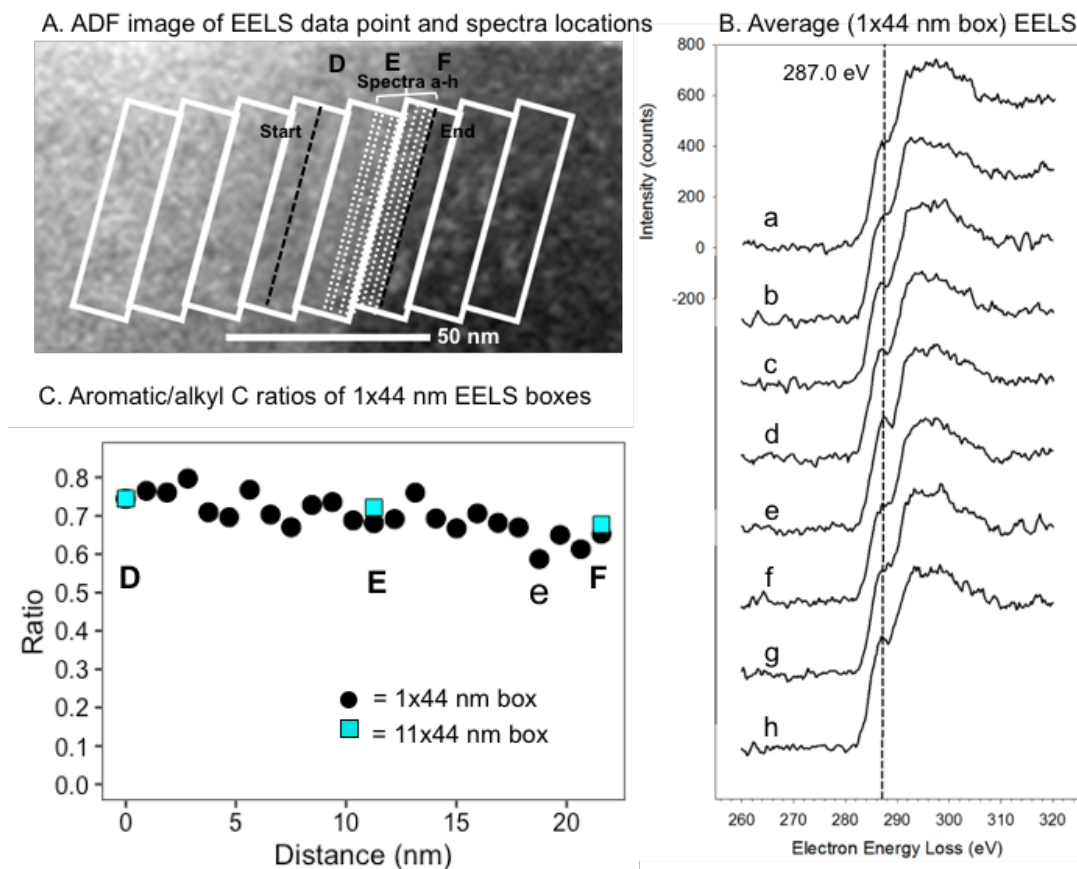
B. Average (11x44 nm box) EELS data





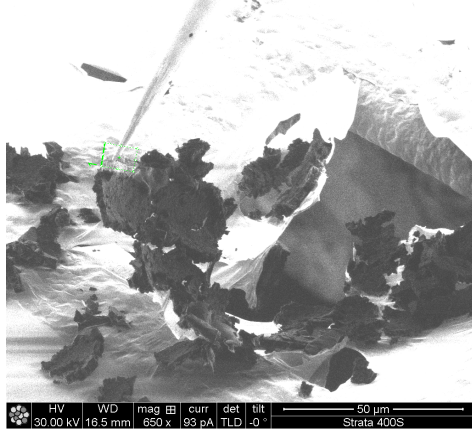
Appendix Figure A3.3.10. Three-component MCR fit results. **A.i.** Two-component fit with the average of the two components. **A.ii.** Three-component MCR fit results, with an intermediate component between component 1 and component 3 detected but no distinctive structure and additional noise compared to the average spectrum in **i.**

B. Component distribution across the analysis area. Component 2 does not vary appreciably across the sample. **C.** Three-component composite image.

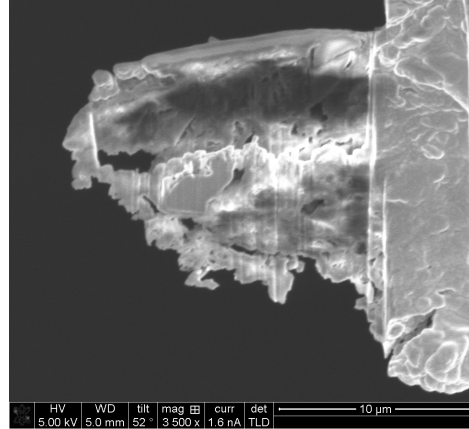


Appendix Figure A3.3.11. Organo-organic interface characterization with 1x44 nm boxes showing variable aromatic/alkyl ratios that track with larger 11x44 nm box averages. **A.** Overview annual dark field (ADF) image with beginning and ending points for 1 nm point data collected across the interface. White dotted lines show locations of spectra a through h shown in B. **B.** Average (1x44 nm box) electron energy loss (EEL) spectra (not normalized) with vertical dashed line showing alkyl C feature at ~287.0 eV. The transition from 285.0 to 287.0 eV occurs gradually over this ~8 nm region, but the increase in alkyl C intensity and associated decrease in aromatic/alkyl C ratio at spectra “e” indicates a potential location and dimensions (<3 nm) causing the alkyl enrichment observed at the interface. **C.** Overall transition of aromatic/alkyl C ratio across the interface, showing relationship between 1x44 nm and 11x44 nm box averages.

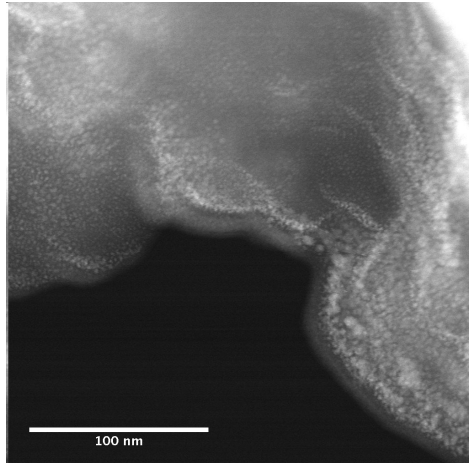
A. Room-temperature FIB lift-out



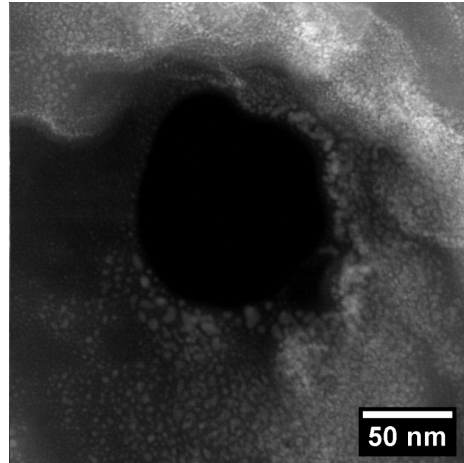
B. Room-temperature FIB sample



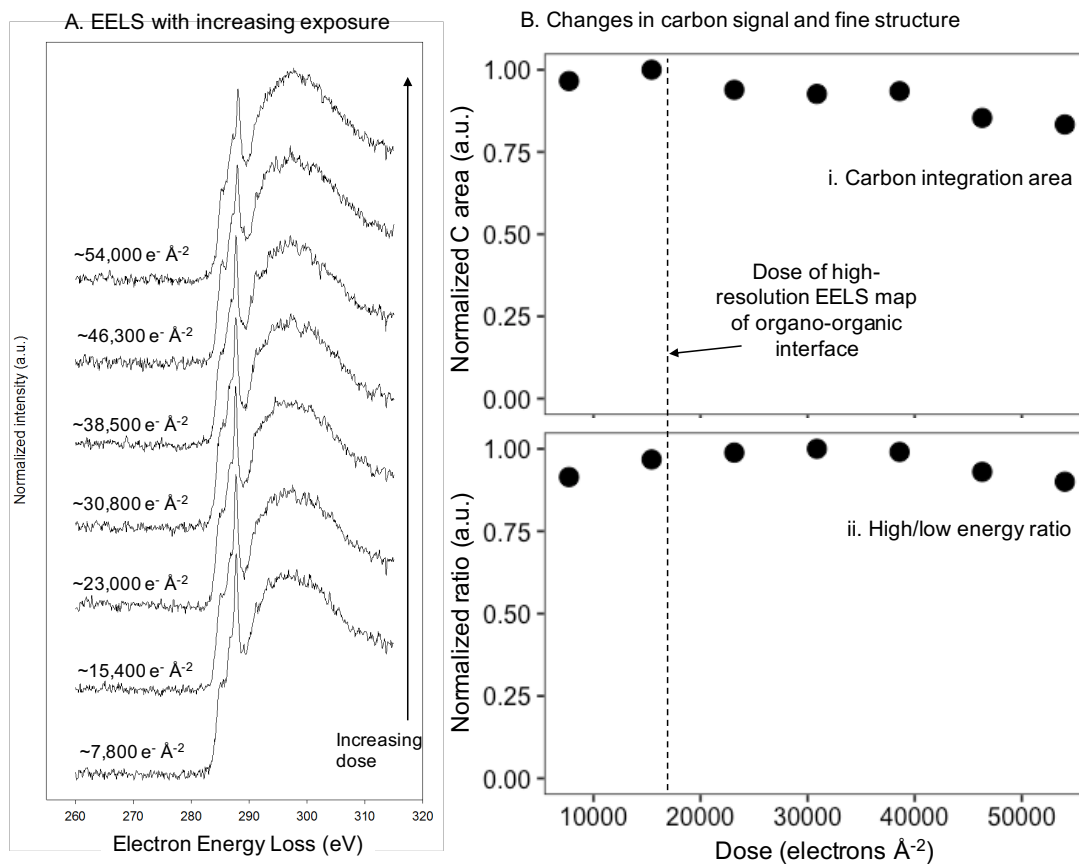
C. ADF image of FIB damage



D. ADF image of FIB damage



Appendix Figure A3.3.12. Evidence of redeposition damage resulting from room temperature focused ion beam (FIB) sample preparation of a volcanic soil sample. **A.** Scanning electron microscope (SEM) image within FIB instrument of soil aggregate thin section damage (fracturing and dispersal) from air-drying. FIB lift-out needle and attachment to broken section also shown. **B.** SEM image showing evidence of curtaining (vertical striations) in soil thin section after lift-out and FIB thinning. **C and D.** Electron microscope annular dark field (ADF) images collected of wavy distortion of sample structure, with irregular spots likely resulting from redeposition and/or gallium (Ga^+) implantation.



Appendix Figure A3.3.13. Repeated carbon (C) K-edge electron energy loss spectroscopy (EELS) measurements of a reference organo-mineral complex sample. **A.** Normalized EEL spectra for doses increasing from ~7,800 - ~54,000 electrons (e⁻) Å⁻². **B.** Effect of electron dose on total C signal (integration from 280.0-315.0 eV). Dose applied to the high-resolution EELS map of an organo-organic interface (Figures 3.2-3.3) is indicated by the dashed vertical line. **C.** Effect of electron dose on ratio of higher-energy (integrated 286.5-289.0 eV area) and lower-energy (integrated 284.5-286.5 eV area) features relative to total C integrated area.

A4. Supplementary Tables

A4.1 Chapter 1 Supplementary Tables

Appendix Table A4.1.1. Carbon (C) K-edge X-ray absorption near-edge structure (XANES) deconvolution model parameters, modified from Heymann et al. (2011).

Description	Function in model	Bond(s)	Transition	Center (eV)	Center range (+/- eV)	Height (a.u.)	FWHM (eV)	FWHM range (eV)	Inflection	Vertical position (a.u.)
Arctangent Edge step	Atan	NA (total C)	NA (total C)	290.00	Floating	1 (fixed)	NA	NA	0.335 (fixed)	0.5 (fixed)
Aromatic Quinone	G1	C=O	1 s-pi*	283.75	0.2*sin(~0)	√~0.4	0.4	0.2*sin(~0)	NA	NA
Aromatic	G2	C=C	1 s-pi*	285.20	0.2*sin(~0)	√~0.4	0.4	0.2*sin(~0)	NA	NA
Aromatic	G3	C=O	1 s-pi*	286.00	0.2*sin(~0)	√~0.4	0.4	0.2*sin(~0)	NA	NA
Aromatic w/substituent	G4	C=C-OH C=O	1 s-pi*	286.70	0.2*sin(~0)	√~0.4	0.4	0.2*sin(~0)	NA	NA
Alkyl	G5	R-(C=O)-R' C-H	1s-pi*	287.30	0.2*sin(~0)	√~0.4	0.4	0.2*sin(~0)	NA	NA
Carboxylic	G6	R-COOH COO C=O	1s-3p/sigma*	288.70	0.2*sin(~0)	√~0.4	0.4	0.2*sin(~0)	NA	NA
O-alkyl	G7	C-OH	1s-pi*	289.35	0.1*sin(~0)	√~0.4	0.4	0.2*sin(~0)	NA	NA
O-alkyl /carbonyl	G8	COO-	1s-pi*	289.85	0.1*sin(~0)	√~0.4	0.4	0.2*sin(~0)	NA	NA

Appendix Table A4.1.2. Carbon K-edge X-ray absorption near-edge structure (XANES) deconvolution results for dissolved organic matter (DOM) samples derived from typical and E podzols, and for DOM-ferrihydrate adsorption and co-precipitation solids prepared at a 10:1 C/Fe ratio. G1-G8 are Gaussian functions.

	Center (eV)	Height (a.u.)	Area (a.u.)	FWHM (eV)	Proportion (%)	Center (eV)	Height (a.u.)	Area (a.u.)	FWHM (eV)	Proportion (%)
G1	283.95	0.01	0.01	0.61	0.64	283.95	0.02	0.02	0.59	1.33
G2	285.16	0.26	0.33	1.2	32.91	285.14	0.32	0.40	1.20	34.07
G3	286.20	0.05	0.04	0.78	3.77	286.20	0.07	0.07	0.92	5.86
G4	286.54	0.08	0.05	0.61	5.16	286.52	0.10	0.08	0.72	6.43
G5	287.24	0.17	0.22	1.19	21.87	287.29	0.20	0.26	1.19	21.63
G6	288.50	0.27	0.34	1.17	34.47	288.51	0.28	0.35	1.19	29.69
G7	289.17	0.00	0.00	0.46	0.07	289.48	0.00	0.00	0.69	0.06
G8	289.76	0.03	0.01	0.41	1.12	289.78	0.02	0.01	0.56	0.93
Co-precipitate (E podzol) ($R^2=0.997$)					Co-precipitate (typical podzol) ($R^2=0.996$)					
G1	283.63	0.00	0.00	0.83	0.00	283.95	0.01	0.01	0.78	0.71
G2	285.12	0.14	0.15	1.06	14.15	285.18	0.22	0.27	1.16	24.03
G3	286.20	0.05	0.03	0.66	3.02	286.20	0.05	0.04	0.89	3.85
G4	286.58	0.09	0.05	0.59	5.00	286.50	0.07	0.05	0.66	4.10
G5	287.18	0.10	0.10	0.90	9.02	287.18	0.16	0.19	1.09	16.65
G6	288.55	0.46	0.57	1.16	52.79	288.50	0.40	0.50	1.18	44.27
G7	289.30	0.11	0.10	0.85	8.97	289.32	0.06	0.05	0.79	4.29
G8	289.77	0.09	0.08	0.79	7.06	289.75	0.06	0.02	0.40	2.10
Adsorption complex (E podzol) ($R^2=0.997$)					Adsorption complex (typical podzol) ($R^2=0.996$)					
G1	283.95	0.00	0.00	0.47	0.03	283.95	0.00	0.00	0.48	0.04
G2	285.12	0.18	0.19	0.98	14.13	285.15	0.19	0.21	1.02	18.39
G3	286.19	0.05	0.04	0.73	2.63	286.18	0.05	0.05	0.89	4.29
G4	286.58	0.07	0.05	0.62	3.61	286.54	0.08	0.05	0.59	4.39
G5	287.30	0.14	0.16	1.04	11.91	287.19	0.15	0.13	0.79	11.02
G6	288.57	0.50	0.61	1.14	45.48	288.50	0.46	0.58	1.20	50.64
G7	289.31	0.13	0.16	1.18	11.91	289.19	0.09	0.06	0.70	5.58
G8	289.81	0.13	0.14	0.97	10.29	289.75	0.10	0.06	0.64	5.65

Appendix Table A4.1.3. Summary of carbon K-edge X-ray absorption near-edge structure (XANES) deconvolution results for standard C compounds. Major NEXAFS features associated with the dominant functional groups for the standard materials are noted with (*).

Standard	Gaussian	Center (eV)	Height (a.u.)	Area (a.u.)	FWHM (eV)	Proportion (%)
Salicylic acid 2-Hydroxybenzoic acid $C_7H_6O_3$ Fit $R^2 = 0.990$	G1	283.63	0.00	0.00	0.83	0.00
	G2	285.12	0.14	0.15	1.06	14.15*
	G3	286.20	0.05	0.03	0.66	3.02
	G4	286.58	0.09	0.05	0.59	5.00
	G5	287.18	0.10	0.10	0.90	9.02
	G6	288.55	0.46	0.57	1.16	52.79*
	G7	289.30	0.11	0.10	0.85	8.97
	G8	289.77	0.09	0.08	0.79	7.06
Citric acid 2-hydroxypropane-1,2,3- tricarboxylic acid $C_6H_8O_7$ Fit $R^2 = 0.996$	G1	283.71	0.00	0.00	1.16	0.00
	G2	285.11	0.02	0.01	0.41	0.73
	G3	286.15	0.00	0.00	0.49	0.18
	G4	286.77	0.13	0.06	0.43	4.66
	G5	287.41	0.17	0.14	0.78	11.27
	G6	288.60	0.63	0.63	0.94	49.34*
	G7	289.17	0.28	0.26	0.89	20.67*
	G8	289.95	0.18	0.17	0.89	13.15*
Sucrose (2R,3R,4S,5S,6R)-2- [(2S,3S,4S,5R)-3,4- dihydroxy-2,5- bis(hydroxymethyl)oxolan- 2-yl]oxy-6- (hydroxymethyl)oxane- 3,4,5-triol $C_{12}H_{22}O_{11}$ Fit $R^2 = 0.994$	G1	283.60	0.00	0.00	0.73	0.00
	G2	285.15	0.02	0.01	0.41	1.23
	G3	286.09	0.02	0.02	0.68	2.32
	G4	286.64	0.05	0.02	0.41	3.09
	G5	287.20	0.00	0.00	0.41	0.05
	G6	288.81	0.33	0.23	0.66	33.16
	G7	289.24	0.30	0.22	0.70	31.69*
	G8	289.85	0.24	0.20	0.78	28.46*

A4.2 Chapter 2 Supplementary Tables

Appendix Table A4.2.1. Field descriptions of sampling locations for typical, Bhs, and E podzols, associated with low, medium, and high saturation frequency, respectively.

Podzol type	Profile	Latitude (decimal degrees)	Longitude (decimal degrees)	Aspect (degrees)	Slope (up) (%)	Slope (down) (%)	Physiography	Land shape	Depth to water table (m)	Depth to redox (m)
Typical (low sat. freq.)	A	43.955533	-71.718826	266	26	30	Backslope	Nose	>1.07	0.30
	B	43.955475	-71.71881	266	26	30	Backslope	Nose	0.97	0.97
	C	43.955513	-71.718896	266	26	30	Backslope	Nose	0.90	0.73
Bhs (medium sat. freq.)	A	43.956993	-71.717263	242	18	15	Shoulder	Hollow foot	0.74	0.48
	B	43.956623	-71.717486	250	23	28	Upper backslope	Hollow	0.28	0.37
	C	43.956623	-71.717486	251	27	26	Not recorded	Hollow	Not recorded	Not recorded
E (high sat. freq.)	A	43.956623	-71.717486	230	56	22	Backslope	Hollow foot	0.21	NA
	B	43.956998	-71.717241	242	18	15	Shoulder	Hollow foot	0.43	0.31
	C	43.956976	-71.717225	242	18	15	Shoulder	Hollow foot	0.35	0.15

Appendix Table A4.2.2. Field soil profiles descriptions for summarized by hydropedological units (typical, Bhs, and E), showing ranges of properties for three replicate HPU profiles. Abbreviations: Texture: SL = sandy loam, LS = loamy sand; Structure: GR = granular, SBK = sub-angular blocky, M = massive; Consistence: FR = friable, FI = firm, VFR = very friable, VFI = very firm; Roots: M = many, C = common, F = few, A = absent.

	Horizon ID	Top (m)	Bottom (m)	Matrix color range	Texture	Structure	Consistence	Coarse (%)	Roots	
Typical	1,2	Oi, Oe	0	0.05-0.11	NA	NA	NA	NA	NA	
	3	Oa	0.03-0.11	0.07-0.22	2.5YR-7.5YR 2.5/1	NA	GR	VFR, FR	0	M
	4	E	0.09-0.22	0.11-0.32	10YR 5/2	SL	GR/SBK	FR	2-7	C
	5	Bhs/Bhs1	0.11-0.32	0.14-0.40	5YR 2.5/1-2.5/2	SL	SBK	FR	2-5	C
	6	Bs/Bhs2	0.14-0.40	0.20-0.60	5YR 3/4-7.5YR 2.5/3	SL	SBK	FR	2-5	F/C
	7	Bs/BC1/Bh	0.20-0.60	0.30-0.73	7.5YR 3/4-10YR 4/4	SL	SBK	FR	2-5	F/C
	8	BC1/BC2/CB	0.30-0.73	0.67-0.90	10YR 3/4-2.5Y 5/3	SL	SBK	FR/FI	3-10	F/C
	9	BC2/CB/Cd	0.67-0.90	0.98-1.02	10YR 4/4-2.5Y 6/2	SL/LS	SBK/M	FR/FI	5-7	F/A
	10	Cd	0.97-1.02	1.07+	2.5Y 5/2-5/3	LS	M	FI/VFI	7-8	F/A
	Bhs	1,2	Oi, Oe	0	0.06-0.07	NA	NA	NA	NA	NA
3		Oa/Oa1	0.06-0.07	0.11-0.18	2.5YR 6/1-7.5YR 2.5/1	NA	GR	VFR	0	M
4		E/Bhs1/Oa2	0.11-0.18	0.17-0.37	7.5YR 2.5/1-5/2	SL	GR/SBK	VFR/FR	0-4	M/C/F
5		Bhs/Bhs1/Bhs2	0.17-0.37	0.26-0.55	5YR 2.5/2-7.5YR 3/2	SL	SBK	FR/FI	3-5	F/M
6		Bhsm/BC/Bhs1	0.26-0.55	0.47-0.74	2.5Y 5/3-7.5YR 3/3	SL	SBK	FI/FR	5-10	C/F/A
7		Bhs3/Cd	0.47-0.74	0.78-0.96	7.5YR 3/2	SL	SBK	FR	5	F
8		CB	0.96	1.21+	2.5Y 4/2	SL	M	FR	5	A
E		1,2	Oi, Oe	0	0.05	NA	NA	NA	NA	NA
	3	Oa/Oa1	0.05	0.10-0.15	5YR 2.5/1-7.5YR 2.5/1	NA	GR	VFR	0-2	M
	4	E/Oa2	0.10-0.15	0.17-0.35	7.5YR 4/2-5YR 2.5/1	SL/LS	GR/SBK	FR/VFR	5-8	F/M
	5	Bs/E1/R	0.17-0.35	0.31-0.45	10YR 5/1-7.5YR 3/4	SL/LS	SBK	FR	3-7	F/A
	6	E2/R	0.31-0.45	0.38	10YR 3/1	SL	SBK	FI	5	F
	7	Bhs	0.38	0.43	7.5YR 7.5/1	SL	SBK	FI	8	F
	8	CB	0.43	0.57	2.5 4/2	SL	M	VFI	5	A
	9	R	0.57+	NA	NA	NA	NA	NA	NA	NA

Appendix Table A4.2.3. Tree (>0.1 m diameter at breast height (DBH)) species identification for hydrogeological units (HPU) sampling sites (0.0314 ha survey area).

HPU	Species	Common name	Basal area (m ² ha ⁻¹)
Typical	<i>Fagus grandifolia</i>	American beech	1.60
	<i>Acer pensylvanicum</i>	Striped maple	1.06
	<i>Acer saccharum</i>	Sugar maple	6.87
	<i>Betula alleghaniensis</i>	Yellow birch	11.73
Bhs	<i>Fagus grandifolia</i>	American beech	1.23
	<i>Abies balsamea</i>	Balsam fir	5.68
	<i>Picea rubens</i>	Red spruce	0.59
	<i>Acer pensylvanicum</i>	Striped maple	1.12
	<i>Acer saccharum</i>	Sugar maple	1.64
	<i>Betula papyrifera</i>	White birch	6.94
	<i>Betula alleghaniensis</i>	Yellow birch	12.62
E	<i>Abies balsamea</i>	Balsam fir	3.41
	<i>Picea rubens</i>	Red spruce	9.02
	<i>Acer pensylvanicum</i>	Striped maple	5.30
	<i>Betula papyrifera</i>	White birch	0.58
	<i>Betula alleghaniensis</i>	Yellow birch	17.23

Appendix Table A4.2.4. List of sample subsets used for (1) incubation, (2) X-ray spectroscopy and hydroxylamine extraction dissolved organic carbon (DOC) mobilization, and (3) nuclear magnetic resonance variable contact time experiments (NMR VCT).

	Saturation Frequency	Profile	Horizon	C content after macro-POM removal (%)
Incubation	Low	A	Bhs1	9.94
	Medium	B	Bhs1	3.47
	High	B	Bhs	1.29
Fe K-edge and C K-edge XAS, hydroxylamine DOC experiment	Low	A	Bhs1	
	Low	B	Bhs1	
	Low	C	Bhs	
	Medium	A	Bhs	
	Medium	B	Bhs1	
	Medium	C	Bhs1	
	High	B	Bhs	
	High	B	BC	
NMR-VCT experiment	High	C	Bs	
	Low	A	Bhs1	
	Low	B	Bhs2	
	Low	C	Bh	
	Medium	A	Bhs	
	Medium	B	Bhs1	
	High	B	Bhs	

Appendix Table A4.2.5. Average (\pm standard deviation) bulk characterization data for mineral soils from eluvial (E), spodic (Bhs/Bh/Bs), transitional (BC/CB), and substratum (Cd) horizons collected from typical, Bhs, and E podzol hydropedological units with low, medium, and high saturation frequency, respectively. NA = not applicable (no horizons of that type identified).

Saturation Frequency	Horizon	pH	Volumetric water content	Total C	Total N	Total Fe	Total Al	Total Mn
			$\text{m}^3 \text{m}^{-3}$			g kg^{-1} dry soil		
Low	Eluvial (n=3)	3.1	22.3	12.9	0.71	6.4	42.6	0.29
		± 0.1	± 3.0	± 5.6	± 0.27	± 0.5	± 3.4	± 0.031
	Spodic (n=8)	3.7	35.8	60.6	2.41	25.7	52.9	0.28
		± 0.3	± 2.8	± 10.9	± 0.56	± 7.0	± 7.9	± 0.087
Transitional (n=6)	4.2	31.4	23.5	0.96	17.0	57.6	0.273.3	
	± 0.1	± 5.3	± 9.2	± 0.34	± 3.4	± 3.3	± 0.057	
Substratum (n=3)	4.5	19.8	3.6	0.18	15.9	60.5	0.31	
	± 0.1	± 1.1	± 0.9	± 0.024	± 0.6	± 1.5	± 0.061	
Medium	Eluvial (n=1)	4.0	33.8	9.9	0.53	5.6	40.2	0.36
		NA	NA	NA	NA	NA	NA	NA
	Spodic (n=7)	3.9	45.1	45.7	1.97	25.7	58.5	0.40
		± 0.2	± 10.9	± 27.2	± 1.41	± 4.7	± 2.0	± 0.086
Transitional (n=1)	4.0	29.6	16.2	0.59	20.1	59.5	0.55	
	NA	NA	NA	NA	NA	NA	NA	
High	Eluvial (n=4)	4.0	29.7	8.0	0.42	6.0	50.0	0.37
		± 0.2	± 1.6	± 2.2	± 0.076	± 1.7	± 5.5	± 0.098
	Spodic (n=2)	4.3	33.8	12.4	0.46	12.6	52.2	0.35
		± 0.1	± 7.0	± 1.5	± 0.046	± 1.7	± 2.4	± 0.063
Transitional (n=1)	4.5	34.4	15.2	0.59	26.6	69.2	0.420	
	NA	NA	NA	NA	NA	NA	NA	

Appendix Table A4.2.6. Average (\pm standard deviation) selective metal extraction values, presented as proportion of total metal content for each iron (Fe), aluminum (Al), and manganese (Mn). Abbreviations: ODOE = optical density of oxalate extract, Abs = absorbance (a.u.), H = hydroxylamine-hydrochloric acid (HCl)-extractable, O = acid ammonium oxalate-extractable, D = citrate-dithionite extractable. NA = not applicable (no horizons of that type identified).

Saturation Frequency	Horizon	ODOE	Fe-O	Al-O	Al-D	Fe-D	Mn-O	Fe-H	Al-H	Mn-H
		<u>Abs</u>				<u>(% total)</u>				
Low	Eluvial (n=3)	0.1 ± 0.1	27.9 ± 5.1	1.4 ± 0.6	0.9 ± 0.4	31.1 ± 4.7	1.7 ± 0.3	19.7 ± 6.4	1.7 ± 0.7	2.9 ± 0.5
	Spodic (n=8)	1.7 ± 0.7	67.0 ± 19.2	23.2 ± 7.3	18.2 ± 5.2	66.1 ± 14.2	4.1 ± 1.1	46.8 ± 13.1	23.3 ± 8.1	6.4 ± 2.7
	Transitional (n=6)	0.4 ± 0.2	30.9 ± 13.3	17.2 ± 6.4	11.8 ± 4.7	35.1 ± 14.5	4.8 ± 2.7	24.6 ± 6.9	18.6 ± 6.5	7.8 ± 2.6
	Substratum (n=3)	0.04 ± 0.0	12.0 ± 2.6	6.3 ± 0.3	3.3 ± 0.4	14.8 ± 1.0	21.8 ± 16.2	15.5 ± 1.9	7.7 ± 0.5	26.0 ± 15.6
	Eluvial (n=1)	0.2 NA	48.4 NA	2.6 NA	1.5 NA	38.0 NA	1.2 NA	37.4 NA	3.6 NA	2.2 NA
	Spodic (n=7)	0.7 ± 0.2	68.3 ± 10.9	12.7 ± 3.5	10.5 ± 2.9	65.6 ± 8.4	2.7 ± 1.7	54.9* ± 7.1	12.7* ± 3.7	4.7 ± 2.0
Medium	Transitional (n=1)	0.4 NA	39.3 NA	7.9 NA	6.0 NA	36.7 NA	0.6 NA	37.6 NA	9.4 NA	3.9 NA
	Eluvial (n=4)	0.2 ± 0.3	17.2 ± 9.4	2.4 ± 1.7	1.6 ± 1.4	20.4 ± 9.6	0.6 ± 0.3	16.9 ± 7.0	2.9 ± 1.6	1.9 ± 1.0
High	Spodic (n=2)	0.2 ± 0.2	44.1 ± 3.0	8.1 ± 2.5	6.2 ± 1.5	43.3 ± 1.1	0.9 ± 0.2	35.9 ± 1.5	8.4 ± 2.8	2.7 ± 0.3
	Transitional (n=1)	0.1 NA	39.1 NA	13.6 NA	9.4 NA	36.1 NA	3.1 NA	32.5 NA	13.8 NA	6.8 NA

*N=6

Appendix Table A4.2.7. Iron K-edge X-ray absorption near-edge structure (XANES) results for soil samples and standards. Edge position, white line, and pre-edge centroid are shown for normalized fluorescent (μE). The 7120.0 eV peak area is determined for the first derivative μE .

	Soil Samples			Fe(III) minerals		Fe(III)/(II) mineral	Fe(II) mineral	Fe(III)-organic complex		Fe(II)- organic
	Low (Typical)	Medium (Bhs)	High (E)	Goethite	Ferrihydrite	Fe(II)- nontronite	Fayalite	Fe (III) citrate	Fe (III) EDTA	Fe (II) citrate
Edge (E_0) (eV)	7127.3 (0.6)	7126.3 (2.1)	7125.0 (1.7)	7123	7127	7124	7123	7125	7126	7124
White line (eV)	7132.0 (0.0)	7131.7 (0.6)	7131.0 (0.0)	7131	7133	7131	7127	7134	7134	7126
Pre- edge centroid (eV)	7114.3 (0.6)	7114.3 (0.6)	7114.7 (0.6)	7114	7114	7113	7112	7114	7113	7113
7120.0 peak area (%)	10.14 (2.8)	14.32 (7.9)	21.90 (3.4)	3.17	1.28	22.10	63.13	11.81	7.57	39.43

Appendix Table A4.2.8. Carbon K-edge near-edge X-ray absorption fine structure peak energy positions (eV) and height (normalized to edge step = 1) for average (n=3 horizons \pm standard deviation in brackets only for bulk soils) spodic horizon bulk soils, soils used for incubation studies with macro (>125 μ m) particulate organic matter (POM) removed, and water-extractable dissolved organic matter derived from incubation soils.

Sample Type	Saturation Frequency	Aromatic (C=C)		Substituted aromatic (C=C-OH)		Carboxylic (C=O)	
		Peak centroid (eV)	Normalized peak height (a.u.)	Peak centroid (eV)	Normalized peak height (a.u.)	Peak centroid (eV)	Normalized peak height (a.u.)
Bulk spodic horizons soils	Low	285.7 (0.2)	0.50 (0.03)	286.7 (0.1)	0.47 (0.02)	288.8 (0.1)	0.70 (0.02)
	Medium	285.8 (0.1)	0.39 (0.06)	286.8 (0.0)	0.41 (0.04)	288.7 (0.0)	0.71 (0.02)
	High	285.6 (0.1)	0.28 (0.03)	286.8 (0.0)	0.31 (0.04)	288.8 (0.1)	0.73 (0.04)
Macro-POM removed	Low	285.7	0.50	286.8	0.50	288.8	0.75
	Medium	285.5	0.29	286.8	0.35	288.8	0.70
	High	285.7	0.32	286.8	0.33	288.9	0.72
Dissolved organic matter	Low	285.6	0.34	286.8	0.40	288.8	0.74
	Medium	285.6	0.27	286.9	0.34	288.8	0.75
	High	285.6	0.33	286.9	0.31	288.9	0.82

A4.3 Chapter 3 Supplementary Tables

Appendix Table A4.3.1. Soil properties of samples used for cryo-STEM-EELS preparations. Two approaches to cryo-FIB milling were completed using similar Andisol samples. Oxalate-extractable Fe, Al, and pH data provided by T. Inagaki (in revision). Total Fe and Al oxide, total organic C (TOC), ^{14}C data provided by K. Grant (Grant, 2019).

	Organo-mineral Interface	Organo-organic Interface
Sample location	Kohala Volcano, HI	Kohala Volcano, HI
Elevation (m)	1195	1271
Precipitation (mm)	1784	1918
Sampling depth (m)	0.7-0.9	0.7-0.9
Fe ₂ O ₃ (wt%)	16.28	18.20
Al ₂ O ₃ (wt%)	32.23	42.28
Oxalate-extractable Fe (g kg ⁻¹)	72.68	11.26
Oxalate-extractable Al (g kg ⁻¹)	106.13	28.68
TOC (mg g ⁻¹)	56.8	150.2
Bulk $\Delta^{14}\text{C}$ (‰)	-	-722.26
Radiocarbon years	-	10,250
pH	6.7	4.7

Appendix Table A4.3.2. Summary of cryo-electron energy loss spectroscopy (EELS) data collection parameters and associated raw data files. ZLP = Zero Loss Peak; mono = monochromator setting; FWHM = Full-width at half-maximum.

Description	Figures	Type	Instrument	Collection time (s)	ZLP correction	Miscellaneous	Energy resolution (eV) (ZLP FWHM)
Organo-mineral interface sample							
Organo-mineral interface linescan	Fig. 3.1 SI 3.1,2,6	Linescan	F20 (200 kV)	5	(+)2.1 eV (adj. region)	Mono 60	1.1
Adjacent C Point 1	Fig. 3.1 SI 3.1,2,7	Point scan	F20 (200 kV)	5	NA	Mono 60	1.1
Adjacent C Point 2	“	Point scan	F20 (200 kV)	8	NA	Mono 40	1.1
Adjacent C Point 3	“	Point scan	F20 (200 kV)	10	NA	Mono 40	1.1
Organo-organic interface sample							
Overview	SI 3.8	Map	Titan (120 kV)	0.01	Paired to DualEELS map	Mag 5 kx, 0.025 nA current, 38mm camera length	1.8
Organic patches at micrometer scale	Fig. 3.2	Map	Titan (120 kV)	0.01	Paired to DualEELS map	Mag 28.x kx, 0.025 nA current, 38 mm camera length	1.8

Appendix Table A4.3.2 continued

Description	Figures	Type	Instrument	Collection time (s)	ZLP correction	Miscellaneous	Energy resolution (eV) (ZLP FWHM)
Interface between organic patches	Fig. 3.2-3, SI Fig. 3.3, 8, 9, 10, 11	Map	Titan (120 kV)	0.01	Paired to DualEELS map	Magnification 320 kx, 0.025 nA current, 38 mm camera length	1.8
Damage test							
7800 electrons ($e^- \text{ \AA}^{-2}$ dose)	SI Fig. 3.13	Point scan	Titan (120 kV)	10	(-)2.5eV (adjacent region)	Mag 640kx, 0.16 nA current	0.5
15,400 $e^- \text{ \AA}^{-2}$	SI Fig. 3.13	Point scan	Titan (120 kV)	20	(-)2.5eV	Mag 640kx, 0.16 nA current	0.5
23,000 $e^- \text{ \AA}^{-2}$	SI Fig. 3.13	Point scan	Titan (120 kV)	30	(-)2.5eV	Mag 640kx, 0.16 nA current	0.5
30,800 $e^- \text{ \AA}^{-2}$	SI Fig. 3.13	Point scan	Titan (120 kV)	40	(-)2.5eV	Mag 640kx, 0.16 nA current	0.5
38,500 $e^- \text{ \AA}^{-2}$	SI Fig. 3.13	Point scan	Titan (120 kV)	50	(-)2.5eV	Mag 640kx, 0.16 nA current	0.5
46,300 $e^- \text{ \AA}^{-2}$	SI Fig. 3.13	Point scan	Titan (120 kV)	60	(-)2.5eV	Mag 640kx, 0.16 nA current	0.5
54,000 $e^- \text{ \AA}^{-2}$	SI Fig. 3.13	Point scan	Titan (120 kV)	70	(-)2.5eV	Mag 640kx, 0.16 nA current	0.5

Appendix Table A4.3.3. Calculated ratios of integrated area for carbon (C) (280.0-315 eV) and nitrogen (N) (395.0-430.0 eV), and ratio of higher-energy (286.6-289.0 eV) (region “b”) to lower-energy (284.0-286.5 eV) (region “a”) integrated intensity normalized to total C integrated intensity at the organo-mineral interface and adjacent C region in a volcanic soil sample (Figure 3.1).

Mineral-organic adjacent C region		
Point	C/N*	High/low energy region (b/a)
1	15.8	1.1
2	47.7	1.0
3	50.1	1.0
Average	43.9	1.0
Linescan of organo-mineral interface		
Point	C/N	High/low energy region (b/a)
A	3.6	1.4
B	4.0	1.5
C	2.6	1.3
D	2.6	1.3
E	2.8	1.3
Average	3.1	1.4
Adjacent vs. interface change (%)		
	C/N	High/low energy region (b/a)
Average	91.6	31.6
Minimum	91.4	18.2
Maximum	94.9	40.0

*The value of calculated EELS edge step ratios does not correspond to exact sample elemental ratios due to cross-sectional area uncertainty.

Appendix Table A4.3.4. Calculated ratios of integrated area for carbon (C) (280.0-315 eV), nitrogen (N) (395.0-430.0 eV), and oxygen (O) (530.0-565.0 eV), and ratio of aromatic (284.25-285.75 eV) to alkyl (286.0-287.5 eV) integrated intensity normalized to total C integrated intensity across the interface between two organic phases in a volcanic soil sample.

Organo-organic interface (Fig. 4)			
Box	C/N*	C/O	Aromatic/alkyl C
C	74.1	25.9	0.75
D	28.6	29.7	0.74
E	12.0	32.6	0.72
F	7.7	59.9	0.68
G	8.2	73.6	0.71
Interface change (%)			
Box F vs. G	-6.1	-18.6	-4.2

*The value of calculated EELS edge step ratios does not correspond to exact sample elemental ratios due to cross-sectional area uncertainty.